

MULTI-WAVELENGTH OBSERVATIONS
OF BARRED, FLOCCULENT GALAXIES

By

DOUGLAS LEE RATAY

A DISSERTATION PRESENTED TO THE GRADUATE SCHOOL
OF THE UNIVERSITY OF FLORIDA IN PARTIAL FULFILLMENT
OF THE REQUIREMENTS FOR THE DEGREE OF
DOCTOR OF PHILOSOPHY

UNIVERSITY OF FLORIDA

2004

Copyright 2004

by

Douglas L. Ratay

To Carlos, Debbie, Dave, Kelly, Rob, and unofficially, Joanna.

ACKNOWLEDGMENTS

From the moment I was born, I have had the amazing fortune of being surrounded by amazing, wonderful, loving, and caring people. The more that I have done, the more I have realized that I have done nothing on my own. I live in the most incredible village.

My parents are the best ever. They have loved and supported me beyond my wildest dreams. No child could imagine better parents. My success as a person is a testament to their love.

I thank Martha Reese, my high school chemistry teacher, for giving me the encouragement to become a scientist, even without saying the words. This dissertation is a direct result of spending two years in her class. Her devotion to learning and knowledge still continues to guide me.

I am incredibly lucky to have known so many wonderful professors at Connecticut College. It has been a pleasure to know and work with my advisor, Leslie Brown. I am honored to be her first Ph.D. from Conn. Catrina Hamilton, newly Dr. Hamilton, has been an incredible teacher and always a true friend.

I owe a deep debt of gratitude to John Beckman (at the Instituto de Astrofísica de Canarias) for allowing me to spend several months at the IAC working with his group. The time I spent at the IAC was very important in my life, and this thesis would not be possible without his support.

My Ph.D. advisor, Stephen Gottesman, has been a fixture in my life since 1998 when I started at the University of Florida. I could not ask for a better advisor. He has

given me the space to find my own interests in education and government, while at the same time keeping me focused on the work of my dissertation. Many advisors are able to work with students who are their mirror images. The best advisors, however, have the wisdom to shape, guide, and encourage students who choose to take a different course.

I would like to thank Jessica, Katie, and Ronald for being my favorite editors in the world. As I look forward to beginning the rest of my life, I am put at ease by knowing how much we've been through and how much strength we have shown. I am looking forward to our journey together.

I would be wrong to not also thank Matt, Adam, Bill, the Conn Labor Day Squad, Abby, the residents of Ramsay Hall, Matt, Karen, William Wyuke, Judd, Emma, Veera, Andrew, Kate, and all my other friends and classmates for their love and support through the years.

I hold Joanna Levine and David Dahari in a special place in my heart. They have been my friends throughout graduate school, and I could not imagine how empty the world would be if I did not know them.

Without the support of Catherine Garland, I would not have completed this dissertation. I will always be in her debt.

Finally, I must thank all of the funding agencies and data sources that made this project possible. This dissertation relies heavily on data from the Two Micron All Sky Survey (2MASS), the Ohio State University Bright Spiral Galaxy Survey (OSUBSGS), the Digitized Sky Survey (DSS), and the NASA Extragalactic Database (NED). The 2MASS database is a joint project of the University of Massachusetts and the Infrared Processing and Analysis Center, funded by NASA and the NSF. The OSUBSGS was

funded by grants from the NSF and the Ohio State University. The DSS was produced at the Space Telescope Science Institute under U.S. Government Grant NAG W-2166. My stipend during part of this project was funded by a NASA Florida Space Grant Fellowship. Travel to the astronomical facilities in the Canary Islands was funded by the Instituto de Astrofísica de Canarias and the University of Florida.

TABLE OF CONTENTS

	<u>Page</u>
ACKNOWLEDGMENTS	iv
LIST OF TABLES	xi
LIST OF FIGURES	xiii
ABSTRACT	xxvii
CHAPTER	
1 PROJECT DESCRIPTION	1
Galaxy Sample	2
Observations	18
Neutral Hydrogen	18
Optical	18
Near-Infrared	19
Data Analysis	19
2 INTRODUCTION TO BARRED, FLOCCULENT GALAXIES	20
The Meaning of Flocculence	20
Flocculent Galaxies with Underlying Spiral Structure	21
Spiral Structure Created By Galactic Bars	23
Spiral Structure Created By Extra-Galactic Companions	24
Implications to Smaller Scales	26
3 OPTICAL AND NEAR-INFRARED OBSERVATIONS OF BARRED, FLOCCULENT GALAXIES	28
Observations	28
NGC 1784	29
NGC 2500	31
NGC 2793	33
NGC 3055	35
NGC 3246	38
NGC 3687	40
NGC 3887	42
NGC 3930	44

	NGC 4793	47
	NGC 4900	49
	NGC 4904	53
	NGC 5147	57
	NGC 5300	59
	NGC 5645	62
	NGC 5783	64
	NGC 6012	66
	Analysis of Optical Bar and Disk Properties	70
4	DESCRIPTION OF NEUTRAL HYDROGEN OBSERVATIONS	76
	Twenty-One Centimeter Hydrogen Emission	76
	Fundamentals of Interferometry	78
	Calibration and Imaging Neutral Hydrogen Data	81
5	NEUTRAL HYDROGEN OBSERVATIONS OF NGC 1784	84
	Observations	84
	Neutral Hydrogen Morphology	86
	Continuum	89
	Low Resolution Neutral Hydrogen Distribution	89
	High Resolution Neutral Hydrogen Distribution	90
	Global Neutral Hydrogen Properties	92
	Neutral Hydrogen Kinematics	93
	Global Position-Velocity Plots	95
	Local Low-Density Region Position-Velocity Plots	100
	Rotation Curves	104
	Model Disks, Velocity Residuals, and Corotation	107
	The Neutral Hydrogen Rings	109
	Summary	112
6	NEUTRAL HYDROGEN OBSERVATIONS OF NGC 3055	114
	Observations	114
	Neutral Hydrogen Morphology	116
	Low Resolution Neutral Hydrogen Morphology	116
	High Resolution Neutral Hydrogen Morphology	119
	Global Neutral Hydrogen Properties	121
	Neutral Hydrogen Kinematics	122
	Position-Velocity Plots	123
	Rotation Curves and Model Disks	126
	Neutral Hydrogen Companions	132
	Summary	136

7	NEUTRAL HYDROGEN OBSERVATIONS OF NGC 3930	138
	Observations	138
	Neutral Hydrogen Morphology	139
	Low Resolution Neutral Hydrogen Morphology	142
	High Resolution Neutral Hydrogen Morphology	143
	Global Neutral Hydrogen Properties	145
	Neutral Hydrogen Kinematics	146
	Position Velocity Plots	149
	Rotation Curves and Model Disks	151
	Summary	159
8	NEUTRAL HYDROGEN OBSERVATIONS OF NGC 4900	160
	Observations	160
	Neutral Hydrogen Morphology	162
	Low Resolution Neutral Hydrogen Morphology	162
	High Resolution Neutral Hydrogen Morphology	169
	Global Neutral Hydrogen Properties	170
	Neutral Hydrogen Kinematics	172
	Position-Velocity Plots	174
	Rotation Curves and Model Disks	178
	Neutral Hydrogen Ring	181
	Summary	185
9	NEUTRAL HYDROGEN OBSERVATIONS OF NGC 4904	186
	Observations	186
	Neutral Hydrogen Morphology	188
	Low Resolution Neutral Hydrogen Morphology	188
	High Resolution Neutral Hydrogen Morphology	192
	Global Neutral Hydrogen Properties	193
	Neutral Hydrogen Kinematics	196
	Position-Velocity Plots	199
	Rotation Curves and Model Disks	203
	Summary	207
10	NEUTRAL HYDROGEN OBSERVATIONS OF NGC 5300	208
	Observations	208
	Neutral Hydrogen Morphology	210
	Low Resolution Neutral Hydrogen Morphology	210
	High Resolution Neutral Hydrogen Morphology	214
	Global Neutral Hydrogen Properties	216
	Neutral Hydrogen Kinematics	217
	Position-Velocity Plots	220
	Rotation Curves and Model Disks	222

Summary.....	225
11 NEUTRAL HYDROGEN OBSERVATIONS OF NGC 6012	228
Observations	228
Neutral Hydrogen Morphology	230
Low Resolution Neutral Hydrogen Morphology	230
High Resolution Neutral Hydrogen Morphology.....	233
Global Neutral Hydrogen Properties	236
Neutral Hydrogen Kinematics.....	237
Position-Velocity Plots.....	240
High Resolution Small Scale P-V Plots	242
Rotation Curves and Model Disks.....	243
Summary.....	250
12 ANALYSIS, SUMMARY, AND FUTURE WORK	253
Are Elmegreen & Elmegreen's (1982) Arm Structure Classifications Valid For Our Sample Galaxies?.....	253
Do the Galaxies in the Sample Possess Near Infrared Spiral Structure?.....	254
Does the Sample of Optically Barred Galaxies Possess Near Infrared Bars?	255
What are the Nature of the Optical and Near-Infrared Bars?	255
Are The Mass Distributions Of Galaxies Similar?	260
Does the Sample of Optically Barred, Flocculent Galaxies Possess Similar Neutral Hydrogen Mass Ratios and Morphologies?.....	262
Do the Optically Barred, Flocculent Galaxies Possess HI Companions?	267
What are the Physical and Orbital Properties of the HI Companions?.....	268
Are Barred, Flocculent Galaxies Different Than the Average Galaxy?	269
Summary.....	271
Future Work.....	273
LIST OF REFERENCES.....	277
BIOGRAPHICAL SKETCH	282

LIST OF TABLES

<u>Table</u>	<u>page</u>
1-1. NGC 1784: Previously observed properties	4
1-2. NGC 2500: Previously observed properties	4
1-3. NGC 2793: Previously observed properties	5
1-4. NGC 3055: Previously observed properties	5
1-5. NGC 3246: Previously observed properties	6
1-6. NGC 3687: Previously observed properties	6
1-7. NGC 3887: Previously observed properties	7
1-8. NGC 3930: Previously observed properties	7
1-9. NGC 4793: Previously observed properties	8
1-10. NGC 4900: Previously observed properties	8
1-11. NGC 4904: Previously observed properties	9
1-12. NGC 5147: Previously observed properties	9
1-13. NGC 5300: Previously observed properties	9
1-14. NGC 5645: Previously observed properties	10
1-15. NGC 5783: Previously observed properties	10
1-16. NGC 6012: Previously observed properties	11
5-1. Parameters of VLA HI observations of NGC 1784.....	85
5-2. Characteristics of Naturally Weighted CLEANed Channel Maps	86
6-1. Parameters of VLA HI observations of NGC 3055.....	115
6-2. Characteristics of Naturally Weighted CLEANed Channel Maps	115

7-1. Parameters of VLA HI observations of NGC 3930.....	138
7-2. Characteristics of Naturally Weighted CLEANed Channel Maps	139
8-1. Parameters of VLA HI observations of NGC 4900.....	161
8-2. Characteristics of Naturally Weighted CLEANed Channel Maps	161
9-1. Parameters of VLA HI observations of NGC 4904.....	187
9-2. Characteristics of Naturally Weighted CLEANed Channel Maps	187
10-1: Parameters of VLA HI observations of NGC 5300.....	209
10-2. Characteristics of Naturally Weighted CLEANed Channel Maps	209
11-1. Parameters of VLA HI observations of NGC 6012.....	229
11-2. Characteristics of Naturally Weighted CLEANed Channel Maps	229

LIST OF FIGURES

<u>Figure</u>	<u>page</u>
1-1. Distribution of Hubble Type within our galaxy sample. This distribution does not take into account bar (B or AB) status.	13
1-2. Hubble bar classification distribution of the galaxy sample.....	14
1-3. Elmegreen arm class distribution of the galaxy sample	14
1-4. Distribution of Hubble Classification and Elmegreen arm classification. The stripes across the bars represent the number of galaxies of a particular arm class (labeled at right) in that Hubble Type.	15
1-5. Distribution of Bar Classification and Elmegreen arm classification. The stripes across the bars represent the number of galaxies of a particular arm class (labeled at right) in that Hubble Type.	15
1-6. Radial velocity distribution of the galaxy sample. Velocity bins are separated by 500 km s^{-1} , corresponding to 7 Mpc, where $H_0=70 \text{ km s}^{-1} \text{ Mpc}^{-1}$	16
1-7. Angular size distribution of galaxy sample	16
1-8. Apparent magnitude distribution of the galaxy sample.....	17
1-9. Distribution of previously measured HI spectrum asymmetry measure in sample galaxies.....	17
3-1. Optical R-band DSS image of NGC 1784.....	30
3-2. R-band DSS image of NGC 2500.....	32
3-3. 2-MASS K-band image of NGC 2500	32
3-4. R-band image of NGC 2793 from IAC80	34
3-5. K-band image of NGC 2793 from 2-MASS. This image is rotated 180° and reflected relative to the y-axis with respect to our IAC80 image in Figure 3-6.....	34
3-6. Optical R-band image of NGC 3055, taken at the IAC80 telescope.....	36
3-7. Optical B-band image of NGC 3055 taken with the IAC80 telescope.....	37

3-8. Near-Infrared K-band image of NGC 3055, taken with the TCS.....	37
3-9. R-band image of NGC 3246 from IAC80	39
3-10. K-band image of NGC 3246 from 2-MASS.....	39
3-11. R-band image of NGC 3687 from IAC80	41
3-12. B-band image of NGC 3687 from IAC80	41
3-13. K-band image of NGC 3687 from 2-MASS.....	42
3-14. R-band image of NGC 3887 from IAC80	43
3-15. K-band image of NGC 3887 from 2-MASS.....	44
3-16. Optical R-band image of NGC 3930 taken with IAC80 telescope.....	45
3-17. Optical B-band image of NGC 3930	46
3-18. B-R color map of NGC 3930. Light grayscale regions are blue in color. Darker grayscale regions correspond to red colors.	46
3-19. R-band image of NGC 4793 from IAC80	48
3-20. K-band image of NGC 4793 from 2-MASS. This image is rotated 180° and flipped along the y-axis relative to the R-band IAC80 image in Figure 3-19.....	49
3-21. Optical R-band image of NGC 4900 taken with the IAC 80 telescope.....	51
3-22. Optical B-band image of NGC 4900 taken at the IAC80 telescope.....	51
3-23. B-R color map of NGC 4900. Light grayscale regions are blue in color. Darker grayscale regions correspond to red colors.	52
3-24. H-band image of NGC 4900 from Ohio State.....	53
3-25. Optical R-band image of NGC 4904 taken with IAC80 telescope.....	55
3-26. Optical B-band image of NGC 4904 taken with IAC 80	55
3-27. B-R color map of NGC 4904. Light grayscale regions are blue in color. Darker grayscale regions correspond to red colors.	56
3-28. K-band image of NGC 4904 taken at TCS.....	56
3-29. R-band image of NGC 5147 from DSS.....	58
3-30. K-band image of NGC 5147 from 2-MASS.....	58

3-31. Optical R-band image of NGC 5300 taken at IAC80.....	59
3-32. Optical B-band image of NGC 5300 taken with IAC80	60
3-33. B-R color map of NGC 5300. Light grayscale regions are blue in color. Darker grayscale regions correspond to red colors.	61
3-34. R-band image of NGC 5645 from IAC80	63
3-35. B-band image of NGC 5645 from IAC80	63
3-36. K-band image of NGC 5645 from 2-MASS. This image is rotated 180° and flipped along the y-axis relative to the R-band IAC80 image in Figure 3-35.....	64
3-37. R-band image of NGC 5783 from IAC80	65
3-38. K-band image of NGC 5783 from 2-MASS.....	66
3-39. Optical R-band image of NGC 6012	68
3-40. Optical B-band image of NGC 6012	69
3-41. B-R color map of NGC 5300. Light grayscale regions are blue in color. Darker grayscale regions correspond to red colors.	69
3-42. K-band image of NGC 6012 taken at TCS.....	70
3-43. Distribution of the optical diameters of galaxies in the sample set. The strips across the columns represent the amount of galaxies from particular Elmegreen arm class (labeled at right) within that size bin.....	73
3-44. Distribution of the optical semi-major axis length in the sample set. The strips across the columns represent the Hubble bar class of that galaxy (labeled at right) within the particular size bin.	73
3-45. Distribution of the bar axis ratio for the sample set. The strips across the columns represent the Hubble bar class of the galaxies (labeled at right) within the particular bar axis ratio bin.	74
3-46. Distribution of the bar axis ratio for the sample set. The strips across the columns represent the Elmegreen arm class of the galaxies (labeled at right) with in the particular bar axis ratio bin.	74
3-47. Distribution of the bar length to galaxy radius ratio for the sample set. The strips across the columns represent the amount of galaxies from particular Elmegreen arm class (labeled at right) within that bar length ratio bin.	75

3-48. Comparison of bar axis ratio to bar/galaxy length ratio. Strips across the columns represent the number of galaxies within a range of bar axis ratio with respect to the bar length bin.	75
5-1. The individual, naturally weighted, CLEANed channel images of the low resolution data.	87
5-2. The individual, naturally weighted, CLEANed channel images of the low resolution data.	88
5-3. Grayscale with contours of the total HI surface density from the low resolution data set.	89
5-4. High Resolution HI surface density maps.	91
5-5. The HI flux density versus velocity for the low resolution data set.	93
5-6. The HI radial density profiles from the low resolution data set (circles) and the high resolution data set (triangles)	94
5-7. Intensity-weighted radial velocity contours of the low resolution data.	94
5-8. Intensity-weighted radial velocity contours of the high resolution data set.	95
5-9. A set of P-V slices parallel to and along the major axis of NGC 1784. The contours are at 2, 3, 5, 10, 15, and 25 σ . The inner ring feature is labeled with "IN" in the plot along the major axis. The central velocity is at $2.308 \times 10^6 \text{ m s}^{-1}$	97
5-10. A set of P-V slices parallel to and along the minor axis of NGC 1784. The contours are at 2, 3, 5, 10, 15, 20, and 25 σ . The systemic velocity of the system is at $2.308 \times 10^6 \text{ m s}^{-1}$	98
5-11. Thick P-V slices of NGC 1784.	99
5-12. A P-V slice through low density region A. Contours are at 2, 3, 5, and 10 σ	102
5-13. A P-V slice through low density region B. Contours are at 2, 3, 5, and 10 σ	103
5-14. A P-V slice through low density region C. Contours are at 2, 3, 5, and 10 σ	103
5-15. A P-V slice through object D. Contours are at 2, 3, 5, and 10 σ	104
5-16. Rotation curve of NGC 1784 from the high resolution data set. Stars represent the approaching half of the galaxy. Triangles represent the receding half of the galaxy. Circles represent the average of both.	105

5-17. Kinematic position angle of NGC 1784 as a function of radius. Stars represent the approaching half of the galaxy. Triangles represent the receding half of the galaxy. Circles represent the average of both.....	106
5-18. Inclination angle of NGC 1784 as a function of radius. Stars represent the approaching half of the galaxy. Triangles represent the receding half of the galaxy. Circles represent the average of both.	107
5-19. Model velocity and residual velocity fields for NGC 1784.	108
5-20. The HI flux versus velocity for the HI rings using the low resolution data set. The velocity resolution here is 20 km s^{-1} . The peak at roughly 2350 km s^{-1} represents the inner ring. The peak at roughly 2450 km s^{-1} represents the outer ring.	111
6-1. Individual, naturally weighted, CLEANed channel images of the low resolution data.	117
6-2. Individual, naturally weighted, CLEANed channel images of the high resolution data.	118
6-3. Grayscale with contours of the total HI surface density from the low resolution data set.	119
6-4. Grayscale and contours of the total HI surface density from the high resolution data set.....	120
6-5. Contours of the high resolution data set overlaid on a DSS image of NGC 3055. The peak flux and contours are the same as in Figure 6-4. The synthesized beam is shown at the bottom left.....	120
6-6. The HI flux density versus velocity for the low resolution data set. The velocity resolution here is 10 km s^{-1} . The spectrum is largely symmetric.....	122
6-7. The HI radial density profiles from the low resolution data set (closed circles) and the high resolution data set (open circles).....	123
6-8. Intensity-weighted radial velocity contours of the low resolution data. Contours are separated by 20 km s^{-1} . Motion toward the observer (the western side of the galaxy) is displayed with black contours and lighter grayscales. The central velocity is 1832 km s^{-1}	124
6-9. Intensity-weighted radial velocity contours of the high resolution data set. Contours are separated by 10 km s^{-1} . Darker grayscales (the eastern side of the galaxy) correspond to motion away from the observer.....	125

6-10. Intensity-weighted radial velocity contours of the high resolution data set overlaid on an optical DSS image of the galaxy. Contours are the same as in Figure 6-9.	125
6-11. A set of P-V slices parallel to and along the major axis of NGC 3055. The contours are at 2, 3, 5, 10, and 25σ . The central velocity of the system is at $1.832 \times 10^6 \text{ m s}^{-1}$	127
6-12. A set of P-V slices parallel to and along the minor axis of NGC 3055. The contours are at 2, 3, 5, 10, and 20σ . The central velocity of the system is at $1.832 \times 10^6 \text{ m s}^{-1}$	128
6-13. Rotation curve of NGC 3055 from the high resolution data set. Plotted data is the average of both sides of the galaxy.	129
6-14. Kinematic position angle of NGC 3055 as a function of radius.	129
6-15. Inclination angle of NGC 3055 as a function of radius.	131
6-16. Model velocity field constructed from kinematical data in Figures 6-13, 6-14, and 6-15. Light grayscales represent approaching velocities.	131
6-17. Residual velocity field made from model in A. Light grayscales represent approaching residuals (contours separated by 5 km s^{-1}).	132
6-18. The HI flux density versus velocity for the "A" HI satellite. The velocity resolution is 10 km s^{-1}	133
6-19. The HI flux density versus velocity for the "B" satellite. The velocity resolution is 10 km s^{-1}	133
6-20. Contours of HI surface density overlaid on an optical DSS image of the "A" satellite. The contours are the same as in Figure 6-3.	134
6-21. Contours of HI surface density overlaid on an optical DSS image of the "B" satellite. The contours are the same as in Figure 6-3.	135
7-1. Individual, naturally weighted, CLEANed channel images of the low resolution data.	140
7-2. Individual, naturally weighted, CLEANed channel images of the high resolution data.	141
7-3. Grayscale with contours of the total HI surface density from the low resolution data set.	142
7-4. Grayscale with contours of the total HI surface density from the low resolution data set. Contours and resolution are the same as in Figure 7-3.	143

7-5. Grayscale and contours of the total HI surface density from the high resolution data set. The peak flux corresponds to $5.8 \times 10^{21} \text{ cm}^{-2}$. Contours are at 1 (the 2σ flux level), 2, 5, 10, 15, 20, 40, 60, 80, and 95% of the peak flux. The synthesized beam (37" x 34") is shown at the bottom left.	144
7-6. Contours of the high resolution HI surface density over a grayscale image of NGC 3930. Contours and resolution are the same as in Figure 7-5.	145
7-8. The HI radial density profiles from the low resolution data set (closed circles) and the high resolution data set (open circles)	147
7-9. Intensity-weighted radial velocity contours of the low resolution data. Contours are separated by 10 km s^{-1} . Motion toward the observer is displayed with black contours and lighter grayscales. The systemic velocity of the galaxy is 919 km s^{-1} . The synthesized beam (59" x 58") is displayed in the lower left.	148
7-10. Intensity-weighted radial velocity contours of the high resolution data set. Contours are separated by 10 km s^{-1} . Darker grayscales correspond to motion away from the observer. The synthesized beam (37" x 34") is displayed in the lower left hand corner.	148
7-11. Intensity-weighted radial velocity contours of the high resolution data set overlaid on an optical DSS image of NGC 3930. Contours are the same as in Figure 7-10.	149
7-12. A set of P-V slices parallel to and along the major axis of NGC 3930. The contours are at 3, 5, 10, 20, 45, and 50σ . The resolution is denoted by a cross in the lower left corner of the bottom left panel.	150
7-13. A set of P-V slices parallel to and along the minor axis of NGC 3930. The contours are at 3, 5, 10, 20, 45, 50σ . The resolution function is shown as a cross in the lower left corner of the bottom left panel.	152
7-14. Rotation curve of NGC 3930 from the high resolution data set. Open squares represent the approaching half of the galaxy. Open circles represent the receding half of the galaxy. Filled circles represent the average of both.	153
7-15. Expansion velocity as a function of radius for NGC 3930. Symbols are the same as in Figure 7-14.	154
7-16. Kinematic position angle of NGC 3930 as a function of radius. Symbols are the same as in Figure 7-14.	155
7-17. Inclination angle of NGC 6012 as a function of radius. Symbols are the same as in Figure 7-14.	155
7-18. Model velocity field constructed from kinematical data in Figures 7-14, 7-16, and 7-17. Light grayscales represent approaching velocities.	157

7-19. Residual velocity field made from model in Figure 7-18. Light grayscales represent approaching residuals. Contours are separated by 5 km s^{-1}	157
7-20. Model velocity field including values for expansion velocity and with all values smoothed at large radii.....	158
7-21. Residual velocity field made with the model from 7-20. Light grayscales indicate motion towards the observer. Contours are separated by 5 km s^{-1}	158
8-1. Individual, naturally weighted, CLEANed channel images of the low resolution data.	163
8-2. Individual, naturally weighted, CLEANed channel images of the low resolution data. The resolution and contour levels are the same as in Figure 8-1.....	164
8-3. Individual, naturally weighted, CLEANed channel images of the high resolution data.	165
8-4. Individual, naturally weighted, CLEANed channel images of the high resolution data. The resolution and contour levels are the same as in Figure 8-3.....	166
8-5. Grayscale with contours of the total HI surface density from the low resolution data set.	167
8-6. Contours of the total HI surface density from the low resolution data set overlaid on an optical DSS image of NGC 4900. Contour levels are the same as in Figure 8-5.....	168
8-7. Grayscale and contours of the total HI surface density from the high resolution data set.	169
8-8. Contours of the total HI surface density from the high resolution data set overlaid on an optical DSS image of NGC 4900. Contours are at the same levels as in Figure 8-7.	170
8-9. The HI flux density versus velocity for the low resolution data set. The velocity resolution here is 10 km s^{-1} . The spectrum does not show the typical galactic double horned pattern.	171
8-10. The HI radial density profiles from the low resolution data set (closed circles) and the high resolution data set (open circles).....	172
8-11. Intensity-weighted radial velocity contours of the low resolution data. Contours are separated by 10 km s^{-1} . Motion toward the observer is displayed with lighter grayscales. The central velocity contour is at 969 km s^{-1} . The synthesized beam ($68'' \times 57''$) is displayed in the lower left.	173

8-12. Intensity-weighted radial velocity contours of the high resolution data set. Contours are separated by 10 km s^{-1} . Darker grayscales correspond to motion away from the observer.	174
8-13. Intensity-weighted radial velocity contours of the high resolution data set overlaid on an optical DSS image. Contours are the same as in Figure 8-12.	175
8-14. A set of P-V slices parallel to and along the major axis of the inner portion of NGC 4900. The contours are at 3, 5, 10, 20, and 40σ	176
8-15. A set of P-V slices parallel to and along the supposed major axis of the outer regions of NGC 4900. The contours are at 3, 5, 10, 20, and 40σ	177
8-16. A set of P-V slices parallel to and along the minor axis of the inner regions of NGC 4900. The contours are at 3, 5, 10, 20, and 40σ	178
8-17. Rotation curve of NGC 1784 from the high resolution data set. Data points represent the average of both the receding and approaching sides of the galaxy. .	179
8-18. Expansion velocity as a function of radius in NGC 4900	182
8-19. Kinematic position angle of NGC 4900 as a function of radius.....	182
8-20. Inclination angle of NGC 4900 as a function of radius.....	183
8-21. Model velocity field constructed from kinematical data of both the inner regions of NGC 4900 and the supposed ring	183
9-1. Individual, naturally weighted, CLEANed channel images of the low resolution data.	189
9-2. Individual, naturally weighted, CLEANed channel images of the high resolution data.	190
9-3. Grayscale with contours of the total HI surface density from the low resolution data set.	191
9-4. Contours of the total HI surface density from the low resolution data set over an optical DSS image of NGC 4904. Resolution and contour levels are the same as Figure 9-3.....	191
9-5. Grayscale and contours of the total HI surface density from the high resolution data set. The peak flux corresponds to $1.7 \times 10^{21} \text{ cm}^{-2}$. Contours are at 1 (the 2σ flux level), 2, 5, 10, 15, 20, 40, 60, 80, and 95% of the peak flux. The synthesized beam ($21'' \times 19''$) is shown at the bottom left.	194

9-6. Contours of the total HI surface density from the high resolution data set overlaid on an optical DSS image of NGC 4904. Resolution and contour levels are the same as Figure 9-5.....	195
9-7. The HI flux density versus velocity for the low resolution data set. The velocity resolution here is 10 km s^{-1}	195
9-8. The HI radial density profiles from the high resolution data set (closed circles) and the low resolution data set (open circles).....	196
9-9. Intensity-weighted radial velocity contours of the low resolution data. Contours are separated by 10 km s^{-1} . Motion toward the observer is displayed with lighter grayscales. The central velocity contour is at 1169 km s^{-1}	197
9-10. Intensity-weighted radial velocity contours of the high resolution data set. Contours are separated by 10 km s^{-1} . Darker grayscales correspond to motion away from the observer.....	198
9-11. Intensity-weighted radial velocity contours of the high resolution data set overlaid on an optical DSS image of the galaxy. Contours are the same as in Figure 9-10.....	198
9-12. A set of P-V slices parallel to and along the major axis of NGC 4904. The contours are at 3, 5, 10, 20, and 30σ	200
9-13. P-V plots along and parallel to the position angle of the outer ring. Contours are at 3, 5, 10, 20, and 30σ	201
9-14. A set of P-V slices parallel to and along the minor axis of NGC 4904. The contours are at 3, 5, 10, 20, and 30σ	202
9-15. Rotation curve of NGC 1784 from the high resolution data set. Data points represent the average of both the approaching and receding sides of the galaxy. .	204
9-16. Kinematic position angle of NGC 1784 as a function of radius.....	204
9-17. Inclination angle of NGC 1784 as a function of radius.....	205
9-18. Model velocity field constructed from kinematical data in Figures 9-15, 9-16, and 9-17. Light grayscales represent approaching velocities.....	206
9-19. Model disk velocity field for NGC 4904 with tilted outer ring. Light grayscales represent approaching velocities.....	206
10-1. Individual, naturally weighted, CLEANed channel images of the low resolution data.	211

10-2. Individual, naturally weighted, CLEANed channel images of the high resolution data.	212
10-3. Grayscale with contours of the total HI surface density from the low resolution data set.	213
10-4. Contours of the total HI surface density from the low resolution data set overlaid on an optical DSS image of NGC 5300. Contours and resolution are the same as in Figure 10-3.....	214
10-5. Grayscale and contours of the total HI surface density from the high resolution data set.	215
10-6. Contours of the high resolution data set overlaid on a DSS image of NGC 5300. Contours and resolution are the same as in Figure 10-5.	216
10-7. The HI flux density versus velocity for the low resolution data set. The velocity resolution here is 10 km s^{-1}	217
10-8. The HI radial density profiles from the low resolution data set (closed circles) and the high resolution data set (open circles).....	218
10-9. Intensity-weighted radial velocity contours of the low resolution data. Contours are separated by 10 km s^{-1}	219
10-10. Intensity-weighted radial velocity contours of the high resolution data set. Contours are separated by 10 km s^{-1}	219
10-11. Intensity-weighted radial velocity contours of the high resolution data set overlaid on an optical DSS image of NGC 5300. Contours are the same as in Figure 10-10.....	220
10-12. A set of P-V slices parallel to and along the major axis of NGC 5300. The contours are at 3, 5, 10, 20σ	221
10-13. A set of P-V slices parallel to and along the minor axis of NGC 5300. The contours are at 3, 5, 10, and 20σ	222
10-14. Rotation curve of NGC 5300 from the high resolution data set. Data points represent the average of both the receding and approaching sides of the galaxy.	223
10-15. Expansion velocity versus as a function of radius for NGC 5300.....	223
10-16. Kinematic position angle of NGC 5300 as a function of radius.....	225
10-17. Inclination angle of NGC 5300 as a function of radius.....	226

10-18. Model velocity field constructed from kinematical data in Figures 10-14, 10-15, and 10-16, and 10-17. Light grayscales represent approaching velocities.....	227
11-1. Individual, naturally weighted, CLEANed channel images of the low resolution data.	231
11-2. Individual, naturally weighted, CLEANed channel images of the high resolution data.	232
11-3. Grayscale with contours of the total HI surface density from the low resolution data set.	234
11-4. Contours of the total HI surface density from the low resolution data set overlaid on an optical DSS image of the galaxy. Resolution and contour levels are the same as in Figure 11-3.....	234
11-5. Grayscale and contours of the total HI surface density from the high resolution data set.	235
11-6. Contours of the high resolution data set overlaid on a DSS image of NGC 6012. The peak flux and contours are the same as in Figure 11-5. The synthesized beam is shown at the bottom left.....	236
11-7. The HI flux density versus velocity for the low resolution data set. The velocity resolution here is 10 km s^{-1}	237
11-8. The HI radial density profiles from the low resolution data set (closed circles) and the high resolution data set (open circles).....	238
11-9. Intensity-weighted radial velocity contours of the low resolution data. Contours are separated by 10 km s^{-1} . Motion toward the observer is displayed with lighter grayscales. The central velocity contour is at 1854 km s^{-1}	239
11-10. Intensity-weighted radial velocity contours of the high resolution data set. Contours are separated by 10 km s^{-1} . Darker grayscales correspond to motion away from the observer.....	239
11-11. Intensity-weighted radial velocity contours of the high resolution data set overlaid on an optical DSS image of NGC 6012. Contours and resolution are the same as in Figure 11-10.....	240
11-12. A set of P-V slices parallel to and along the major axis of NGC 6012. The contours are at 3, 5, 10, 20, and 40σ	241
11-13. A set of P-V slices parallel to and along the minor axis of NGC 6012. The contours are at 3, 5, 10, 20, and 40σ	243

11-14. Small scale P-V plots made through HI holes found in Figure 11-5. The slices on the left are parallel to the major kinematic axis of NGC 6012. The slices on the right are made parallel to the minor axis of NGC 6012.	244
11-15. Rotation curve of NGC 6012 from the high resolution data set. Data points represent the average of values from both the approaching and receding sides of the galaxy.	245
11-16. Expansion velocity as a function of radius for NGC 6012.....	246
11-17: Kinematic position angle of NGC 6012 as a function of radius.....	246
11-18. Inclination angle of NGC 6012 as a function of radius.....	247
11-19. Model velocity field constructed from kinematical data in Figures 11-16, 11-17, 11-18, and 11-19. Light grayscales represent approaching velocities.	247
11-20. Residual velocity field made from model in Figure 11-20. Light grayscales represent approaching residuals. Contours are separated by 5 km s^{-1} . Concentric circles at the center of the galaxy denote where azimuthal profiles were made for later figures.....	248
11-21. Azimuthal plot of NGC 6012's residual velocity field made at a radius of $20''$..	251
11-22. Azimuthal plot of NGC 6012's residual velocity field made at a radius of $40''$..	251
11-23. Azimuthal plot of NGC 6012's residual velocity field made at a radius of $80''$..	252
11-24. Azimuthal plot of NGC 6012's residual velocity field made at a radius of $120''$..	252
12-1. Distribution of the bar axis ratio for the sample set. The strips across the columns represent the Elmegreen arm class of the galaxies (labeled at right) with in the particular bar axis ratio bin.	256
12-2. Distribution of the bar length to galaxy radius ratio for the sample set. The strips across the columns represent the amount of galaxies from particular Elmegreen arm class (labeled at right) within that bar length ratio bin.	256
12-3. Comparison of bar axis ratio to bar/galaxy length ratio. Strips across the columns represent the number of galaxies within a range of bar axis ratio with respect to the bar length bin.	257
12-4. Distribution of bar symmetries for the sample set. Strips across the columns represent the different Elmegreen arm classes.	258
12-5. Distribution of bar length to galaxy radius ratio in the sample set. Strips across the columns represent the symmetry status of the bar.	259

12-6. Distribution of HI Rotation curve shapes within the sample set. Strips across the columns represent the different Elmegreen arm classifications. We did not observe in HI any galaxies that were in Elmegreen arm class "1".....	261
12-7. Distribution of Bar length to galaxy radius ratio in galaxies observed in HI. Strips across the columns represent the shape of the rotation curve.....	261
12-8. Distribution of HI diameters in the sample set.....	263
12-9. Distribution of HI to Optical Diameter Ratios within the sample set. Strips across the columns correspond to the symmetry of the HI distribution.....	263
12-10. Distribution of HI to optical diameter ratios. Strips across the bar represent the bar to galaxy length ratio.....	264
12-11. Distribution of HI masses in the sample set.....	265
12-12. Distribution of HI Mass fraction for the sample set. The strips across the columns represent the distribution of HI to optical diameter ratios.....	266
12-13. Distribution of HI Mass fraction for the sample set. The strips across the columns represent the Elmegreen arm classification of the set.	266
12-14. Distribution of Elmegreen arm classes in the control sample set.....	274
12-15. Distribution of Hubble Types in the control sample set. Strips across the columns represent the Elmegreen arm classes within the group.	275
12-16. Bar classification distribution of the control sample. Strips across the column indicate the Elmegreen arm class of the control set.....	275

Abstract of Dissertation Presented to the Graduate School
of the University of Florida in Partial Fulfillment of the
Requirements for the Degree of Doctor of Philosophy

MULTI-WAVELENGTH OBSERVATIONS
OF BARRED, FLOCCULENT GALAXIES

By

Douglas Lee Ratay

August 2004

Chair: Dr. Stephen Gottesman
Major Department: Astronomy

Although it is generally accepted that large galaxies form through the assemblage of smaller objects, an explanation for the morphology of galaxies is not available. Any complete theory of galaxy morphology must include production and dissolution mechanisms for galactic bars, rings, nuclear bars, spiral arms, and companions. This theory does not exist because of the lack of detailed data from many types of galaxies in different environments.

We have defined a new sample of galaxies which are simultaneously flocculent, barred, and isolated. We have performed optical, near-infrared, and radio (HI) observations of the galaxies in this sample.

We measured properties of our galaxies including bar length, bar axis ratio, HI diameter, HI mass, and dynamical mass. We found that our sample group is heterogeneous, and compares well to a standard samples of galaxies. We found two of our galaxies to possess companions, and two others to show evidence of current

interactions. This is consistent with other observations indicating that local isolated galaxies do not possess a large number of small companions. We cannot rule out the possibility of very small companions. We find that as a group our sample is slightly less luminous than normal galaxies and may be more likely to be involved in interactions.

We conclude that the bar and spiral arm features in our sample are due to processes internal to the galaxies, likely involving the interaction between the galactic disk and halo. We defined a control sample of barred, grand design galaxies to further determine the acceptability of barred, flocculent galaxies as a physically meaningful subset of galaxies.

CHAPTER 1 PROJECT DESCRIPTION

Recent advances in observational technology have greatly opened the study of extragalactic astronomy. Observations in the near-IR by Block & Puerari (1999) of grand design and flocculent, disk galaxies have thrown a new level of complexity into the previous optical arm classification scheme of Elmegreen & Elmegreen (1982). This near-infrared work possibly shows the existence of two decoupled dynamical systems, one composed of Population I stars and gas, and the other composed of Population II stars, cohabitating in the same galaxy. Galaxies have been found to be grand design in one system while flocculent in the other (Cepa et al. 1988; Elmegreen et al. 1996; Thornley 1996; Block & Puerari 1999).

There is no clear understanding as to why a galaxy is either flocculent (possesses no discernable spiral structure), grand design (possesses two strong spiral arms), or somewhere in between. Block & Puerari (1999) go even farther saying that even if we know the arm morphology of a galaxy in one wave length regime, we cannot predict the arm morphology of the galaxy in the other. This is a result of presumed dynamical decoupling. Still, it has been assumed in the past that the presence of a bar or a companion is correlated with spiral density waves (Kormendy & Norman 1979; Elmegreen & Elmegreen 1982; Elmegreen & Elmegreen 1983; Elmegreen & Elmegreen 1985; Seigar & James 1998a,b).

A sizable minority of galaxies exist that are flocculent in the optical while possessing bars and possibly companions (Elmegreen & Elmegreen 1982; Elmegreen &

Elmegreen 1987; Haynes et al. 1998). Our study examined that population. Flocculent galaxies with bars have not been critically examined in the past. Only 2 of the 15 galaxies in our sample have been observed in the spectral line mode of the Very Large Array. Our study aimed to extend the work of Block & Puerari (1999) by choosing our sample differently (only flocculent, barred) and by extending wavelength coverage (21 cm, near-IR, and optical). We hoped to provide answers to the following questions:

- Are Elmegreen & Elmegreen's (1982) arm classifications valid?
- Do the galaxies in our sample possess near-infrared spiral structure?
- Does the sample of optically barred flocculent galaxies possess near-infrared bars?
- What is the nature (relative size, surface brightness distribution) of the optical and near-infrared bars?
- Does the sample of optically barred, flocculent galaxies possess similar neutral hydrogen mass ratios and morphologies?
- How many of these optically barred flocculent galaxies possess HI companions?
- Of the galaxies that possess companions, what are the physical and orbital properties of the companions? Are the properties similar?
- If there are similar characteristics of optically flocculent, barred galaxies, are these properties similar to or different from flocculent non-barred galaxies and optically grand design galaxies?

Galaxy Sample

This project is the first to define barred, flocculent galaxies as a distinct class for study. The galaxies selected for this work were taken from the original research, that classified galaxies as flocculent or grand design, by Elmegreen & Elmegreen (1982). Objects were selected from Elmegreen & Elmegreen's (1982) list if they met the following criteria: bar type of SAB or SB; flocculent arm classification (<4); Hubble Type later than Sa and no later than Sd; classified as isolated by Elmegreen & Elmegreen (1982).

The bar classification criteria provide us with galaxies that show any type of bar feature or oval distortion. The arm classification criteria give all galaxies classified as flocculent. Although arm classification is done primarily by eye on blue images (leading to some uncertainty), all other papers in the literature use the Elmegreen & Elmegreen (1982) scheme, so we adopted it also. The Hubble Classification criteria were used to include only "regular" spiral galaxies. It is assumed that smaller Magellenic type galaxies or peculiar and irregular galaxies may have other processes operating on their morphology (which would not allow data gained from them to be compared easily to other large galaxies). Also, we wanted to observe galaxies large enough to determine detail with normal 21 cm observations. Isolation criteria were used to eliminate galaxies with obviously interacting large companions, or those in groups. Dynamics of such interactions and effects on the morphologies of constituent galaxies are poorly understood. We looked solely at the possible effects of bars on the disk of a galaxy.

The galaxies selected for our study have not been previously well studied. Of the 15 in the sample, only 2 were previously observed for any amount of time in the HI spectral line mode of the Very Large Array (VLA). Near infrared observations are essentially non-existent for the sample. Tables 1 through 16 present relevant data for all objects in the sample.

Table 1-1. NGC 1784: Previously observed properties

Property of NGC 1784	Value	Reference
Right ascension (2000)	05h 05m 27.1s	de Vaucouleurs et al. (1991)
Declination (2000)	-11 52' 17.5"	de Vaucouleurs et al. (1991)
V_{radial}	2308 km s ⁻¹	de Vaucouleurs et al. (1991)
Hubble classification	SB(r)c	de Vaucouleurs et al. (1991)
Galaxy size	4.0' x 2.5'	de Vaucouleurs et al. (1991)
Arm classification	3	Elmegreen & Elmegreen (1982)
Position angle	105°	Tully (1988)
Inclination	55°	Tully (1988)
Bar semi-major axis	34"	Martin (1995)
Bar semi-minor axis	14"	Martin (1995)
Blue magnitude	12.44	de Vaucouleurs et al. (1991)

Table 1-2. NGC 2500: Previously observed properties

Property of NGC 2500	Value	Reference
Right ascension (2000)	08h 01m 53.1s	de Vaucouleurs et al. (1991)
Declination (2000)	+50 44' 15"	de Vaucouleurs et al. (1991)
Distance	12.0 Mpc	Grosbol (1985)
V_{radial}	514 km s ⁻¹	de Vaucouleurs et al. (1991)
Hubble classification	SB(rs)d	de Vaucouleurs et al. (1991)
Angular size	2.9' x 2.6'	de Vaucouleurs et al. (1991)
Arm classification	1	Elmegreen & Elmegreen (1982)
Inclination	25	Grosbol (1985)
Position angle	58	Grosbol (1985)
D_{25}	125"	Martin (1995)
Bar length	21"	Elmegreen & Elmegreen (1985)
Bar to galaxy length ratio	0.24	Elmegreen & Elmegreen (1985)
Bar light profile	Exponential	Elmegreen & Elmegreen (1985)
Bar ellipticity class	6	Martin (1995)
HI flux	33.61 Jy km s ⁻¹	Haynes et al. (1998)
HI line width	100 km s ⁻¹	Haynes et al. (1998)
HI asymmetry measure	1.04	Haynes et al. (1998)
Apparent magnitude	12.20	de Vaucouleurs et al. (1991)
M_B	-17.96	Elmegreen & Salzer (1999)
H α luminosity	2.75×10^{40} erg s ⁻¹	Elmegreen & Salzer (1999)
May possess a nuclear bar		van den Bergh (1995)
Shows nuclear emission of H α .		Ho et al. (1995)
Classified as having an HII nucleus		Ho et al. (1995)
Bar shows no twists in near-IR		Elmegreen et al. (1996)
Bar may be shorter in NIR than in optical		Elmegreen et al. (1996)

Table 1-3. NGC 2793: Previously observed properties

Property of NGC 2793	Value	Reference
Right ascension (2000)	09h 16m 47.2s	de Vaucouluers et al. (1991)
Declination (2000)	+34 25' 48"	de Vaucouluers et al. (1991)
V_{radial}	1687 km s ⁻¹	de Vaucouluers et al. (1991)
Hubble class	SB(s)d	de Vaucouluers et al. (1991)
Arm classification	1	Elmegreen & Elmegreen (1982)
Angular size	1.3' x 1.1'	de Vaucouluers et al. (1991)
Apparent magnitude	13.58	de Vaucouluers et al. (1991)
Classified as a ring galaxy		Thompson (1977)
Not in the projected nearby cluster		Thompson (1977)
Involved in a head on encounter with a companion		Mazzei (1995)
Currently in a starburst phase		Mazzei (1995)

Table 1-4. NGC 3055: Previously observed properties

Property of NGC 3055	Value	Reference
Right ascension (2000)	09h 55m 18.1s	de Vaucouluers et al. (1991)
Declination (2000)	+4 16m 12s	de Vaucouluers et al. (1991)
Distance	23.4 Mpc	Marquez & Moles (1996)
V_{radial}	1832 km s ⁻¹	de Vaucouluers et al. (1991)
Hubble classification	SAB(s)c	de Vaucouluers et al. (1991)
Arm classification	4	Elmegreen & Elmegreen (1982)
M_{total}	$3 \times 10^{10} M_{\odot}$	Marquez & Moles (1996)
Angular size	2.1' x 1.3'	de Vaucouluers et al. (1991)
D_{25}	125"	Martin (1995)
Inclination	24	Martin (1995)
Position angle	63	Martin (1995)
Bar length	7"	Martin (1995)
Bar width	3"	Martin (1995)
Bar ellipticity class	6	Martin (1995)
Bar/galaxy length ratio	0.11	Martin (1995)
Apparent magnitude	12.7	de Vaucouluers et al. (1991)
$\text{EWH}\alpha$	$59 \pm 7 \text{ \AA}$	Romanishin (1990)
$\log F_{\text{H}\alpha}$	11.68	Romanishin (1990)
Not classified as a starburst galaxy		Devereux (1989)
Possesses a rising rotation curve through 40"		Sperandio et al. (1995)
Mass distribution does not fall into normal classes		Sperandio et al. (1995)
NGC 3055 is an isolated spiral		Marquez & Moles (1996)

Table 1-5. NGC 3246: Previously observed properties

Property of NGC 3246	Value	Reference
Right ascension (2000)	10h 26m 41.8s	de Vaucouleurs et al. (1991)
Declination(2000)	+3 51' 43"	de Vaucouleurs et al. (1991)
V_{radial}	2150 km s ⁻¹	de Vaucouleurs et al. (1991)
Hubble classification	SABd	de Vaucouleurs et al. (1991)
Arm classification	1	Elmegreen & Elmegreen (1982)
D_{25}	2.3'	Warmels (1988)
M_{total}	$1.2 \times 10^{11} M_{\odot}$	Pisano & Wilcots (1999)
Apparent magnitude	13.2	de Vaucouleurs et al. (1991)
Inclination	54°	Warmels (1988)
HI flux	21.5 Jy km s ⁻¹	Warmels (1988)
D_{HI}	4.2'	Warmels (1988)
HI line width	266 km s ⁻¹	Pisano & Wilcots (1999)
M_{HI}	$5.6 \times 10^9 M_{\odot}$	Pisano & Wilcots (1999)
Possesses an asymmetric HI spectrum		Warmels (1988)
Shows an asymmetric HI morphology		Pisano & Wilcots (1999)

Table 1-6. NGC 3687: Previously observed properties

Property of NGC 3687	Value	Reference
Right ascension (2000)	11h 28m 00.5s	de Vaucouleurs et al. (1991)
Declination (2000)	+29 30m 39s	de Vaucouleurs et al. (1991)
V_{radial}	2507 km s ⁻¹	de Vaucouleurs et al. (1991)
Hubble classification	(R')SAB(r)bc	de Vaucouleurs et al. (1991)
Arm classification	4	Elmegreen & Elmegreen (1982)
Angular size	1.9' x 1.9'	de Vaucouleurs et al. (1991)
HI line width	190 km s ⁻¹	Lewis (1987)
HI flux	8.1 Jy km s ⁻¹	Lewis (1987)
M_{HI}	$5 \times 10^9 M_{\odot}$	Lewis (1987)
Apparent magnitude	12.82	de Vaucouleurs et al. (1991)
$EW_{\text{H}\alpha}$	$17 \pm 4 \text{ \AA}$	Romanishin (1990)
$\log F_{\text{H}\alpha}$	12.29	Romanishin (1990)
Also known as Markarian 736		
Possesses a symmetric HI spectrum		Lewis (1987)

Table 1-7. NGC 3887: Previously observed properties

Property of NGC 3887	Value	Reference
Right ascension (2000)	11h 47m 4.6s	de Vaucouleurs et al. (1991)
Declination (2000)	-16 51' 16"	de Vaucouleurs et al. (1991)
Distance	14.8 Mpc	Jungwiert et al. (1997)
V_{radial}	1208 km s ⁻¹	de Vaucouleurs et al. (1991)
Hubble classification	SB(r)bc	de Vaucouleurs et al. (1991)
Arm classification	2	Elmegreen & Elmegreen (1982)
D_{25}	3.3'	Haynes et al. (1998)
Angular size	3.3' x 2.5'	de Vaucouleurs et al. (1991)
Inclination	30°	Martin (1995)
Bar length	23"	Martin (1995)
Bar width	11"	Martin (1995)
Bar to galaxy ratio	0.23	Martin (1995)
Bar ellipticity class	5	Martin (1995)
HI flux	46.26 Jy km s ⁻¹	Haynes et al. (1998)
HI line width	236 km s ⁻¹	Haynes et al. (1998)
HI asymmetry measure	1.03	Haynes et al. (1998)
Apparent magnitude	11.41	Haynes et al. (1998)
L_{FIR}	2.0×10^{43} erg s ⁻¹	David et al. (1992)
L_{B}	3.3×10^{43} erg s ⁻¹	David et al. (1992)
L_{Xray}	6.5×10^{39} erg s ⁻¹	David et al. (1992)
Not classified as active or starburst		David et al. (1992)
Shows a strong bar and low star formation rate.		Martinet & Friedeli (1997)
Possesses a NIR twist in its bar		Jungwiert et al. (1997)

Table 1-8. NGC 3930: Previously observed properties

Property of NGC 3930	Value	Reference
Right ascension (2000)	11h 51m 46.0s	de Vaucouleurs et al. (1991)
Declination (2000)	+38 00' 54"	de Vaucouleurs et al. (1991)
V_{radial}	919 km s ⁻¹	de Vaucouleurs et al. (1991)
Hubble classification	SAB(s)c	de Vaucouleurs et al. (1991)
Arm classification	4	Elmegreen & Elmegreen (1982)
D_{25}	3.2'	Haynes et al. (1998)
Angular size	3.2' x 2.4'	de Vaucouleurs et al. (1991)
HI flux	28.78 Jy km s ⁻¹	Haynes et al. (1998)
HI line width	152 km s ⁻¹	Haynes et al. (1998)
HI asymmetry measure	1.14	Haynes et al. (1998)
Apparent magnitude	13.1	de Vaucouleurs et al. (1991)
$EW_{\text{H}\alpha}$	24 ± 5 Å	Romanishin (1990)
$\log F_{\text{H}\alpha}$	12.57	Romanishin (1990)

Table 1-9. NGC 4793: Previously observed properties

Property of NGC 4793	Value	Reference
Right ascension (2000)	12h 54m 40.7s	de Vaucouleurs et al. (1991)
Declination (2000)	+28 56' 19"	de Vaucouleurs et al. (1991)
Distance	49.2 Mpc	Condon et al. (1991)
V_{radial}	2484 km s ⁻¹	de Vaucouleurs et al. (1991)
Hubble classification	SAB(rs)c	de Vaucouleurs et al. (1991)
Arm classification	1	Elmegreen & Elmegreen (1982)
Angular size	2.8' x 1.5'	de Vaucouleurs et al. (1991)
HI line width	204 km s ⁻¹	Sanders et al. (1991)
Apparent magnitude	12.3	de Vaucouleurs et al. (1991)
$EW_{\text{H}\alpha}$	54 ± 2 Å	Romanishin (1990)
$\log F_{\text{H}\alpha}$	11.55	Romanishin (1990)
M_{B}	-21.2	Condon et al. (1991)
$\log M_{\text{H}_2}$	9.38 M _⊙	Sanders et al. (1991)
$\log M_{\text{dust}}$	7.11 M _⊙	Sanders et al. (1991)
$\log L_{\text{FIR}}$	10.76 L _⊙	Sanders et al. (1991)
Not classified as a starburst galaxy.		Devereux (1989)
Primary energy source at 4.8 GHz is stars		Condon et al. (1991)
NGC 4793 is a luminous IR galaxy		Sanders et al. (1991)
Luminous CO source, due to an interaction		Sanders et al. (1991)

Table 1-10. NGC 4900: Previously observed properties

Property of NGC 4900	Value	Reference
Right ascension (2000)	13h 00m 39.1s	de Vaucouleurs et al. (1991)
Declination (2000)	+2 30' 05"	de Vaucouleurs et al. (1991)
V_{radial}	969 km s ⁻¹	de Vaucouleurs et al. (1991)
Hubble classification	SB(rs)c	de Vaucouleurs et al. (1991)
Arm classification	3	Elmegreen & Elmegreen (1982)
Angular size	2.2' x 2.1'	de Vaucouleurs et al. (1991)
Apparent magnitude	11.90	de Vaucouleurs et al. (1991)
B - V	.55	Belfort et al. (1987)
$\log EW_{\text{H}\alpha}$	1.48	Belfort et al. (1987)
$L_{\text{IR}} / L_{\text{B}}$	1.1 (Normal)	Belfort et al. (1987)
$\log L_{\text{FIR}}$	9.69 L _⊙	Ashby et al. (1995)
$\log \text{OIII} / \text{H}\beta$	-0.89	Ashby et al. (1995)
$\log \text{NII} / \text{H}\alpha$	-0.41	Ashby et al. (1995)
$\log \text{SII} / \text{H}\alpha$	-0.7	Ashby et al. (1995)
$\log \text{H}\alpha / \text{H}\beta$	0.41	Ashby et al. (1995)
Not classified as a starburst galaxy		Devereux (1989)
Not deficient in HI		Giraud (1986)
Not detected in 20 cm continuum		Puxley et al. (1988)
The FIR emission in NGC 4900 is due to stars		Ashby et al. (1995)

Table 1-11. NGC 4904: Previously observed properties

Property of NGC 4904	Value	Reference
Right ascension (2000)	13h 00m 58.9s	de Vaucouleurs et al. (1991)
Declination (2000)	-00 01' 42"	de Vaucouleurs et al. (1991)
V_{radial}	1169 km s ⁻¹	de Vaucouleurs et al. (1991)
Hubble classification	SB(s)cd	de Vaucouleurs et al. (1991)
Arm classification	2	Elmegreen & Elmegreen (1982)
Angular size	2.2' x 1.4'	de Vaucouleurs et al. (1991)
Inclination	47.7°	Chapelon et al. (1999)
Bar length	16.4"	Chapelon et al. (1999)
Bar ellipticity (b/a)	0.32	Chapelon et al. (1999)
Bar to galaxy ratio	0.35	Chapelon et al. (1999)
HI line width	200 km s ⁻¹	Lewis et al. (1985)
HI asymmetry measure	1.04	Lewis et al. (1985)
HI flux	10.76 Jy km s ⁻¹	Lewis et al. (1985)
HI mass	1.28 x 10 ⁹ M _⊙	Lewis et al. (1985)
Apparent magnitude	12.6	de Vaucouleurs et al. (1991)
$L_{\text{FIR}}/L_{\text{B}}$	1.36	Mazzarella et al. (1991)
log L_{FIR}	9.04	Chapelon et al. (1999)
Not deficient in HI		Giraud (1986)
Also known as Markarian 1341		

Table 1-12. NGC 5147: Previously observed properties

Property of NGC 5147	Value	Reference
Right ascension (J2000)	13h 26m 19.6s	de Vaucouleurs et al. (1991)
Declination (J2000)	2 06' 02"	de Vaucouleurs et al. (1991)
V_{radial}	1088 km s ⁻¹	de Vaucouleurs et al. (1991)
Hubble classification	SB(s)dm	de Vaucouleurs et al. (1991)
Arm classification	2	Elmegreen & Elmegreen (1982)
Angular size	1.9' x 1.5'	de Vaucouleurs et al. (1991)
Apparent magnitude	12.29	de Vaucouleurs et al. (1991)

Table 1-13. NGC 5300: Previously observed properties

Property of NGC 5300	Value	Reference
Right ascension (J2000)	13h 48m 15.9s	de Vaucouleurs et al. (1991)
Declination (J2000)	+3 57' 03"	de Vaucouleurs et al. (1991)
V_{radial}	1171 km s ⁻¹	de Vaucouleurs et al. (1991)
Hubble classification	SAB(r)c	de Vaucouleurs et al. (1991)
Arm classification	2	Elmegreen & Elmegreen (1982)
log Mass	10.22	Xu et al. (1994)
Angular size	3.9' x 2.6'	de Vaucouleurs et al. (1991)
D_{25}	3.8'	Marquez & Moles (1992)
Apparent magnitude	12.11	de Vaucouleurs et al. (1991)
$EW_{\text{H}\alpha}$	22 ± 4 Å	Romanishin (1990)
log $F_{\text{H}\alpha}$	11.94	Romanishin (1990)
H-band magnitude	10.38	Xu et al. (1994)

Table 1-14. NGC 5645: Previously observed properties

Property of NGC 5645	Value	Reference
Right ascension (J2000)	14h 30m 39.5s	de Vaucouluers et al. (1991)
Declination (J2000)	7 16' 29"	de Vaucouluers et al. (1991)
V_{radial}	1370 km s ⁻¹	de Vaucouluers et al. (1991)
Hubble classification	SB(s)d	de Vaucouluers et al. (1991)
Arm classification	1	Elmegreen & Elmegreen (1982)
D_{25}	2.4'	Haynes et al. (1998)
Angular size	2.4' x 1.5'	de Vaucouluers et al. (1991)
HI flux	19.45 Jy km s ⁻¹	Haynes et al. (1998)
HI line width	181 km s ⁻¹	Haynes et al. (1998)
HI asymmetry measure	1.35	Haynes et al. (1998)
Apparent magnitude	13.0	de Vaucouluers et al. (1991)
Possesses a nuclear bar		Van den Bergh (1995)
Lies near a background continuum source		Corbelli & Schneider (1990)

Table 1-15. NGC 5783: Previously observed properties

Property of NGC 5783	Value	Reference
Right ascension (J2000)	14h 53m 28.2s	de Vaucouluers et al. (1991)
Declination (J2000)	+52 4' 34"	de Vaucouluers et al. (1991)
Distance	36.6 Mpc	Rhee & van Albada (1996)
V_{radial}	2337 km s ⁻¹	de Vaucouluers et al. (1991)
Hubble classification	SAB(s)c	de Vaucouluers et al. (1991)
Arm classification	2	Elmegreen & Elmegreen (1982)
D_{25}	2.8'	Rhee & van Albada (1996)
Total mass	1.13 x 10 ¹¹ M _⊙	Rhee & van Albada (1996)
Inclination	53°	Rhee & van Albada (1996)
HI line width	270 km s ⁻¹	Rhee & van Albada (1996)
HI line flux	20 Jy km s ⁻¹	Rhee & van Albada (1996)
HI mass	6.39 x 10 ⁹ M _⊙	Rhee & van Albada (1996)
$EW_{\text{H}\alpha}$	20 ± 4 Å	Romanishin (1990)
log $F_{\text{H}\alpha}$	12.28	Romanishin (1990)
B magnitude	13.0	Rhee & van Albada (1996)

Table 1-16. NGC 6012: Previously observed properties

Property of NGC 6012	Value	Reference
Right ascension (J2000)	15h 54m 13.9s	de Vaucouleurs et al. (1991)
Declination (J2000)	+14 36' 04"	de Vaucouleurs et al. (1991)
V_{radial}	1854 km s ⁻¹	de Vaucouleurs et al. (1991)
Hubble classification	(R)SB(r)ab	de Vaucouleurs et al. (1991)
Arm classification	3	Elmegreen & Elmegreen (1982)
Angular size	2.1' x 1.5'	de Vaucouleurs et al. (1991)
HI line width	177 km s ⁻¹	van den Bergh (1985)
HI flux	12.1 Jy km s ⁻¹	van den Bergh (1985)
HI mass	4.87 x 10 ⁹ M _☉	van den Bergh (1985)
HI asymmetry measure	1.08	van den Bergh(1985)
Apparent magnitude	12.69	de Vaucouleurs et al. (1991)
Shows a mostly normal HI profile		van den Bergh (1985)

Figures 1-1 through 1-7 summarize several of the major properties of the sample set, so that a global sense of the sample is possible. Figure 1-1 shows the distribution of Hubble Type (Vaucouleurs et al.1991) for our sample set. Most of our galaxies are late type; however, there are spirals of all types in the sample. There is likely a bias for flocculent galaxies to be classified as late types, since the pitch angle of the spiral arms of a galaxy is considered in giving a galaxy a Hubble type. Where arms are not present, particularly strong, or chaotic looking, a bias toward classifying them as late type will most likely be introduced. Having most of the galaxies be late type, however, also means that most galaxies in the sample do not show optical bulges. This may indicate either that the optical bars in the galaxy sample are young enough not to have dissipated significantly, or that there were not earlier generations of bars present in the galaxies.

Figure 1-2 shows that there are roughly equal numbers of AB and B type bars in our sample. In a similar manner, Figure 1-3 shows that there is an even distribution of Elmegreen arm class distributions in our sample. This shows that there is not a bias toward a certain type (one-armed or particularly chaotic) of arm structure when choosing

a sample of barred, flocculent galaxies. Figure 1-4 again shows the distribution of Hubble types (Figure 1-1) within the sample, but is further modified by the Elmegreen arm class. Our most populous Hubble type (S_c), does not show a bias toward one Hubble type. Earlier galaxies do tend toward the less chaotic arm classes, but the numbers of galaxies in these bins (3), are very small. It is unclear whether this would be a trend in a larger sample. Our latest type galaxies (S_d), do show a trend toward the more chaotic arm classes. This is most likely evidence of the bias mentioned before, whereby galaxies with chaotic arms are by definition going to be given later Hubble types. Care must be taken in the study of barred, flocculent galaxies, to ensure that these galaxies (chaotic armed, and late type) are of a similar nature to the earlier typed galaxies in the sample. Figure 1-5 shows this same analysis done on the bar type of the galaxies. There do not seem to be any systematic differences among bar types in the Elmegreen arm classes.

Figures 1-6, 1-7, and 1-8 show some of the other diagnostic features of the galaxy sample set. The distribution of radial velocities in Figure 1-6 shows that galaxies in the sample are evenly distributed in the local universe. The nearest galaxy has a recessional velocity of 514 km s^{-1} , and the most distant has a recessional velocity of 2507 km s^{-1} . Figure 1-7 shows that the typical galaxy in the sample has an angular size on the order of $2' - 3'$. Physical units of diameter are discussed in later chapters. Figure 1-8 shows that the average apparent magnitude of the sample is about 12.5. Overall, these three figures show that the sample is (on average) made of relatively nearby and smallish galaxies of moderate brightness.

Finally, Figure 1-9 shows the distribution of previously determined HI asymmetry measures of the galaxy sample. The HI asymmetry measure, typically made from single dish observations of galaxies, is a measure of how well a galaxy's HI spectrum resembles the typical two-horned pattern of differential rotation. A high measure of asymmetry indicates that either a galaxy possesses an unusual morphology or has a significant amount of gas at non-circular velocities. The HI asymmetry measure is often used to search for galaxies that may be undergoing an interaction. Haynes et al. (1998) performed a recent large survey of spiral galaxies examining this measure. In our sample, we find that a plurality of galaxies have low asymmetry measures, but a few do have rather high values (1.35 in one case), indicating that these galaxies may be very interesting when studied with an interferometer.

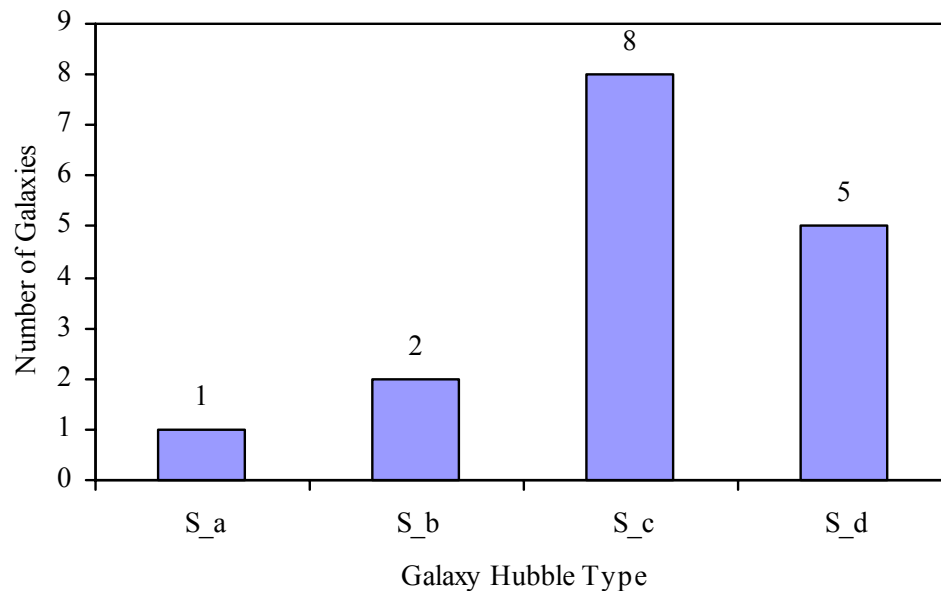


Figure 1-1. Distribution of Hubble Type within our galaxy sample. This distribution does not take into account bar (B or AB) status.

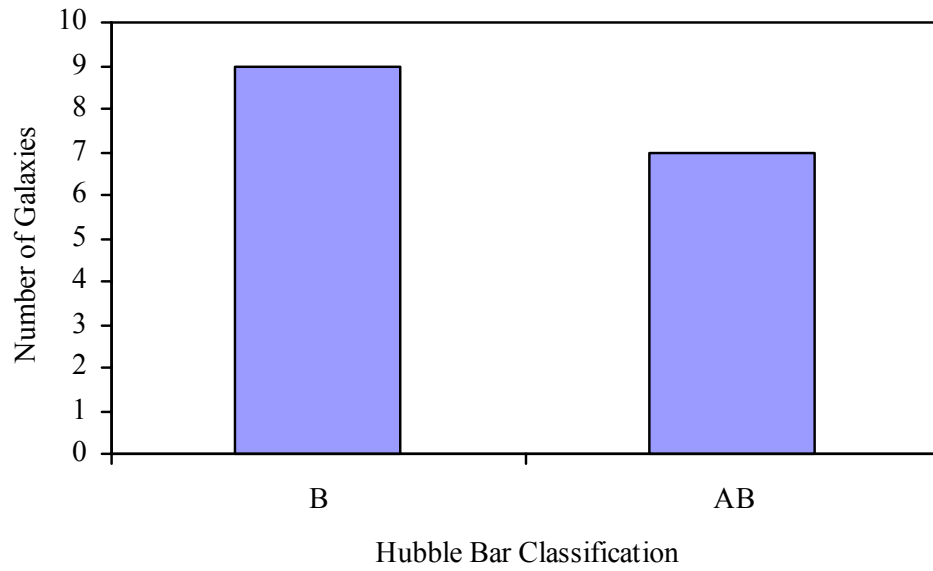


Figure 1-2. Hubble bar classification distribution of the galaxy sample

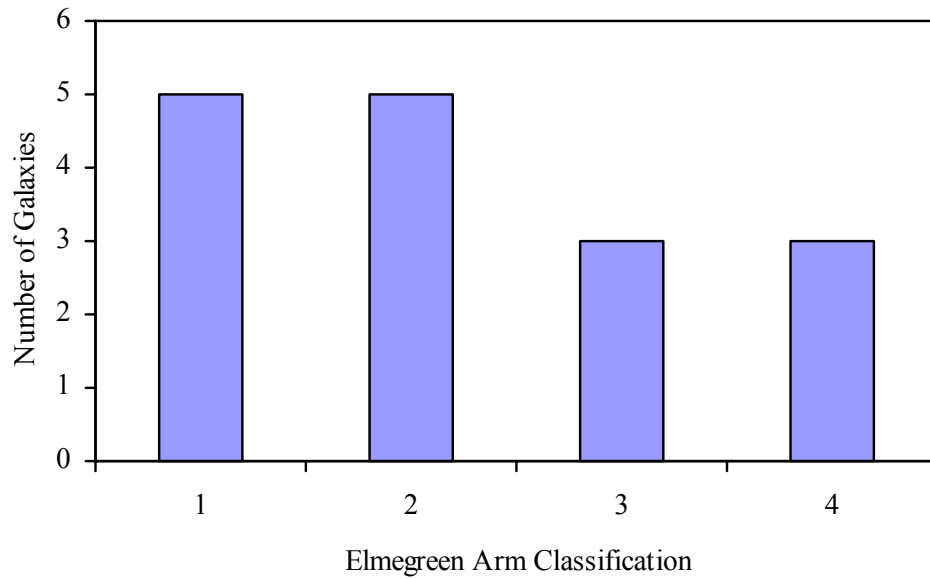


Figure 1-3. Elmegreen arm class distribution of the galaxy sample

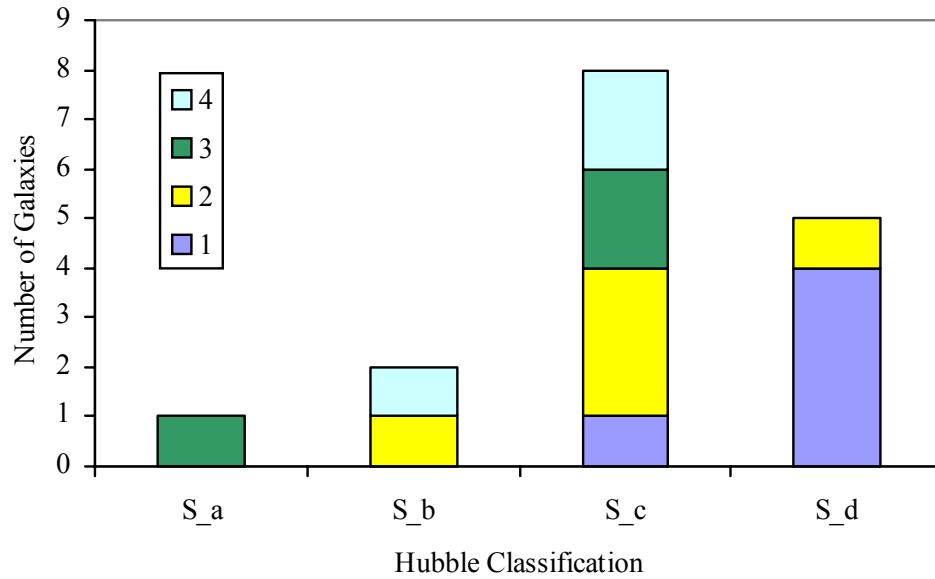


Figure 1-4. Distribution of Hubble Classification and Elmegreen arm classification. The stripes across the bars represent the number of galaxies of a particular arm class (labeled at right) in that Hubble Type.

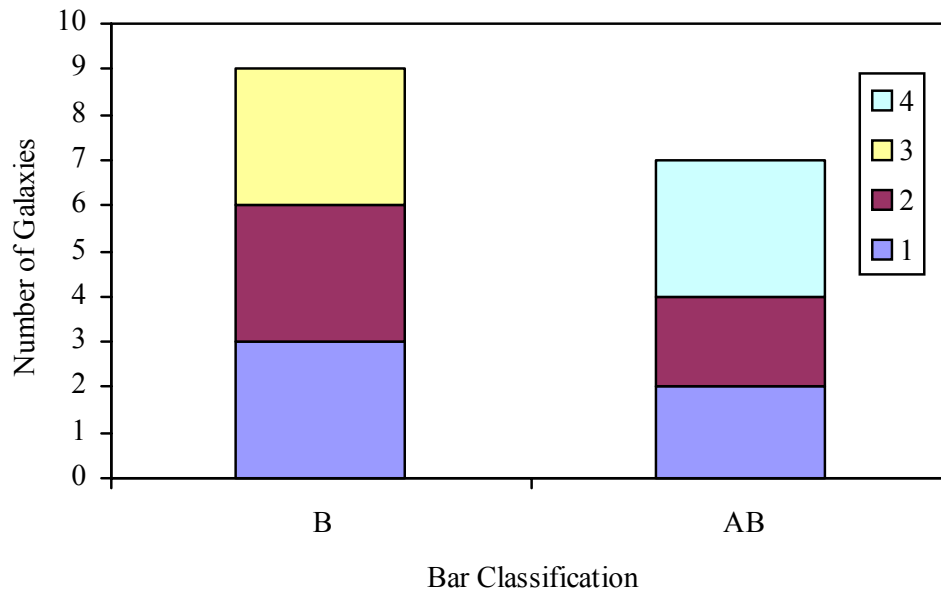


Figure 1-5. Distribution of Bar Classification and Elmegreen arm classification. The stripes across the bars represent the number of galaxies of a particular arm class (labeled at right) in that Hubble Type.

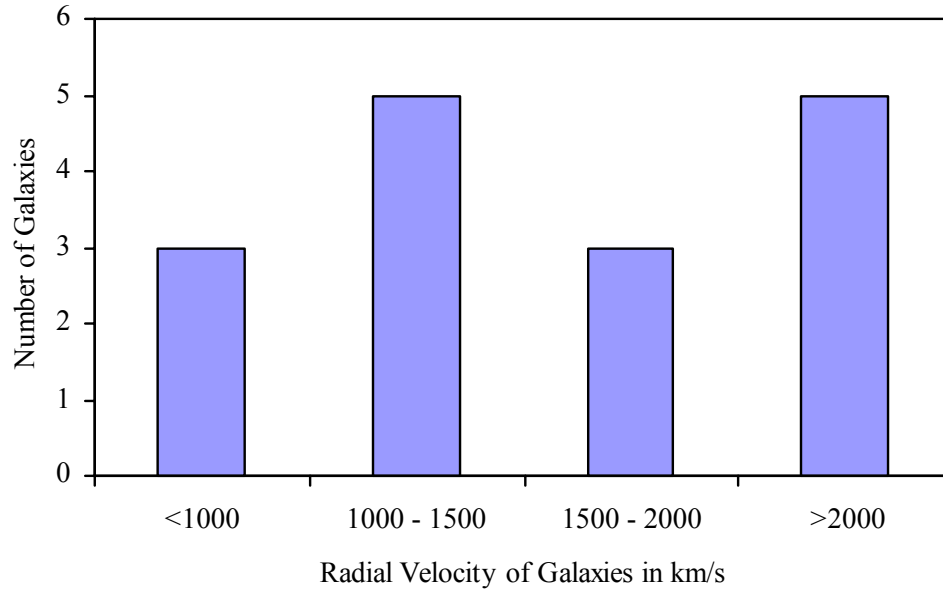


Figure 1-6. Radial velocity distribution of the galaxy sample. Velocity bins are separated by 500 km s^{-1} , corresponding to 7 Mpc , where $H_0=70 \text{ km s}^{-1} \text{ Mpc}^{-1}$.

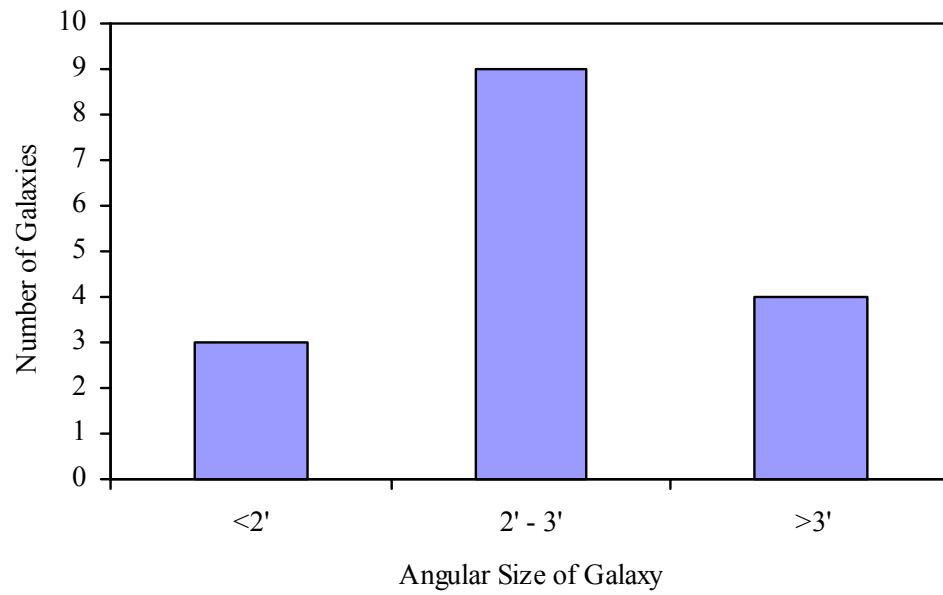


Figure 1-7. Angular size distribution of galaxy sample

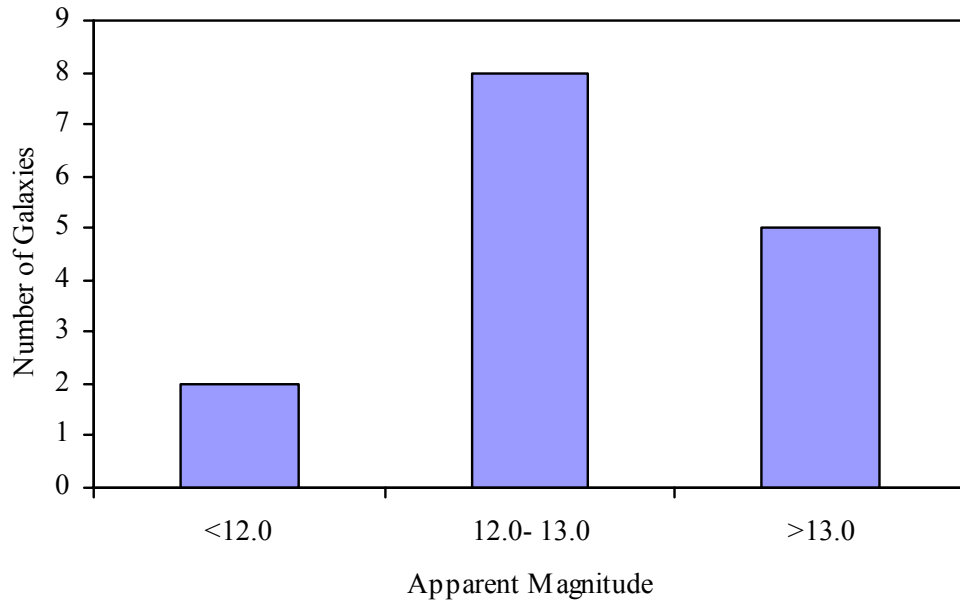


Figure 1-8. Apparent magnitude distribution of the galaxy sample

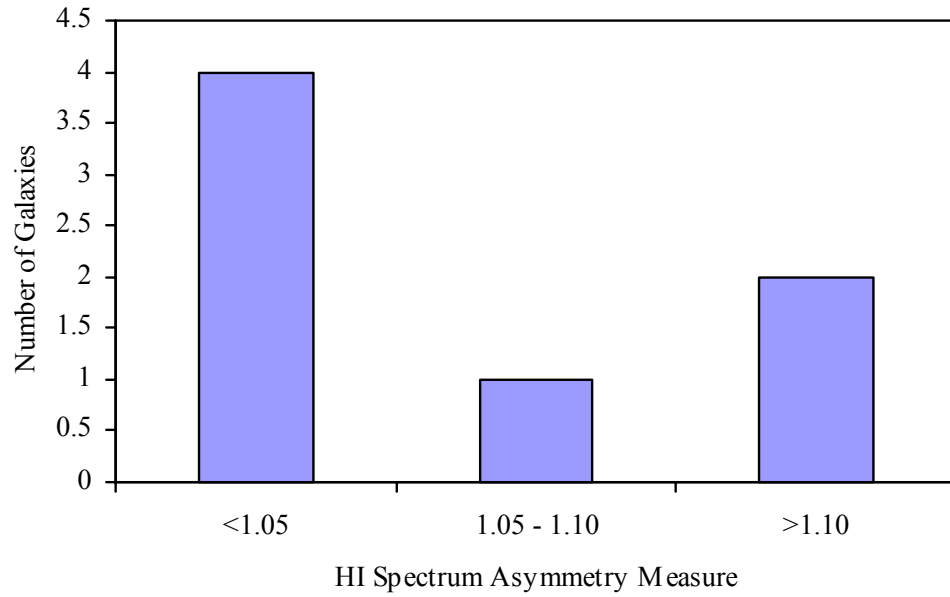


Figure 1-9. Distribution of previously measured HI spectrum asymmetry measure in sample galaxies

Observations

Our study used multi-wavelength observations of flocculent, barred galaxies. Other studies attempting to understand the nature of flocculence or bars have only looked at one or perhaps two wavelength regimes (Elmegreen & Elmegreen 1982; Grosbol & Patsis 1998; Block & Puerari 1999). We attempted to observe our sample in three dynamically important wavelength regimes (HI, near-infrared, and optical).

Neutral Hydrogen

We have obtained HI observations from the Very Large Array in D (60" resolution), C (20" resolution), and B (7" resolution) configurations for half of our sample galaxies. HI has traditionally been overlooked in studies of flocculent galaxies. However, it is important to consider galaxies in this wavelength regime. HI traces the recent history of the galaxy. It is estimated that 1 to 5 M_{\odot} of pristine HI falls onto the disk of the Milky Way per year. This infall most likely occurs in a lumpy fashion in the form of $10^7 M_{\odot}$ clouds (Casuso & Beckman 2001). The manner in which clouds of this size fall on the galaxy could potentially influence the optical morphology of star formation within the galaxy. Because HI is a dissipative medium, the effects of galactic cannibalism on a galaxy's HI distribution are not long-lasting. Thus, a disturbed HI morphology can act like a clock on recent interactions.

Optical

We obtained optical B, R, and I band images of our sample galaxies. These observations show the distribution and magnitude of star formation within these galaxies. We are interested in the size and morphology of the galaxy, size and morphology of optical bars, and location and amount of star formation. These observations serve as a

bridge to the HI observations as the cold neutral gas will be associated with star formation in many cases.

Near-Infrared

We have obtained near-infrared K-band images of four galaxies in our sample. These observations show the distribution of low mass dwarf stars within the galaxy. Some light at K-band is due to higher mass giant stars. However, pushing farther out into the infrared eliminates the effect of these stars. About 20% of the integrated galactic light in K-band is due to giant stars. These stars form the true stellar potential (Frogel et al. 1996). Since stars in a galaxy make up a collisionless fluid, the potential they form is long lasting and not greatly affected by minor mergers. From these observations we can get a sense of the galaxy's history over a long time scale.

Data Analysis

The focus of our study rests primarily on neutral hydrogen observations of the barred, flocculent galaxies. Near-infrared and optical observations are primarily used in a qualitative way to examine global features of the galaxies, such as the presence and number of spiral arms, stellar bars, star formation regions, surface brightness, and galactic size. Other than in these qualitative ways, we did not compare our optical and near-infrared observations with our neutral hydrogen observations.

CHAPTER 2 INTRODUCTION TO BARRED, FLOCCULENT GALAXIES

The Meaning of Flocculence

Elmegreen & Elmegreen (1982) provided us with the first large scale classification scheme for disk galaxy arm structure. They divided all disk galaxies into 12 groups based on the strength of their spiral arms. Groups one through four are called flocculent; five through nine are called multi-armed; ten through twelve are called grand design. A grand design galaxy is defined to have two long, prominent symmetric arms.

In further work with the same data set, Elmegreen & Elmegreen (1985) found that the minor spiral arms present in flocculent galaxies are blue relative to the surrounding interarm region, even if the region is not significantly brighter than the rest of the galaxy. Arm-interarm contrasts are as great as 2 magnitudes in both optical B and I bands for grand design galaxies. Arm-interarm contrasts are much less in flocculent galaxies and only appear in the optical B band (Elmegreen et al. 1996). Grand design spirals are dominated by a spiral density wave that triggers star formation, while star formation in flocculent galaxies is dominated by a stochastic self-propagating star formation. Differences in arm shape between flocculent galaxies are due to different shear rates in different galaxies (Elmegreen & Thomasson 1993; Gerritsen & Icke 1997). Elmegreen & Elmegreen (1985) also found that azimuthal light profiles in the optical B and I bands were chaotic looking for flocculent galaxies.

Other studies have found structural differences between optically flocculent and grand design galaxies. Romanishin (1985) found that grand design spirals are bluer than

flocculent galaxies, but the atomic hydrogen content is similar between classes. Cepa & Beckman (1990) found that grand design galaxies have longer scale lengths and are more massive in both stars and gas than flocculent galaxies. They note, however, that the mass surface density of the stars and gas does not vary between arm class. Elmegreen & Elmegreen (1987) also found that grand design galaxies were larger in optical wavelengths than flocculents, but there was no correlation between arm class and diameter of the atomic hydrogen content of the galaxy. Elmegreen & Elmegreen (1990) found that grand design galaxies generally have falling rotation curves at their extremities, while flocculent and multi-armed galaxies have flat or rising rotation curves. Presumably, this is an indication that grand design galaxies have relatively more mass in their disk than flocculent galaxies (Cepa & Beckman 1990; Elmegreen & Elmegreen 1990; Elmegreen & Thomason 1993). Models by Rautiainen & Salo (2001) show that galaxies with more massive halos compared to their disk masses, form flocculent spiral structure more readily than those with more massive disks. Elmegreen & Elmegreen (1990) note that the middle class of multi-armed spirals have rotation curves similar to flocculent galaxies, when naively one would assume the presence of spiral density waves in the multi-armed galaxies should give rotation curves like those of grand design galaxies. Molecular line studies of flocculent galaxies, such as Sakamoto (1996) seem to indicate that non-barred, flocculent galaxies may have central CO holes.

Flocculent Galaxies with Underlying Spiral Structure

Within the last decade, improvements in near-infrared detectors have allowed a new look at galactic structure. Optical images are able to reveal where young stars are located in the galactic disk. However, galaxies are optically thick at visible wavelengths (Block & Puerari 1999). This means that the old stellar population is not imaged in the

optical. Since the young, population I stars only compose about 5% of the dynamical mass of a galaxy, we miss a great deal of the available information in a galaxy by only observing it in the optical (Puerari et al. 2000).

Near-infrared observations of flocculent galaxies give an interesting twist to what we would expect of galaxies as seen in the optical. Cepa et al. (1988) found that the flocculent galaxy NGC 2403 displays grand design structure in J, H, and K bands. Thornley (1996) repeated this result for NGC 2403 and added three more galaxies to the list of optical flocculents with near-infrared grand design spiral structure. Grosbol & Patsis (1998), Elmegreen et al. (1996), and Puerari et al. (2000) added 10 more galaxies to this list. Thornley & Mundy (1997) found that CO and HI were enhanced along the near-infrared arms of one of these galaxies, NGC 5055.

The conclusion drawn by Block & Puerari (1999) based on the mounting observational evidence for flocculent spirals having near-infrared grand design structure is that there are two separate dynamical systems at work in a galaxy. The first system is the gas dominated population I disk. The second is the stellar dominated population II disk. Bertin & Lin (1996) show theoretically that two different morphologies can exist within one disk. The global mode of a galaxy is composed of spiral wave packets traveling radially inward and outward (i.e., a standing wave). The wave packets are trapped between the corotation circle and the bulge. The Inner Lindblad Resonance can serve to interrupt the wave packets in the stellar disk. The Inner Lindblad Resonance will not be as strong in the gaseous disk, thus allowing the standing wave to exist. In this situation, the galaxy could have two different morphologies at different observational wavelengths.

Spiral Structure Created By Galactic Bars

The ability of bars to create structure in galaxies has been a debatable topic for some time. There is evidence to suggest that barred spirals are correlated with grand design structure. From their original work, Elmegreen & Elmegreen (1982) find that in a large sample, barred spirals tend to be grand design. They find that for field galaxies, three fourths of barred spirals have grand design structure. Conversely, they find that for field galaxies without bars, only 30% are grand design.

Modeling done by Sellwood & Sparke (1988), on the other hand, found that a realistic bar-oval potential has a fairly weak effect on spiral arms within a disk. They found that a strong bar is necessary to produce a spiral response in the disk at large radii. In addition to this, they found that the pattern speed of the spiral arms and the bars were different. Sellwood (1993) pointed out that two prototypical barred, grand design galaxies (NGC 1300 and NGC 3992) have spiral patterns that are not bar driven. They concluded that spirals and bars are independent patterns except in the cases where the bar is very large. Infrared observations by Seigar & James (1998a,b) seem to show that at best, bars only weakly drive spiral structure. Other authors seem to believe that triaxial bulges may be able to drive the weak near-IR spiral waves of some optically flocculent galaxies (Block et al. 1996; Elmegreen et al. 1996).

Elmegreen & Elmegreen (1989) raise the issue that bars may not be so simple an animal. They find that there may actually be two different types of bars, one for early type disk galaxies, the other for late type. Early type bars tend to emit a higher fraction of the galaxy's light and are uniform in their light distribution. They are also longer relative to their host galaxy. This finding is also supported by the work of Martin (1995). Early type bars are strongly associated with grand design structure. Late type bars are

generally not associated with grand design structure. Elmegreen & Elmegreen (1989) suggest that the bars in early type galaxies extend to corotation, while late type bars do not. Bars that extend to corotation may have more influence in driving a spiral pattern far out in the disk. It has also been observed that early type bars have flat light profiles, while late type bars have exponential profiles (Elmegreen et al. 1996). Flat profiles in early type galaxies result from excess old and young stars piling up at the bar's end near the 4:1 ultraharmonic resonance. The bar in an early type galaxy ends because of orbital resonance scattering beyond the 4:1 resonance. In early type galaxies, the bar corotates with the spiral pattern (Elmegreen et al. 1996).

The different types of bars are also associated with galactic activity. Chapelon et al. (1999) suggests that galaxies with long bars are mostly active. Shocks along the leading edges of bars cause gas to fall towards the center of the galaxy (Athanasoula 1992; Patsis & Athanasoula 2001). Active late type galaxies have strong, long bars, while early type galaxy bars all tend to be strong. They suggest that the difference between late type and early type bars arises from different formation mechanisms. Late type bars possibly form slowly from instabilities, while early type bars form quickly from interactions. This leads to an evolution scenario, where late type galaxies develop bars, which then grow and dissipate to become bulges in early type galaxies (Chapelon et al. 1999). Bars should not form more than once in the life of a galaxy. Destruction of a bar leaves the disk too hot to form another bar unless an enormous amount of cold gas is dumped on the galaxy (Debattista & Sellwood 2000).

Spiral Structure Created By Extra-Galactic Companions

Companions have also been thought to be a cause of grand design structure in galaxies. Elmegreen & Elmegreen (1982) found that disk galaxies in either binary

systems or groups were more likely to have grand design structure than field galaxies, regardless of their bar classification. Looking more closely at the group galaxies in their original study, Elmegreen & Elmegreen (1983) found that interactions between a flocculent galaxy and either multiple companions or a group potential could be responsible for the number of grand design structure galaxies seen in groups. They found that group density was the most important factor in determining the fraction of non-barred spirals with grand design structure. They also found that grand design structure would last for many galactic rotations. Elmegreen & Elmegreen (1987) found that groups with small crossing rates have statistically more flocculent galaxies. Interactions may not only create, but also enhance weak spiral density waves already present (Elmegreen & Elmegreen 1990; Thornley & Mundy 1997). However, it seems that having a companion may not be a necessary and sufficient condition for the existence of spiral density waves (Elmegreen et al. 1996).

Computer simulations have also shown that interactions can create grand design structure within galaxies (Byrd & Howard 1992). Their simulations lead them to claim that a grazing 1% mass ratio interaction will create grand design structure. Also, they propose that 80 - 99% of galaxies have grand design structure because of interactions with companions. Their simulations show that structure will work inward during the course of an interaction. Simulations by Mihos & Hernquist (1994) show that infalling satellites will create an $m=2$ mode in the large galaxy. Retrograde encounters seem to affect a disk less than prograde encounters due to the shorter timescale of interaction (Andersen 1996). Gas will also be driven to the center of the large galaxy. Laine &

Heller (1999) were able to successfully model a long tidal arm resulting from a minor interaction in a simulation of NGC 7479.

Beyond just creating structure, it is thought that interactions with companions may induce bars. In their modeling of NGC 7479, Laine & Heller (1999) found that the interaction also created an observed bar in the main galaxy. They found that the companion galaxy only needed to be 10% of the main galaxy mass for this to occur. Andersen (1996) found that barred spirals are found preferentially closer to the center of the Virgo Cluster. Andersen (1996) concluded that interaction with the cluster potential is probably mostly responsible for this effect.

Again, it is also possible that interactions with companions may destroy structure in a disk galaxy. Sellwood (1993) as well as Debattista & Sellwood (2000) state that an interaction with a minor companion may destroy a bar in a disk galaxy, but not necessarily the disk. Accretion events could also create asymmetries in galaxy disks. These asymmetries may be amplified into the $m=1$ mode (Pisano et al. 1998).

Implications to Smaller Scales

Despite the fact that there may be large scale physical differences between flocculent and grand design galaxies, it seems that many of their smaller scale properties are similar. Elmegreen & Elmegreen (1985) and Romanishin (1985) found that the star formation rates of flocculent and grand design galaxies are approximately the same over a Hubble Time. Romanishin (1985) suggests that there may be a slightly different initial stellar mass function (IMF) operating in the two galaxies. If grand design galaxies produce about two times more massive stars, their bluer colors can be explained. Romanishin (1985) does not suggest why the two different morphological types would possess different IMF's. Other properties related to star formation such as CO surface

brightness, percentage of H α emission in HII complexes and far infrared emission, seem to be similar between the galaxy classes (Stark et al. 1987; Elmegreen & Salzer 1999). Bars do seem to have an effect on the star formation rates of galaxies, however. Martinet & Friedli (1997) found that bars which are relatively bright and long relative to the galaxy's radius have higher star formation rates. Barred galaxies in general have higher star formation rates (Kandalyan et al. 2000; Roussel et al. 2001). Bar ellipticity may be correlated with global star formation rate (Aguerri 1999). Late type bars seem to have higher star formation rates, but the cause is uncertain (Martin & Friedli 1999). Most of the star formation in the bar occurs at the time of bar formation. No simple relationship exists between bulge/disk ratio, bar classification, and the starburst properties of a galaxy (Roussel et al. 2001). HII regions in bars do not seem to be different than in spirals (Martin & Friedli 1999). A definite link between bars, star formation, and Hubble Type is still unclear (Martinet & Friedli 1997).

CHAPTER 3 OPTICAL AND NEAR-INFRARED OBSERVATIONS OF BARRED, FLOCCULENT GALAXIES

In this chapter, we review the optical and near-infrared observations made of the sample galaxies. These observations were made in order to study the bar and spiral arm properties of the galaxy sample in different wavelength regimes.

Observations

Optical observations for this chapter were obtained in May 2002 at the Instituto de Astrofísica de Canarias 80 cm (IAC80) telescope, an f/13.5 Cassegrain reflecting telescope at the Observatorio del Teide, Tenerife. We used a 1056 x 1024 pixel CCD with a plate scale of 0.4325"/pixel, yielding a field of view of about 7' x 7'. We obtained B and R images for our sample. The average seeing was on the order of 2".

Near Infrared observations of the sample galaxies were obtained in May 2002 at the 1.5 m Telescopio Carlos Sanchez (TCS), an f/13.8 Cassegrain reflecting telescope at the Observatorio del Teide, Tenerife. We used the 256 x 256 pixel CAIN-II camera with the wide field of view setting (plate scale of 1"/pixel), yielding a field of view of about 4' x 4'. We observed our sample galaxies in the K_s filter ($\lambda = 2.25\mu\text{m}$). Our seeing was on the order of 3" for these observations.

Data reduction for both the optical and near infrared data was performed using IRAF. Optical data reduction followed the typical procedure of dark and bias subtraction, flat field correction, and image combination. Many of the galaxy fields contained bright stars which required us to take a number of short exposure time images

that were later combined. Data reduction for near-infrared data involved subtracting dark images from both an on-source and off-source image and then subtracting the off-source image from the on-source image. These sky subtracted images were then flat field corrected and combined with other images of the same galaxy field. Problems including thick clouds and paint on the secondary mirror of the TCS prevented us from obtaining K_s images of better quality.

This chapter also relies heavily on optical images from the Digitized Sky Survey (DSS) and near infrared images from the 2 Micron All Sky Survey (2MASS) and the Ohio State University Bright Spiral Galaxy Survey (Eskridge 2002)

NGC 1784

As seen in Chapter 1 (Table 1-1), NGC 1784 is one of our most distant galaxies (33 Mpc) and is the physically largest (D_{25} of 49kpc) in the sample. Optical observations of the galaxy show that it is flocculent, but not because of a lack of star formation. Figure 3-1, an optical DSS image of the galaxy shows a prominent bar and inner ring. Two small arms seem to begin off of the ends of the bar, but dissipate quickly. The outer regions of the galaxy seem to be dominated by many little armlets, rather than by some overall 2-armed pattern. Elmegreen & Elmegreen's (1982) classification of this galaxy in to arm category "3" seems appropriate. The galaxy does show some spiral structure, but not on a large scale. Martin (1995) observed the properties of the bar in NGC 1784 and found the bar to have a semi-major axis length of 34" (5.4 kpc) and a semi-minor axis length of 7" (1.1 kpc). The ratio of the bar semi-major axis to the semi-minor axis is 0.21. The ratio of the bar length to the diameter of the galaxy is 0.20. Within the sample, we define increasing bar strength to be relative to the increasing size of the bar with respect to the galaxy diameter. NGC 1784 possesses a particularly large value within the

sample for this diagnostic. Longer bars with respect to the galaxy diameter will possess more mass and presumably have more dynamical influence on the galaxy. We also define the bar strength to go as inversely to the bar axis ratio. These values are similar to Martin's (1995) bar ellipticity class where round, SAB galaxies typically fall into class "1", and narrow, long bars are placed into class "6". The optical bar and disk properties of all galaxies will be summarized at the end of the chapter.

We find the bar to be asymmetric. The eastern edge of the bar is flat, while the western edge is more pointed. The bar looks like the head of a ball-peen hammer. However, neither Elmegreen et al. (1996) nor Jungweirt et al. (1997) found twists in the bar. Even still, this type of bar structure may be indicative of some type of interaction or dynamical instability, even though the majority of the optical galaxy does not show any large disturbances.

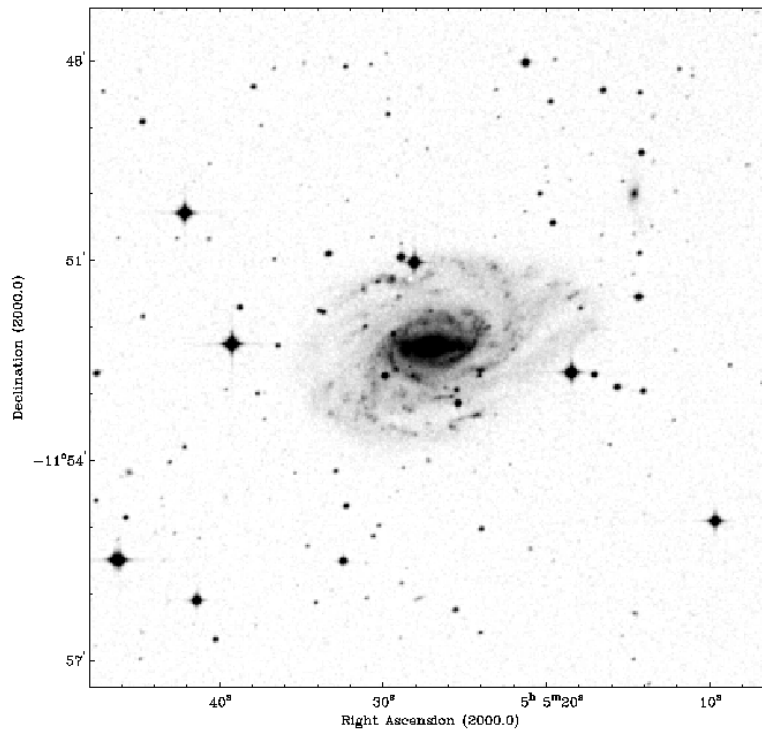


Figure 3-1. Optical R-band DSS image of NGC 1784

NGC 2500

Optical images of NGC 2500 (Figure 3-2) are dominated by the central bar and a few short chaotic spiral arms appearing to originate from this bar. Elmegreen & Elmegreen (1982) place this galaxy into arm classification bin "1", meaning that it is among the galaxies with the weakest arms. NGC 2500 clearly presents itself differently than does NGC 1784 which seem to have weak arms that stretch to the edge of the galaxy. In NGC 2500, there only appears to be a disk of stars beyond about half of the radius of the galaxy.

NGC 2500 has a reasonable angular size for observations (D_{25} of 135"), but has a small physical diameter of 7.8 kpc. Elmegreen & Elmegreen (1985) give the semi-major axis of the optical bar as 21", corresponding to a physical length of 1.2 kpc. From the DSS image below, we calculate a bar semi-minor axis of 4", a physical length of 0.2 kpc. We find a bar axis ratio of 0.19, and Elmegreen & Elmegreen (1985) give a bar to galaxy ratio of 0.24. Elmegreen & Elmegreen (1985) give the light profile of the bar as exponential, which is consistent with NGC 2500 being a late type galaxy (SBd).

K_s -band observations of NGC 2500 from the 2-MASS survey are presented in Figure 3-3. The sensitivity is very low in this image, but we do again see the bar is the most prominent feature of the galaxy. The bar region appears to be somewhat smaller than in the optical image, but this effect is more likely due to low signal. The near infrared bar is aligned with the optical bar. There does not appear to be any spiral structure in the near infrared disk of the galaxy, but again low sensitivity prevents us from commenting in detail

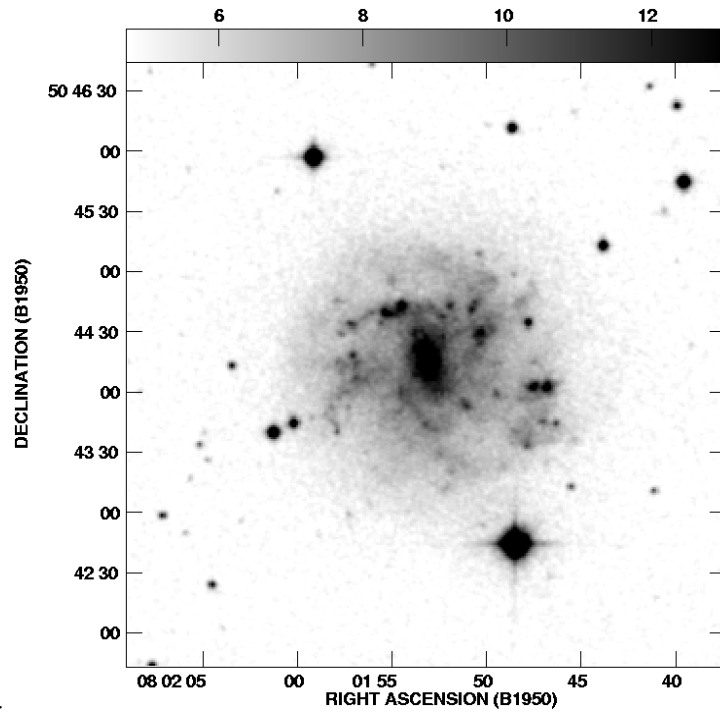


Figure 3-2. R-band DSS image of NGC 2500

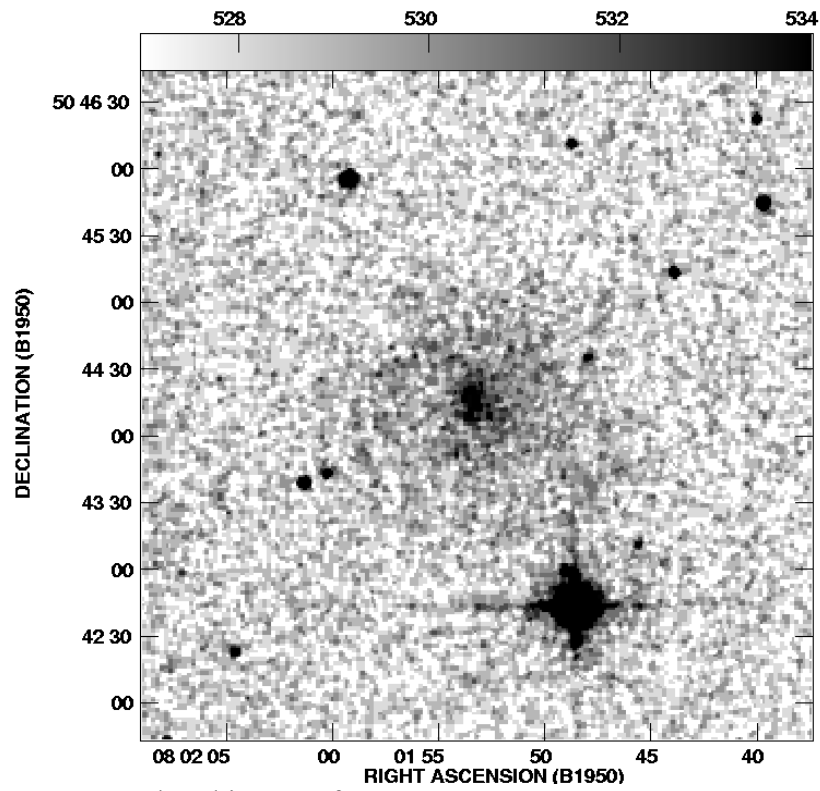


Figure 3-3. 2-MASS K-band image of NGC 2500

NGC 2793

Compared to the other galaxies in this sample, NGC 2793 is unique, because it is the only one that appears in the optical to have been in an interaction (Figure 3-4). It is unclear if the small galaxy present to the southwest of NGC 2793 is responsible for the interaction. Previous authors do not comment on this object and there have not been HI observations of either galaxy. Thompson (1977) and Mazzei (1995) note that the galaxy is a typical ring galaxy and is currently undergoing a starburst because of this interaction. The galaxy is small with an angular size of $1.3'$, corresponding to a physical diameter of 9 kpc. Elmegreen & Elmegreen (1982) give this galaxy an arm classification of "1". Our optical image shows nothing resembling optical spiral structure. The features prominent in the image are a bright bar and a ring of star formation to the southeast of the galaxy. We calculate the bar semi-major axis to be $7''$, corresponding to a physical length of 0.8 kpc. We calculate a bar semi-minor axis of $2''$, corresponding to a physical length of 0.2 kpc. The bar axis ratio for NGC 2793 is 0.28 and the bar to galaxy length ratio is 0.17.

Figure 3-5 shows a K_s -band near infrared image of NGC 2793 from the 2-MASS survey. The only structure present in this image is the bar, due to low sensitivity. We find that the near infrared bar is aligned similarly to the optical bar, and is on the order of the same length. There does not appear to be any signal from the disk region, so it is impossible to comment on the structure of the ring in the older star population.

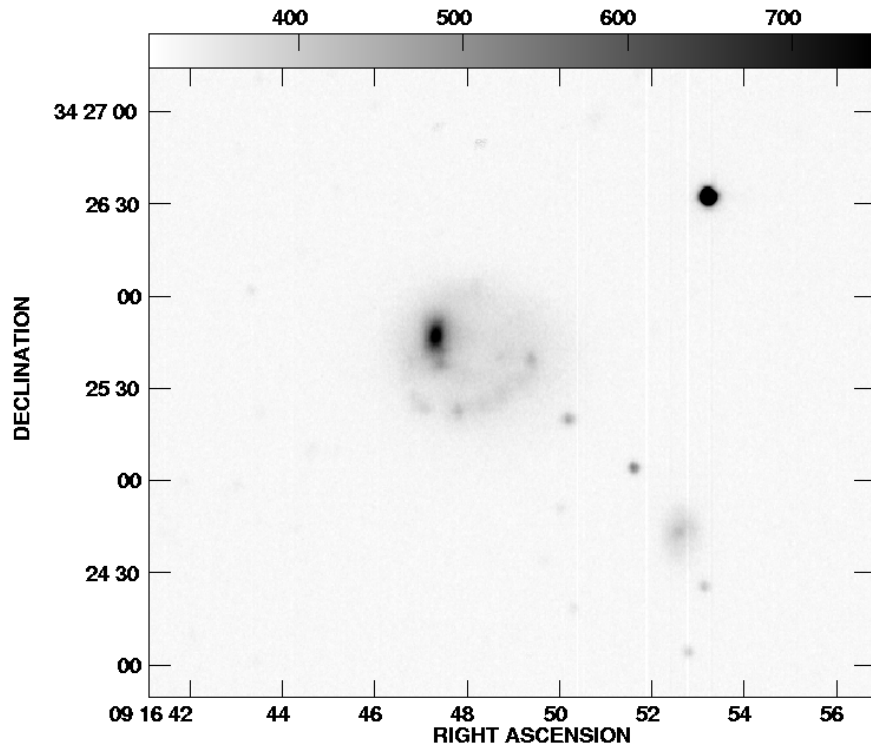


Figure 3-4. R-band image of NGC 2793 from IAC80

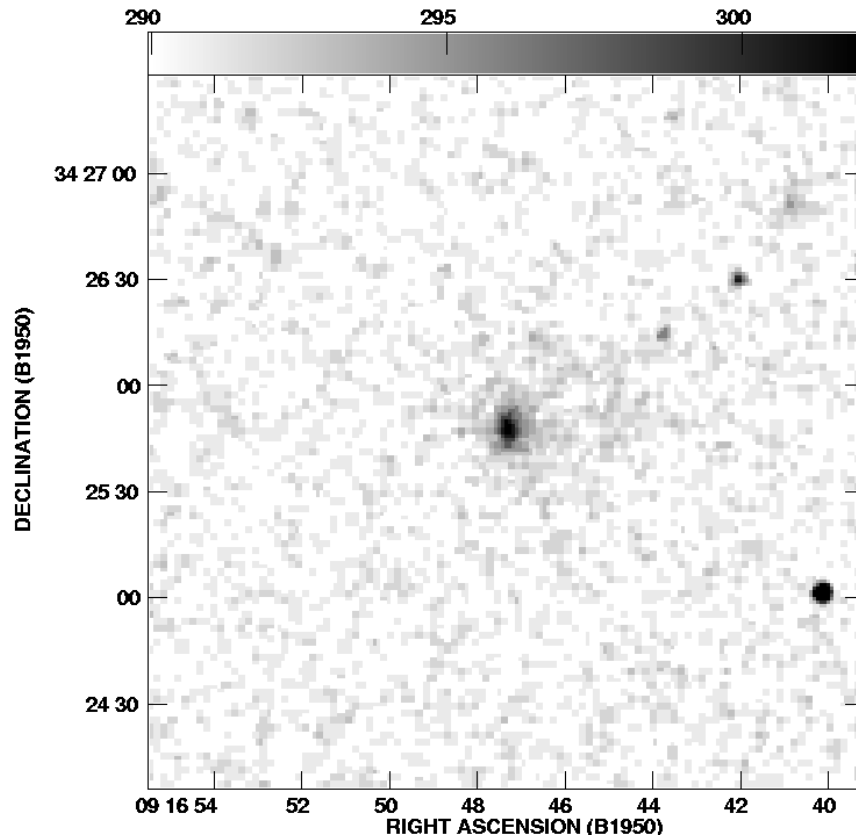


Figure 3-5. K-band image of NGC 2793 from 2-MASS. This image is rotated 180° and reflected relative to the y-axis with respect to our IAC80 image in Figure 3-6.

NGC 3055

From Table 1-4, we see that NGC 3055 is both a distant and small galaxy within our sample. It was found to have an optical diameter of 125" (14 kpc) by Martin (1995). Optical R and B band images of NGC 3055 (Figures 3-6 and 3-7) show a relatively undisturbed smooth stellar disk with a somewhat oblong bar. We agree with Elmegreen & Elmegreen's (1982) classification of this galaxy as belonging to arm class "3". A one armed structure along the southern side of the galaxy is the prominent structure in the disk of the galaxy. The outer regions seem to be too smooth in intensity. Martin (1995) found the bar to have a semi-major axis of 7" (0.8 kpc) and a semi-minor axis of 3" (0.3 kpc). Our B band image shows a similar result for the size of the bar. We calculate a ratio of the semi-major axis of the bar to the radius of the galaxy to be 0.11.

The B band image seems to indicate a one arm structure originating on the southern midpoint of the bar, curving westward through a large HII region and around to the north of the galaxy. The HII region is unusually large given the size of the galaxy. We calculate a diameter for the region to be 5" (0.6 kpc). The size of this object is near to the seeing limit of our observations, and may have undergone some beam smearing. There must be a significant amount of star formation occurring within this region, enough perhaps, to influence the gas dynamics of other areas in the galaxy. The B band image shows other regions of heightened star formation regions, notably along the inner parts of the one-arm structure, and a few diffuse regions on the eastern side of the galaxy. The scattered and separated nature of the star formation in this galaxy may be a result of the stochastic star formation processes theorized for flocculent galaxies.

The observed one armed feature may be a signature of an interaction, but there are no other asymmetric features associated with the optical morphology of the galaxy. We

produced a B-R color map for NGC 3055, but poor seeing at the time of observation and bad resolution did not allow us to produce a reasonable image.

Our K_s -band image (Figure 3-8) of NGC 3055 shows the prominent bar region of the galaxy, the large HII region, and hints at the one-armed feature circling the galaxy to the north. Given the resolution limits on our K_s observations, we calculate the same bar size in the infrared as the optical. We also observe the same disk structure present in the infrared as the optical. Deeper images would be necessary to probe further into the disk.

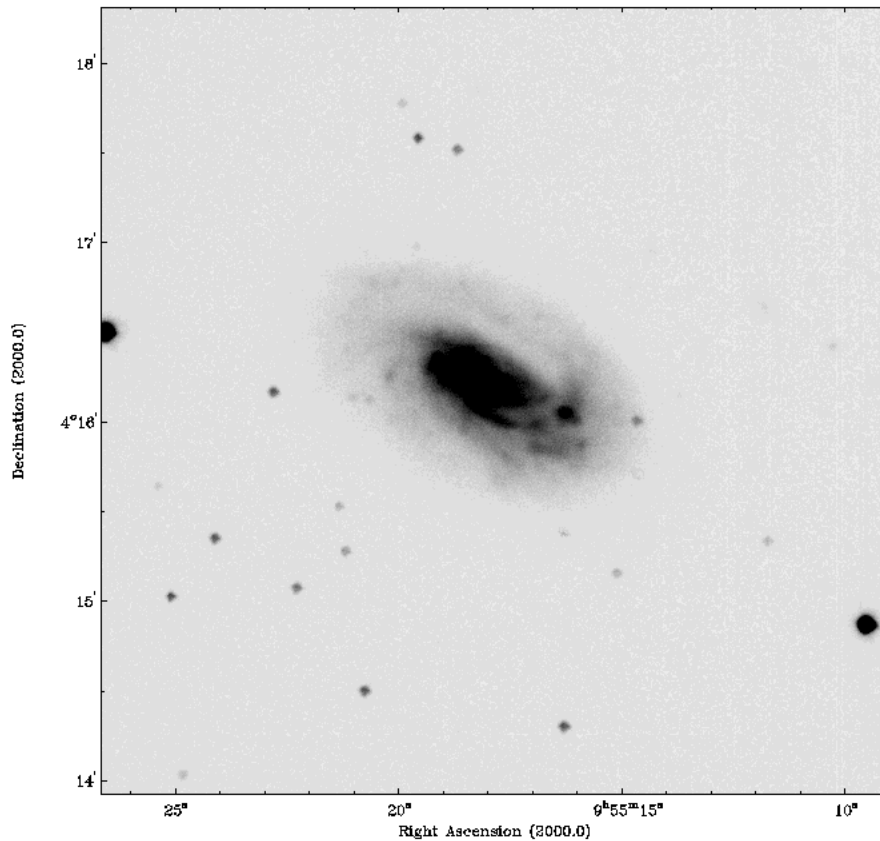


Figure 3-6. Optical R-band image of NGC 3055, taken at the IAC80 telescope

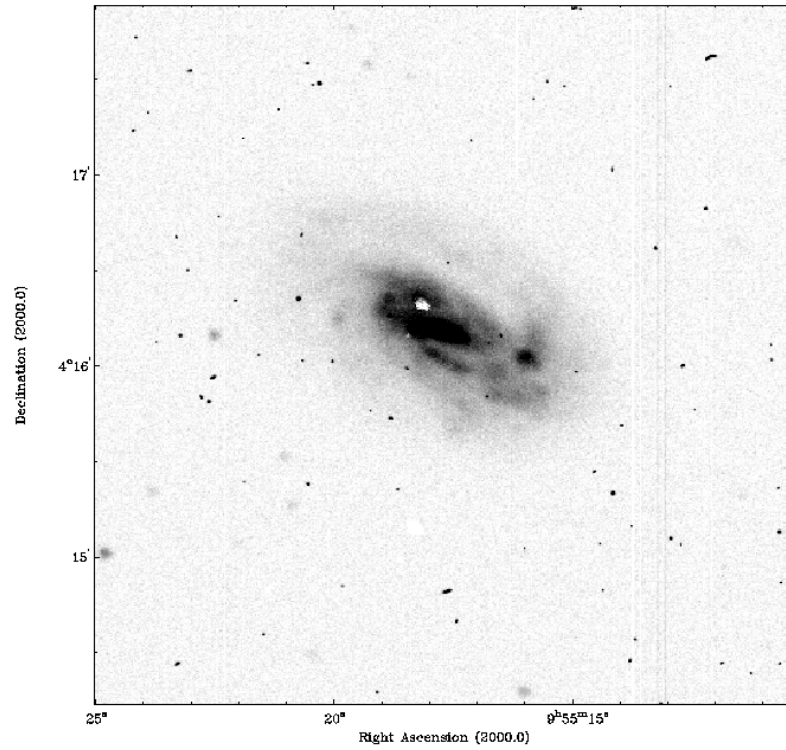


Figure 3-7. Optical B-band image of NGC 3055 taken with the IAC80 telescope

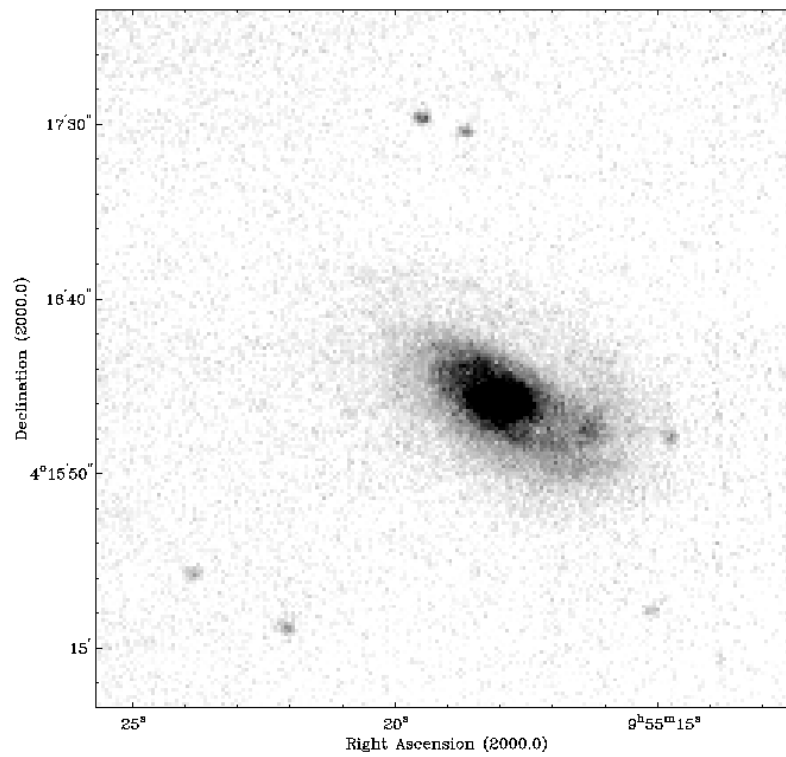


Figure 3-8. Near-Infrared K-band image of NGC 3055, taken with the TCS

NGC 3246

NGC 3246 is another galaxy that falls into the Elmegreen & Elmegreen (1982) arm class "1", indicating its extremely weak spiral arms. An optical DSS image (Figure 3-9) shows that the galaxy consists of an oval bar with the hint of one spiral arm leading off to the west of the galaxy. There is little other structure present in the disk beyond a few chaotic star forming regions. The galaxy appears to be squeezed in the north-south direction, more than what would be expected from typical inclination effects. In HI observations, Pisano & Wilcots (1999) found that the HI morphology of the galaxy was disturbed and that there was evidence for an unresolved HI companion very near to the galaxy. Knowing this, the optical presentation of the galaxy is not out of line with an interaction. Even though there appear to be several galaxies in the optical image, Pisano & Wilcots (1999) found that NGC 3246 was isolated in their HI observations.

Warmels (1988) calculated an optical D_{25} of 2.3' for this galaxy, corresponding to a physical diameter of 22 kpc, making this one of the larger galaxies in the sample. We calculate a bar semi-major axis of 10" corresponding to a physical length of 1.6 kpc and a bar semi-minor axis of 5", corresponding to a physical length of 0.8 kpc. We find the bar axis ratio to be 0.5 and the bar to galaxy length ratio to be 0.14. NGC 3246 has one of the more round bars in the sample, but it is on the high side of the sample in terms of the bar to galaxy length ratio.

The K_s -band image of NGC 3246 from the 2-MASS survey shows almost no signal from NGC 3246 except from the bar region. We find that the near infrared bar of NGC 3246 is aligned with the optical bar, and is about the same size. Unfortunately, we cannot comment on the disk structure of the galaxy, however. It would be interesting to examine

the morphology of the old stars in this galaxy given the likelihood of an interaction from Pisano & Wilcot's (1999) observations.

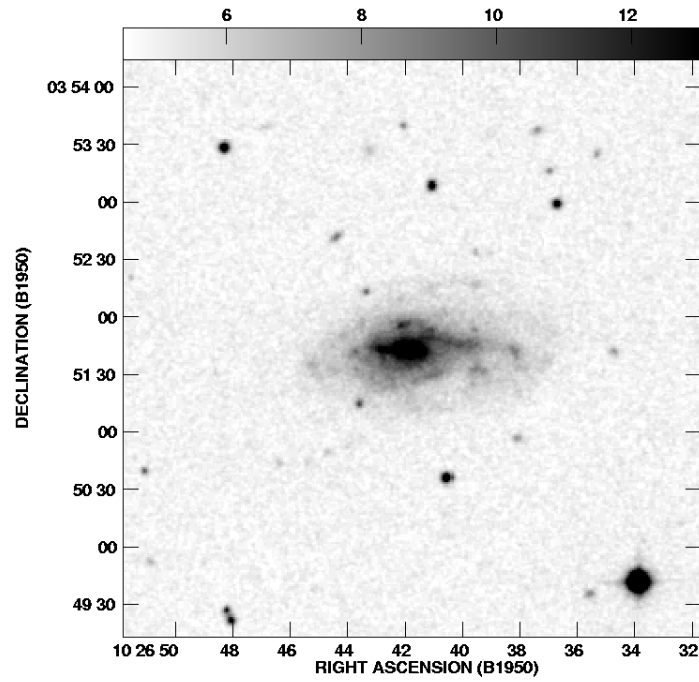


Figure 3-9. R-band image of NGC 3246 from IAC80

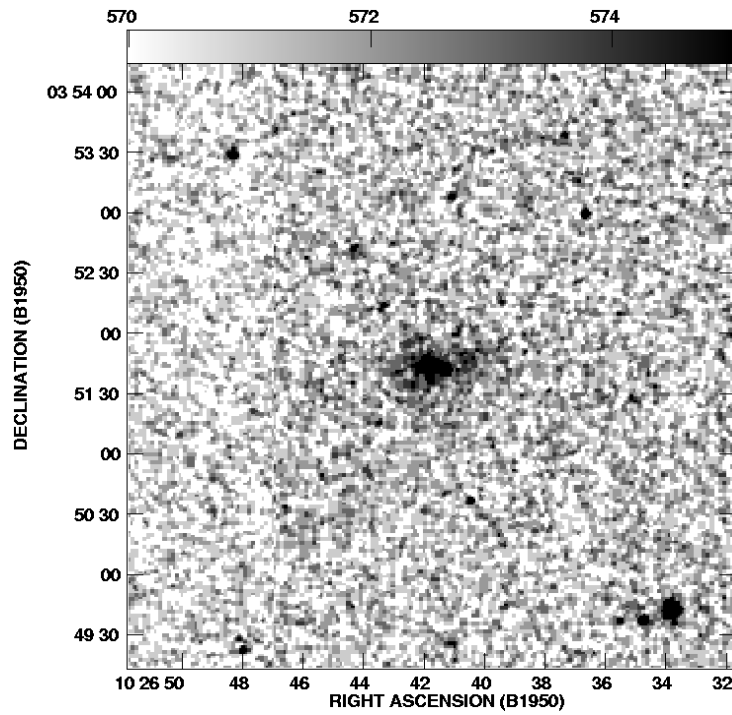


Figure 3-10. K-band image of NGC 3246 from 2-MASS

NGC 3687

NGC 3687 is the most distant galaxy in our sample with a recessional velocity of 2507 km s^{-1} , corresponding to a distance of 35.8 Mpc ($H_0 = 70 \text{ km s}^{-1} \text{ Mpc}^{-1}$) (de Vaucouleurs et al. 1991). Due to its large distance, its small optical angular size ($1.9''$) corresponds to a reasonably, for the sample, large 19.7 kpc physical size. Our R-band IAC80 image (Figure 3-11) of NGC 3687 shows that the galaxy has a prominent bar and regular, but dim, spiral arms. Elmegreen & Elmegreen (1982) give this galaxy an arm class of "4", meaning it is among the flocculents with the most structure. The underlying spiral structure is more apparent in the B-band image of the galaxy in Figure 3-12. The arms do seem to bifurcate in the outer regions of the galaxy and there does not seem to be a two-armed pattern, but rather a many-armed pattern. Given this arm pattern and the relative dimness of the arms compared to the optical bar, the classification of "4" for this galaxy seems appropriate. In the B-band image there appears to be a ring of stars at about half of the galaxy radius.

We calculate a bar semi-major axis of $7''$ from the R-band image of NGC 3687. This corresponds to a physical bar length of 1.2 kpc. We calculate a bar semi-minor axis of $5''$, corresponding to a physical length of 0.9 kpc. The bar is very round, having a bar axis ratio of 0.71, and not particularly long compared to the galaxy, having a bar to galaxy radius ratio of 0.12. There is reason to believe that the bar is longer than this measurement. There seems to be the slightest hint of a connection between the bar and the star forming ring in the B-band image. Further dynamical study of this galaxy would be necessary to determine whether this optical emission was related to the bar or small spiral arms linking the bar to the ring.

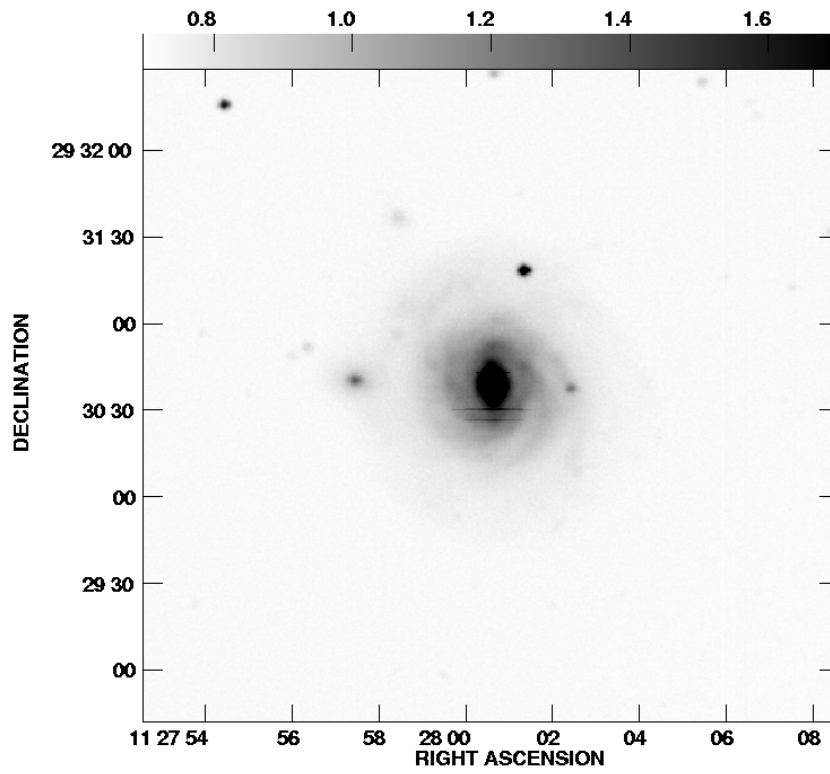


Figure 3-11. R-band image of NGC 3687 from IAC80

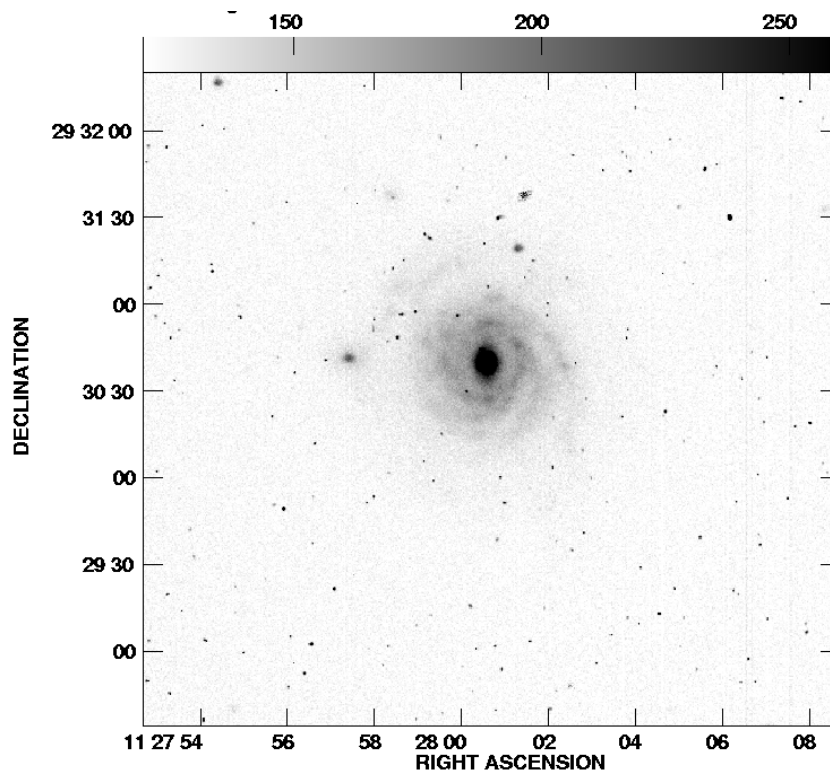


Figure 3-12. B-band image of NGC 3687 from IAC80

The K_s -band image of NGC 3687 from the 2-MASS survey shows that the optical bar present in the R-band image may not exist at infrared wavelengths. This low sensitivity image shows an almost circular feature at the center of the galaxy. Deeper images are necessary to determine if an oval pattern emerges outside of this feature at a lower surface brightness. Further dynamical study of the galaxy would also be interesting to determine the properties of this circular feature.

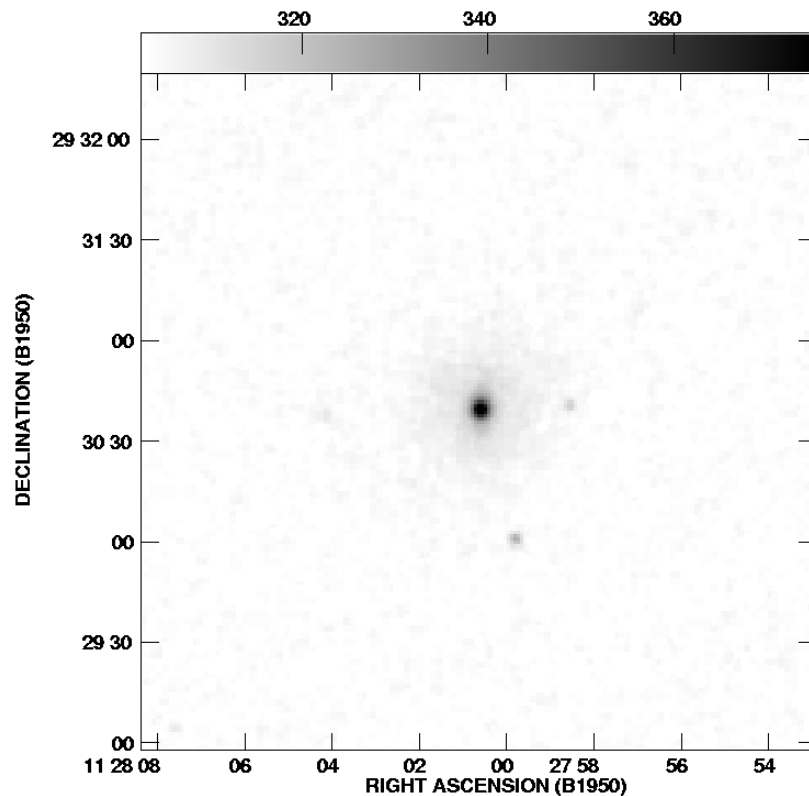


Figure 3-13. K-band image of NGC 3687 from 2-MASS

NGC 3887

NGC 3887 is given an arm classification of "2" by Elmegreen & Elmegreen (1982). The galaxy possesses a bright oval bar and limited spiral structure in an optical R-band image (Figure 3-14). There appear to be spiral arms originating from the ends of the bar, but the spiral that continues to the east of the galaxy is the only one that exists for an appreciable distance. The arms quickly bifurcate near the outer edge of the galaxy and

dissipate into an even disk of stars. There also appear to be knots of star formation throughout the disk. Some appear to be associated with spiral arms, while others are isolated in the disk.

NGC 3887 has an angular size of $3.3'$, corresponding to a physical diameter of 16.5 kpc (Haynes et al. 1998). Martin (1995) calculated a bar semi-major axis length of $11.5''$ and a semi-minor axis length of $5.5''$. These values correspond to physical distances of 1 kpc and 0.5 kpc, respectively. From these values, we find a bar axis ratio of 0.5 and a bar to galaxy radius ratio of 0.12.

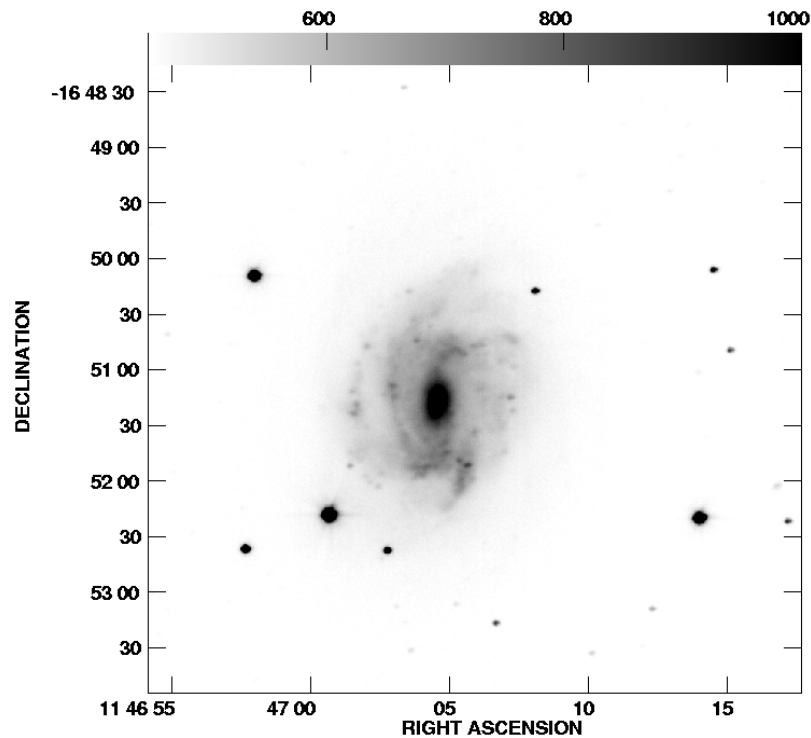


Figure 3-14. R-band image of NGC 3887 from IAC80

Figure 3-15 shows a K_s -band image of NGC 3887 from the 2-MASS survey. Here we again see the bar regions of the galaxy and evidence of the inner spiral arms. The near infrared bar appears to be a bit shorter than the optical bar, here looking to have a semi-major axis of $5''$. However, without strong signal in this image, it is impossible to be confident in this value. We see near infrared counterparts of the inner spiral arms seen

in the optical image, but no evidence for spiral structure further out into the disk. Jungwiert et al. (1997) reported twisted isophotes in the bar of NGC 3887, often a signature of previous interactions. We see no evidence of that here, however, our data does not possess the same resolution or sensitivity.

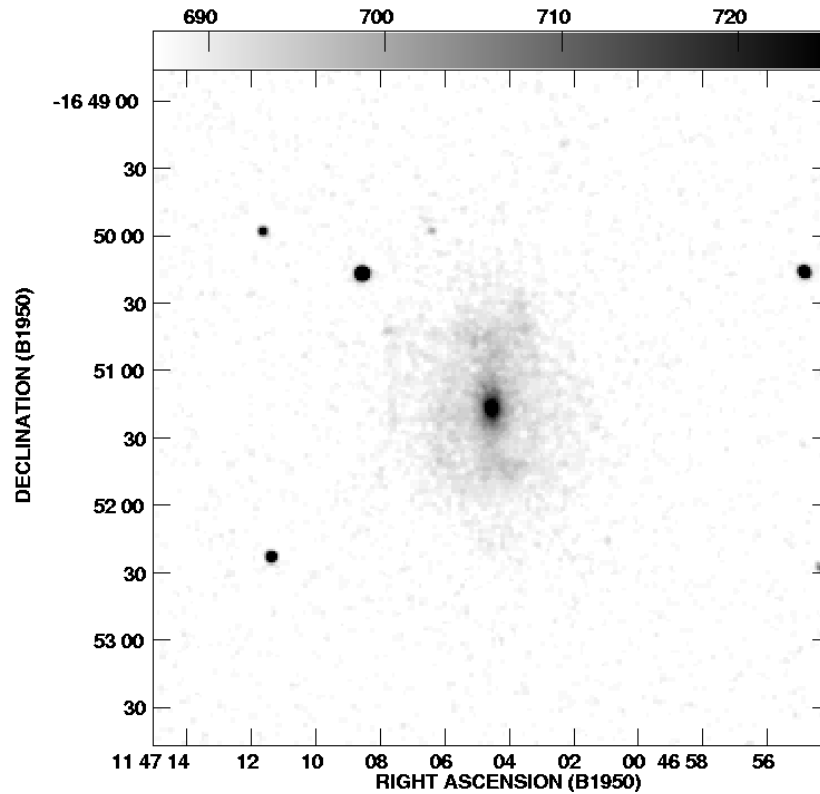


Figure 3-15. K-band image of NGC 3887 from 2-MASS

NGC 3930

NGC 3930 presents the most optically grand design structure in the entire galaxy sample. However, it is the asymmetry in strength between its two arms that causes Elmegreen & Elmegreen to place it into arm class 4, and call it flocculent. In Figure 3-16, a R-band image of NGC 3930 taken at the IAC80, and especially in Figure 3-17, a B-band image of NGC 3930, we see that the southern arm of the galaxy is much longer and stronger than the northern. In the B-band image, the southern arm extends almost all the way to the edge of the optical emission, while the northern arm extends to only about 1/2

of the radius of the galaxy. Haynes et al. (1998) calculated a D_{25} for NGC 3930 of 3.2' (12 kpc) meaning that the southern arm is somewhat longer than this distance, while the northern arm is on the order of 8 kpc. One-armed spirals have been associated with interactions, and this is certainly possible in this case, but we see no other large asymmetries in the optical image of NGC 3930.

NGC 3930 does not possess a particularly prominent bar. It is classified by de Vaucouleurs et al. (1991) as an SAB galaxy. Our optical images show that there is not much of a bar region, but more of an oval area where the two inner spiral arms connect. We calculate a semi-major axis of 12" (0.8 kpc) and a semi-minor axis of 5" (0.3 kpc). The ratio of the bar semi-major axis to the galaxy radius is 0.06 for NGC 3930.

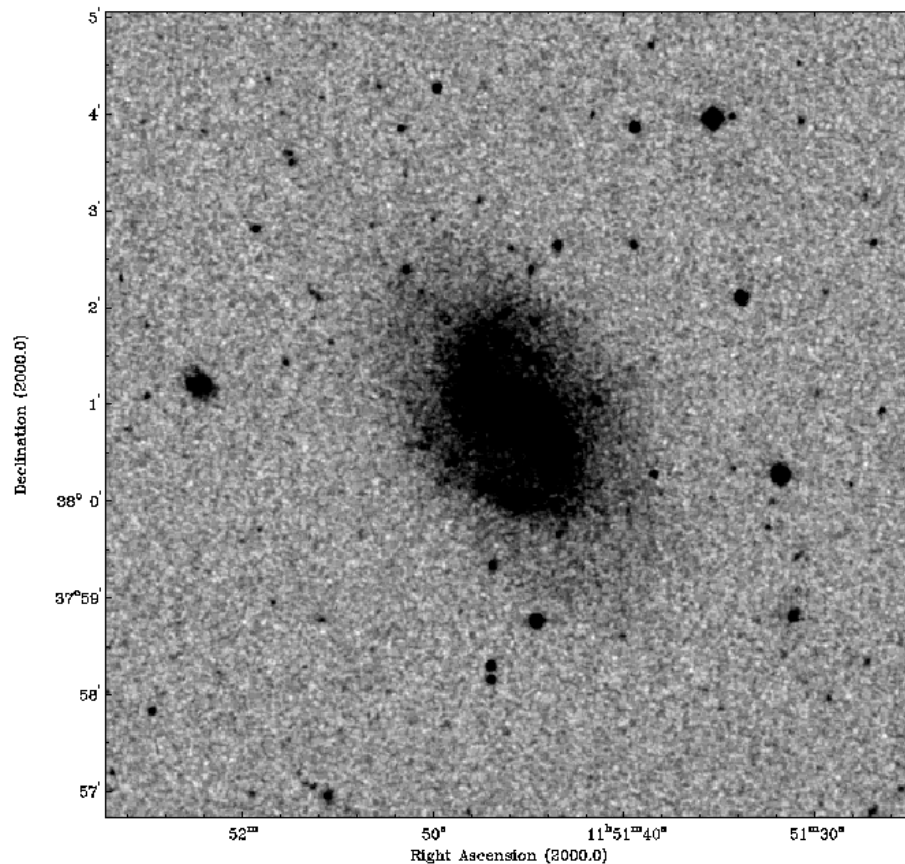


Figure 3-16. Optical R-band image of NGC 3930 taken with IAC80 telescope

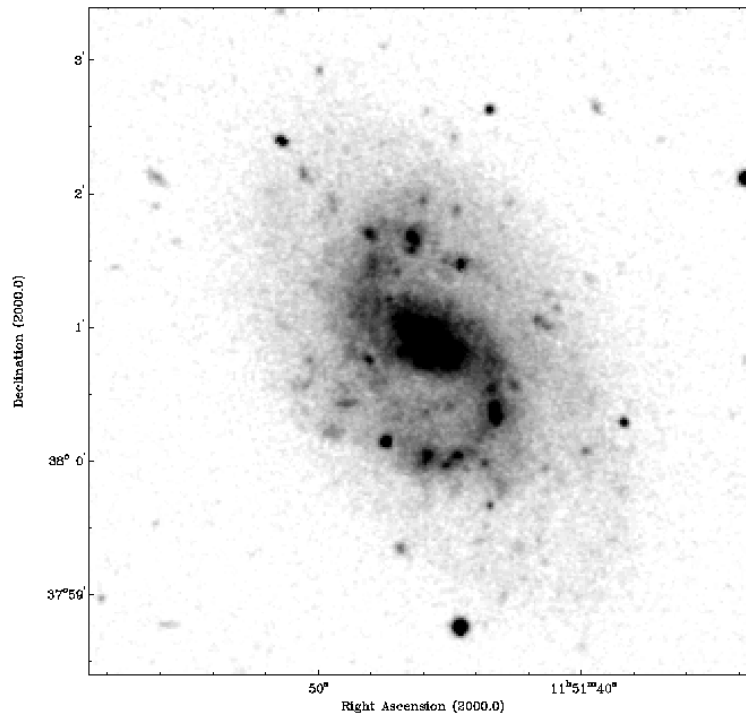


Figure 3-17. Optical B-band image of NGC 3930

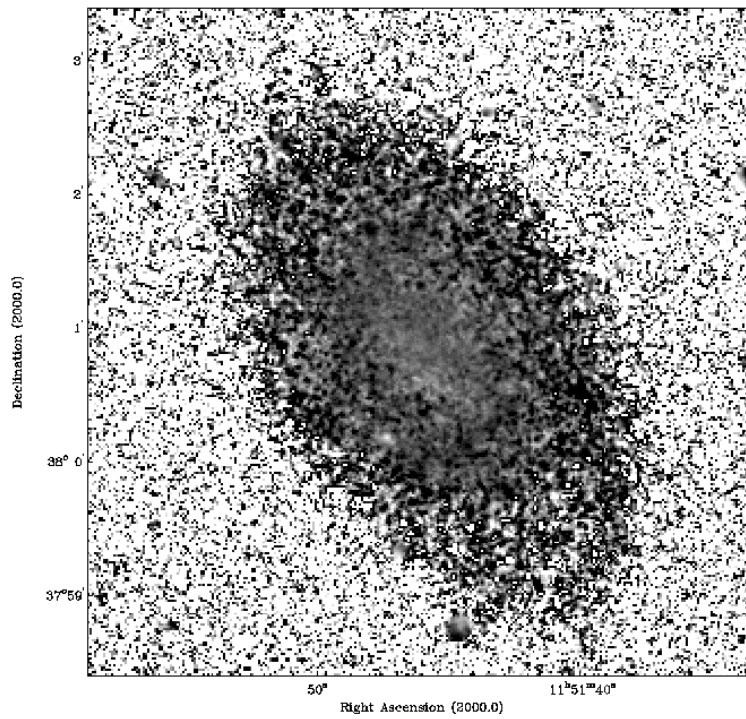


Figure 3-18. B-R color map of NGC 3930. Light grayscale regions are blue in color. Darker grayscale regions correspond to red colors.

Figure 3-18 shows a B-R color map of NGC 3930. This map does not show much structure in the disk of NGC 3930. The low resolution of this image may be smearing out color effects of the spiral arms, but it seems that they are not particularly blue. The region immediately south of the bar appears to be bluer than the bar itself, indicating star formation in this region. This region may coincide with the southern spiral arm. However, the sensitivity and resolution are again not high enough to comment in detail on the processes active in this region.

NGC 4793

NGC 4793 possesses an interesting optical morphology. Figure 3-19 shows an R-band image of the galaxy taken with the IAC80 telescope. NGC 4793 possess a very bright central bar region that appears to be connected to several spiral arms in the south. These spiral arms appear to be dotted with large star forming regions, and one curves along most of the southern edge of the galaxy. The northern end of the bar does not appear to have any spiral structure. There is one isolated, large star forming region in the northern region of the galaxy. Elmegreen & Elmegreen (1982) classify this galaxy as a "1" due to its overall lack of spiral structure. To the west and north of the galaxy, there are several knots of optical emission forming an arc about the galaxy. These regions may form a tidal tail produced by a previous interaction. Overall, the galaxy does appear disturbed, which is consistent with Sanders et al. (1991) CO observations.

The angular size of the galaxy is $2.8'$, corresponding to a physical size of 28.9 kpc, making this the second largest galaxy in the sample. Condon et al. (1991) quotes the distance to the galaxy as 49 Mpc, however, this was made with a H_0 value of $50 \text{ km s}^{-1} \text{ Mpc}^{-1}$. We adopt a more realistic value of $70 \text{ km s}^{-1} \text{ Mpc}^{-1}$ for H_0 and thus calculate a distance of 35.5 Mpc. We calculate the bar in NGC 4793 to have an angular semi-major

axis of 10" and a semi-minor axis length of 4". These values correspond to physical distances of 1.7 kpc and 0.7 kpc, respectively. The bar axis ratio is 0.4 and the bar length to galaxy radius ratio is 0.06. It is particularly difficult to determine the bar length in this galaxy as some of the spiral arm features south of the bar can easily blend into the bar at the right isophote levels. We believe that these objects should not be considered part of the bar, and from this get a small value for the bar semi-major axis length.

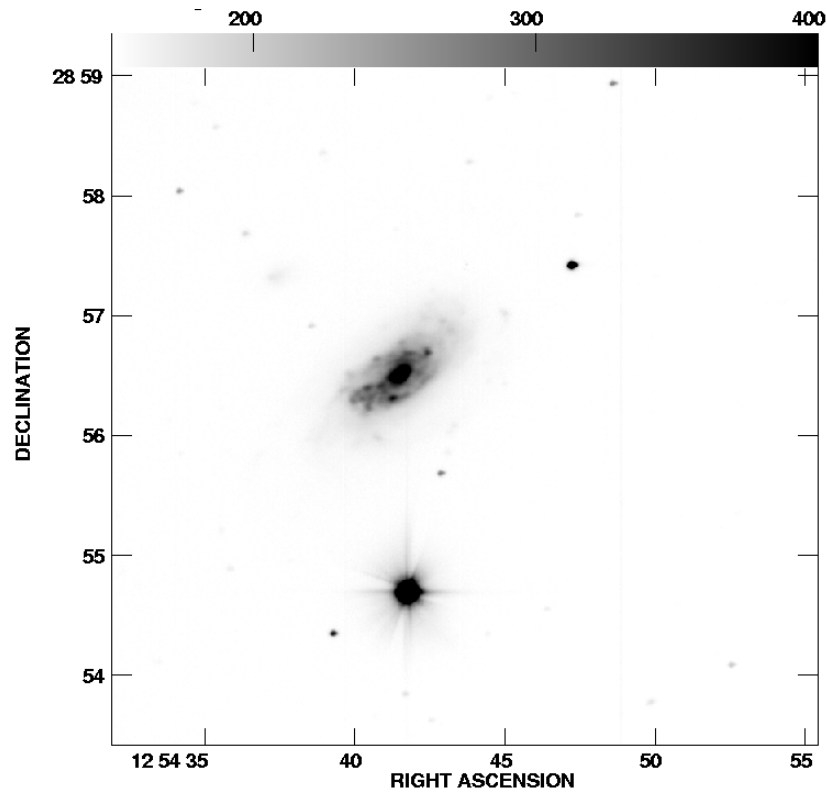


Figure 3-19. R-band image of NGC 4793 from IAC80

Figure 3-20 shows a K_s -band image of NGC 4793 from the 2-MASS survey. Here we see the spiral arm structures south of the bar are unresolved into a general region of near infrared emission (this image is flipped and rotated, so the previously southern features are now in the north). The bright bar region may be slightly smaller in the near infrared than in the optical, but at this resolution it is difficult to tell. The near infrared and optical bars are aligned similarly. Beyond the unresolved spiral arms south of the

bar, we do not see any other evidence of spiral structure in the near infrared disk of NGC 4793.

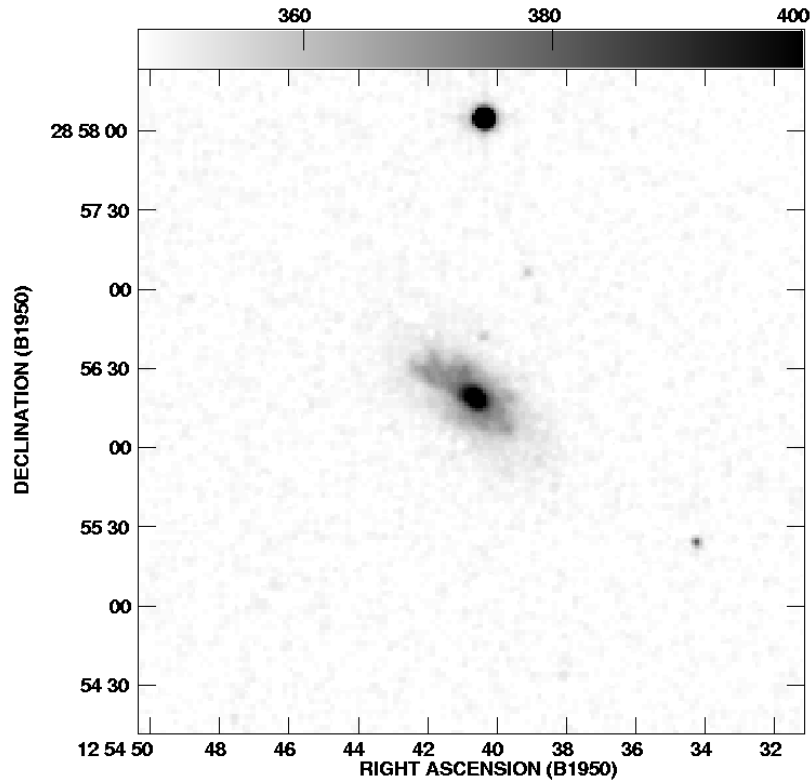


Figure 3-20. K-band image of NGC 4793 from 2-MASS. This image is rotated 180° and flipped along the y-axis relative to the R-band IAC80 image in Figure 3-19.

NGC 4900

Optical images of NGC 4900 show obvious signs of disturbance. Figure 3-21 shows an R-band image of NGC 4900 taken with the IAC80. We see a bright, prominent bar surrounded by small star forming regions with no discernable structure present in the disk. Elmegreen & Elmegreen (1982) place NGC 4900 in arm class "3". This is perhaps an overstatement of the structure present in the galaxy, as it seems that there is no overall spiral pattern in this galaxy. The very bright point source at the southeastern limit of the galaxy is a foreground star and not associated with the galaxy.

The galaxy itself is very small, having an optical diameter of $2.2'$ (9 kpc). We calculate a bar semi-major axis of $10''$ (0.7 kpc) and a semi-minor axis of $5''$ (0.4 kpc).

The value for semi-major axis does not include the wispy region north of the bar. It is unclear if this region is a low surface brightness extension of the bar, or simply star forming regions in the disk. Higher resolution observations would be necessary to determine this. We calculate a value of 0.08 for the ratio of bar semi-major axis to galaxy radius.

Figure 3-22 shows a B-band optical image of NGC 4900 taken with the IAC80 telescope. Again, we see the bright bar surrounded by chaotic star forming regions. The B-band image seems to show more arc like structures joining the star forming regions, but there is nothing approaching grand design spiral structures. The individual star forming regions are point sources in our observations, having a diameter on the order of 2" - 3" (0.1 - 0.2 kpc). The overall distribution of these star forming regions, and the strength of the bar seems to indicate that NGC 4900 has been involved in some type of recent interaction. However, there does not appear to be any optical emission outside of the optical disk of the galaxy associated with any companion galaxies.

Figure 3-23 is an optical B-R color map of NGC 4900. We find that the center of the bar is blue relative to the edges, indicating that there is star formation occurring within the bar and that the edges are obscured by dust. Both Devereaux (1989) and Ashby et al. (1995) do not classify the galaxy as starburst or active, so the color must come from normal star formation processes and not an AGN. We also see that several of the star forming regions mentioned above appear blue in the color map, indicating their status as HII regions. Again, there does not appear to be any global spiral structure pattern in the color map.

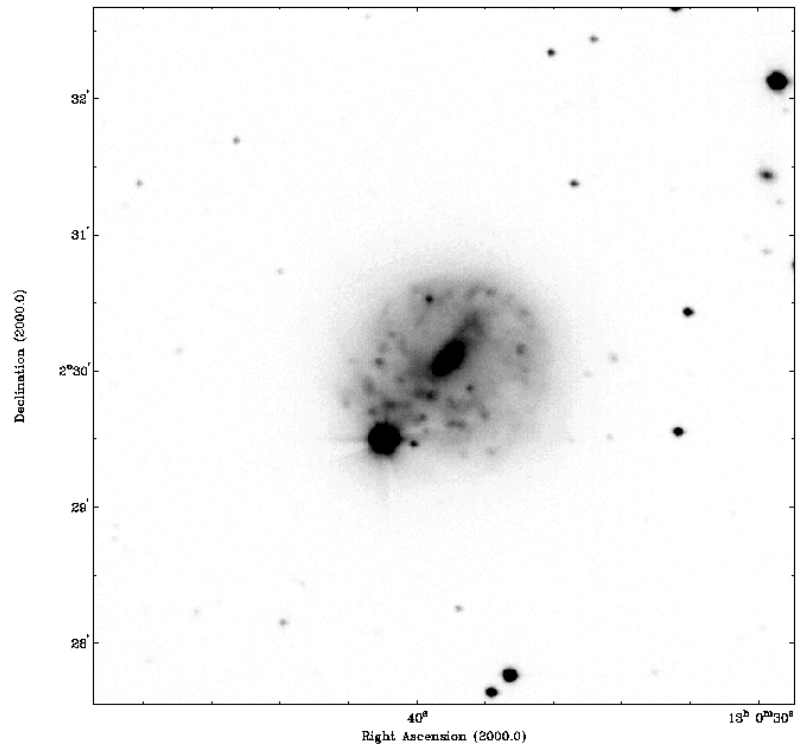


Figure 3-21. Optical R-band image of NGC 4900 taken with the IAC 80 telescope

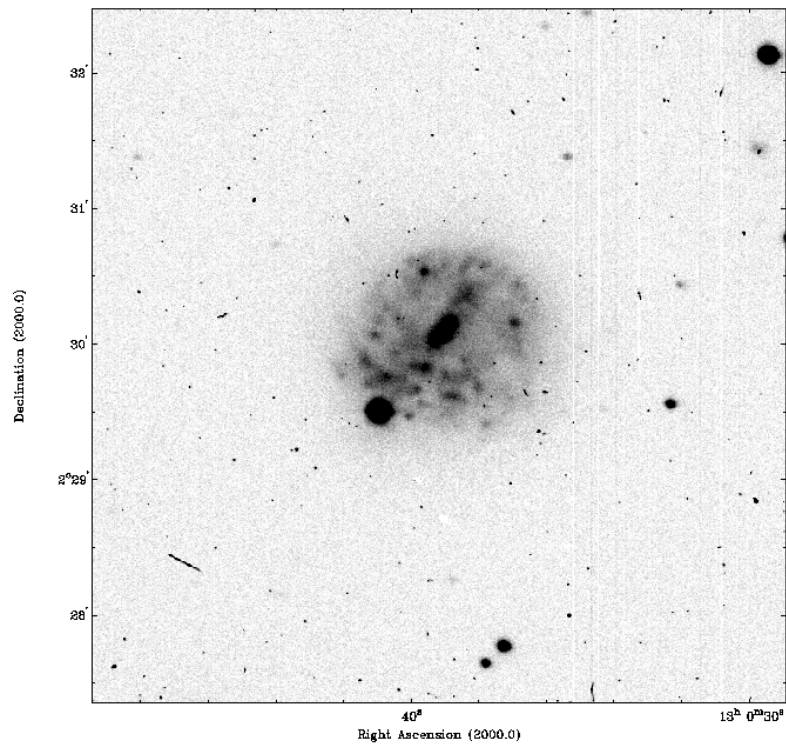


Figure 3-22. Optical B-band image of NGC 4900 taken at the IAC80 telescope

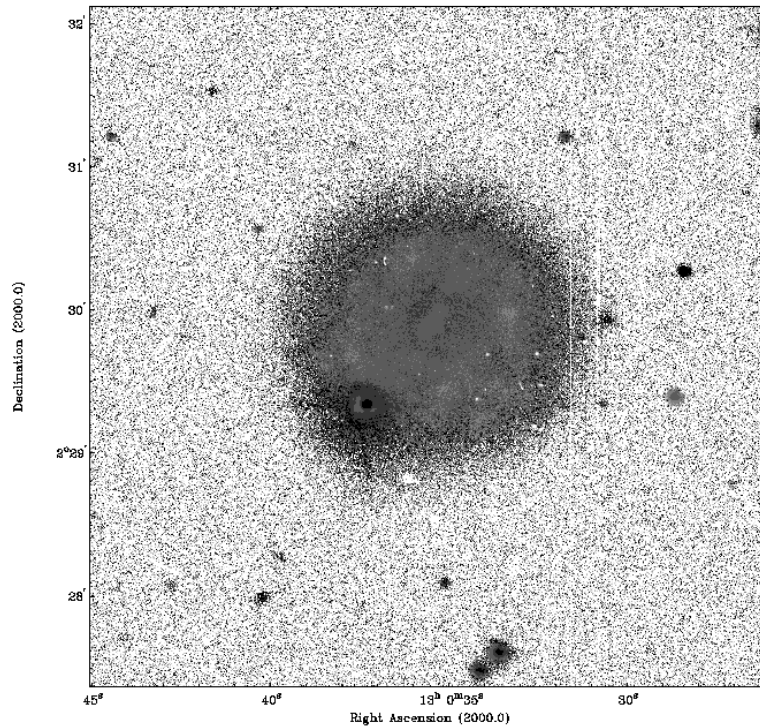


Figure 3-23. B-R color map of NGC 4900. Light grayscale regions are blue in color. Darker grayscale regions correspond to red colors.

Figure 3-24 is an H-band near infrared image of NGC 4900 from the Ohio State Bright Galaxy Survey (Eskridge 2002). The resolution here is less than with the optical images above, but we see largely the same features in the near infrared. There is a bright bar surrounded by arcs of star forming regions. In this image, there may be slightly more coherence to the arcs of star formation, but they do not appear to originate with the bar as typical spiral arms do. The bar is larger in this image compared to the optical images above. The wispy northern end of the bar in the R and B-band images is filled in the near infrared. This could be due to the dynamic range of the H-band observations, or the stellar make up of the northern end of the bar is different and contains more old, low mass stars than the central parts of the bar.

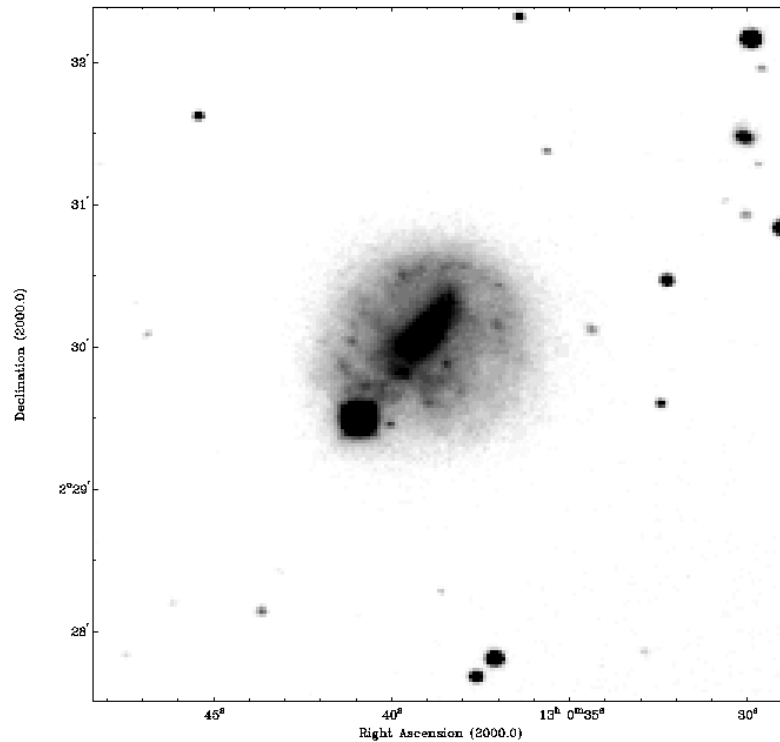


Figure 3-24. H-band image of NGC 4900 from Ohio State

NGC 4904

NGC 4904 is another galaxy that appears to show signs of disturbance in its optical emission. Elmegreen & Elmegreen (1982) place the galaxy in arm class "2" making it among the most flocculent in our sample. Figure 3-25 is an R-band optical image of the galaxy taken with the IAC80 Telescope. NGC 4904 possesses a very large bar relative to the galaxy itself and diffuse emission outside of the bar. There appears to be one arm emanating from the southeastern end of the bar, and another arm and loop of emission related to the northwestern end of the bar.

The galaxy has an angular size of 2.2' corresponding to a physical diameter of 10.4 kpc, making this another small galaxy. The bar was measured by Chapelon et al. (1999) to have a semi-major axis of 16" (1.1 kpc) and a semi-minor axis of 7" (0.5 kpc). The bar semi-major axis to galaxy radius ratio is 0.2.

Figure 3-26, a B-band optical IAC80 image of NGC 4904 shows that the bar itself has some interesting structure. The bar appears to be shaped like a bent peanut. Where the central region the bar was the thickest in the R-band image, the middle of the bar is narrow in B-band image. Overall, the bar is skinnier in the B-band image as well. There is a faint hint of 3-armed structure in the galaxy in the B-band image. As with 1-armed structure in NGC 3055 and NGC 3930, 3-armed structure in galaxies has also been associated with interactions. We do not find any optical emission external to the galaxy related to any satellites.

Figure 3-27 is a B-R color map of NGC 4904 made with data from the IAC80 telescope. We observe a very strong dust lane through the center of the bar region of the galaxy. Both long edges of the bar appear blue in this image, but the center of the bar is red. A dust lane such as this is typical of a bar in the process of forming stars. This indicates that the bar is most likely young, and could have been produced by a recent interaction, the same interaction that presumably disturbed the disk of NGC 4904. There is structure inside of the bar region, as there is a prominent red area at the northern end of the bar. This could potentially be a large, dust obscured HII region that was not observed in the broadband optical images. The arm regions in the south of the galaxy appear to be red. That would indicate that the arms in NGC 4904 are either made of older stars, have a significant quantity of dust within them, or are vigorously producing stars.

Figure 3-28 shows the K_s image taken of NGC 4904 with the TCS. The sensitivity of this image is very low. The prominent feature of the galaxy in the infrared is the bar. Within the resolution of the image, the bar is similar in size and shape to the bar seen in

the optical images of the galaxy. We do not see any real indication of spiral arms in the near infrared image of NGC 4904, but this may be due to the low sensitivity of the image.

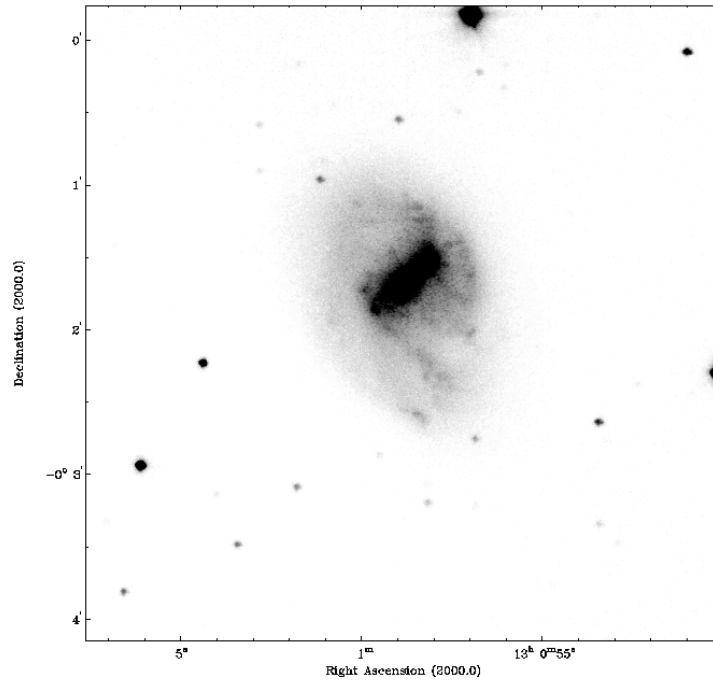


Figure 3-25. Optical R-band image of NGC 4904 taken with IAC80 telescope

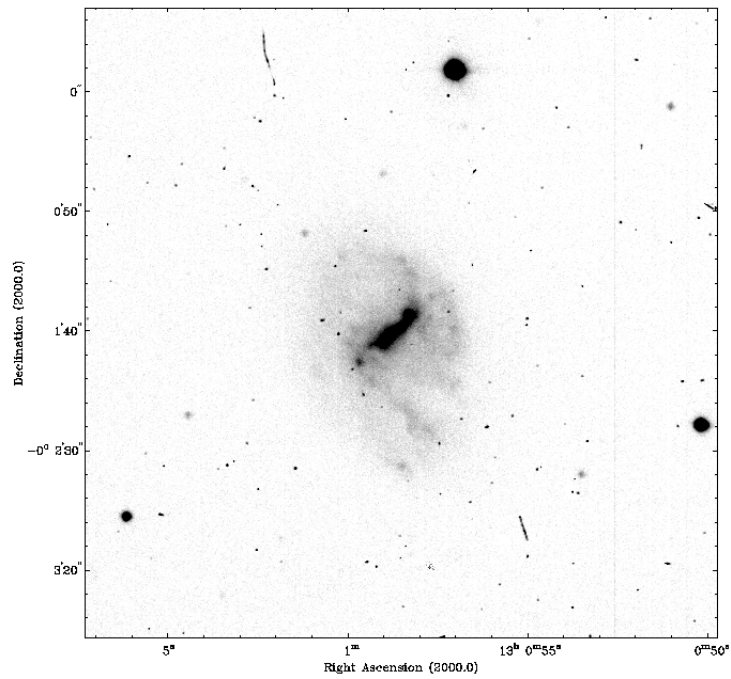


Figure 3-26. Optical B-band image of NGC 4904 taken with IAC 80

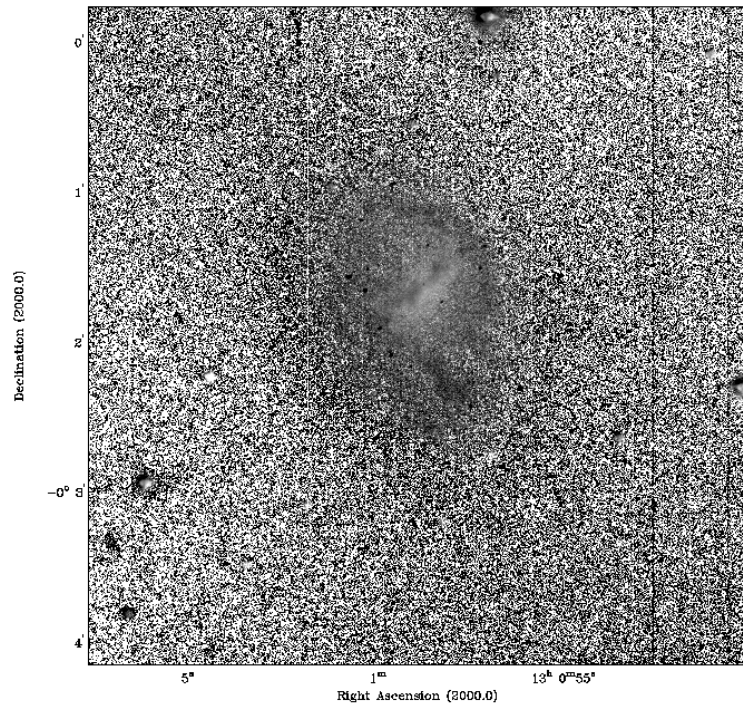


Figure 3-27. B-R color map of NGC 4904. Light grayscale regions are blue in color. Darker grayscale regions correspond to red colors.

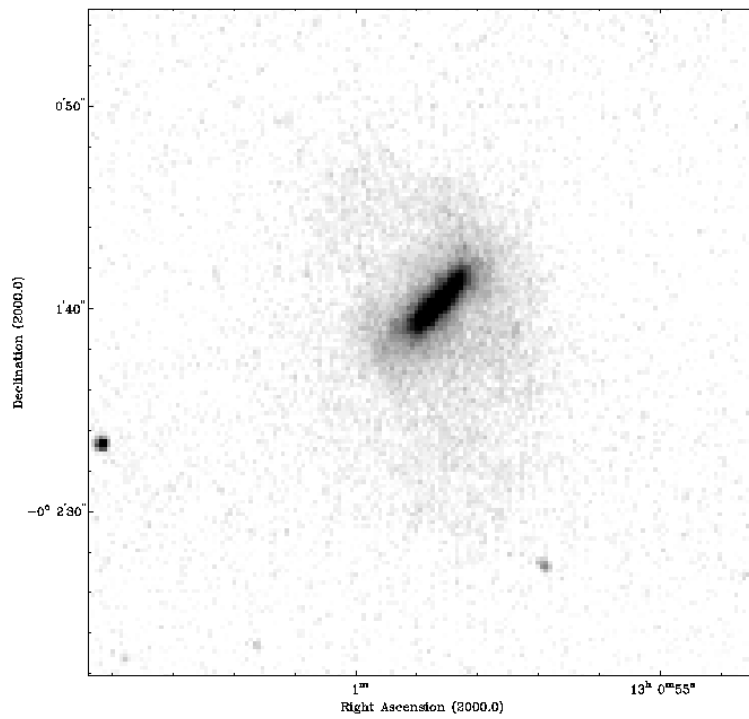


Figure 3-28. K-band image of NGC 4904 taken at TCS

NGC 5147

There has been little previous study of NGC 5147. Elmegreen & Elmegreen (1982) place this galaxy in arm class "2". The optical image of NGC 5147 shown in Figure 3-29 shows a galaxy with a not particularly strong bar surrounded by seemingly chaotic star formation. A few arcs of star formation appear to be in the south of the galaxy, but there is little overall structure. This galaxy appears to be similar in disk structure to NGC 4900, but without the strong bar at its center.

The galaxy has an optical angular diameter of 1.9', corresponding to a physical diameter of 8.6 kpc, making it similar in size to NGC 4900 as well. The bar in this galaxy appears to be very sky and misaligned with the morphological position angle of the overall galaxy. The bar appears to be twisted, or at least thicker at the southern end. We calculate a semi-major bar axis length of 5" and a semi-minor bar axis length of 2". These values correspond to physical distances of 0.4 kpc and 0.1 kpc, respectively. The bar axis ratio is 0.2 and the bar to galaxy radius ratio is 0.09. Deeper and higher resolution study of this galaxy is necessary to determine its bar structure and properties.

Figure 3-30 shows a K_s -band image of NGC 5147 from the 2-MASS survey. The resolution in this image is poor compared to the size of the galaxy. It is difficult to determine the bar properties of the galaxy in this image. In fact, it's difficult to determine if there is a bar at all. The arcs of star formation to the south of the galaxy are apparent in this image as well.

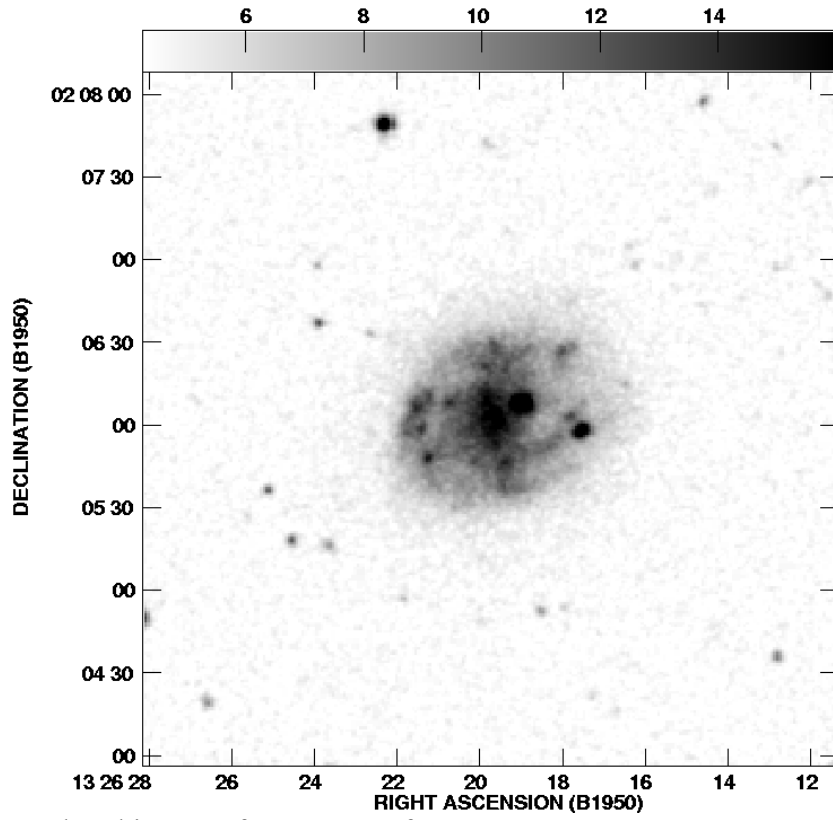


Figure 3-29. R-band image of NGC 5147 from DSS

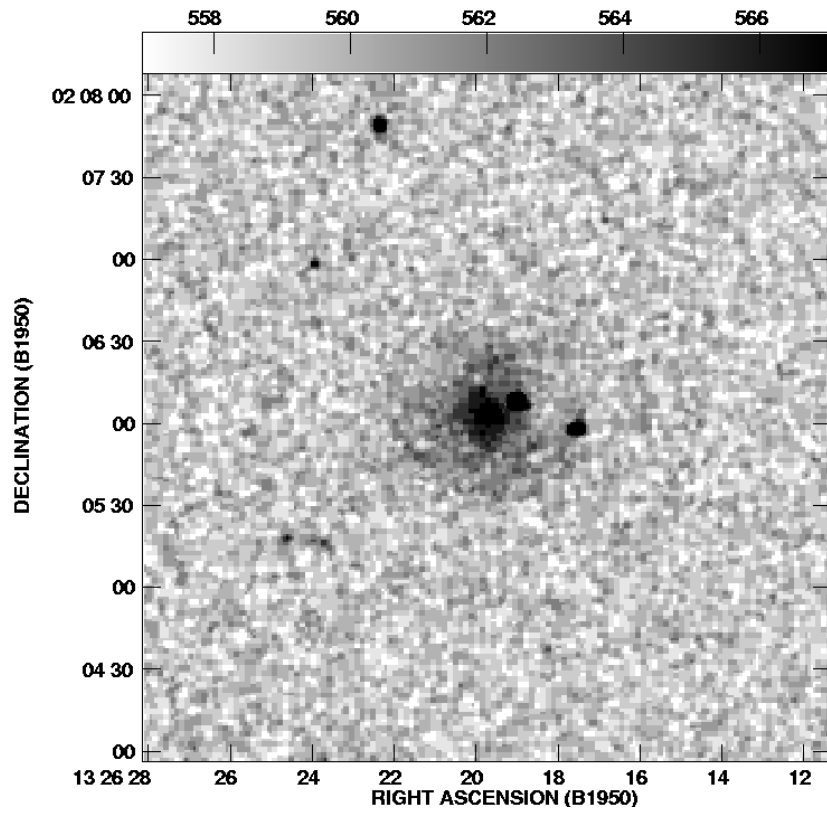


Figure 3-30. K-band image of NGC 5147 from 2-MASS

NGC 5300

NGC 5300 lies at a distance of 17 Mpc, and has an angular diameter of 3.8', corresponding to a physical size of 18kpc. Compared to the other galaxies in the sample, NGC 5300, is probably the most 'normal' of the set. The R-band IAC80 image (Figure 3-31) shows that the galaxy does not possess any large scale asymmetries. Elmegreen & Elmegreen (1982) place the galaxy into arm class "2" indicating that it does not have a global spiral arm structure. We see a similar habitus in our images. There appears to be small armlets in the central part of the galaxy, and then chaotic star forming arcs in the outer regions. The spiral density waves that may exist in the inner parts of the galaxy do not continue far out into the disk. A one-armed structure begins off of the northern end of the bar region and curls around to the east, but this feature ends fairly quickly, within 1' (5 kpc). We do not detect any evidence of optical satellites associated with this galaxy.

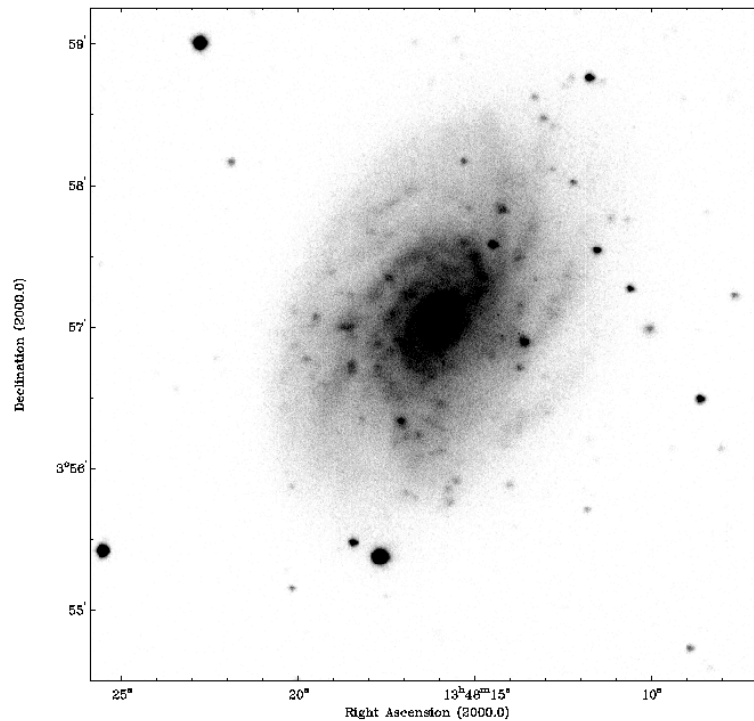


Figure 3-31. Optical R-band image of NGC 5300 taken at IAC80

The bar region of NGC 5300 is not well formed. It is difficult to define the bar in either the R-band or B-band image (Figure 3-32) of this galaxy. We measure a semi-major axis of 8" (0.7 kpc) and a semi-minor axis of 6" (0.5 kpc) for the bar in NGC 5300 for the R-band image. The ratio of bar semi-major axis to galaxy radius is 0.08. The B-band image of NGC 5300 may indicate that the optical bar is slightly misaligned from the position angle of the galaxy, and the starting points of the armlets emanating from it. We see more evidence for small arms in the B-band image, where the northern one-armed feature is de-emphasized and possibly a total of three armlets are originating off of the bar. The B-band image shows that the arms are very knotty, and broken up into HII regions that are on the order of the resolution of the image, 2" - 3" (0.2 - 0.3 kpc).

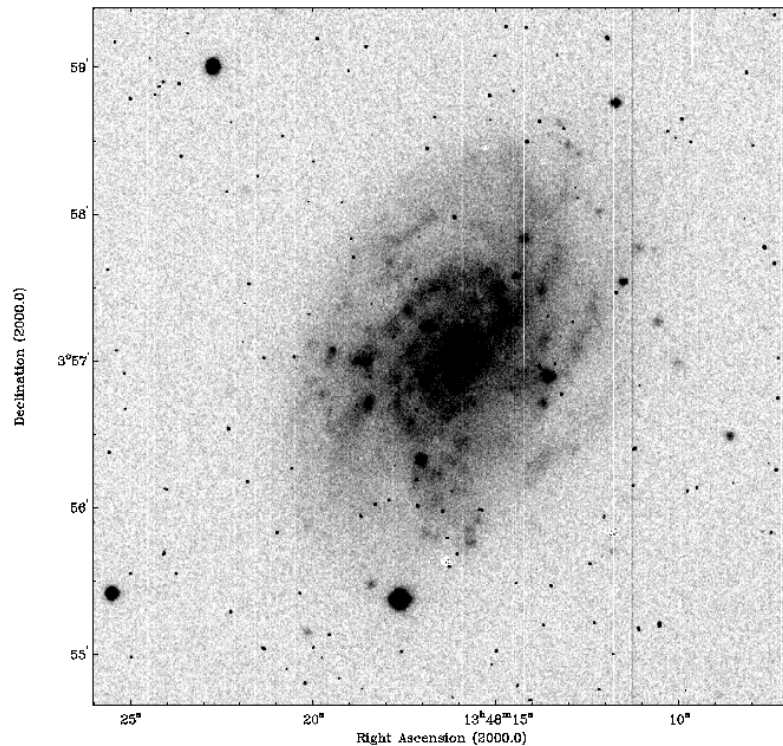


Figure 3-32. Optical B-band image of NGC 5300 taken with IAC80

Figure 3-33 shows a B-R optical color map made with data from the IAC80. We do not observe a great deal of structure in this image. The central regions of the galaxy

appear to be redder than the outside regions, indicating that the bar is not producing a great deal of stars. This is consistent with the bar being so small relative to the size of the galaxy. We do not observe evidence of the spiral arms or HII regions in the color map. This is either due to the limited spatial resolution of our observations, or the fact that the small spiral arms are not particularly bluer than the inter-arm regions, typical for flocculent galaxies. The outer regions of the galaxy appear to have a blue color relative to the center. This effect is due to the relative sensitivities of the R and B images used to make Figure 3-33. More sensitive observations with a larger telescope will be needed to determine the colors of the spiral arms in this galaxy.

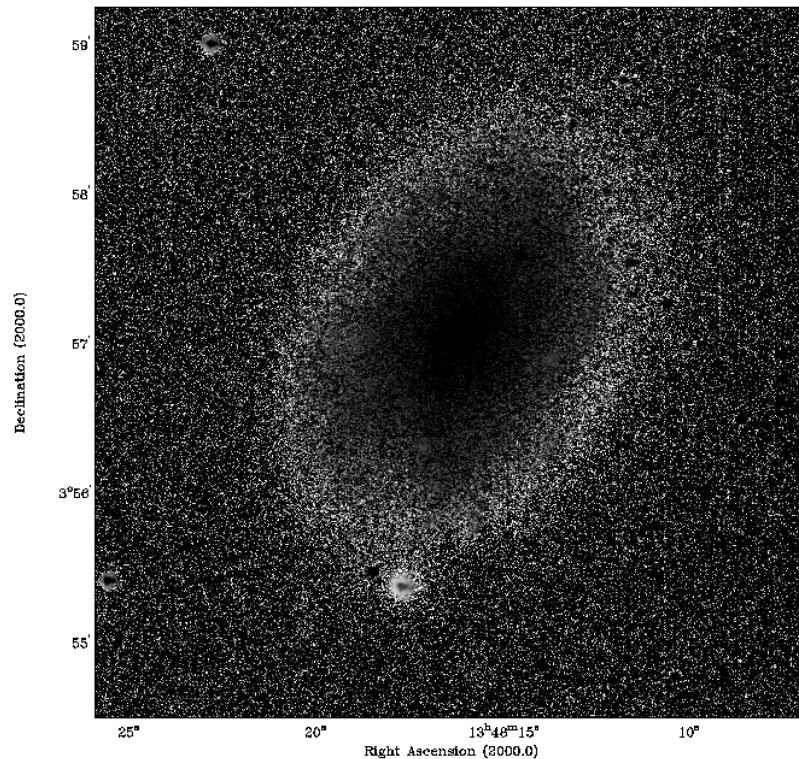


Figure 3-33. B-R color map of NGC 5300. Light grayscale regions are blue in color. Darker grayscale regions correspond to red colors.

NGC 5645

NGC 5645 is a small galaxy with a bright elliptical bar. The galaxy is classified by Elmegreen & Elmegreen (1982) as a "1" with almost no appreciable spiral structure. In Figure 3-34, a R-band IAC80 image of NGC 5645, we see that there is star formation and some spiral arcs associated with the southern end of the bar. This is similar in appearance to NGC 4793. Also similar to NGC 4793 is a small patch of optical emission separated from the northeast of the galaxy. This object may be part of a tidal arm or a satellite galaxy. Haynes et al. (1998) found that NGC 5645's HI spectrum was rather asymmetric, and indicates that the galaxy may have been involved in a recent interaction. The B-band image of the galaxy in Figure 3-35 shows a similar morphology, but the bar appears to be smaller and more twisted, again indicative of a possible interaction.

The angular size of NGC 5645 was measured by Haynes et al. (1998) to be 2.4', corresponding to a physical diameter of 13.7 kpc. We measure a bar semi-major axis length of 9" and a semi-minor axis length of 3". These values correspond to physical distances of 0.9 kpc and 0.3 kpc, respectively. The bar axis ratio is then 0.3, and the bar to galaxy radius ratio is 0.13.

Figure 3-36 shows a K_s -band image of NGC 5645 from the 2-MASS survey. This image shows the bar (rotated and flipped from the IAC80 image in Figures 3-34 and 3-35) to be the same size and orientation as in the optical images. The bar appears to be peanut shaped and twisted in the infrared, indicating again, that this galaxy has undergone some type of recent interaction. Because of the low sensitivity in this image, we do not see near infrared emission from the disk of NGC 5645, and can not comment on the arm structure in this wavelength regime.

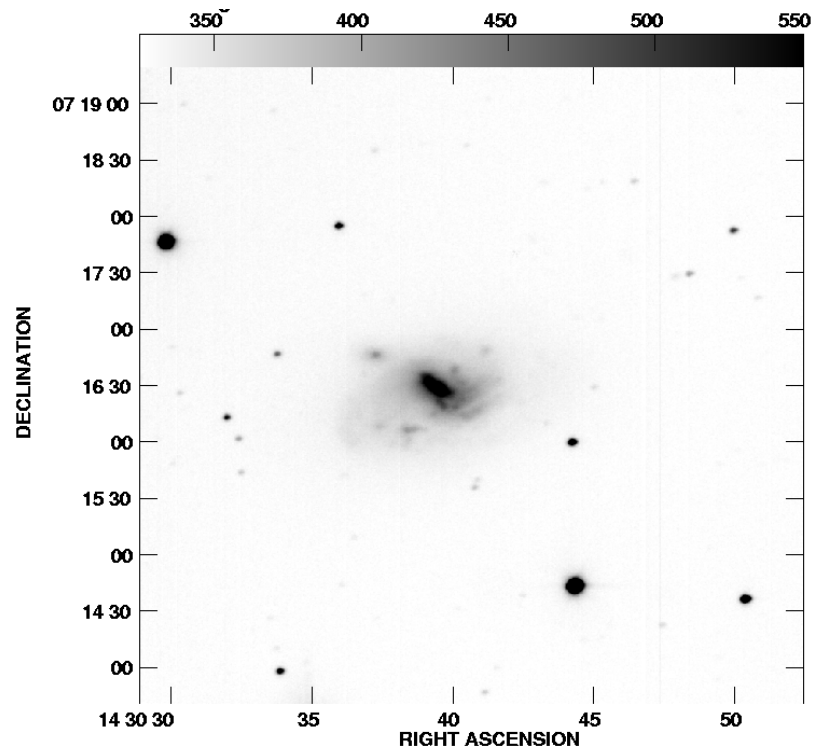


Figure 3-34. R-band image of NGC 5645 from IAC80

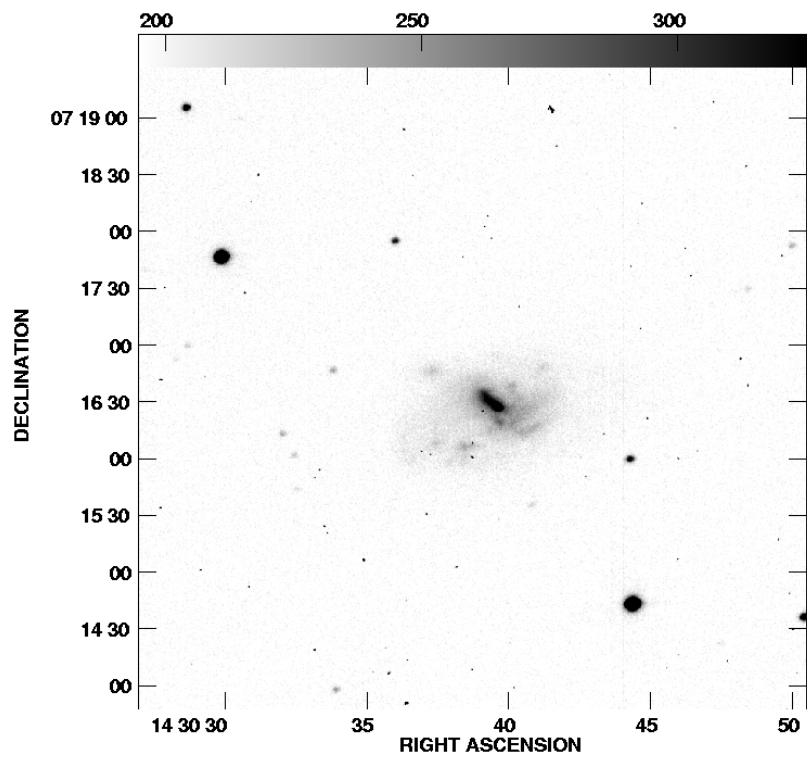


Figure 3-35. B-band image of NGC 5645 from IAC80

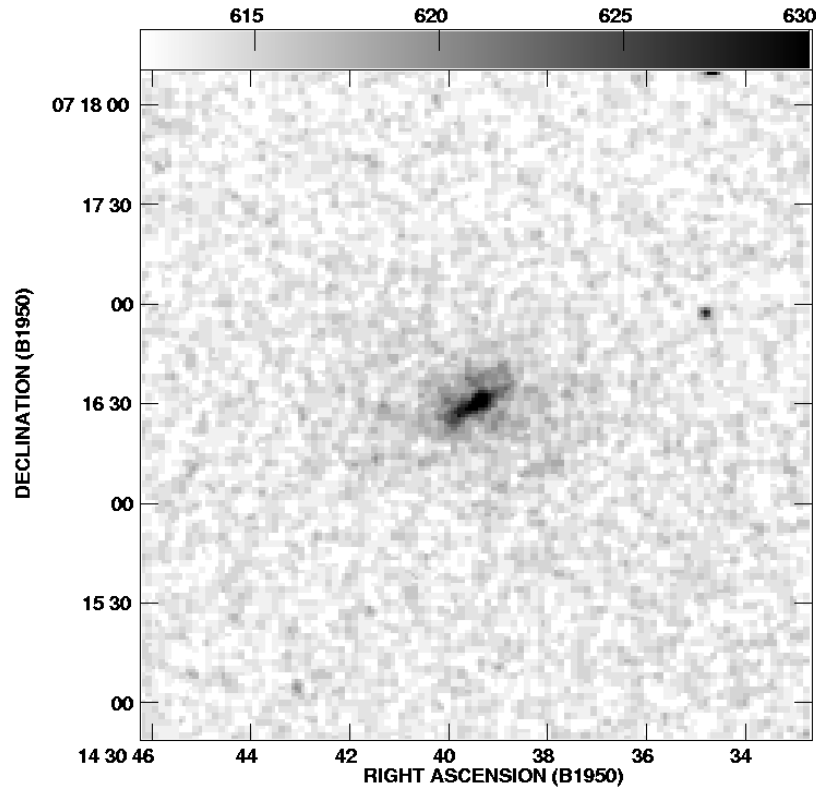


Figure 3-36. K-band image of NGC 5645 from 2-MASS. This image is rotated 180° and flipped along the y-axis relative to the R-band IAC80 image in Figure 3-35.

NGC 5783

As with the other galaxies in the sample that exhibit a one-armed influenced spiral structure, NGC 5783 is placed by Elmegreen & Elmegreen (1982) into arm class "4". Figure 3-37, an R-band image of the galaxy, shows the one main arm of NGC 5783 leaves the central regions of the galaxy towards the north and then curves around to the east. This arm stretches retains its structure to nearly the end of the optical galaxy. The corresponding arm on the opposite side of the galaxy is not as bright and only reaches to about half of the radius of the galaxy. NGC 5783 does not appear to possess an appreciable bar, and resembles the central structure of NGC's 3930 and 5300. Several smaller galaxies are in the field of view, but previous single dish HI observations of the region by Rhee & Albada (1996) showed NGC 5783 to be isolated.

Rhee & Albada (1996) give the D_{25} angular size of the galaxy to be $2.8'$. Using a H_0 of $70 \text{ km s}^{-1} \text{ Mpc}^{-1}$, we calculate a distance to the galaxy of 33.4 Mpc . We calculate the physical diameter of the galaxy to be 27.2 kpc , making this a sizable galaxy in our sample. Given the close linkage between the bar and the stronger arm, it is difficult to calculate a bar length for this galaxy. We estimate a bar semi-major axis length of $6''$ and a semi-minor axis length of $5''$. These correspond to physical sizes of 1 kpc and 0.8 kpc , respectively. We calculate a bar axis ratio of 0.8 and a bar to galaxy radius ratio of 0.07 .

Figure 3-38 shows a K_s -band image of NGC 5783 from the 2-MASS survey. This image, although lacking in sensitivity, shows that this galaxy does not possess an elliptical bar. The central bright region is circular within the resolution constraints of this image. We do not find evidence for near infrared spiral structure in this galaxy, however, there is not enough signal present to comment on that finding.

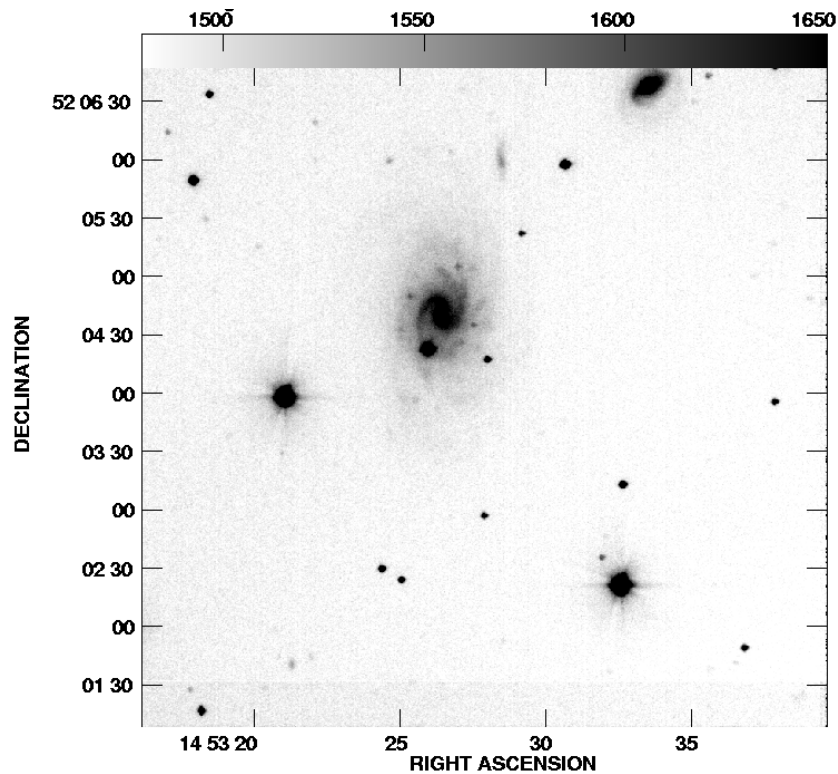


Figure 3-37. R-band image of NGC 5783 from IAC80

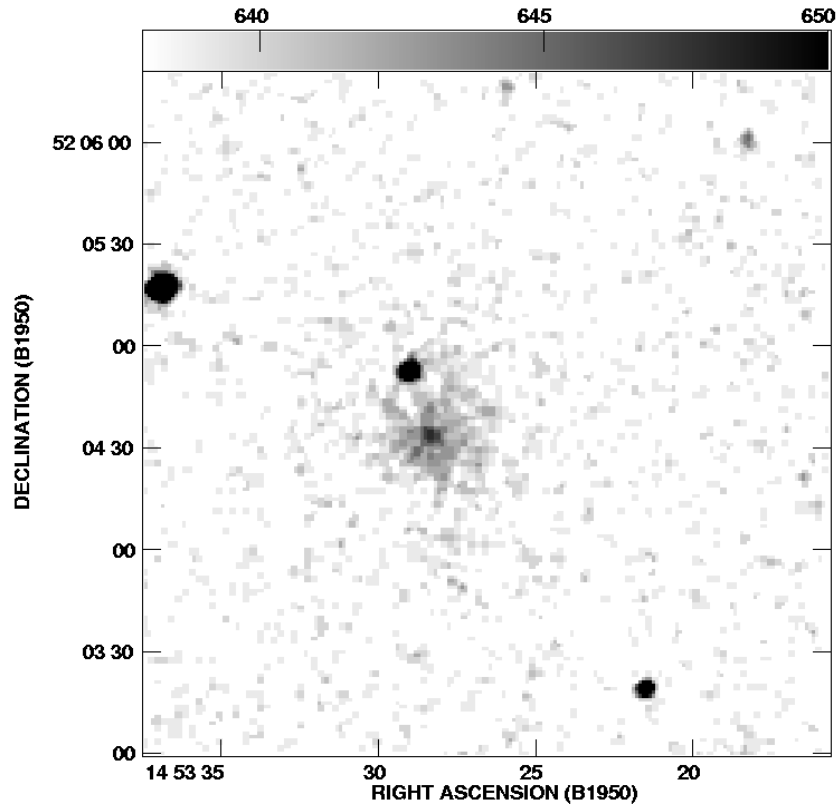


Figure 3-38. K-band image of NGC 5783 from 2-MASS

NGC 6012

Our R-band image of NGC 6012 (Figure 3-39) shows a galaxy that is primarily composed of a large, strong, and bright bar surrounded by low levels of optical emission. The galaxy itself is not particularly large on the sky, having an angular size of 2.1', corresponding to a physical diameter of 15 kpc. We find very little evidence for spiral structure in the R-band image except at the extremes of the galaxy. There appears to be emission leading to the east of the northern end of the bar and to the west at the southern edge of the bar, but these are at the limits of our sensitivity. Elmegreen & Elmegreen (1982) place NGC 6012 in arm class "3". The galaxy is certainly flocculent, but may be even more so than this classification. There does not appear to be star formation

anywhere outside of the bar in the R-band image, nor does there appear to be any evidence for optical companions.

We measure the bar of NGC 6012 to have a semi-major axis of 25" (3.1 kpc) and a semi-minor axis of 5" (0.6 kpc), making this one of the most elliptical bars in the sample. The ratio of the bar axes is 0.2 and the ratio of bar semi-major axis to galaxy radius is 0.4, the largest in the sample. In the R-band image, the bar appears to have some structure. The central region is the brightest, and the emission diminishes until the north and south tips. In the north, there seems to be a bright region of star formation approximately 3" (0.4 kpc) in diameter. In the south of the bar, there is a loop of emission surrounding a region of approximately the same size.

In the B-band image (Figure 3-40), we see the same structure in the bar. We also see the presence of a ring around the bar, with most of its emission concentrated in the north. Rings are typically associated with resonances. A ring at this location may be a result of either the 4:1 ultraharmonic resonance, or corotation. Higher resolution studies as well as velocity information would be needed to determine which. Again, there does not appear to be evidence of spiral structure or companion galaxies in this image.

Figure 3-41 shows a B-R color map of NGC 6012 made from IAC80 images. We again see the very distinctive structure in the bar. The star forming region appears to be blue relative to the rest of the bar. We conclude that this region is a large HII region due to its color, and stars are actively forming at the bar's northern edge. The center of the bar appears to be red. Either this is due to a large dust lane obscuring the young, blue stars, or this region of the bar has evolved into something more similar to a stellar bulge which is no longer forming stars. The southern tip of the bar again shows the loop

structure present in the B and R-band images. The loop itself is blue while the central region is more red. We conclude that the southern tip of the bar is similar to the northern, but the central HII region is obscured by dust. This leads us to believe that the southern end of the bar is inclined away from us, as the blue light from this HII region has to pass through a longer path length of dust to reach us. Our images did not possess enough sensitivity to examine the colors of the disk region of NGC 6012.

Figure 3-42 shows our K_{short} image of NGC 6012 taken with the TCS. Here we see a similar structure to the optical images of this galaxy. There is a large bar, with little optical emission outside of it. We see no evidence for spiral structure in near infrared emission from this galaxy, but do see a very similar bar. The bar does not appear to possess the loop structure on its southern end, presumably because the K_{short} band light is able to penetrate most of the obscuring light. We do not see evidence for companions at this wavelength regime either. Deeper and higher resolution observations would allow us to determine better the structure of the bar and the presence of any possible spiral features.

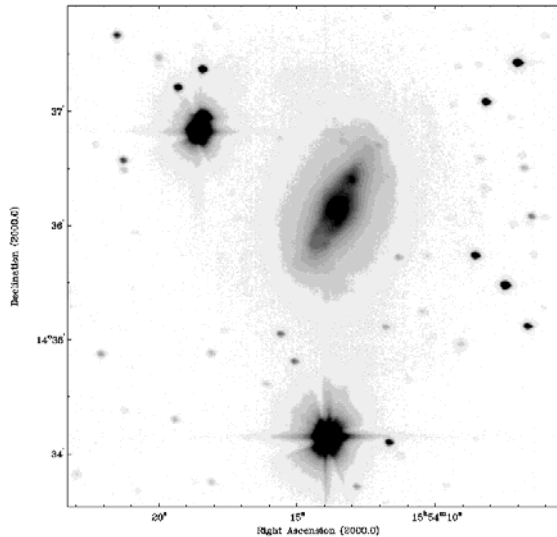


Figure 3-39. Optical R-band image of NGC 6012

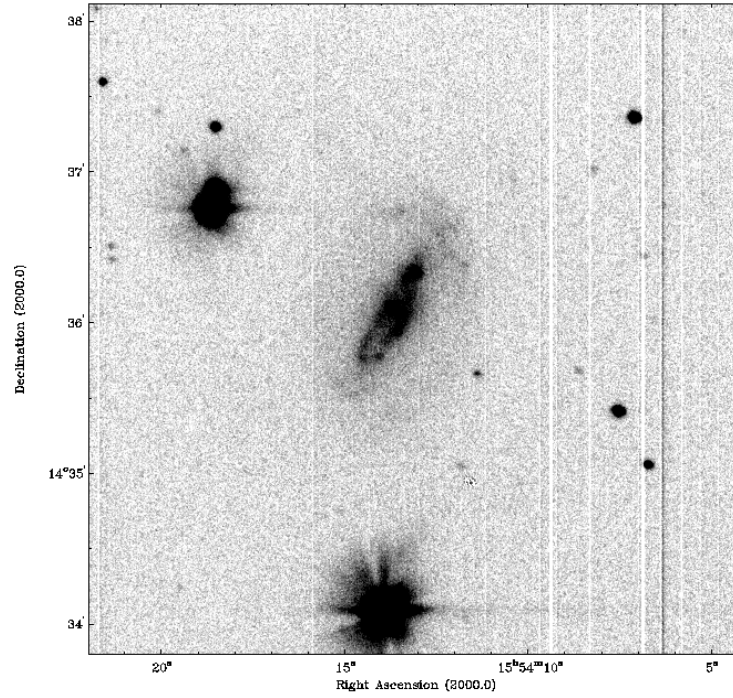


Figure 3-40. Optical B-band image of NGC 6012

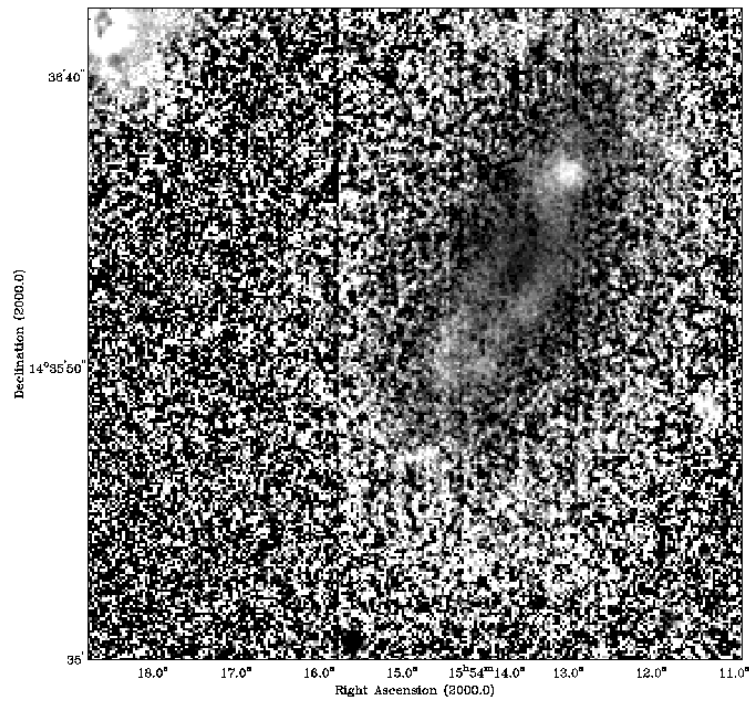


Figure 3-41. B-R color map of NGC 5300. Light grayscale regions are blue in color. Darker grayscale regions correspond to red colors.

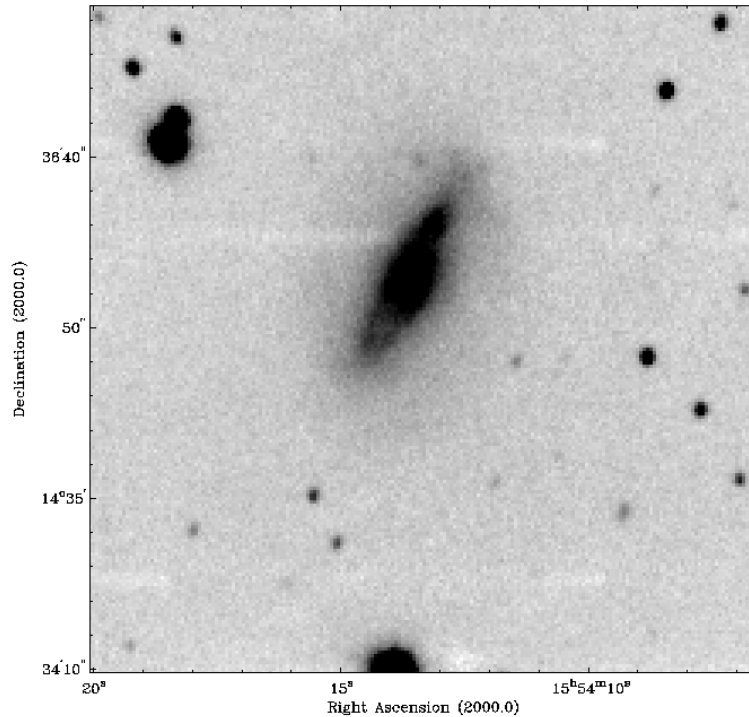


Figure 3-42. K-band image of NGC 6012 taken at TCS

Analysis of Optical Bar and Disk Properties

Figures 3-43 through 3-48 summarize several diagnostics of the optical and near infrared images. In Figure 3-43 we plot the distribution of optical diameters in the sample set. This is further compared with the Elmegreen arm class with respect to the optical diameter. We find that the majority of galaxies fall into the 10 - 20 kpc range. The smallest galaxy is NGC 2500 at a diameter of 7.8 kpc, while the largest is NGC 1784 at 49 kpc. At the low end of the size spectrum, there is a continuous distribution of sizes. NGC 1784, on the other hand is significantly bigger (20 kpc) than the second largest galaxy, NGC 4793. The large difference in size may mean that NGC 1784 has undergone different formation processes. We examine the masses of galaxies in later chapters. We find that there does not appear to be a selection of Elmegreen arm classes among the different sized galaxies. One might naively expect the smallest galaxies to fall

in the lowest arm class, since they may not possess the disk mass to drive even small spiral density waves. We do not see this, however, as the smallest galaxies in our sample show examples of all the Elmegreen arm classes. It is actually the larger galaxies with diameters between 20 and 30 kpc that show preferentially low arm classes. We must keep in mind our small sample size, however, when examining these trends.

Figure 3-44 shows the distribution of the optical bar semi-major axis length of our sample galaxies. Again, the largest bar is from NGC 1784 (~5 kpc) and is significantly larger than the next largest bar, NGC 6012 (~3 kpc). We find an even distribution of bar lengths with the majority of bars at about 1 kpc in length. Only one bar was found to be shorter than 0.5 kpc, belonging to NGC 5147. Figure 3-44 also compares the bar length to the Hubble bar classification from de Vaucouleurs et al. (1991). We find that the bar classes are distributed evenly over bar length. This is to be expected as the bar classification is based more on the shape and intensity of the bar as opposed to solely length.

We plot the distribution of bar axis ratio, found from the optical images, in Figure 3-45. We find an even distribution, where a majority of galaxies have a bar axis ratio of around 0.5. This means that the average bar in our sample is not particularly elliptical. We do find, however, that 4 of the galaxies do have very skinny bars (<0.25). These skinny bars are associated with galaxies classified as SB, meaning that their bars are prominent and intense. Overall, we find that the skinnier bars are more likely to be classified as SB and rounder bars are classified as SAB. This shows that our sample of barred, flocculent galaxies is not different than the general galaxy population in its bar classifications.

Figure 3-46 shows the same plot, but this time the distribution of bar axis ratios is compared with Elmegreen arm classes. We do not find an overall trend between arm classification and bar type within our barred, flocculent sample set. We believe that this plot indicates that there are not similar physical properties among the sample driving both the bar and disk structure simultaneously. It is likely that the sample must be broken down further to find galaxies undergoing similar physical processes.

In Figure 3-47 we plot the distribution of the ratio of bar semi-major axis length and galaxy radius. We find a bimodal trend in this plot where the majority of galaxies have a radius length ratio of around 0.1, but some galaxies show a value of approximately .2 or higher. NGC 6012 has a ratio of 0.4, which is the largest in the sample, and almost two times greater than the nearest value. We compare these radius length ratios to Elmegreen arm classes in this plot, and find no overall trend to this data. The Elmegreen arm classes seem to be independent of the relative size of the bar.

We find a different result when we plot the same distribution in Figure 3-48 but compare it to the bar semi-major / semi-minor axis ratio. Here we find that skinny bars (with low axis ratio values) are preferentially long compared to the size of the galaxy. The main outlier from this trend is NGC 5147, which has a skinny, 0.2, but short, .09, bar. The measurements for this galaxy should be taken with caution, however, because of the disturbed morphology of this system. It was difficult to define the exact nature of the bar in the R-band image of the galaxy. It is very likely that another measurement of the bar length in this galaxy could push it up to a higher bin. We find that since long bars are typically thin, there must be a physical connection between these two properties.

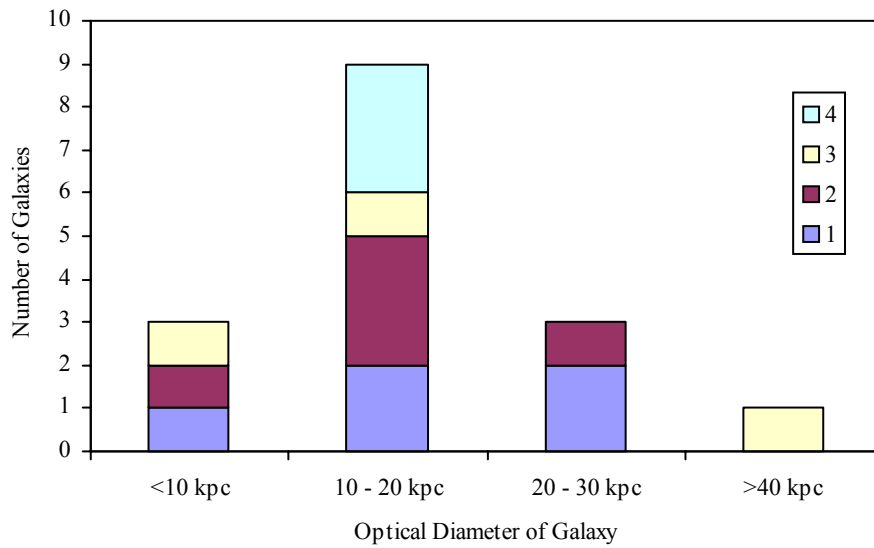


Figure 3-43. Distribution of the optical diameters of galaxies in the sample set. The strips across the columns represent the amount of galaxies from particular Elmegreen arm class (labeled at right) within that size bin.

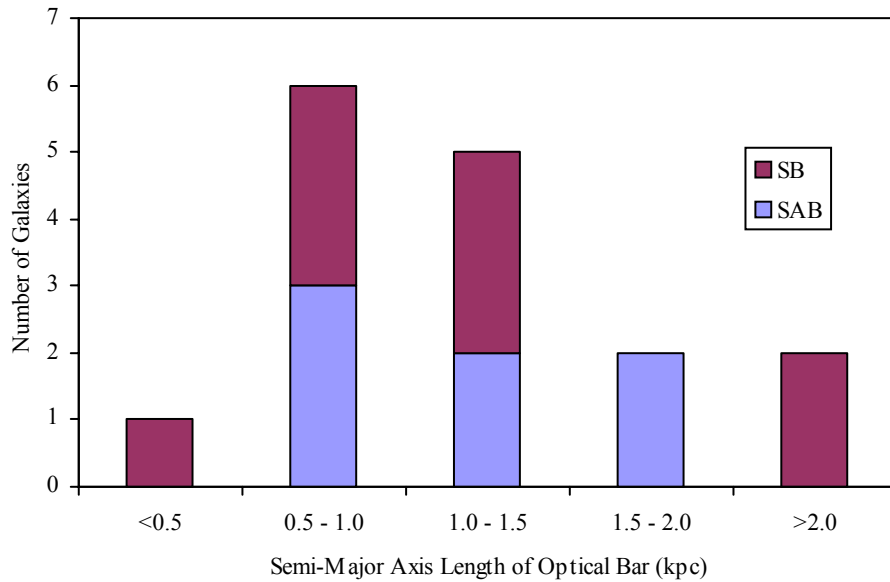


Figure 3-44. Distribution of the optical semi-major axis length in the sample set. The strips across the columns represent the Hubble bar class of that galaxy (labeled at right) within the particular size bin.

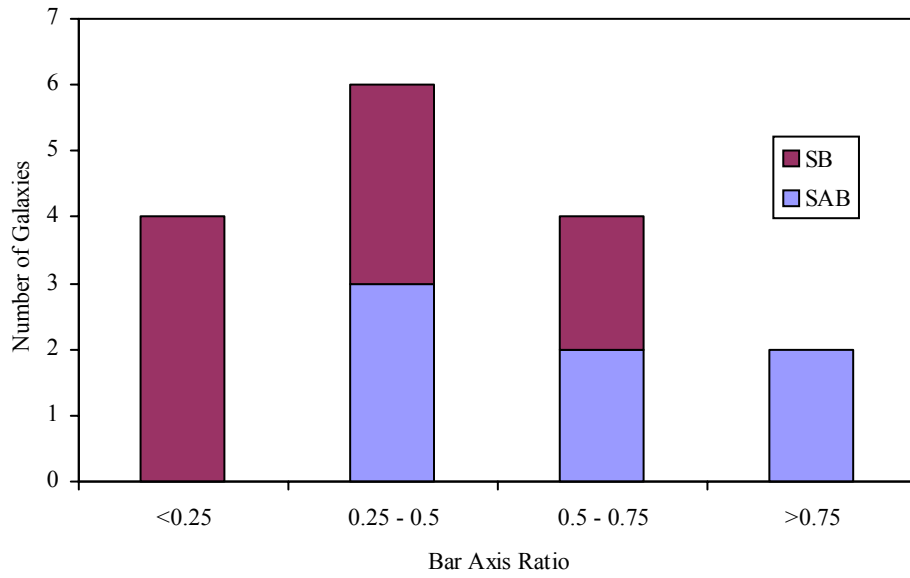


Figure 3-45. Distribution of the bar axis ratio for the sample set. The strips across the columns represent the Hubble bar class of the galaxies (labeled at right) within the particular bar axis ratio bin.

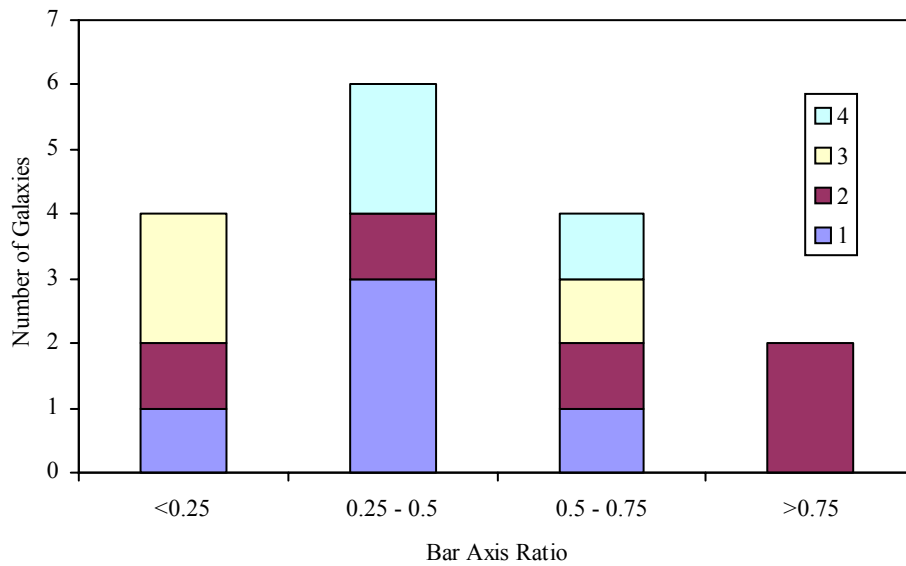


Figure 3-46. Distribution of the bar axis ratio for the sample set. The strips across the columns represent the Elmegreen arm class of the galaxies (labeled at right) within the particular bar axis ratio bin.

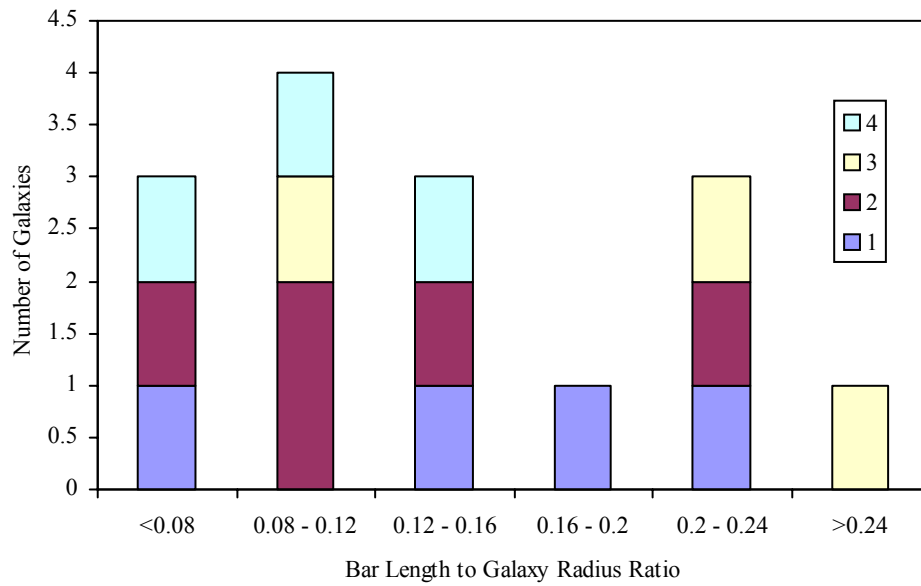


Figure 3-47. Distribution of the bar length to galaxy radius ratio for the sample set. The strips across the columns represent the amount of galaxies from particular Elmegreen arm class (labeled at right) within that bar length ratio bin.

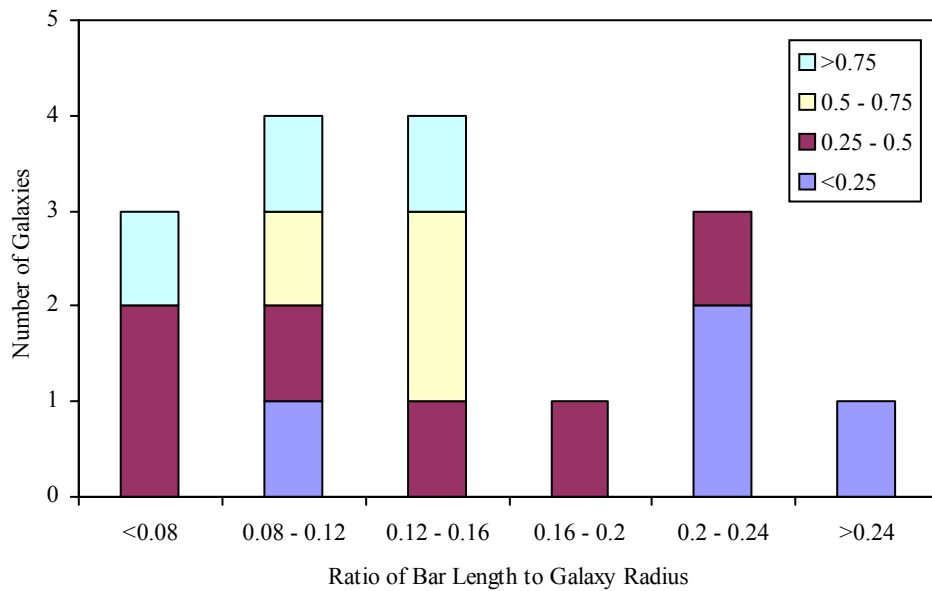


Figure 3-48. Comparison of bar axis ratio to bar/galaxy length ratio. Strips across the columns represent the number of galaxies within a range of bar axis ratio with respect to the bar length bin.

CHAPTER 4 DESCRIPTION OF NEUTRAL HYDROGEN OBSERVATIONS

This chapter provides a brief summary of 21cm Hydrogen emission and the process by which it is observed. All radio observations for this study were obtained at the Very Large Array (VLA) using the B, C, and D configurations. The VLA is run by the National Radio Astronomy Observatory, which is operated by Associated Universities, Inc, under cooperative agreement with the National Science Foundation. For a more detailed description of 21cm emission, please see Mihalas & Binney (1981). For a more detailed description of the principles of radio interferometry, please see Florkowski (1980), Christiansen & Hogbom (1985), or England (1986).

Twenty-One Centimeter Hydrogen Emission

Typical electronic transitions in hydrogen have energies on the order of 1 eV. These transitions release photons in the visible, UV, and infrared. Hydrogen also possesses a transition between the hyperfine levels associated with the magnetic dipole moments of the electron and proton. When the spin of both the electron and proton are in the same sense (orthohydrogen), the atom is in a higher energy state than when they are in the opposite sense (parahydrogen). The energy difference between these two states is 6×10^{-6} eV, corresponding to a photon with a wavelength of 21.1 cm.

Spontaneous spin-flip transitions (as these hyperfine transitions are described) are very rare, however. The Einstein probability coefficient, A_{21} , for a radiative transition is $2.8689 \times 10^{-15} \text{ s}^{-1}$, corresponding to an average transition time of 1.1×10^7 years (Rohlfs

1990). Collisional deexcitation of an excited hydrogen atom is much more common, and will occur once every 10^2 or 10^3 years at normal conditions in the interstellar medium.

The high likelihood of collisional deexcitation, allows us to assume a state of approximate thermodynamic equilibrium. With the collisional probabilities, C_{12} , and C_{21} , we have:

$$n_1 C_{12} = n_2 (C_{21} + A_{21})$$

Since A_{21} is small, with typical ISM conditions, $n_2 A_{21}$ will disappear, and we have:

$$n_1 C_{12} = n_2 C_{21}$$

We can relate the populations of the states through the Boltzmann Equation

$$\frac{n_2}{n_1} = \frac{g_2}{g_1} e^{-\frac{h\nu}{kT_s}}$$

For hydrogen, $g_2 = 3$ and $g_1 = 1$ because of the degeneracy of the upper state. The typical spin temperature (T_s) of an HI cloud is on the order of 100K. Thus,

$$e^{-\frac{h\nu}{kT_s}} \approx 1$$

We get finally, that

$$\frac{n_2}{n_1} = 3$$

Therefore, even though collisional deexcitation is a much more common process than radiative deexcitation, a sizable fraction of the HI gas will remain in the excited state. Given the high quantities of HI in galaxies, the 21cm line becomes one of the most easily observed spectral lines in the Universe.

To determine the column density of HI, we integrate the spin temperature of the HI over all frequencies:

$$N_{HI} = 3.88 \times 10^{14} \int T_s \tau_\nu d_\nu$$

where τ_ν is the optical depth. Changing spin temperature to the observed brightness temperature, we get:

$$T_B = T_s (1 - e^{-\tau_\nu})$$

We assume that the HI content of a galaxy is optically thin, implying that $T_B \sim T_s \tau_\nu$. Our column density becomes:

$$N_{HI} = 3.88 \times 10^{14} \int T_B(\alpha, \delta) d\nu$$

Where we have introduced the observable quantities of position (α, δ) and velocity (ν).

Further, we can rewrite column density in terms of flux in Janskys to be:

$$N_{HI} = 2.4888 \times 10^{21} \lambda^2 \int \frac{S \cdot d\nu}{\theta^2}$$

where λ is the wavelength of the observation, S is the flux density in Janskys, and θ is the angular resolution of the observations (beam size).

The mass of an HI region can be found by integrating over the angular size of the source and incorporating the distance to the object:

$$M_{HI} = 2.356 \times 10^5 D^2 \int S(\nu) d\nu$$

where D is the distance in Mpc, ν is the velocity in km s^{-1} , and M_{HI} is expressed in solar masses.

Fundamentals of Interferometry

Because of the long wavelengths involved in radio observations, single dish telescopes are not practical for high resolution work. Radio astronomers must utilize interferometers to reach resolutions necessary to map the hydrogen content of galaxies.

This section will provide a very brief overview of several of the principles involved in interferometric observations.

The voltages resultant from N elements of an interferometer go as:

$$V(t) = \sum^N \Delta V_i(t)$$

The total power is proportional to the time averaged voltage:

$$\langle P \rangle \propto \sum \langle (\Delta V_i \cdot \Delta V_k) \rangle$$

This is the sum of the products of all the individual voltages from all the possible pairs of elements. A large aperture could be simulated by a large number of smaller apertures filling out the shape of that larger aperture (such as with the proposed Square Kilometer Array). The VLA, however, does not physically fill in all the space of its synthesized aperture, but uses the rotation of the Earth to simulate this effect over time. This process is known as Earth-rotation aperture synthesis.

Interferometers correlate signals of several separated antennae observing the same source. These antennae observe the intensity distribution of the source, composed of the superposition of many components of an electro-magnetic field wave. The output of the interferometer is this superposition further weighted with the reception pattern of the interferometer elements (the beam pattern). The brightness distribution of the target source is the Fourier Transform of the interferometer pattern.

The signal from the interferometer is:

$$V_{obs}(u, v) = \iint I_{obs}(x, y) e^{-2\pi i(ux+vy)} dx dy$$

where V_{obs} is the observed complex visibility function, I_{obs} is the observed brightness distribution, x and y are east and north distances from the pointing center in the sky

plane, and u and v are the east and north spacings of the projected baselines. The complex visibility corresponds to a particular baseline measuring a single Fourier component of the observed brightness distribution (England 1986).

We can invert the Fourier Transform to obtain the brightness distribution of the source:

$$I_{obs}(x, y) = \iint V_{obs}(u, v) e^{2\pi i(ux+vy)} du dv$$

However, as mentioned above, I_{obs} contains both the source brightness distribution weighted by synthesized beam pattern:

$$I_{obs}(x, y) = I_{true}(x, y) * B(x, y)$$

where $B(x, y)$ is the synthesized beam, and $*$ denotes a convolution.

Spectral line observations are made by observing several independent, narrow band channels. These channels are produced by introducing a time delay, τ_j , into the signal path which destroys the coherence of the signal except for a specified range centered on a given frequency, ν_j . We find:

$$V_{obs}(u, v, \tau) = \int V(u, v, \nu) e^{2\pi i \nu \tau} d\nu$$

The relationship for the complex visibility and observed intensity integrated over the entire bandwidth becomes:

$$V_{obs}(u, v, \tau) = \iiint I_{obs}(x, y, \nu) F(\nu) e^{-i[2\pi \nu \tau + 2\pi \nu(ux+vy)]} dx dy d\nu$$

where $F(\nu)$ is the frequency dependant bandpass function (Hjellming & Bignell 1982; England 1986). Taking the Fourier transform of the real part of this equation with respect to τ and then ν , we get:

$$\int \text{Re}\{V_{obs}(u, v, \tau)\} e^{i2\pi \nu \tau} d\tau = \iint I_{obs}(x, y, \nu) F(\nu) e^{-i2\pi \nu(ux+vy)} dx dy$$

This visibility function contains all of the necessary information to map the source at frequency, ν (Hjellming & Bignell 1982). The bandpass function, $F(\nu)$ can be determined by observing a strong continuum source, for which the flux density is constant across the frequencies that determine the band pass.

Calibration and Imaging Neutral Hydrogen Data

In order to produce images from the complex visibility function, the visibilities must be calibrated for instrumental effects and then Fourier transformed onto the image plane. In addition, the synthesized beam must be deconvolved from the brightness distribution of the target source. This is accomplished through a process known as CLEANing.

Along with the target object, every observing run at the VLA contains observations of a primary calibrator and a secondary (phase) calibrator. Primary calibrators are very bright sources (~ 10 Jy), with a well determined, stable flux. Phase calibrators are known continuum sources with well determined fluxes and positions. Phase calibrators need not be as bright as flux calibrators. A flux calibrator is typically observed once or twice for several minutes during a several hour observing run. Phase calibrators are observed for several minute stretches about once every 30 minutes. The frequency of phase calibration observations depends on the configuration of the VLA, with the higher resolution B configuration requiring more frequent calibrations.

The initial phases of calibration are performed on "channel zero" data, which is a pseudo-continuum channel consisting of the inner 75% of the bandwidth. This "channel zero" has high signal to noise than individual narrow-band channels, and makes calibration easier. Data from the target source, flux, and phase calibrators are first edited

for interference. This is done by eliminating visibilities that are well outside of the 3σ limits of the data.

The flux of the primary calibrator is obtained from a well determined relationship for that calibrator between flux density and frequency. The antenna gain solutions for the array with respect to time are determined from the equation:

$$G_{ij}(t) = a_i(t)a_j(t)e^{i(\phi_i(t)-\phi_j(t))} + \varepsilon_{ij}$$

where $a(t)$ is an antenna based amplitude correction normalized so that $\sum a_i(t) = 1$, $\phi(t)$ is an antenna based phase correction normalized so that $\sum \phi_i(t) = 0$, and ε_{ij} are the closure errors (Martin 1995; Fomalont & Perely 1989). The values of ε_{ij} should be minimized to ensure the best approximation of $G_{ij}(t)$.

To continue the calibration process, the flux densities of the phase calibrators are determined using the flux calibrator. Then the calibration is applied to the target source using a box car average over all observation times. The solutions determined from the calibration process must then be transferred from the "channel zero" data to the narrow bandwidth channels. Finally, the flux calibrator is used to correct for any changes in instrumental response as a function of frequency across the bandwidth. Continuum sources, often not related to the target source can also be subtracted from the dataset at this point.

A map, or image, of the target source's brightness distribution can be made by taking the Fourier transform of the calibrated data. The procedures associated with data from the VLA use a Fast Fourier Transform (FFT) to accomplish this task. An FFT is used as opposed to a Direct Fourier Transform (DFT) because of the large volume of data associated with VLA observations. The visibility data is first smoothed and then gridded

into an N_x by N_y complex array, where N_x and N_y are powers of two. A cell (or pixel) size (measured in arcseconds) is assigned to the data so that there are approximately three or four cells per beam width (Hjellming & Bignell 1982; England 1986).

The Fourier transformed data set becomes an image cube with axes of right ascension, declination, and frequency/velocity. The initial transform produces a "dirty" image of the data, meaning that the source intensity is still convolved with the dirty beam, where the dirty beam is the Fourier transform of the sampling function. To correct for the dirty beam, the image is "cleaned" by using a Clark CLEAN algorithm (England 1986). This algorithm operates by centering the dirty beam pattern on the peak emission point in an image, convolving the beam with a point source at 10% of the peak emission, and subtracting the result from the image. This is performed as an iterative process until the peak residual emission decreases to at least 2σ level of the image. The model of a point source is then convolved with the "clean" beam (an elliptical Gaussian fitted to the dirty beam) and added back into the image.

At this point, the data is ready for analysis. A total intensity (zeroth moment of the data), temperature weighted velocity field (first moment), and temperature weighted velocity dispersion field (second moment) can be easily obtained. The data cube can be analyzed by velocity channel or flipped on its side to be viewed as slices in declination (referred to as a Position-Velocity plot). All of these techniques will be utilized in the following chapters to examine the HI morphology and kinematics of barred, flocculent galaxies.

CHAPTER 5 NEUTRAL HYDROGEN OBSERVATIONS OF NGC 1784

NGC 1784 was originally selected for HI observations because the Digitized Sky Survey (DSS) shows it to be a large, optically undisturbed, barred spiral galaxy. NGC 1784 has a strong bar and weak spiral arms. Our intention in these observations was to gain an understanding of how bar dynamics affect the gaseous component of the outer disk. Optical images do not show NGC 1784 to be involved in any interaction. NGC 1784 is classified as an SB(R)c galaxy and is at a distance of 33 Mpc ($H_0 = 70$, $V_{\text{sys}} = 2308 \text{ km s}^{-1}$) (de Vaucouleurs et al. 1991). It is a fairly large galaxy, with a D_{25} of 240" (49 kpc), it possesses a strong bar with a deprojected bar axis ratio of 0.58, and a ring located at the end of the bar (de Vaucouleurs et al. 1991; Martin 1995). The galaxy is inclined at 55° , making it very suitable for HI observations (Tully 1988).

The limited previous observations of NGC 1784 have shown it to be a quiescent galaxy. Rush et al. (1993) determined NGC 1784 not to be active. Both Elmegreen et al. (1996) and Jungwiert et al. (1997) found no twisted isophotes in the bar of NGC 1784 in near-infrared light. In the following sections, we discuss the kinematics and morphology of NGC 1784 employing high and low resolution HI observations.

Observations

Observations of NGC 1784 were obtained at the Very Large Array in February 1992, February 1993, April 2001, and November 2001 using the DnC, C, B, and D configurations, respectively. The DnC configuration is a hybrid between the more compact D and extended C configurations. This hybrid with the long arm stretching

toward the north allows for higher resolution observations of southern sources, such as NGC 1784. The spectrometer was composed of 32 Hanning Smoothed channels with a 20.9 km s^{-1} . The observing parameters for the various runs are summarized in Table 5-1.

Table 5-1. Parameters of VLA HI observations of NGC 1784

Configuration	B	C	DnC	D
Number of antennae	27	26	27	27
V_{sys} (km s^{-1})	2308	2308	2308	2308
Phase calibrator	0503+020	0503+020	0503+020	0503+020
Flux calibrator	0137+331	0137+331	0137+331	0137+331
Time on source	17.3	7.0	3.7	9.2

Each of the individual data sets were edited, calibrated, and continuum subtracted using the typical procedures of the Astronomical Image Processing System (AIPS) package. We combined the B, C, DnC, and D data sets using the AIPS task DBCON.

The combined data sets were imaged twice using the AIPS task IMAGR to provide with two image cubes (α , β , ν) reflecting the maximum range of spatial resolution and sensitivity that our data would allow. We created a low resolution/high sensitivity cube by using a natural weighting scheme and multiplying the data in the u-v plane with a narrow Gaussian ($\text{FWHM} \approx 5 \text{ kilo-}\lambda$). This method was somewhat better than displaying only the imaged D + DnC data cube because it included the short baselines present particularly in the C configuration data.

A high resolution data cube was created by imaging the data using a natural weighting scheme without a convolution. Although we were able to obtain higher resolution by imaging with a uniform weighting scheme, they were not sensitive to low surface brightness features. They will prove to be most useful in comparing HI with H α in future work.

The high and low resolution data cubes were CLEANed in AIPS down to an rms level of 0.33 and 0.17 mJy beam⁻¹ for the low resolution and high resolution images, respectively. Details of the statistics for these two data cubes can be seen in Table 5-2. Analysis on completed and CLEANed image cubes was conducted using the Gronigen Image Processing System (GIPSY) packages.

Table 5-2. Characteristics of Naturally Weighted CLEANed Channel Maps

Parameter	Low Resolution	High Resolution
FWHP synthesized beam (")	50.3" x 40.1"	10.4" x 9.3"
FWHP synthesized beam (kpc)	9.0 x 7.2	1.8 x 1.6
Theoretical rms noise (mJy beam ⁻¹)	0.28	0.16
Observed rms noise (mJy beam ⁻¹)	0.33	0.17
Rms noise (K)	0.10	0.51
Peak temperature (K)	22.8	46.8
Peak S/N	230	92

In addition, we created a middle resolution data cube (20"x 20") by convolving the high resolution image in the image plane. This data cube was used in the construction of Position-Velocity diagrams.

Neutral Hydrogen Morphology

The channel maps shown in Figures 5-1 and 5-2 were used in a moment analysis to obtain the global density and temperature weighted radial velocity images of the neutral hydrogen. Moment maps were constructed with the AIPS task MOMNT. A flux cut off of two times the rms noise level (σ) of the unsmoothed data was used. The naturally weighted global distribution of the neutral hydrogen in NGC 1784 from the low resolution data is shown in grayscale in Figure 5-3 and overlaid on an optical image in Figure 5-4. The high resolution data is shown in grayscale in Figure 5-5 and overlaid on an optical image in Figure 5-6. The lowest contours are drawn at the 2σ level.

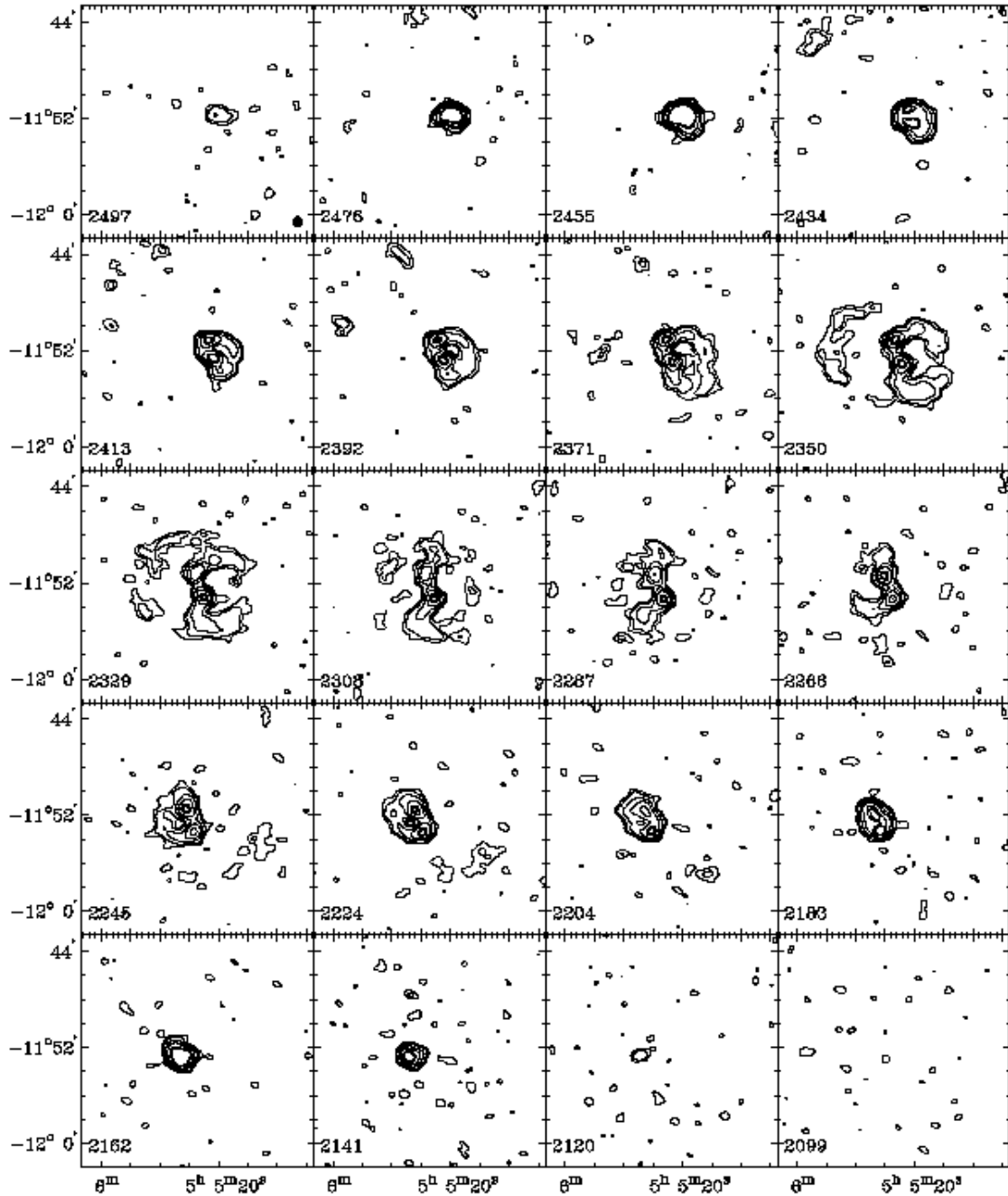


Figure 5-1. The individual, naturally weighted, CLEANed channel images of the low resolution data. Channel velocities are given in the lower left hand corner of each panel in km s⁻¹. The synthesized beam (50" x 40") is shown above the velocity information in the upper right hand panel. Contours are at 1, 2, 5, 10, 20, 25 times the 3 σ flux level, corresponding to 8.8×10^{18} cm⁻².

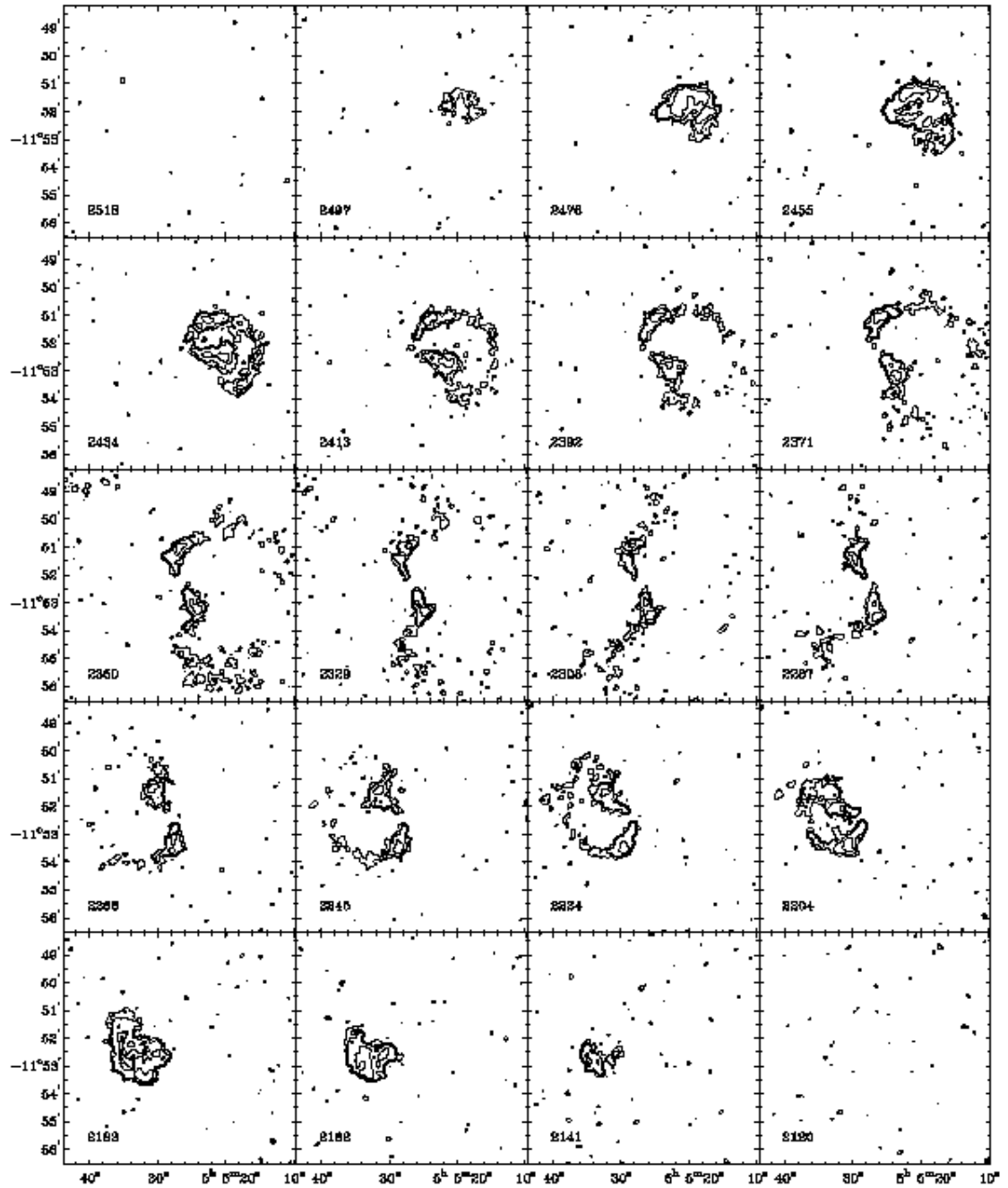


Figure 5-2. The individual, naturally weighted, CLEANed channel images of the low resolution data. Channel velocities are given in the lower left hand corner of each panel in km s⁻¹. The synthesized beam (10" x 9") is shown at the bottom right of the lower left hand channel ma. Contours are at 1, 2, and 5 times the 3 σ flux level, corresponding to 1.5 x 10²⁰ cm⁻².

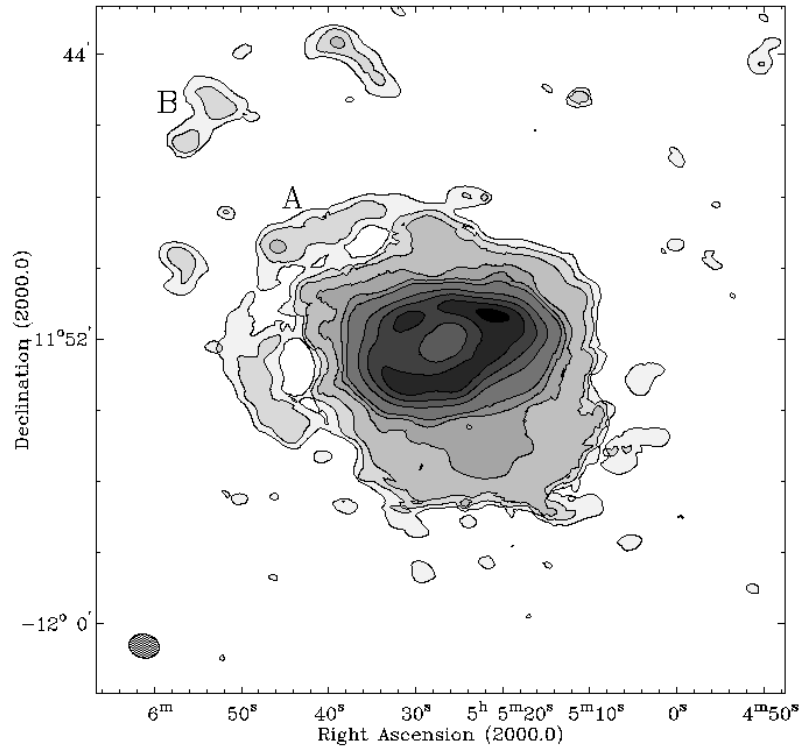


Figure 5-3. Grayscale with contours of the total HI surface density from the low resolution data set. The peak flux corresponds to a column density of $1.2 \times 10^{21} \text{ cm}^{-2}$. Contours are at 1 (the 2σ flux level), 2, 3, 5, 10, 20, 40, 60, 80, and 95% of the peak flux. The synthesized beam ($50'' \times 40''$) is shown at the bottom left. "A" and "B" denote the inner and outer rings (see text).

Continuum

One continuum point source is located at a position corresponding to the optical center of the galaxy. Another continuum source is located 4' north of the center of the galaxy. It is unlikely that this source is associated with NGC 1784. A search at the coordinates of this point in the NASA Extra Galactic Database (NED) did not result in any coincidences.

Low Resolution Neutral Hydrogen Distribution

Figure 5-3 shows the low resolution total HI surface density map. The most striking dysmorphic features of this map are the two partial HI rings (visible most prominently to the northeast of the galaxy) encircling NGC 1784, and the extended HI

emission south of the galaxy. Excluding HI emission from the features that are obviously part of the partial ring systems, we find the HI diameter of NGC 1784 to be 8' (corresponding to 85 kpc) at the 2σ ($1.2 \times 10^{19} \text{ cm}^{-2}$) level. Assuming that there are two separate rings (a later section), the inner, more complete (labeled "A"), ring has a projected radius of 4' (42 kpc), while the outer ring (labeled "B") has a projected radius of 8' (85 kpc) assuming circularity. The peak brightness in these patchy rings is similar, and corresponds to a column density of $4.8 \times 10^{19} \text{ cm}^{-2}$.

The inner regions of the galaxy also appear to be somewhat asymmetric. The peak brightness of the system, corresponding to a column density of $1.2 \times 10^{21} \text{ cm}^{-2}$, is located in the western half of the galaxy in a large area of high flux that has no counterpart on the eastern side of the galaxy. It is likely that this feature is the result of a warp in the inner disk of NGC 1784.

High Resolution Neutral Hydrogen Distribution

Figure 5-4a shows the high resolution total HI surface density map. Figure 5-6 shows this map overlaid on an optical DSS image of NGC 1784. The physical extent of the HI gas, down to a level of $1.2 \times 10^{20} \text{ cm}^{-2}$, is similar to the optical size of the galaxy, about 4' x 2'. The areas with the highest HI emission in these maps correspond to an oval ring that lies on top of the outer most regions of star formation in NGC 1784.

In NGC 3319, a barred, flocculent galaxy similar to NGC 1784, Moore & Gottesman (1998) found a close correlation between areas of star formation in the optical image and HI column densities higher than $1.5 \times 10^{20} \text{ cm}^{-2}$. Figure 5-4b shows that we broadly find the same result in NGC 1784. However, the two regions with the highest HI

column densities (corresponding to $2.4 \times 10^{21} \text{ cm}^{-2}$) do not correlate with obvious star formation.

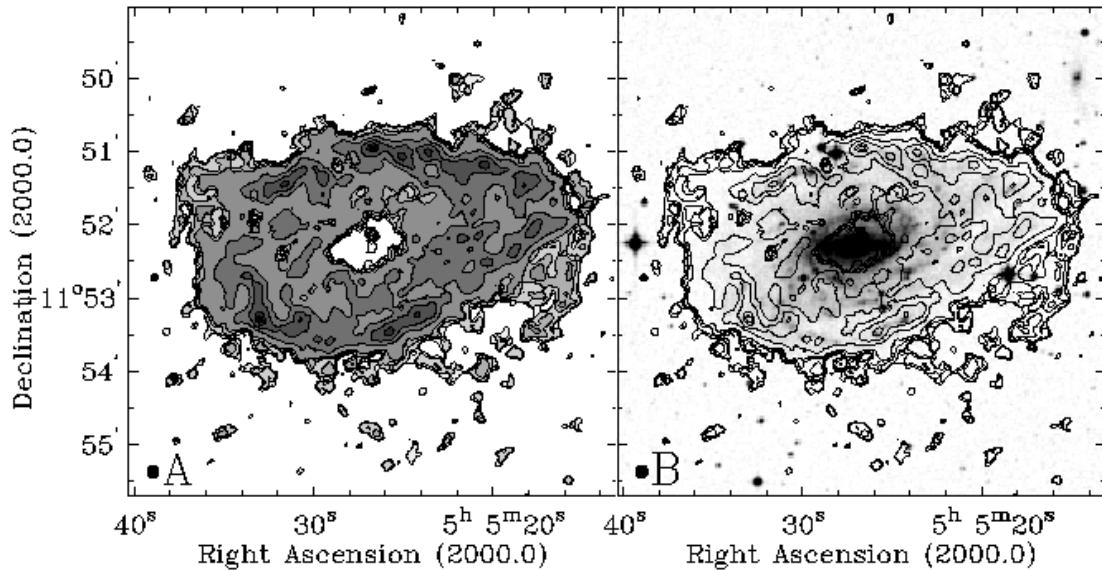


Figure 5-4. High Resolution HI surface density maps. A) Grayscale and contours of the total HI surface density from the high resolution data set. The peak flux corresponds to $2.4 \times 10^{21} \text{ cm}^{-2}$. Contours are at 5 (the 2σ flux level), 10, 15, 20, 40, 60, 80, and 95% of the peak flux. The synthesized beam ($10'' \times 9''$) is shown at the bottom left. B) Contours of the high resolution data set overlaid on a DSS image of NGC 1784. The peak flux and contours are the same as in A. The synthesized beam is shown at the bottom left.

There is a central hole in the HI emission which corresponds to the bar zone. The hole seems to follow the shape of the bar more closely on its southern edge than the northern. An HI hole associated with a bar is typical of early type disk galaxies. A bar in these galaxies will sweep HI into the central regions of the galaxy where it is consumed by star formation (Hunter & Gottesman 1996; Laine & Gottesman 1998). Other smaller holes in the HI distribution are apparent on the eastern side of the galaxy. These holes were examined for the presence of expanding gas, as in Moore & Gottesman (1998).

South of the galaxy, the large expanse of HI emission visible in the low resolution image breaks up into a number of smaller HI clumps, which have typical hydrogen

masses on the order of $10^7 M_{\odot}$. The velocity of these objects as determined through the channel maps in Figure 5-1 is consistent with them being part of the galaxy. These features are associated with the highly disturbed outer region of the galaxy. Some of them may be associated with a family of objects falling back into the plane of NGC 1784 with low velocity, on the order of 10 km s^{-1} .

Global Neutral Hydrogen Properties

Figure 5-5 shows the HI spectrum of NGC 1784 created with the data from the low resolution data cube. The spectrum is decidedly asymmetric, and shows a middle horn instead of the two horns present in typical disk galaxies. This is caused by significant HI gas at forbidden velocities, as we show in later sections.

Figure 5-6 shows the radial HI distribution made with both the high and low resolution data sets. This profile is similar to observations of other disk galaxies (Knapen 1997; Laine & Gottesman 1998; Moore & Gottesman 1998), and is consistent with the work of Maloney (1993) who postulated a sharp edge to HI disks owing to the intergalactic UV radiation field. Maloney (1993) cites an HI column density of $\sim 5 \times 10^{19} \text{ cm}^{-2}$ as the expected value of this cut off density. Our 2σ value for N_{HI} of $1.2 \times 10^{19} \text{ cm}^{-2}$ is slightly below, but still of the same order. Jörsäter & van Moorsel (1995) find a similar result from deep observations of NGC 1365.

We calculate the total HI flux of NGC 1784 to be $60.4 \pm 0.5 \text{ Jy km s}^{-1}$, which corresponds to an HI mass of $(1.55 \pm 0.03) \times 10^{10} M_{\odot}$. This value compares with other published single dish measurements of the HI flux from NGC 1784, which fall in the range of $60 \pm 2 \text{ Jy km s}^{-1}$ (Huchtmeier & Richter 1989). From our spectrum of NGC 1784, we calculate a 3σ HI flux level of 0.006 Jy . This corresponds to a conservative

minimum mass detection level of $4.6 \times 10^7 M_{\odot}$ for an isolated HI cloud, assuming that it appears in 3 continuous channels.

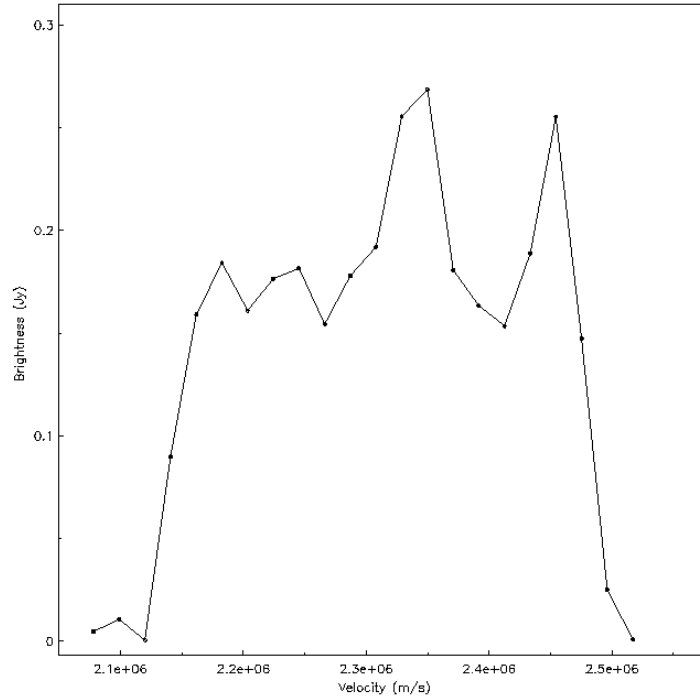


Figure 5-5. The HI flux density versus velocity for the low resolution data set. The velocity resolution here is 20 km s^{-1} . The spectrum is very asymmetric. More of the total flux comes from the receding side of the galaxy. The central spike is most likely due to extra HI found south east of the galaxy in Figure 5-3.

Neutral Hydrogen Kinematics

The velocity field created with the low resolution data is shown in Figure 5-7.

The velocity field created with the high resolution data is shown in Figure 5-8. The disk shows significant evidence of warping at its edges. At both the eastern and western extremes of the galaxy, the iso-velocity curves take a pronounced 90° turn to the north and south, respectively.

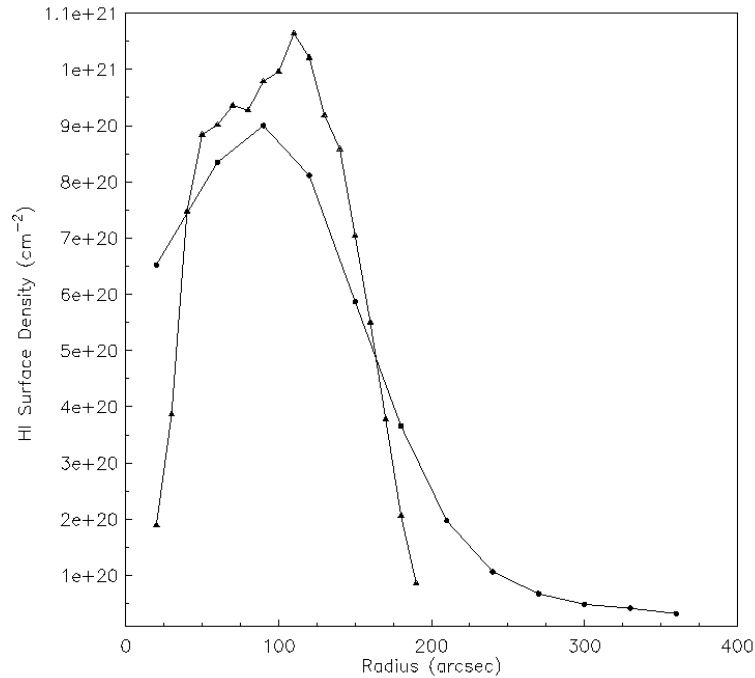


Figure 5-6. The HI radial density profiles from the low resolution data set (circles) and the high resolution data set (triangles)

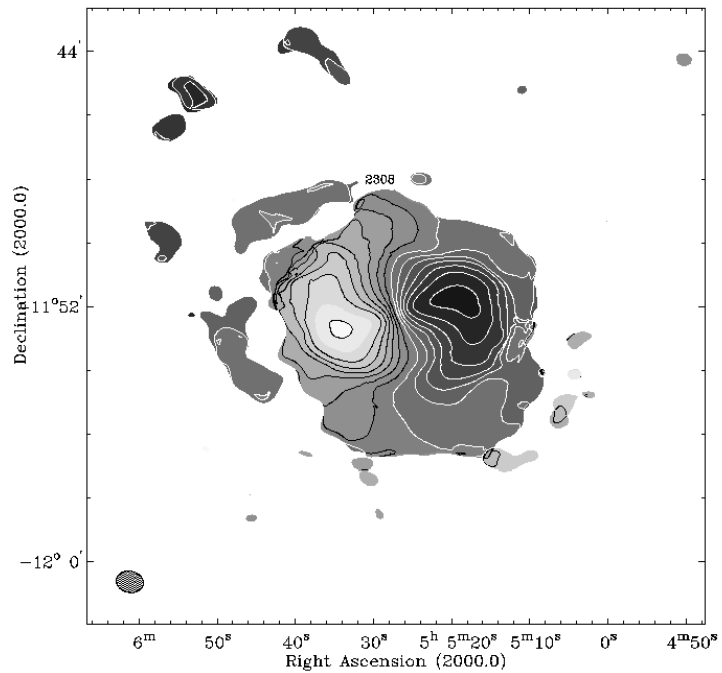


Figure 5-7. Intensity-weighted radial velocity contours of the low resolution data. Contours are separated by 20 km s^{-1} . Motion toward the observer is displayed with black contours and lighter grayscales. The central velocity contour (2308 km s^{-1}) is labeled above the galaxy. The synthesized beam ($50'' \times 40''$) is displayed in the lower left.

Along the northern half of the disk, the iso-velocity curves begin at a constant position angle. After passing through a bump about midway through the disk, the iso-velocity curves turn consistently towards the west. The bump is likely due to some type of streaming motion associated with weak spiral arms in the system. The same process occurs, but in the opposite sense for iso-velocity curves along the southern half of the disk.

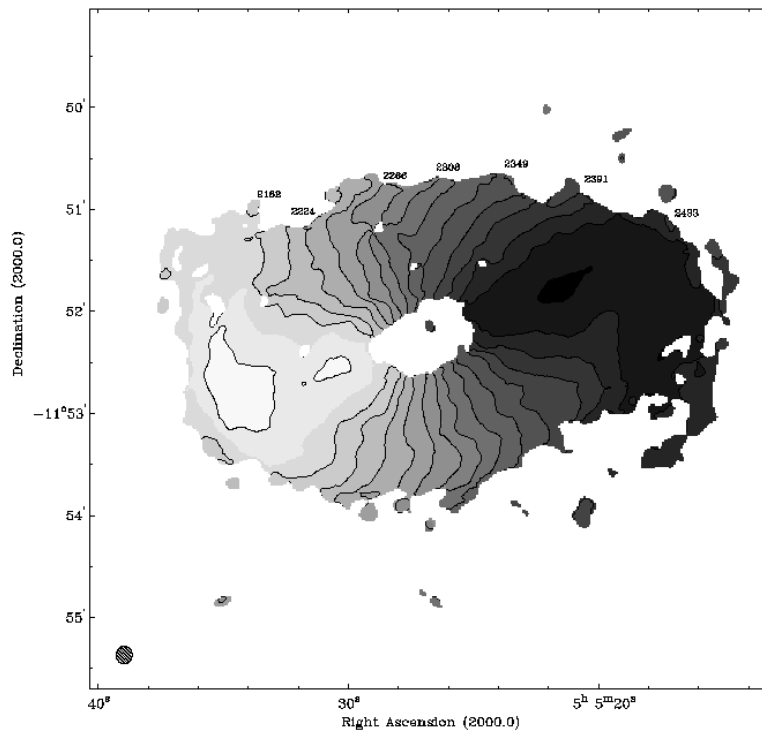


Figure 5-8. Intensity-weighted radial velocity contours of the high resolution data set. Contours are separated by 20 km s^{-1} . Every other contour is labeled with its corresponding velocity in km s^{-1} . Darker grayscales correspond to motion away from the observer. The synthesized beam ($10'' \times 9''$) is displayed in the lower left hand corner.

Global Position-Velocity Plots

Figure 5-9 shows Position-Velocity (P-V) plots of the high resolution image cube smoothed to $20''$ resolution. The slices have been made parallel to the major axis and separated by $20''$. The lowest contour is drawn at the 2σ level ($0.6 \text{ mJy beam}^{-1}$) in order

to emphasize possible gas at forbidden velocities. We searched for evidence of gas associated with the thick disk of NGC 1784 as Fraternali et al. (2002) did with NGC 2403. We did not find significant "bearding" in the same manner as in NGC 2403. However, this may be caused by observational constraints. Fraternali et al. (2002) possessed 40+ hours of C configuration observations. Our data, although similar in total time on-source, contained a significant amount of B configuration observations. This reduced our relative signal to noise ratio. In addition, our velocity resolution was significantly broader (20 km s^{-1} compared to 5 km s^{-1}).

We did find evidence of gas at non-circular velocities both at the edge of the optical disk and beyond. All declination cuts parallel to or at the major axis show a tail at low column densities that falls faster in velocity than a Keplerian curve. In Figure 5-10, cuts parallel to the minor axis from the same data set as Figure 5-9 show similar features. On the north (left) sides of the plots, the HI velocities always deviate from the global trend toward blue velocities within the disk of NGC 1784. The commencement point of this deviation coincides with the twist in the iso-velocity curves on Figure 5-8. To the south (right side of the galaxy in Figure 5-8), we see extended emission in all slices at velocities near the systemic velocity. This gas is associated with the southern HI extension seen in Figure 5-3.

In all cases, the gas associated with these non-circular velocity trends seems to flow smoothly from gas corresponding to circular velocities in the disk. This continuity implies that the gas in non-circular motion is primarily associated with the main body of NGC 1784. Only in the case of the inner ring (labeled with "IN" in the major axis slice of Figure 5-9), do we see gas that is obviously separated from the main body of NGC

1784 in both column density and velocity. The non-circular tails on both the major and minor axis P-V plots indicate a warped disk. Assuming that NGC 1784 has trailing arms, the velocity field (Figure 5-7) implies that the north side of NGC 1784 is pointing toward the observer. The P-V plots show that gas on the north and west sides of NGC 1784 is moving toward the observer, while gas on the south and east is moving away. The column densities of the warped gas are much higher and physically closer to the galaxy center on the north side of the galaxy.

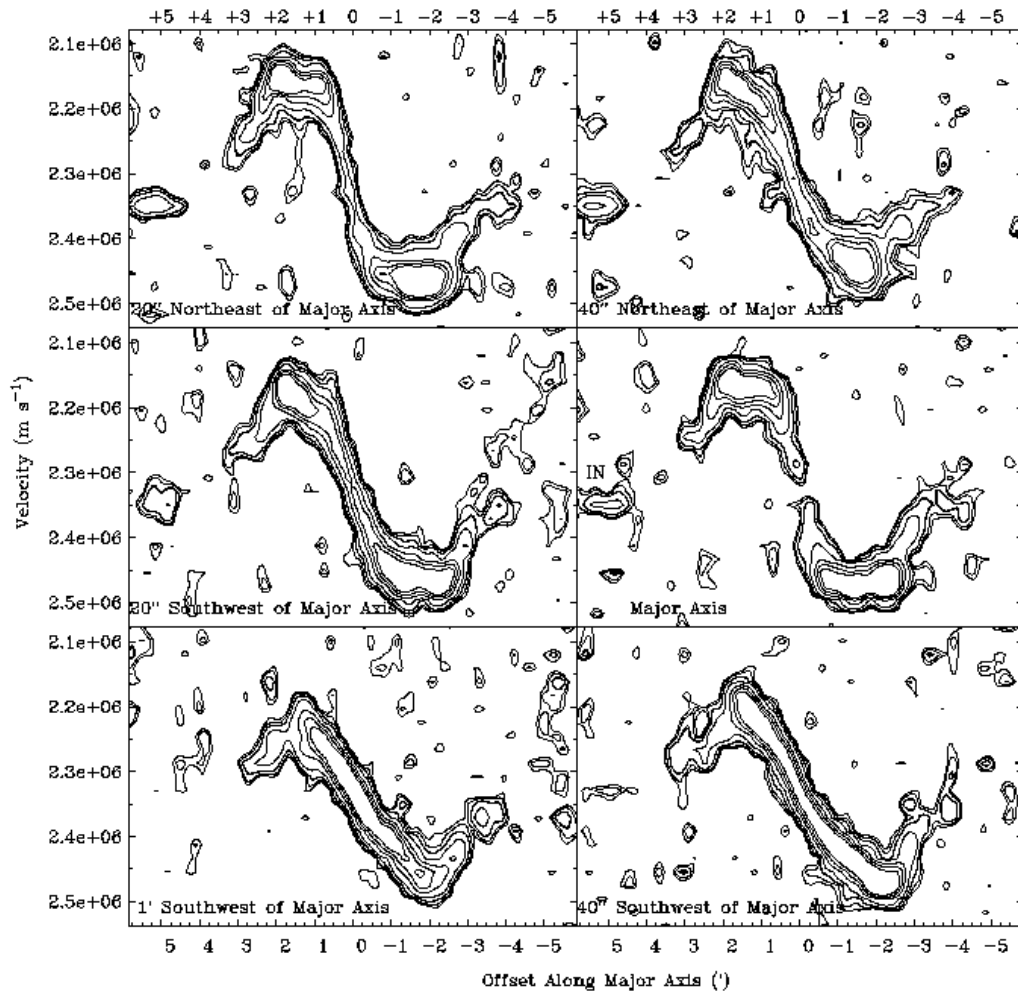


Figure 5-9. A set of P-V slices parallel to and along the major axis of NGC 1784. The contours are at 2, 3, 5, 10, 15, and 25 σ . The inner ring feature is labeled with "IN" in the plot along the major axis. The central velocity is at $2.308 \times 10^6 \text{ m s}^{-1}$.

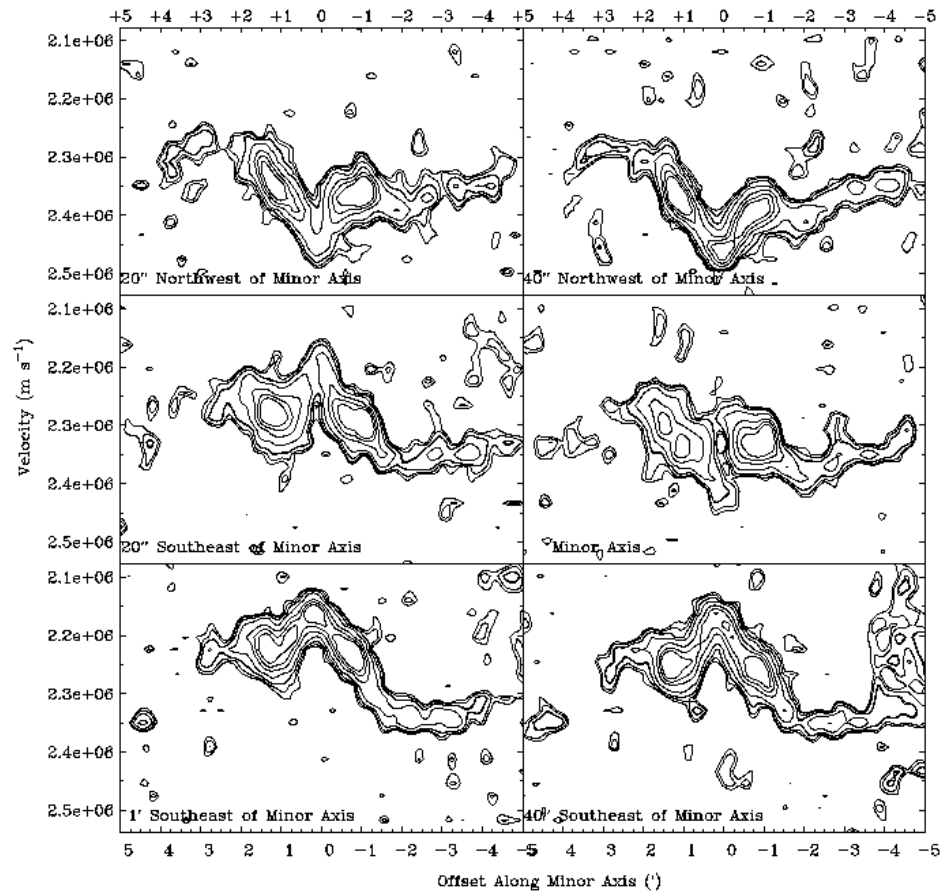


Figure 5-10. A set of P-V slices parallel to and along the minor axis of NGC 1784. The contours are at $2, 3, 5, 10, 15, 20,$ and 25σ . The systemic velocity of the system is at $2.308 \times 10^6 \text{ m s}^{-1}$.

In order to probe more deeply some of the velocity characteristics of the gas, in Figure 5-11 we produced P-V plots with $1'$ thick slices as opposed to the $1''$ slices in Figures 5-9 and 5-10. Figure 5-11a shows a $1'$ thick slice centered on the major axis. Here we see the tail of the receding side of the galaxy extends almost beyond the systemic velocity (the lowest contour is at the 2σ or 0.4 mJy level). We also see a double peaked spectrum, as this gas at non-circular velocities is at the same RA offset as a small extension of gas that continues a flat rotation curve beyond $-2'$. As the non-circular tail and flat rotation extension have roughly the same physical extent (at a radius just shy of -

4'), we conclude that this gas has been pulled out of circular velocities as opposed to being of external origin. On the other side of the galaxy, we see a similar strong non-circular tail, as well as the signature of the inner ring. Throughout the image, we see 2 and 3σ signals of gas at forbidden velocities. If these signals are real, they would speak to the disturbance of the system in the outer disk.

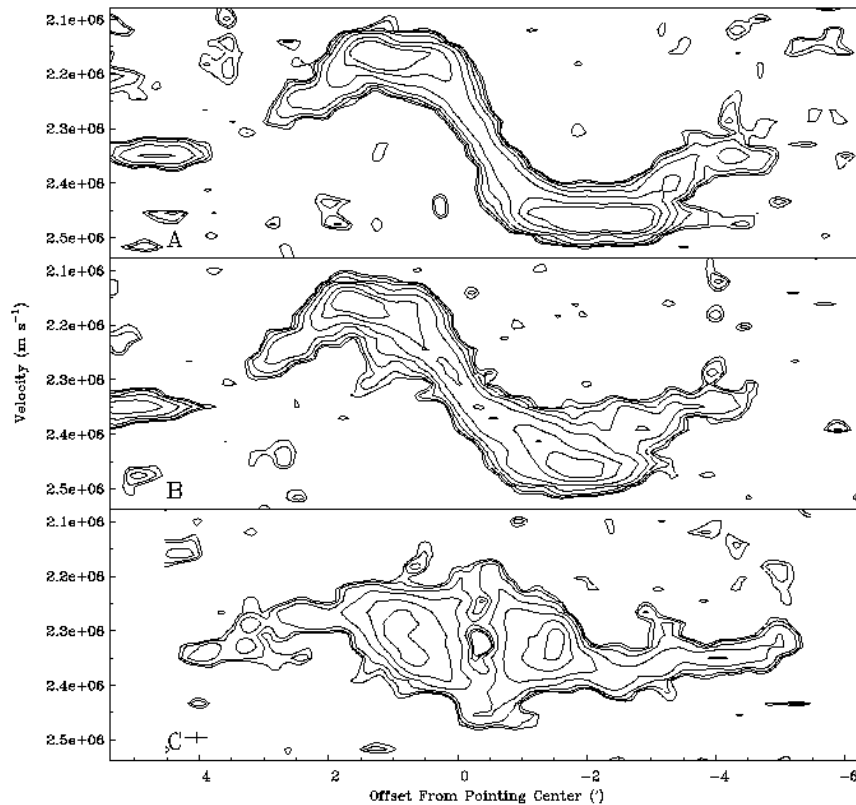


Figure 5-11. Thick P-V slices of NGC 1784. A) 1' thick P-V slice along the major axis. Contours are at 2, 3, 5, 10, 15, 20, and 25σ . B) A 1' thick P-V slice 40'' northwest and parallel to the major axis. The contours are the same as in A. C) A 1' thick P-V slice along the minor axis. The contours are the same as in A. The resolution function is denoted by a cross in the lower left hand corner of C. The central velocity of all plots is $2.308 \times 10^6 \text{ m s}^{-1}$.

Figure 5-11b shows a 1' thick slice taken 40'' northeast of but parallel to the major axis. This figure was constructed to examine with higher signal to noise ratio a feature that looked to be an expanding bubble in the corresponding 1'' wide slice in Figure 5-11.

This structure shows up in Figure 5-11b at +2' and slightly below the systemic velocity as a finger stretching downward to the right of the non-circular HI tail. Although the finger of gas does not possess extremely large column densities, its 1' length (11 kpc) spread over 70 km s^{-1} indicates that a great deal of energy, on the order of 10^{54} ergs must have been required to create it. This feature is too energetic to be the result of a single supernova. However, features this large could be caused by the passage of a small HI cloud through the plane of the galaxy (Brinks & Bajaja 1986; van der Hulst & Sancisi 1988). Unfortunately, because of the low column densities involved, we were unable to find additional evidence of this feature in other analysis techniques.

Another possible example of an expanding bubble or disrupted cloud or satellite can be seen in the 1' thick minor axis plot (Figure 5-11c). In this plot, we see a $2 - 3\sigma$ signal of a large arc of gas stretching from 5' south of the galaxy to the galactic center at velocities blue-ward of the systemic value.

Local Low-Density Region Position-Velocity Plots

In Figure 5-4, we noted the presence of several low-density HI regions (or holes), labeled A, B, and C as well as the presence of one anomalous region in the bar, labeled D. Holes in the HI distribution of a disk galaxy have been studied in some detail in the past and are thought, depending on their size, to be either due to supernovae, stellar winds resultant from OB associations, or HVC's passing through a galactic disk (Brinks & Bajaja 1986; Tenorio-Tagle & Bodenheimer 1988; van der Hulst & Sancisi 1988). The holes that we examined in NGC 1784 are on the order of a beam size, or 1 to 2 kpc in diameter. The gas densities in these regions fall below our 2σ column densities ($1 \times 10^{20} \text{ cm}^{-2}$) at their centers. The energy associated with moving this much gas (over 10^{54} ergs)

is beyond the capabilities of a simple supernovae process. Typically, HI holes coincident with OB associations are smaller than 300pc (Brinks & Bajaja 1986).

We explore these regions with localized P-V plots in order to search for evidence of expanding gas. Figure 5-12 presents 40" (7 kpc) long slices on and near to hole "A" in Figure 5-4. These slices, and all other localized slices are taken from our high resolution data cube. Figure 5-13 shows 40" long slices on and near hole "B". Figure 5-14 shows 40" long slices on and near hole "C". All slices were made from west to east across the galaxy. The slices around each hole are separated by 7" in declination.

Only in the low density region labeled A (Figure 5-12), were we able to find anything resembling the expansion signatures shown in NGC 3319 by Moore & Gottesman (1998). We note that the hole is skewed, but lack the velocity resolution to comment in detail. This hole is at the position where the iso-velocity curves change direction into the warp on the north side of the galaxy (Figure 5-8). Thus, it is interesting that we see a shift in the velocity of the gas across the hole and some bubbling in Figure 5-14. The other two holes appear to be just that. They are low density regions with no difference in velocity structure from the gas around them.

Lastly, we examined the object labeled "D" in Figure 5-4. This is the only HI that appeared within the bar region in our total HI intensity map. It also showed a slightly different velocity from the gas around it (Figure 5-8). We investigated object "D" to determine if it was associated with the galaxy or possibly infalling material. Figure 5-15, a slice made in the same manner as the other localized slices, shows that object "D" is most likely associated with the galaxy, as it lies on the trend of HI from other slices. This object probably represents a small HI region that has not been completely destroyed by

processes within the bar. The plot through the center of feature "D" shows an object that is isolated both in angle and in velocity from the main gas of the galaxy. The parallel slices show its size is small, and the total HI mass is on the order of $10^7 M_{\odot}$. While we cannot preclude that this object is not an HVC that has fallen into the center, the energy of such a collision make it unlikely that the cloud could retain such a well ordered structure. The kinetic energy of the infalling object is about 10^3 times larger than the probable binding energy of the cloud.

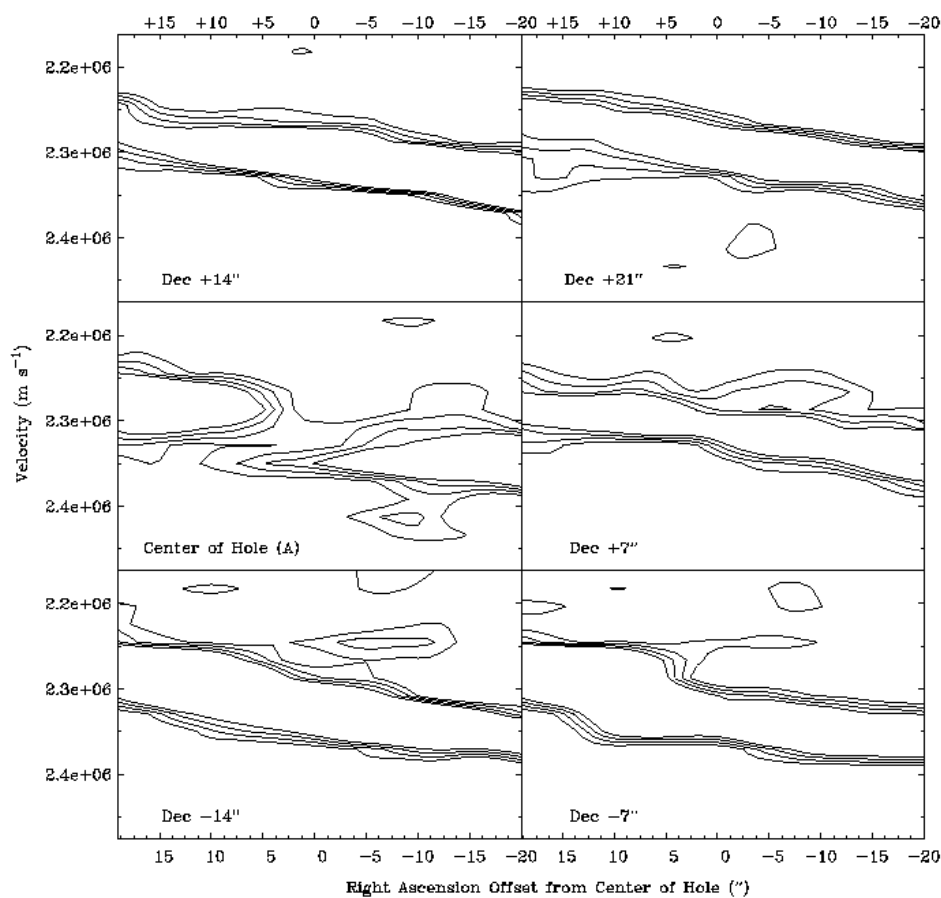


Figure 5-12. A P-V slice through low density region A. Contours are at 2, 3, 5, and 10σ .

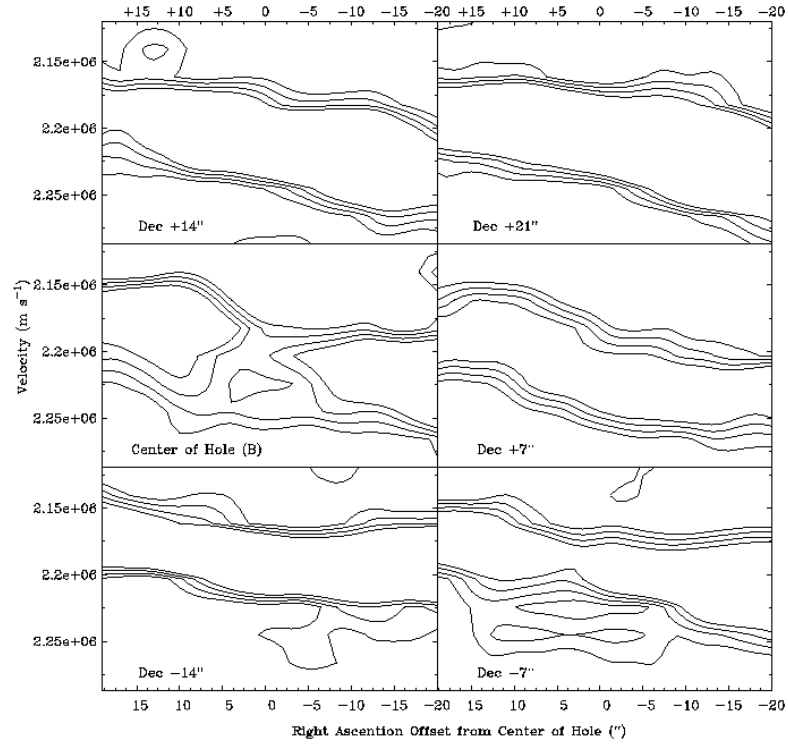


Figure 5-13. A P-V slice through low density region B. Contours are at 2, 3, 5, and 10σ .

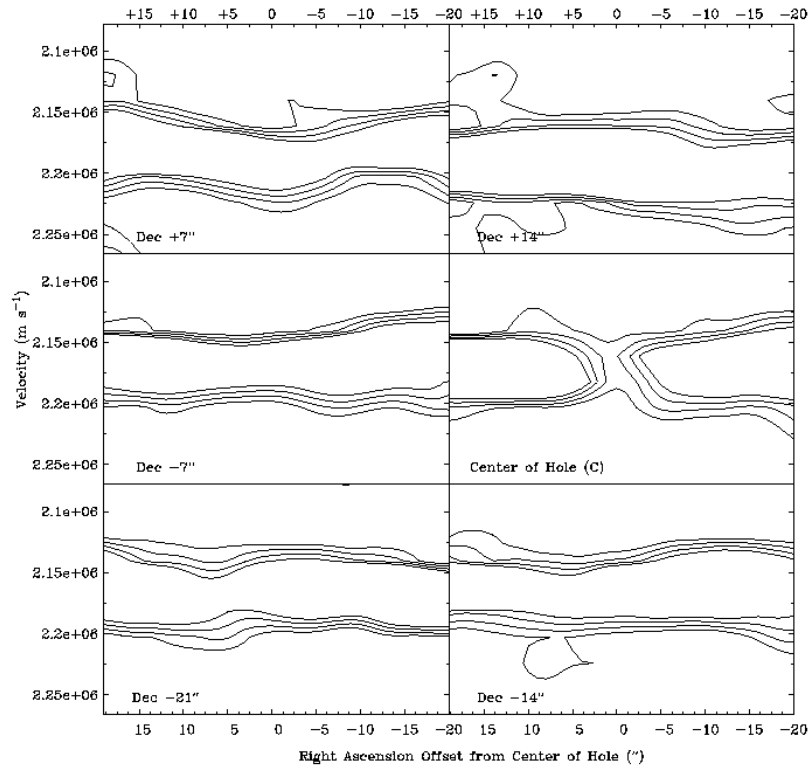


Figure 5-14. A P-V slice through low density region C. Contours are at 2, 3, 5, and 10σ .

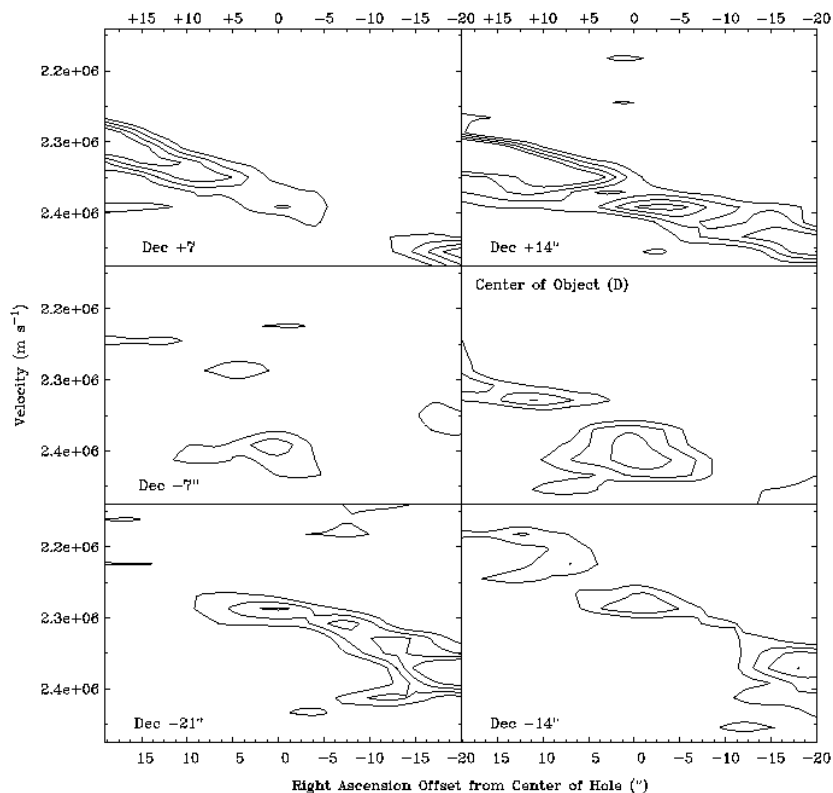


Figure 5-15. A P-V slice through object D. Contours are at 2, 3, 5, and 10σ .

Rotation Curves

We used the GIPSY task 'reswri' to calculate a rotation curve by fitting tilted rings to the velocity field of NGC 1784. To create our rotation curve, we used our high resolution data set. We fit rotational velocities to radii ranging from 20" to 160" in 10" wide annuli. We used the high resolution data to prevent beam smearing, which causes underestimation of the velocities in the inner regions of the galaxy. Our values at the center of the galaxy possess higher uncertainties because of the lower flux density values in the bar. It was impossible to fit a rotational velocity inside of 20" owing to the lack of flux.

In order to fit the rotation curve, we held fixed the values for the position of the kinematic center and systemic velocity. We allowed the rotational velocity, position angle, and inclination to be free parameters. We fit curves to the receding and

approaching sides of the galaxy, as well as calculated an average. The plot of rotational velocity versus radius is shown in Figure 5-16. The plot of position angle versus radius is shown in Figure 5-17. The plot of inclination versus radius is shown in figure 5-18.

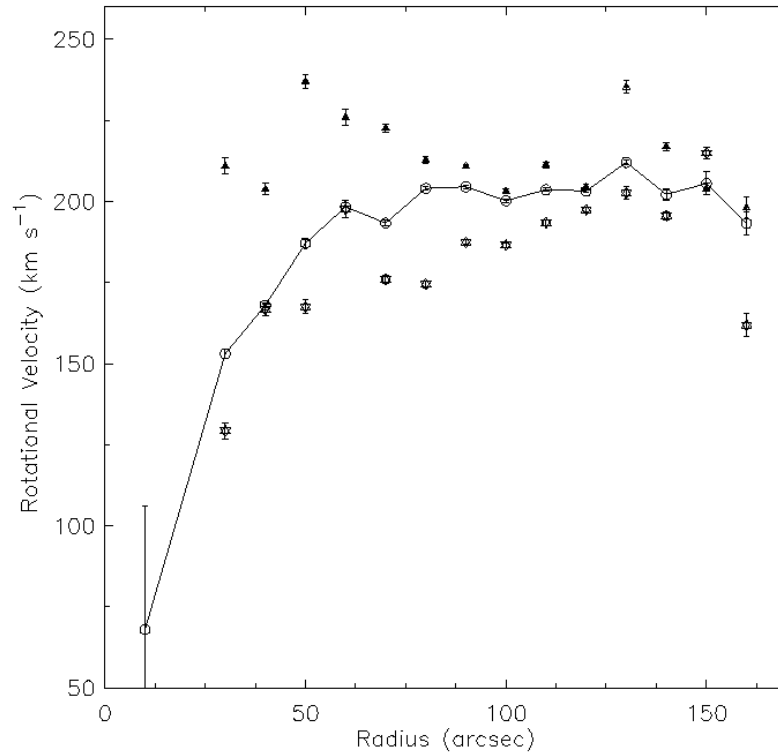


Figure 5-16. Rotation curve of NGC 1784 from the high resolution data set. Stars represent the approaching half of the galaxy. Triangles represent the receding half of the galaxy. Circles represent the average of both.

The averaged data shows that NGC 1784 has a flat rotation curve out to 160". This is consistent with other flocculent galaxies, and has been theorized to represent a greater relative abundance of dark matter in flocculents compared to grand design galaxies (Elmegreen & Elmegreen 1990). The curve for the approaching side of the galaxy mimics the average curve, but with lower velocities. The curve for the receding side is falling throughout and carries higher uncertainties. This is likely caused by the warp (i.e. the twisting of iso-velocity curves) being more pronounced on the receding (east) side of the galaxy.

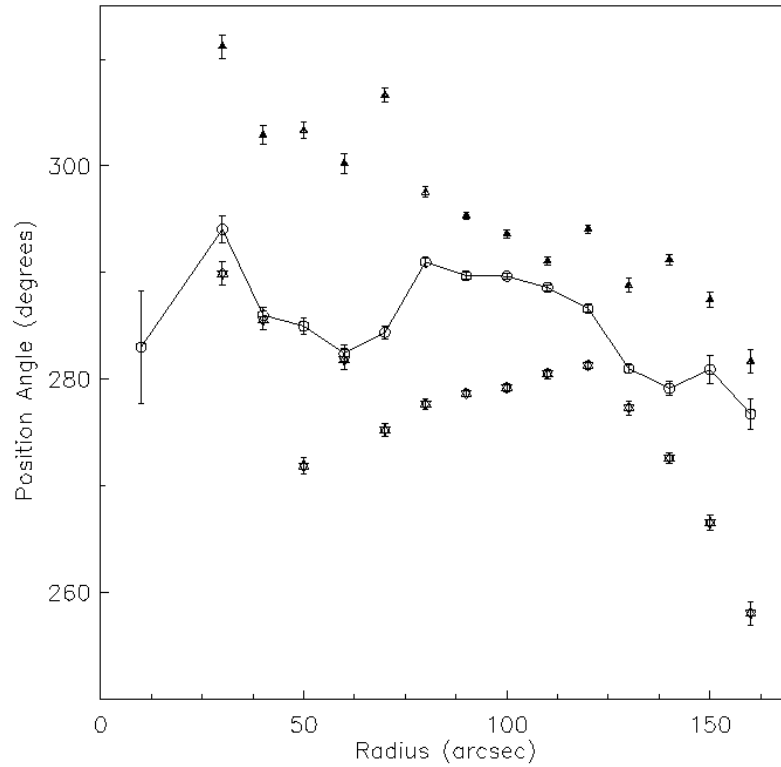


Figure 5-17. Kinematic position angle of NGC 1784 as a function of radius. Stars represent the approaching half of the galaxy. Triangles represent the receding half of the galaxy. Circles represent the average of both.

Using the final data point of the rotation curve, we calculated a value for the total mass of NGC 1784 interior to 160". Using a Keplerian, $M = V^2 R G^{-1}$, to model the disk and halo, where $R = 160'' = 28 \text{ kpc}$ and $V(28 \text{ kpc}) = 215 \text{ km s}^{-1}$, we find $M(R) 3.06 \pm 0.28 \times 10^{11} M_{\odot}$. Comparing this with the HI mass found above, we find an $M_{\text{HI}} / M(R)$ ratio of 5% for NGC 1784. This value is in line with other typical barred spirals (Moore & Gottesman 1998).

The warp is most evident in the position angle and inclination plots. In the inner parts of the galaxy, the position angle and the inclination of both halves of the galaxy are different. The two values both trend lower at the outer limits of the optical disk, but it is apparent that this trend is complicated. Not only is the disk of the galaxy bent like the brim of a hat, it is also twisted along a second axis.

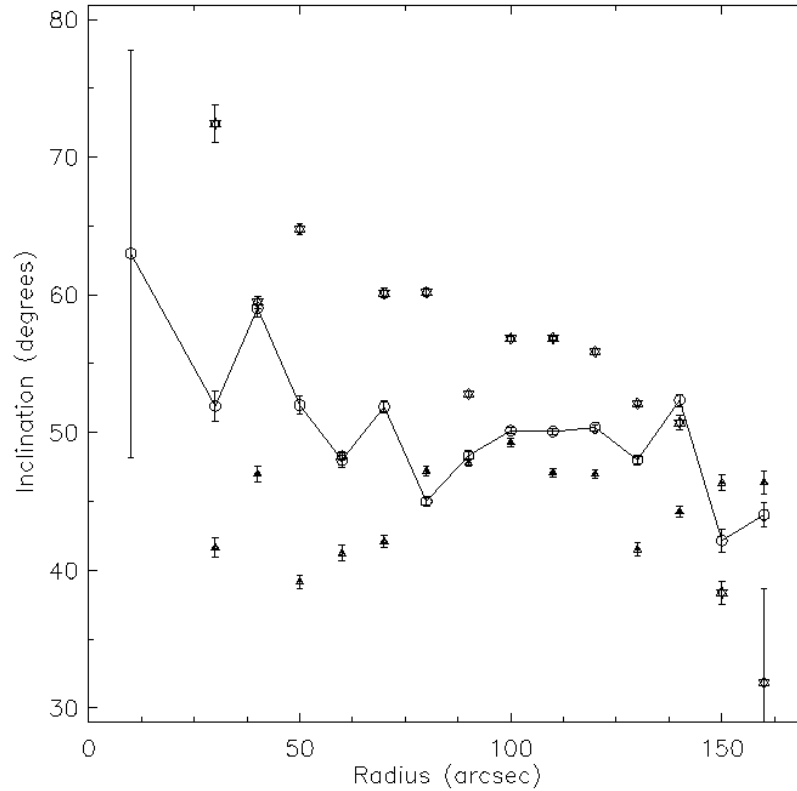


Figure 5-18. Inclination angle of NGC 1784 as a function of radius. Stars represent the approaching half of the galaxy. Triangles represent the receding half of the galaxy. Circles represent the average of both.

Model Disks, Velocity Residuals, and Corrotation

The rotational velocities shown in Figure 5-18 were fit with a model rotation curve using the GIPSY task 'fit'. This model curve was then turned into a model disk with the GIPSY task 'velfi'. The model disk was then subtracted from our observed, high resolution velocity field, to create a map of residual velocities. The model disk is shown in Figure 5-19a, and the residual field is shown in Figure 5-19c. The residual map reflects the trends we reported in the P-V diagrams in a previous section, where the gas deviates significantly from a naïve model at the edge of the optical disk. Here we see the contours pile up rapidly at the edge of the optical galaxy. The pattern of the residuals resembles one receding/approaching pair of spirals. Canzian (1993) shows that for a first

order density-wave analysis, the corotation point of a galaxy can be found to be where this one pair of approaching/receding spirals turns into two pairs. There is no clear evidence of this in Figure 5-19c.

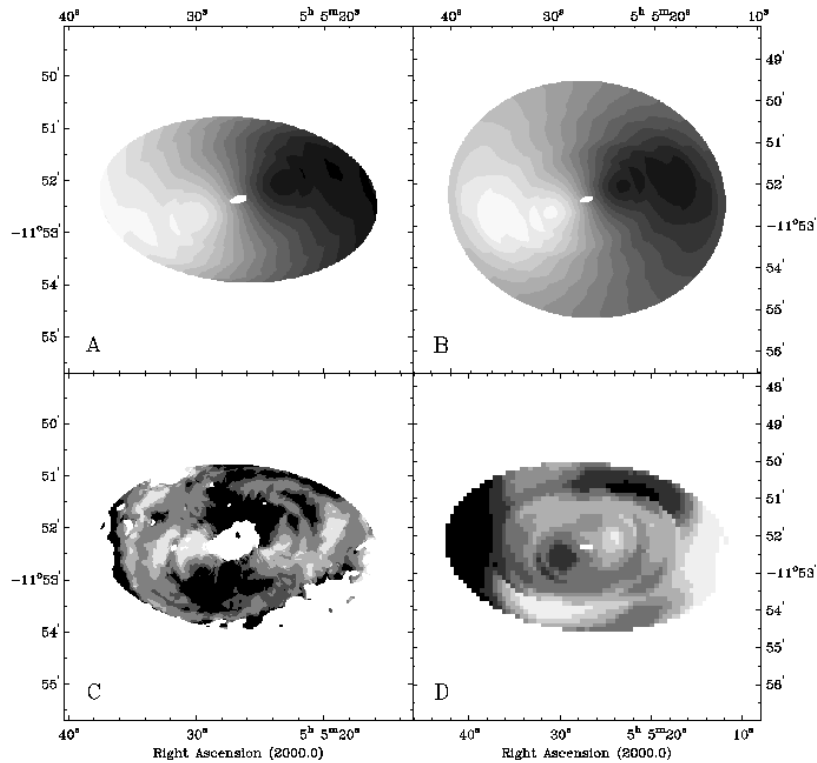


Figure 5-19. Model velocity and residual velocity fields for NGC 1784. A) Model velocity field constructed from kinematical data in Figures 17, 18, and 19. Light grayscales represent approaching velocities. B) Model velocity field constructed from rotation curve data in Figures 17, 18, 19, and extended to larger radii. Light grayscales represent approaching velocity. C) Residual velocity field made from model in A. Light grayscales represent approaching residuals (max = 30 km s^{-1}). D) Residual velocity field made from model in B. Light grayscales represent approaching residuals (max = 30 km s^{-1}).

To explore the possibility of finding the corotation point, we increased the range of our model curve to $240''$, created a new model disk, and subtracted this model from our low resolution velocity field. The model velocity field is shown in Figure 5-19b, and the residual velocity field from this process is shown in Figure 5-19d. Here, outside the optical extent of the galaxy, we do find three approaching/receding pairs. This would put

the corotation radius at well over twice the bar radius (about 20 kpc). This is significantly beyond the location of corotation reported in other galaxies (Aguerri et al. 2001). Elmegreen & Elmegreen (1990) suggest that corotation in late-type galaxies could lie at a radius of two times the bar radius. However, owing to the fact that the position angle and inclination change of the length of the disk in NGC 1784, our models must be treated with caution. Warner et al. (1973) point to systematic offsets in the residual map when using incorrect values of position angle. Owing to the uncertainty, this value for the corotation radius must be compared with others obtained from methods such as abundance gradients in the disk and Fourier analysis (Zaritsky et al. 1994; Aguerri et al. 2001). NGC 1784 does seem to be an excellent candidate for detailed study of its corotation parameter owing to its large bar and lack of consistent spiral structure.

The Neutral Hydrogen Rings

In this section we will discuss the HI rings seen in Figure 5-1, which have been so far ignored in deference to the disk of NGC 1784. Figure 5-3 shows three large clumps of HI (about 2' in length) northeast of the galaxy, forming an outer arc around NGC 1784. There is a more complete arc of gas, some 8' long, closer in to the body of NGC 1784 on the northwest side. Finally, there are several clumps of HI on the southwest side of the galaxy which appear to be part of these ring systems as well. Figures 5-1, 5-7, and 5-9 the low resolution channel maps, velocity field, and major axis P-V plots, show that these rings are in apparent counter rotation to the disk. The two ring arcs on the western side of the galaxy show receding velocities more appropriate to the eastern side of the galaxy's main body. While the few clumps southeast of the galaxy show an approaching velocity more appropriate to the western side of the galaxy's main body. Although these rings are likely inclined to the plane of NGC 1784, they would have to be in an almost polar orbit

in order to be moving in a prograde sense. The more probable description is of a retrograde orbit.

The channel maps indicate that, besides being at forbidden velocities, the gas in these rings has a narrow velocity width. A spectrum of the area containing both the inner and outer ring arcs on the eastern side of the galaxy is shown in Figure 5-20. The peak at lower velocity (and higher signal) is due to the inner ring, while the second peak is due to the outer three clumps. We calculate an HI mass for both rings in total to be $5 \times 10^8 M_{\odot}$, with the inner ring comprising two thirds of that value. The average HI mass of the 3 clumps in the outer ring is $6 \times 10^7 M_{\odot}$. From the channel maps, it seems that most of the gas that is obviously involved in the rings is on the east side of the galaxy. We determine an upper limit on the total HI mass of the rings to be $1 \times 10^9 M_{\odot}$.

We estimate a total mass of the central clump in the outer ring to be on the order of $2 \times 10^9 M_{\odot}$ from a simple Keplerian calculation where $v = 30 \text{ km s}^{-1}$ and $R_{\text{clump}} = 10 \text{ kpc}$. This value leads to an $M_{\text{HI}} / M_{\text{tot}}$ value of 60% of the value for NGC 1784 itself. This is probably an upper limit, as the clump is significantly elongated. Since the velocity width of the clump is narrow, it is unlikely that the object is greatly extended out of the orbital plane, but observations with higher velocity resolution would be helpful in determining its structure and whether it is rotationally supported.

The large HI rings around NGC 1784 are most likely caused by past interactions with a reasonable sized companion galaxy ($M_{\text{tot}} = 10^{10} M_{\odot}$). We can not determine if both rings are the result of a long term interaction with one cloud spiraling into the galaxy or the result of two separate interactions. However, a rough calculation shows the tidal disruption radius of NGC 1784 is on the order of 50kpc; we assume the mass density of

the companion is similar to NGC 1784 and adopt a radius of 21 kpc for NGC 1784. The outer ring has a projected radius of 62 kpc, close to the distance at which we would expect a satellite to begin breaking up as it spirals in. This is similar to an analysis of the orbit of the LMC about the Milky Way (Binney & Tremaine 1987).

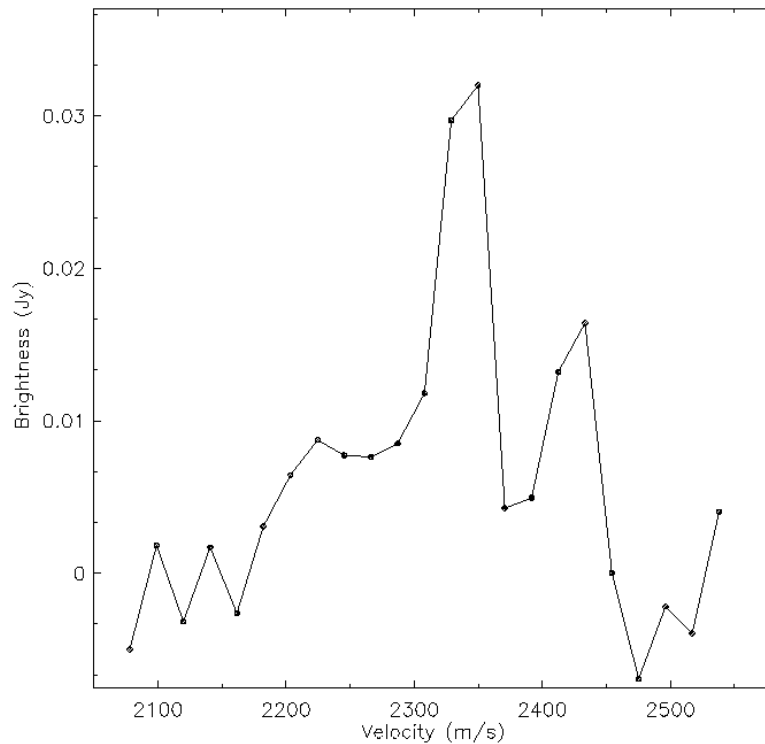


Figure 5-20. The HI flux versus velocity for the HI rings using the low resolution data set. The velocity resolution here is 20 km s^{-1} . The peak at roughly 2350 km s^{-1} represents the inner ring. The peak at roughly 2450 km s^{-1} represents the outer ring.

If the rings are the result of the tidal dissipation of a smaller companion, we can calculate an approximate timescale for the interaction. Using Eq 7-27 from Binney & Tremaine (1987) and assuming that the rotation curve of NGC 1784 is flat out to 63 kpc, as Binney & Tremaine (1987) do for the Milky Way, we find the decay time for NGC 1784's satellite to be 7×10^9 years. This timescale is long, on the order of 30 rotation periods, and is consistent with the other features present in NGC 1784. For example,

owing to the lack of HI gas, the bar in NGC 1784 is most likely an old bar similar to the one present in the flocculent system, NGC 3319 (Moore & Gottesman 1998). However, optical and near infrared studies of the stellar population would be necessary to confirm this. The length of the bar is also indicative of its old age. According to Athanassoula (1992), angular momentum transfer from the inner disk to outer disk and halo is the primary aging process of the bar. As the bar transfers angular momentum outward, it becomes longer, thinner, and stronger. The narrowness and length of this bar indicates that it is long lived.

Modeling will be necessary to determine both the orbit of the possible satellite and the dynamical response of the disk (the warp). Galactic warps are also believed to be long lasting phenomenon (García-Ruiz, I.; Kuijken, K.; Dubinski, J.-Ruiz et al. 2002a). Recent work appears to indicate that galactic warps are more likely caused by interactions with a field of numerous small clouds as opposed to interactions with larger companions (Castro-Rodriguez et al. 2002; García-Ruiz, I.; Kuijken, K.; Dubinski, J.-Ruiz et al. 2002b; Lopez-Corredoira et al. 2002). However, in the case of NGC 1784, the most plausible explanation for the warp is an interaction with an LMC type system, the remnants of which we see in the rings. The marginal objects and features discussed with regards to figure 5-4 may be detritus of fragments produced by this interaction.

Summary

We have presented deep HI observations of the flocculent, barred spiral, NGC 1784. We have found the presence of two anomalous HI rings about the galaxy, and a distorted HI disk, in contrast to the inner optical structure of the galaxy, which is quite regular. We find that the rings are in apparent counter rotation. We argue that they are the result of the tidal break up of a $10^{10} M_{\odot}$ cloud several 10^9 years ago. We further

argue that a close passage of this cloud is the cause of a significant warp in the HI of NGC 1784's outer disk. We find that NGC 1784 possesses a flat rotation curve similar to other flocculent galaxies.

Our observations of NGC 1784 and the discovery of anomalous HI features imply that often moderately distant, well ordered, spiral galaxies are understudied in HI emission. A simple VLA snapshot observation of this system would have never revealed its rich dynamic properties. With deep observations, we have uncovered an object which can provide us with more knowledge of how intergalactic gas influences the structure of large galaxies.

CHAPTER 6 NEUTRAL HYDROGEN OBSERVATIONS OF NGC 3055

NGC 3055 is a small, isolated disk galaxy (Marquez & Moles 1996). The optical diameter of NGC 3055 is 125", the smallest angular size in our study. It has a physical size of 14 kpc, making it somewhat bigger than several other galaxies in our study. Marquez & Moles (1996) found it to have a total mass of $3 \times 10^{10} M_{\odot}$. It is classified as an SAB(s)c late type galaxy and has a spiral arm classification of "4" (meaning that it has a one armed appearance), placing it in the flocculent range (Elmegreen & Elmegreen 1982; de Vaucouleurs et al. 1991). NGC 3055 has a systemic recessional velocity of 1832 km s^{-1} , corresponding to a distance of 23 Mpc, where H_0 is $70 \text{ km s}^{-1} \text{ Mpc}^{-1}$. NGC 3055 is a good candidate for radio study because of its proximity and favorable orientation. Unfortunately, however, its small size prevents us from learning a great deal about its gas/star interaction at typical radio wavelength resolutions.

Previous optical observations have found it to be quiescent with a small bar (Devereux 1989; de Vaucouleurs et al. 1991; Martin 1995). Sperandio et al. (1995) found a possibly unusual mass distribution using stellar velocities, but this was only out to a radius of 40". No other studies have included NGC 3055.

Observations

Radio observations of NGC 3055 were obtained at the Very Large Array in January and September of 2002 using the D and C configurations, respectively. The spectrometer was composed of 64 channels with a 10.5 km s^{-1} velocity resolution. The total band width

was 3.125 MHz (640 km s^{-1}), and the central heliocentric velocity was 1832 km s^{-1} . The observing parameters for the two runs are summarized in table 6-1.

Table 6-1. Parameters of VLA HI observations of NGC 3055

Configuration	C	D
Number of antennae	27	27
V_{sys} (km s^{-1})	1832	1832
Phase calibrator	0925+003	0925+003
Flux calibrator	0137+331	0137+331
Time on source	7.1	3.8

Table 6-2. Characteristics of Naturally Weighted CLEANed Channel Maps

Parameter	Low Resolution	High Resolution
FWHP synthesized beam (")	52" x 42"	22" x 16"
FWHP synthesized beam (kpc)	5.8 x 4.7	2.4 x 1.8
Theoretical rms noise (mJy beam^{-1})	0.37	0.37
Observed rms noise (mJy beam^{-1})	0.43	0.47
Rms noise (K)	0.11	1.11
Peak temperature (K)	5.7	5.2
Peak S/N	51	5

Both the C and D configuration data sets were edited, calibrated and continuum subtracted using the typical procedures of the Astronomical Image Processing System (AIPS) package. We combined the C and D data sets into one using the AIPS task DBCON. The combined data set was imaged twice using the AIPS task IMAGR to provide us with two image cubes (a, d, v) reflecting the maximum range of spatial resolution and sensitivity that our data would allow. We created a low resolution cube by using a natural weighting scheme and a high resolution data cube by imaging the data with a uniform weighting scheme. We CLEANed the data cubes in AIPS down to an rms level of 0.43 and $0.47 \text{ mJy beam}^{-1}$ for the low resolution and high resolution images, respectively. Further details of the statistics for each data cube are presented in Table 6-

2. Analysis on the completed and CLEANed image cubes was conducted using the Gronigen Image Processing System (GIPSY) package.

Neutral Hydrogen Morphology

The channel maps shown in Figures 6-1 and 6-2 were used in moment analyses to obtain global density and temperature weighted radial velocity images of the neutral hydrogen in NGC 3055. Moment maps were constructed with the AIPS task MOMNT. A flux cut off of three times the rms noise level (σ) of the unsmoothed data was used. The naturally weighted global distribution of the neutral hydrogen in NGC 3055 is shown in grayscale in Figure 6-3. The uniformly weighted global distribution of the neutral hydrogen is shown in grayscale in Figure 6-5 and overlaid on an optical DSS image in Figure 6-6. The lowest contours are drawn at the 2σ level.

Low Resolution Neutral Hydrogen Morphology

Figure 6-3 shows the low resolution total HI surface density map of NGC 3055. NGC 3055 itself is fairly regular and symmetric in its HI distribution. The peak HI emission from the galaxy (corresponding to a column density of $1.53 \times 10^{21} \text{ cm}^{-2}$) lies slightly off center. We find the HI diameter to be $3.5'$ (24kpc) at the 2σ level, or 1.7 times the optical D_{25} of NGC 3055.

Most notable in this image are two HI companions located about $10'$ north and west of NGC 3055. For discussion in later sections we label the northernmost satellite "A", and the western satellite "B". Satellite "A" is separated by $13.5'$ (92 kpc) to the north-northeast of NGC 3055. It has a peak column density of $7.64 \times 10^{19} \text{ cm}^{-2}$ and an HI diameter of $1.5'$ (10 kpc). Satellite "B" is separated by $12.5'$ (85 kpc) to the the west-northwest of NGC 3055. It has a peak column density of $1.53 \times 10^{20} \text{ cm}^{-2}$ and an HI

diameter of 1.5' (10 kpc). Both satellites are fairly circular and symmetric. The kinematics and optical properties of the satellites will be discussed in a later section.

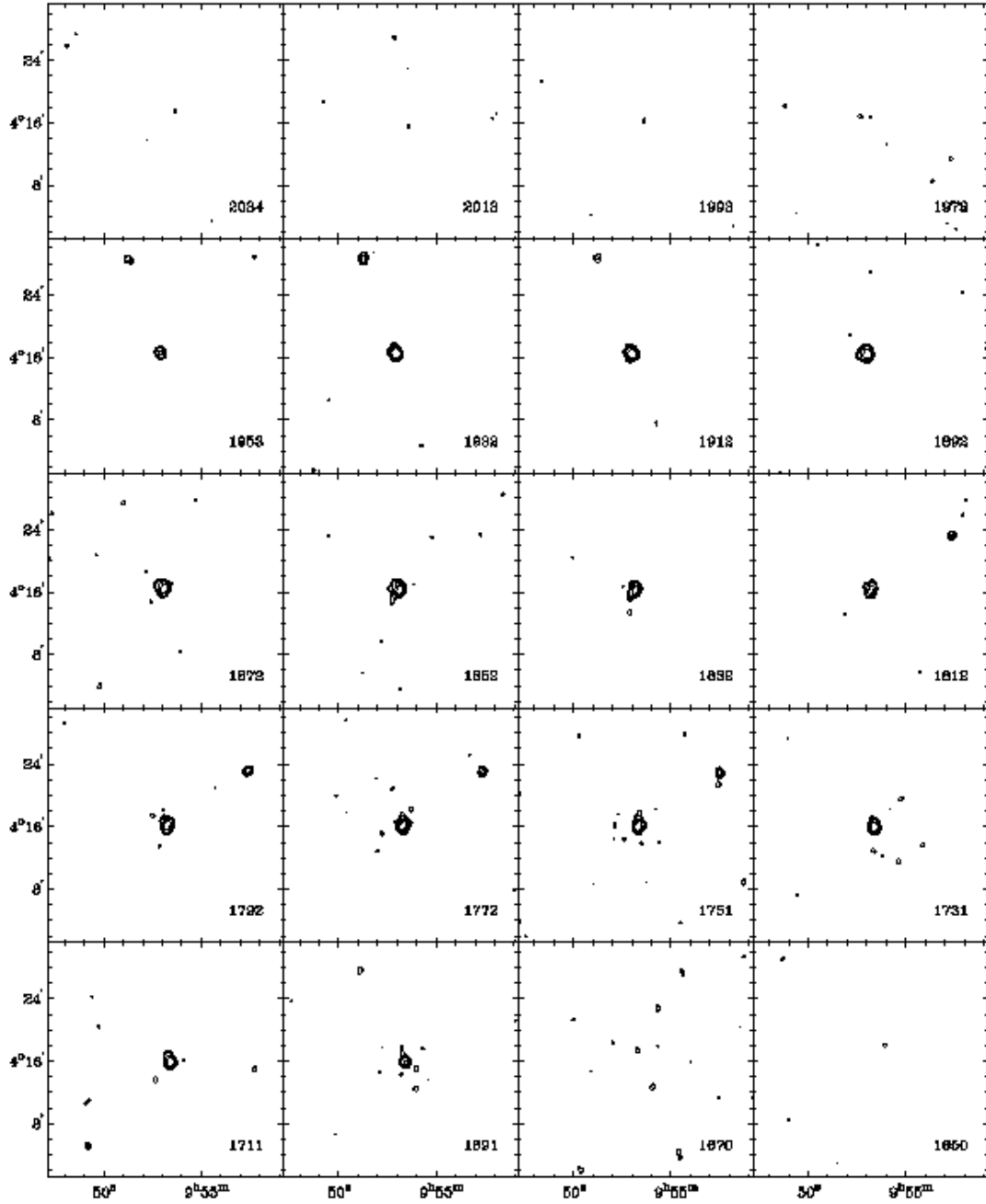


Figure 6-1. Individual, naturally weighted, CLEANed channel images of the low resolution data. Channel velocities are given in the lower left hand corner of each panel in km s^{-1} . The synthesized beam ($52'' \times 42''$) is shown above the velocity information in the upper right hand panel. Contours are at 3 ($8.1 \times 10^{18} \text{ cm}^{-2}$), 5, 10, and 25σ flux density levels.

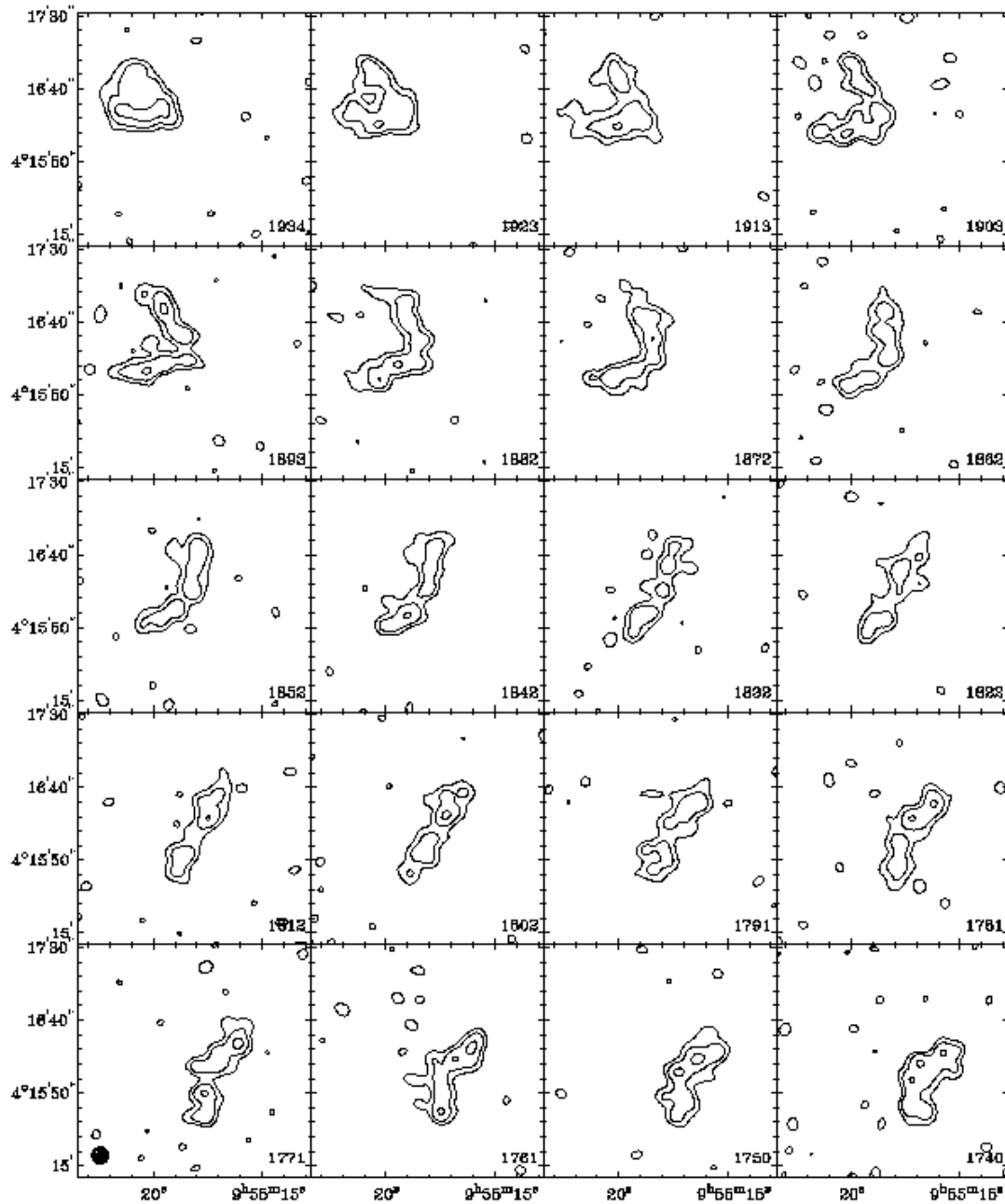


Figure 6-2. Individual, naturally weighted, CLEANed channel images of the high resolution data. Channel velocities are given in the lower left hand corner of the each panel in km s^{-1} . The synthesized beam ($22'' \times 16''$) is shown at the bottom right of the lower left hand channel map. Contours are at the 3 ($3.8 \times 10^{19} \text{ cm}^{-2}$), 6, and 10σ flux density levels.

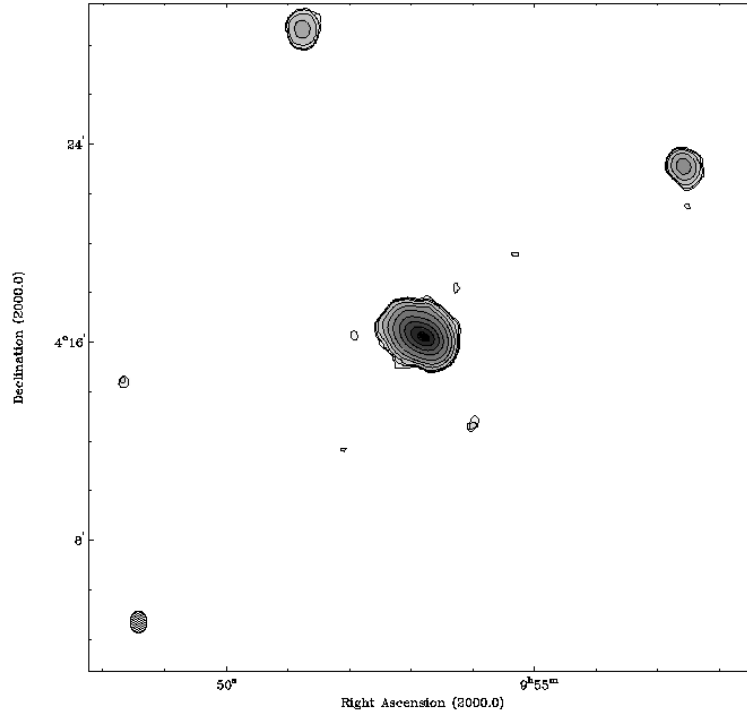


Figure 6-3. Grayscale with contours of the total HI surface density from the low resolution data set. The peak flux corresponds to a column density of $1.53 \times 10^{21} \text{ cm}^{-2}$. Contours are at 1 (the 2σ flux level), 2, 3, 5, 10, 20, 40, 60, 80, and 95% of the peak flux. The synthesized beam ($52'' \times 42''$) is shown at the bottom left.

High Resolution Neutral Hydrogen Morphology

Figure 6-4 presents the high resolution total HI surface density map. Figure 6-5 shows this map overlaid on a DSS optical R-band image of the galaxy. The extent of the gas, about $2' \times 1'$ in diameter, down to the level of $1.36 \times 10^{19} \text{ cm}^{-2}$ is slightly larger than the optical galaxy. The area of highest emission corresponds to the center of the bar region, and has a column density of $2.36 \times 10^{21} \text{ cm}^{-2}$. This is typical of late type galaxies, and probably indicates that the bar in NGC 3055 is young (Hunter & Gottesman 1996; Laine & Gottesman 1998). There has not been time for the bar to sweep the gas into the inner regions of the galaxy.

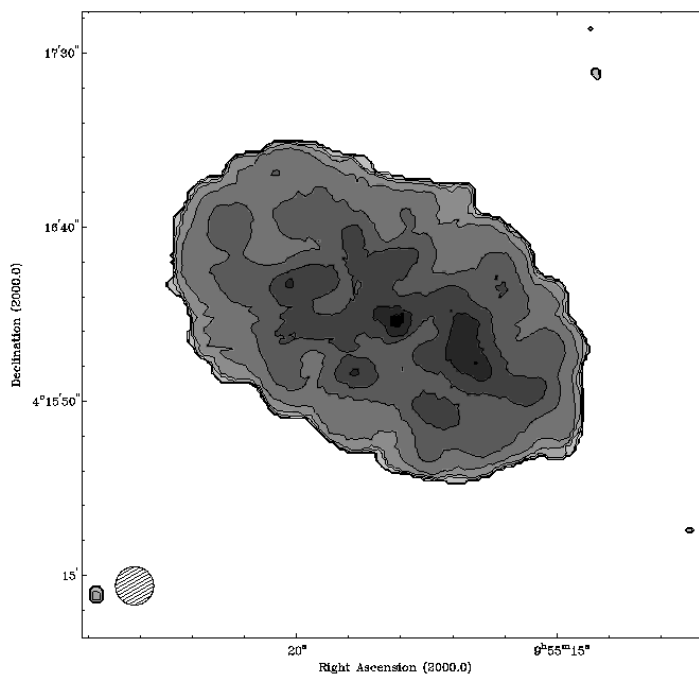


Figure 6-4. Grayscale and contours of the total HI surface density from the high resolution data set. The peak flux corresponds to $2.36 \times 10^{21} \text{ cm}^{-2}$. Contours are at 5 (the 2σ flux level), 10, 15, 20, 40, 60, 80, and 95% of the peak flux. The synthesized beam ($22'' \times 16''$) is shown at the bottom left.

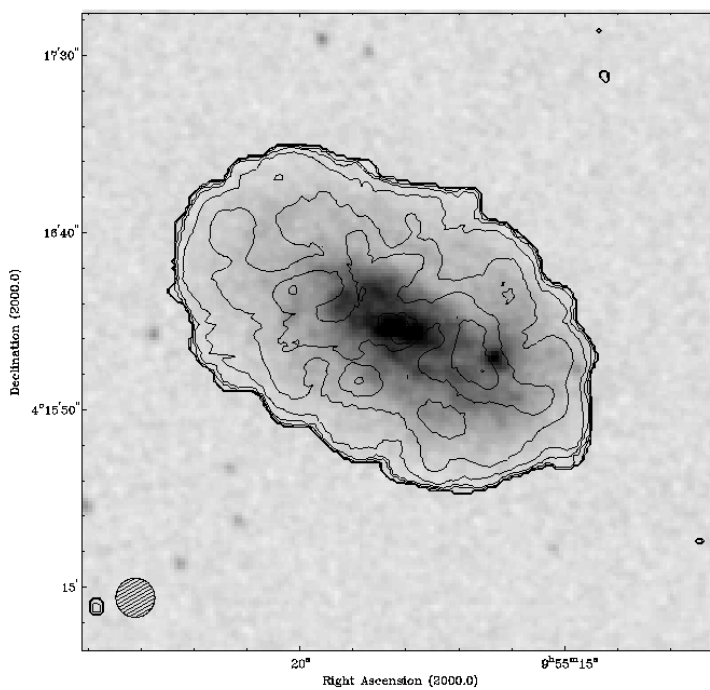


Figure 6-5. Contours of the high resolution data set overlaid on a DSS image of NGC 3055. The peak flux and contours are the same as in Figure 6-4. The synthesized beam is shown at the bottom left.

In other galaxies, star forming regions were found to be associated with HI column densities higher than $1.5 \times 10^{21} \text{ cm}^{-2}$ (Moore & Gottesman 1998). In NGC 3055, we do not see this strong correlation. The highest column density is associated with the center of the bar, and although optically the brightest feature in the galaxy, our color maps show this region to be red. There is a large region of elevated HI column density near the bright HII region in the west of the galaxy. However, the HI peak lies some 10" (1 kpc) to the east of the HII region. This whole area shows up as blue in our color map, so we conclude that the HI is associated with star formation, but processes such as stellar winds and conversion to H_2 must have removed HI from the optical center of the HII region. Higher resolution HI and optical observations will be needed to examine these processes. No other HI peaks correspond to regions of obvious star formation.

Global Neutral Hydrogen Properties

Figure 6-6 presents the HI spectrum of NGC 3055 made from our low resolution data cube. The spectrum is fairly symmetric and follows a double horned pattern. There is a dip in the flux on the red side of the galaxy, but we were not able to determine any unusual features in the corresponding channel map.

We calculate the total HI flux of NGC 3055 to be $11.2 \pm 0.9 \text{ Jy km s}^{-1}$, which corresponds to an HI mass of $1.45 \pm 0.12 \times 10^9 M_{\odot}$. This flux value is similar to published single dish measurements of the mass for this galaxy, such as in the RC3 (de Vaucouleurs et al. 1991).

Figure 6-7 is the radial HI profile from both the high and low resolution data set. This galaxy shows a similar profile to other late type galaxies (Moore & Gottesman 1998). The total HI radius for NGC 3055 is about 2', making it smaller than the other

galaxies in this sample. We find that the HI emission cuts off at below the $1 \times 10^{20} \text{ cm}^{-2}$ level in accordance with the predictions of Maloney (1993). From our spectrum of NGC 3055, we calculate a 3σ HI flux level of 0.009 Jy. This corresponds to a conservative minimum mass detection level of $4.3 \times 10^7 M_{\odot}$ for an isolated HI cloud, assuming that it appears in 3 continuous channels.

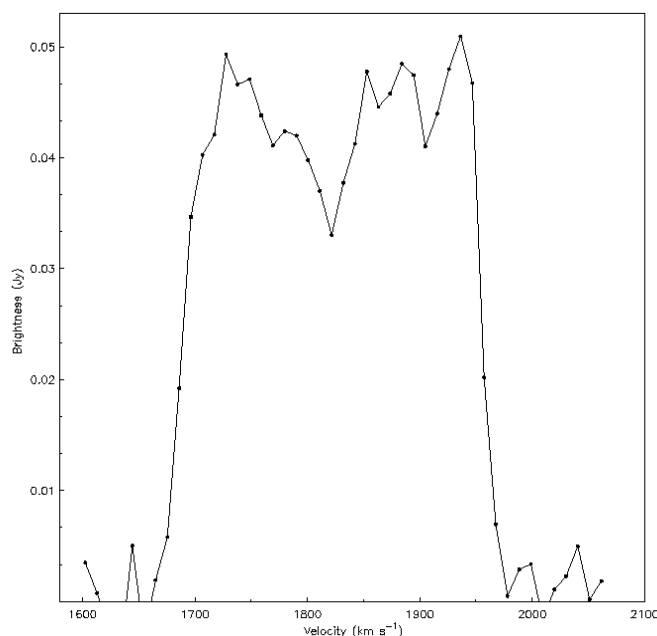


Figure 6-6. The HI flux density versus velocity for the low resolution data set. The velocity resolution here is 10 km s^{-1} . The spectrum is largely symmetric.

Neutral Hydrogen Kinematics

Figure 6-8 shows the HI velocity field of NGC 3055 created with the low resolution data set. Figure 6-9 shows the HI velocity field for NGC 3055 constructed with the high resolution data set. Figure 6-10 shows this same velocity field overlaid on an optical R-band image of the galaxy. The high resolution velocity field shows a largely symmetric pattern. The only global asymmetry is that the velocity field closes on the west side of the galaxy but does not on the east. This reflects the slight asymmetry in the total HI distribution of the low resolution data (Figure 6-6). Otherwise, the only other

notable feature is that there are kinks in the iso-velocity curves that seem to be associated with the faint optical arm on the north side of the galaxy. The velocity field does not seem to be affected on a large scale by either the bar or the large HII region on the west side of the galaxy. However, our resolution is not high enough to probe the small scale effects of these features. These velocity field images do not seem to indicate significant warping in the disk.

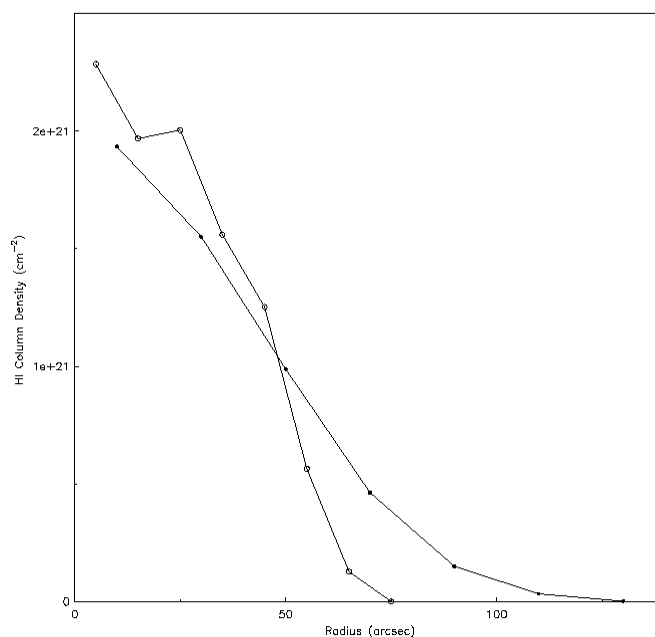


Figure 6-7. The HI radial density profiles from the low resolution data set (closed circles) and the high resolution data set (open circles)

Position-Velocity Plots

Figure 6-11 shows Position-Velocity (P-V) plots parallel to the major axis from the high resolution data set. The lowest contour is at the 3σ level ($1.2 \text{ mJy beam}^{-1}$) to emphasize possible gas at non-circular velocities. We find some evidence of "bearding" and gas at non-circular velocities, most notably the finger of gas stretching upwards from the lower left the galaxy in the bottom panels of figure 6-11. This feature could represent some type of disk warp, because of its similarity to structures seen in NGC 1784.

However, the amount of gas involved in this feature is substantially less. We calculate a mass for this region to be on the order of a couple $10^7 M_{\odot}$, using the 3σ flux value, an angular size corresponding to about 2 beam widths, and a velocity spread of 50 km s^{-1} . This mass value is large enough to consider the possibility of the existence of tidal debris or a small companion located close to NGC 3055. An examination of the channel maps of corresponding to these velocities ($\sim 1880 \text{ km s}^{-1}$) shows that the gas distribution is slightly more elongated than in channel map corresponding to the other side of the galaxy ($\sim 1780 \text{ km s}^{-1}$). There does not appear to be any separate structures of HI gas in these channel maps. We conclude then, that the tongues present in the P-V plots of Figure 6-11 are not the result of tidal debris, but of a small warp in the outer disk of NGC 3055.

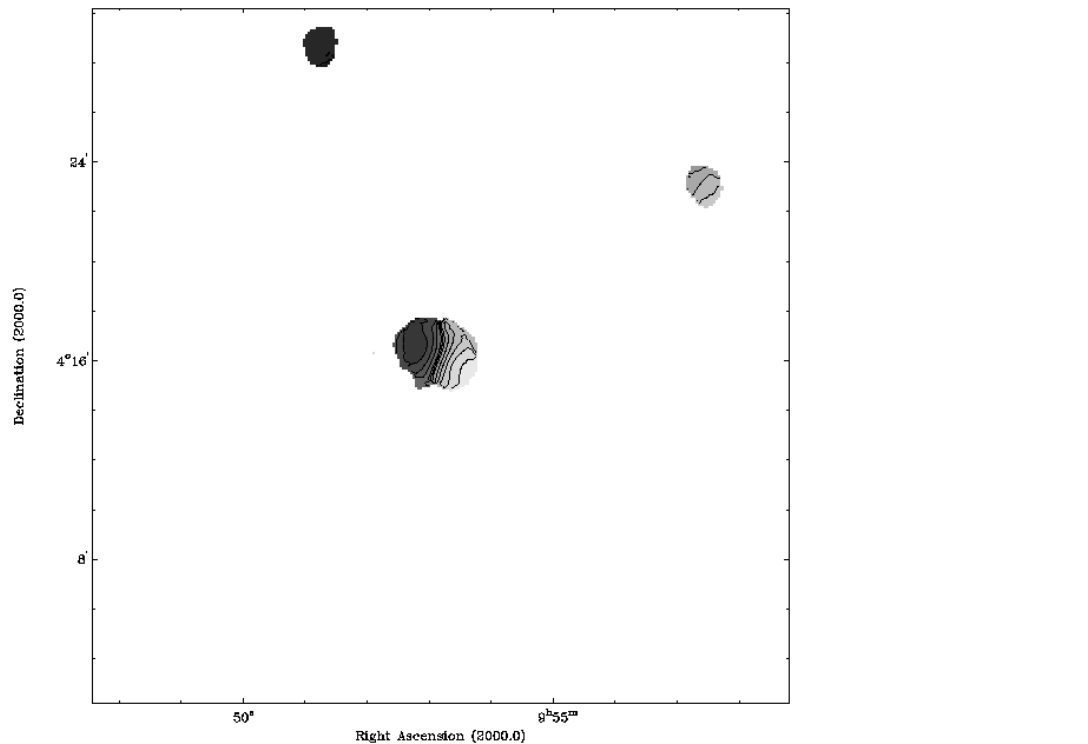


Figure 6-8. Intensity-weighted radial velocity contours of the low resolution data. Contours are separated by 20 km s^{-1} . Motion toward the observer (the western side of the galaxy) is displayed with black contours and lighter grayscales. The central velocity is 1832 km s^{-1} .

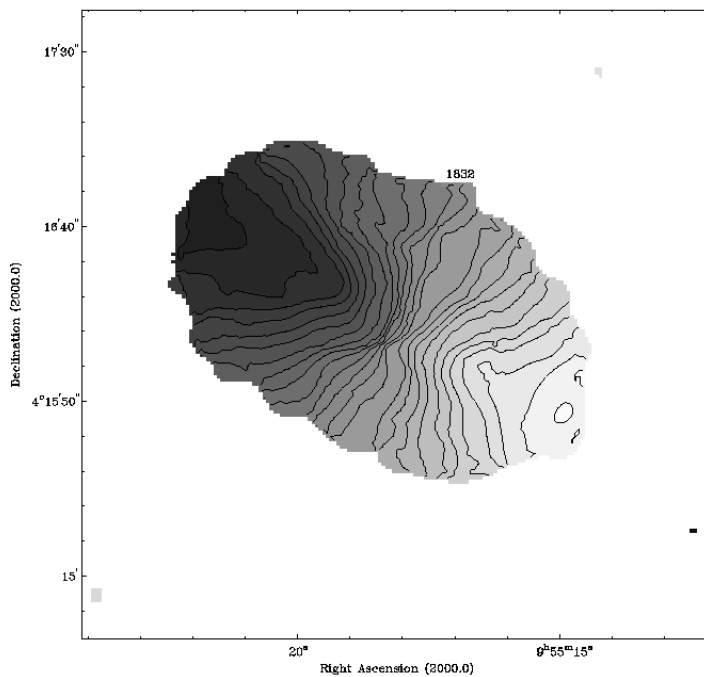


Figure 6-9. Intensity-weighted radial velocity contours of the high resolution data set. Contours are separated by 10 km s^{-1} . Darker grayscales (the eastern side of the galaxy) correspond to motion away from the observer.

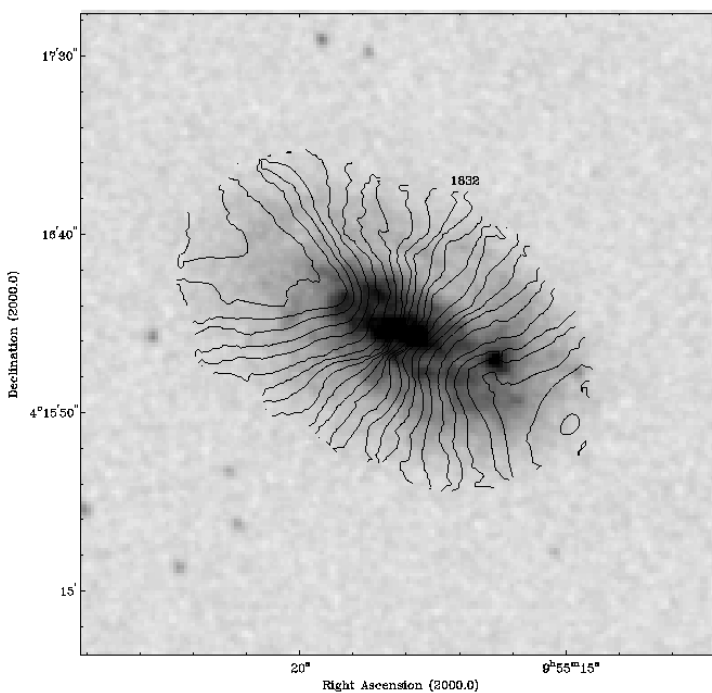


Figure 6-10. Intensity-weighted radial velocity contours of the high resolution data set overlaid on an optical DSS image of the galaxy. Contours are the same as in Figure 6-9.

The P-V plots shown in Figure 6-11 are somewhat asymmetric even beyond the feature described above. The column density of HI is much higher on the eastern, higher velocity side of the galaxy. Also, the velocity trend of the gas on the eastern side of the galaxy becomes flat after 30", while the gas on the western side of the galaxy never quite achieves this trend. This is certainly associated with the overall asymmetry seen in the HI intensity map (Figure 6-4), and is likely associated with the warp mentioned above. These features may be related to the two companion galaxies, and this possibility will be explored in a later section.

Figure 6-12 shows P-V plots of the high resolution data made parallel to the minor axis of NGC 3055. These images are fairly regular, but broad. The plot made along the minor axis may have a slight trend upwards and to the right, indicating a possible radial expansion, but our resolution and sensitivity are not good enough to explore this further at this time. There do not appear to be any features indicative of tidal debris or companions. The global asymmetry mentioned above is not as apparent in these images since the asymmetry seems to be oriented along the major axis.

Rotation Curves and Model Disks

In order to make rotation curves and model disks of NGC 3055, we used the GIPSY task 'reswri' to fit tilted rings to the velocity field. We used our high resolution data set to create our rotation curve. We fit rotational velocities at radii ranging from 10" to 80" in 10" wide annuli. We were able to fit our curve close to the center of the galaxy because of the presence of gas in the bar of NGC 3055. We held the position of the kinematic center of the galaxy and the systemic velocity of the galaxy as fixed parameters, and let the rotational velocity, position angle, and inclination be set by the fit. We took the average of both the receding and approaching sides of the galaxy for our

plot. This was largely due to the small signal present from the gas at the outer edge of the galaxy at high resolution. We plot the rotation velocity versus radius in Figure 6-13, position angle versus radius in Figure 6-14, and inclination versus radius in Figure 6-15.

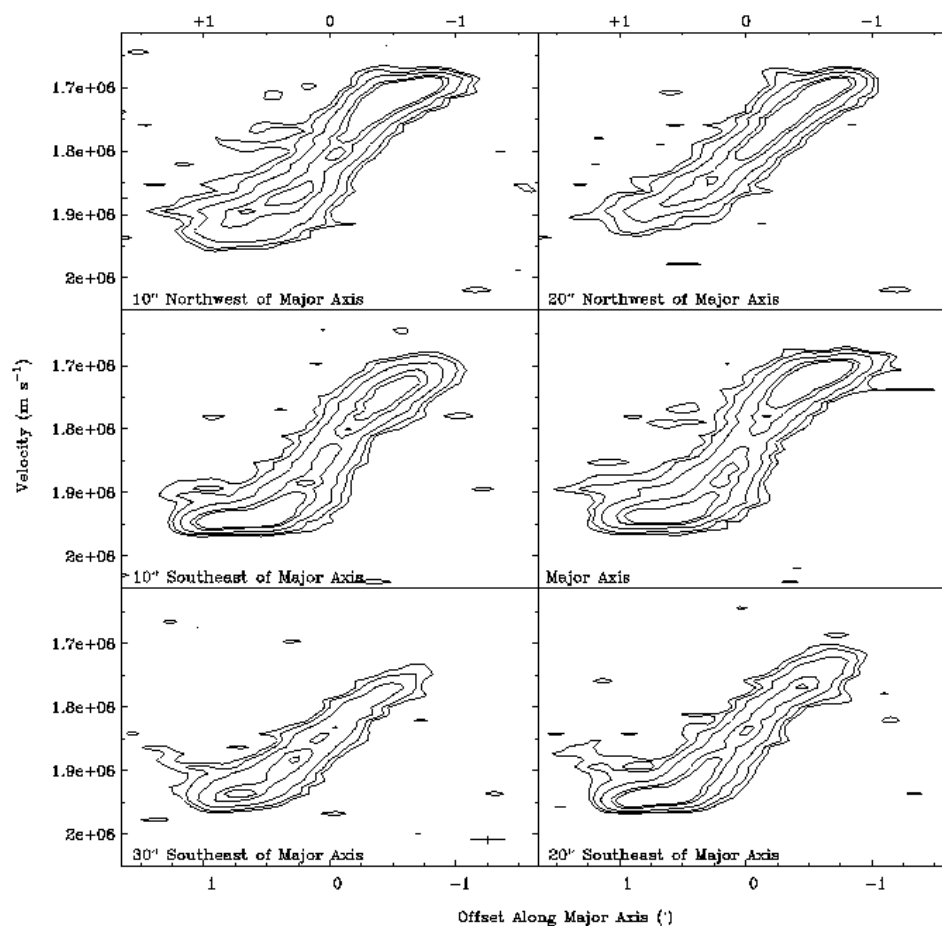


Figure 6-11. A set of P-V slices parallel to and along the major axis of NGC 3055. The contours are at 2, 3, 5, 10, and 25 σ . The central velocity of the system is at $1.832 \times 10^6 \text{ m s}^{-1}$.

Figure 6-13 shows that NGC 3055 has a flat or falling curve beyond a radius of 70'' (7 kpc). The last point has a large error bar because of the limited flux at this radius. Elmegreen & Elmegreen (1990) found that flocculent galaxies have flat or rising rotation curves consistent with these galaxies having a relatively less massive disk compared to the halo. Because of the lack of flux at the outer point in NGC 3055, it is impossible to comment on the extended dark matter structure of this galaxy. The quickness that HI

column densities drop off in the outer reaches of the galaxy does make NGC 3055 different from others in this sample. Deeper, medium resolution images of this galaxy will allow us to fix the rotation curve.

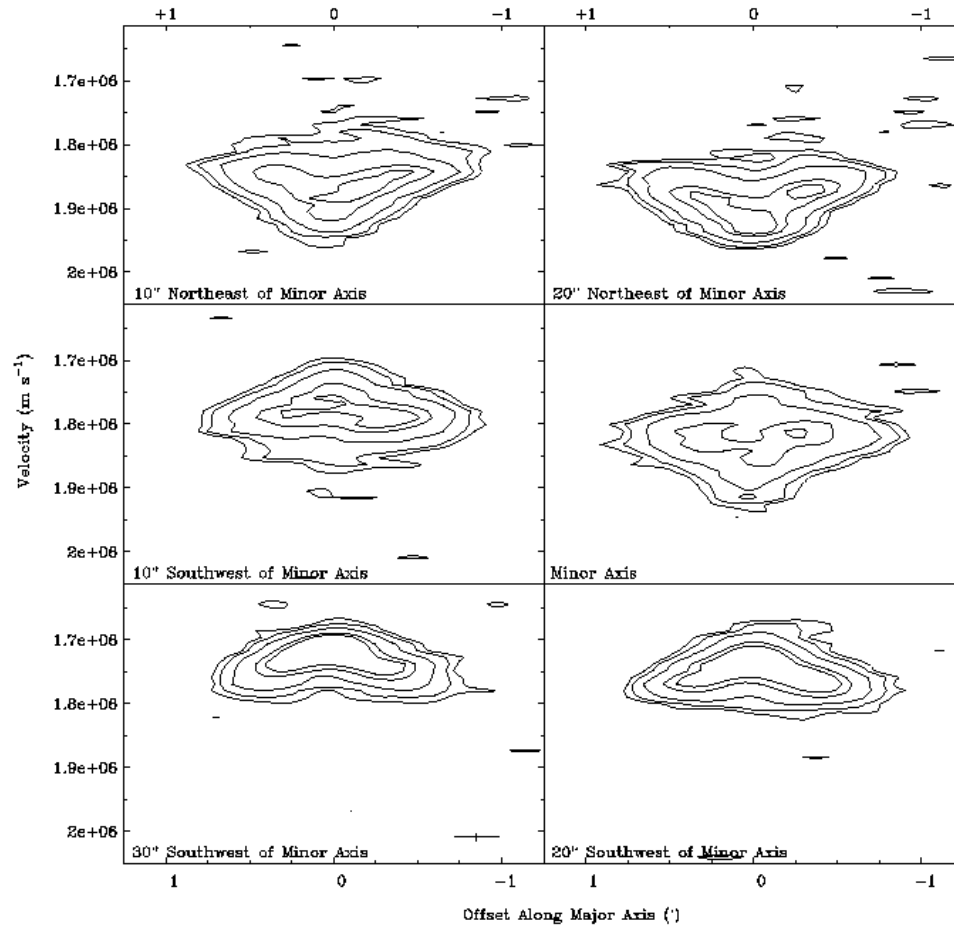


Figure 6-12. A set of P-V slices parallel to and along the minor axis of NGC 3055. The contours are at 2, 3, 5, 10, and 20 σ . The central velocity of the system is at $1.832 \times 10^6 \text{ m s}^{-1}$.

Using the final data point of the rotation curve, we calculated a value for the total mass of NGC 1784 interior to 80". Using a Keplerian, $M = V^2 R G^{-1}$, to model the disk and halo, where $R = 80''$ (9 kpc) and $V(9 \text{ kpc}) = 150 \text{ km s}^{-1}$, we find $M(R) 4.77 \pm 0.51 \times 10^{10} M_{\odot}$. Comparing this with the HI mass calculated above, we find a value for the ratio $M_{\text{HI}} / M(R)$ of 3% for NGC 3055.

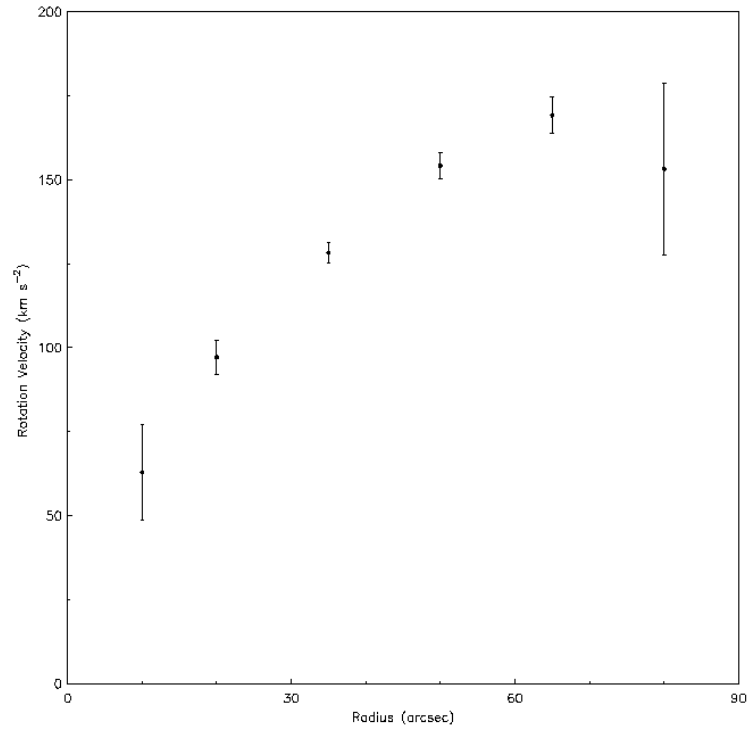


Figure 6-13. Rotation curve of NGC 3055 from the high resolution data set. Plotted data is the average of both sides of the galaxy.

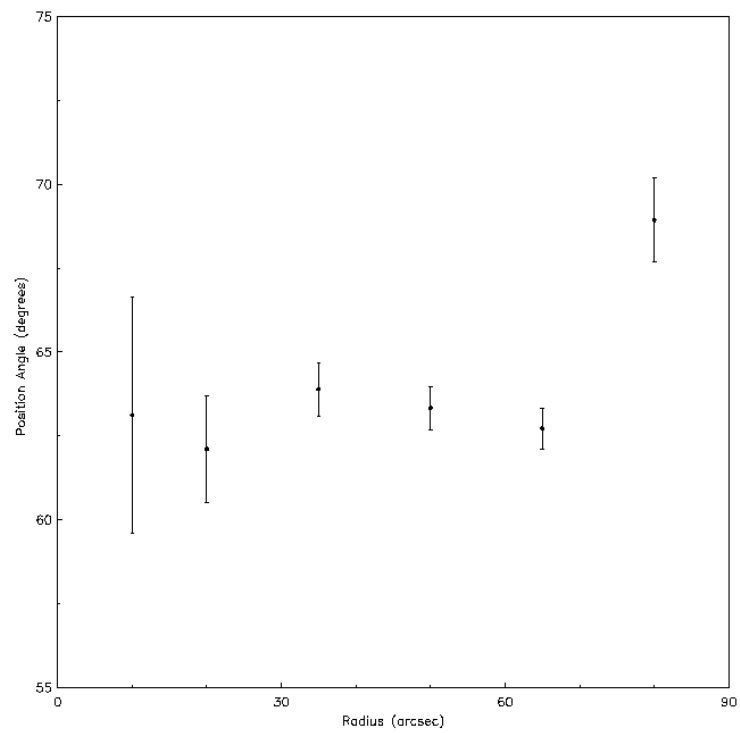


Figure 6-14. Kinematic position angle of NGC 3055 as a function of radius

The position angle curve, shown in Figure 6-14, shows that NGC 3055 has a relatively constant position angle through much of its inner, optical disk. It is only at the very extremes of our measurements that we find deviation from this trend. The large deviation for the outer most position angle point could be an artifact of there being little flux at this radius. However, this position angle change does occur at a similar radii to the warping effects (tongues) shown in the P-V plots of the previous section. The trend of the position angle in Figure 6-14 is evidence of a twist in the disk of NGC 3055 at large radii.

Twisting is apparent in the inclination curve of Figure 6-15, but this time in the inner regions of the galaxy. The inclination changes by nearly 20° over the inner 30" of the galaxy. The presence of the bar is the most likely explanation for this trend. We do not see a deviation in inclination at large radii as with position angle, indicating that the warp present in NGC 3055 is more of a twist and contained within the plane of the disk.

We used the values of rotational velocity, position angle, and inclination to construct a model disk for NGC 3055 with the GIPSY task 'velfi'. The model disk is shown in Figure 6-16. We then subtracted this model field from our high resolution velocity field (Figure 6-9), to create a map of residual velocities. The residual velocity field is shown in Figure 6-17. The residual field is complicated and largely shows a one arm spiral ($m=2$) pattern, although this is not as pronounced as in other galaxies such as NGC 1784. There is no indication of corotation as in Canzian (1993). However this is not unexpected given the small size of the galaxy and our comparatively low resolution.

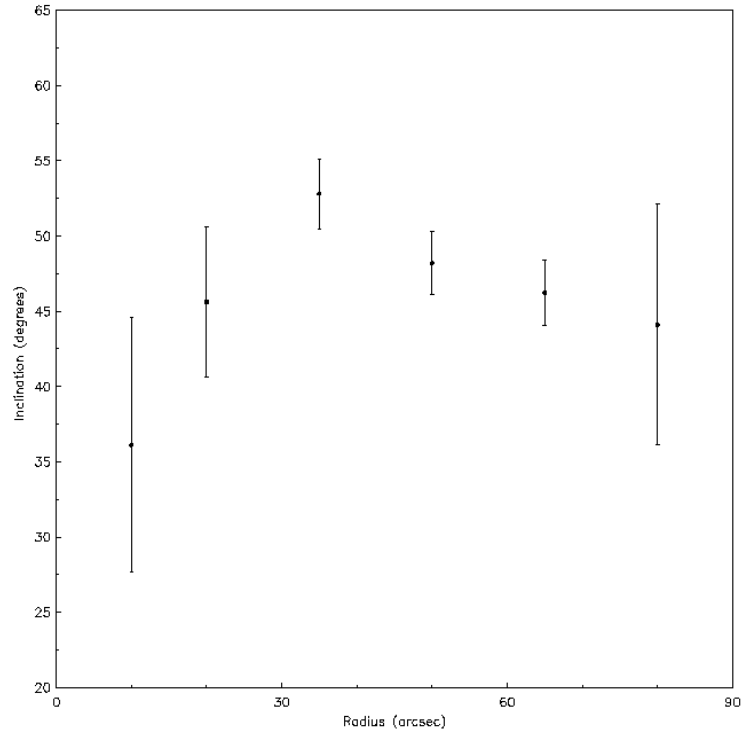


Figure 6-15. Inclination angle of NGC 3055 as a function of radius

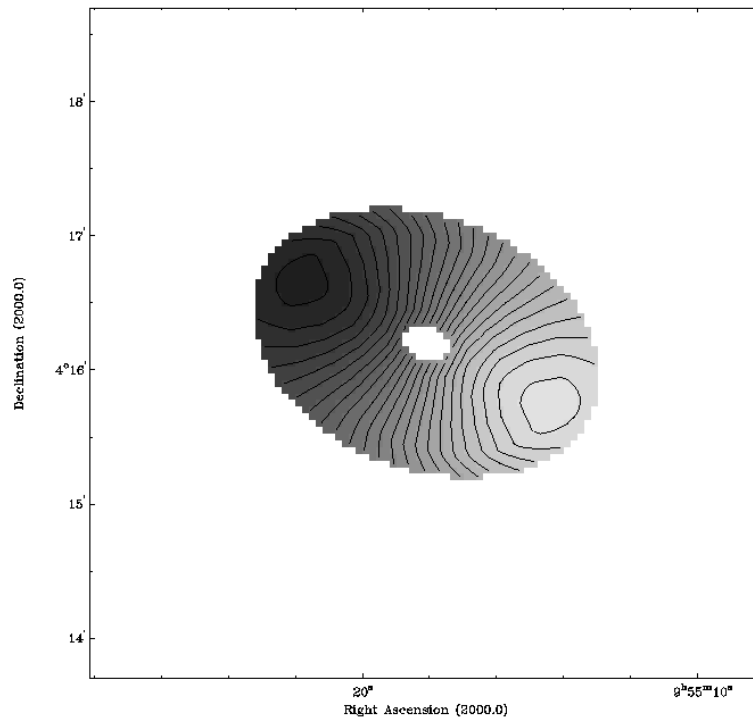


Figure 6-16. Model velocity field constructed from kinematical data in Figures 6-13, 6-14, and 6-15. Light grayscales represent approaching velocities.

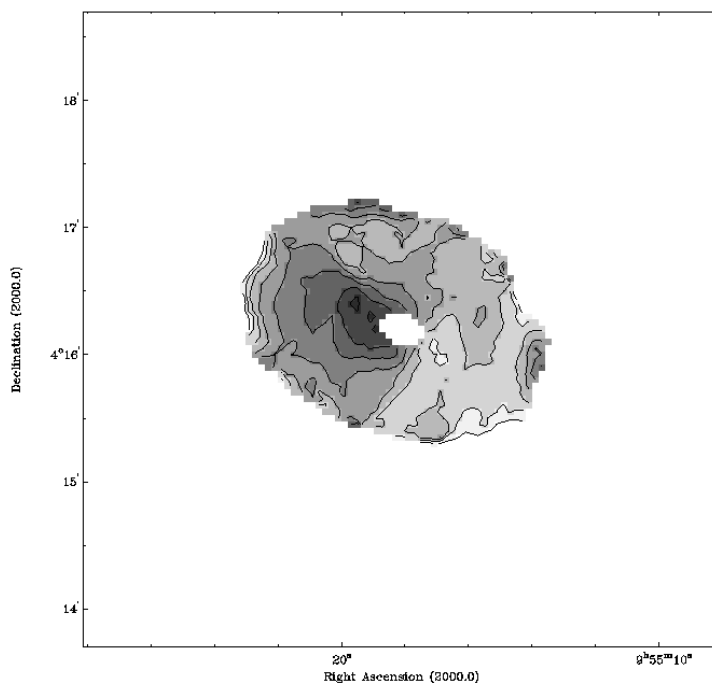


Figure 6-17. Residual velocity field made from model in A. Light grayscales represent approaching residuals (contours separated by 5 km s^{-1}).

Neutral Hydrogen Companions

Figure 6-3, the low resolution total HI intensity map, shows that NGC 3055 is accompanied by two satellite systems. Figure 6-8, the low resolution HI velocity field shows that the velocities of these two satellites are similar to that of NGC 3055, itself. The "A" satellite, north of NGC 3055, reflects the velocities of the eastern half of the galaxy, and the "B" satellite, northwest of NGC 3055, reflects the velocities of the west side of the galaxy.

Even though both companions are of about the same angular size ($R_{\text{HI}} \sim 1'$ or 7 kpc), the "A" satellite is the less massive of the two. Figure 6-18 shows an HI spectrum of the satellite. The spectrum is weak and narrow, only having appreciable signal in 3 channels (a velocity width of 30 km s^{-1}). We calculate an HI mass of $6 \times 10^7 M_{\odot}$, and using a V^2R calculation, a total mass of about $10^9 M_{\odot}$.

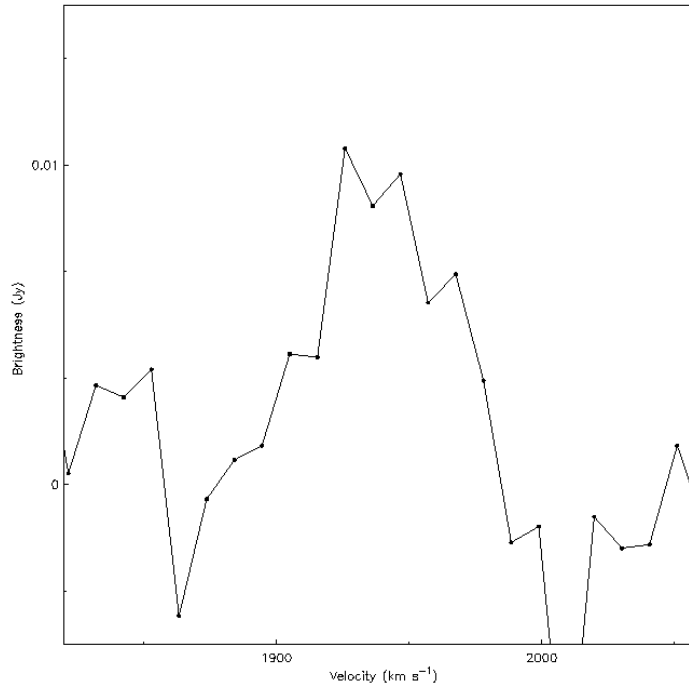


Figure 6-18. The HI flux density versus velocity for the "A" HI satellite. The velocity resolution is 10 km s^{-1} .

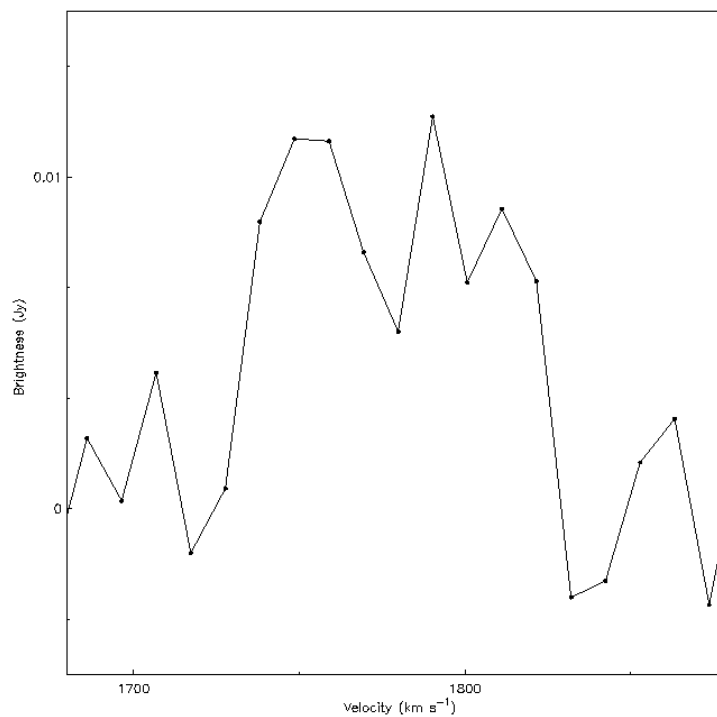


Figure 6-19. The HI flux density versus velocity for the "B" satellite. The velocity resolution is 10 km s^{-1} .

The "B" satellite has a broader HI spectrum (Figure 6-19), covering about 80 km s^{-1} . The iso-velocity curves for satellite "B" in Figure 6-8 are well ordered and are in a similar orientation to the iso-velocity curves in NGC 3055. We calculate an HI mass of $10^8 M_{\odot}$ and a total mass of $10^{10} M_{\odot}$.

We searched DSS images (the field of view for our IAC80 images was too small) in the location of the two satellites to determine if they had optical counterparts. Figures 6-20 and 6-21 show that these two HI companions do indeed have optical emission. The HI here is plotted in contours on top of the DSS image. Satellite "A" even though having a lower gas and total mass has a significantly brighter optical counterpart. It seems to have a dense center and an elongated outer structure. Satellite "B" has a wispy, ellipsoidal optical counterpart. Further deep, multiple color observations of these satellites is warranted to determine their stellar ages with respect to NGC 3055.

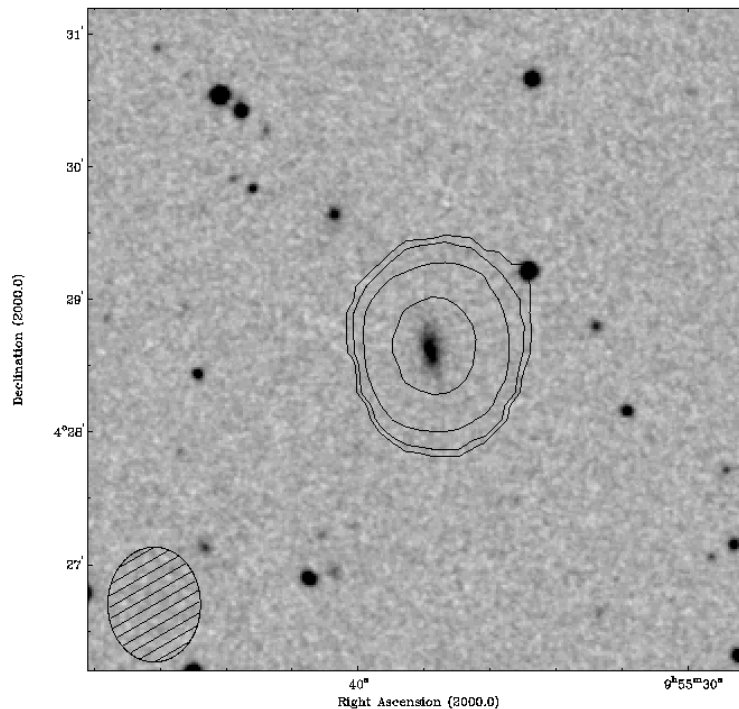


Figure 6-20. Contours of HI surface density overlaid on an optical DSS image of the "A" satellite. The contours are the same as in Figure 6-3.

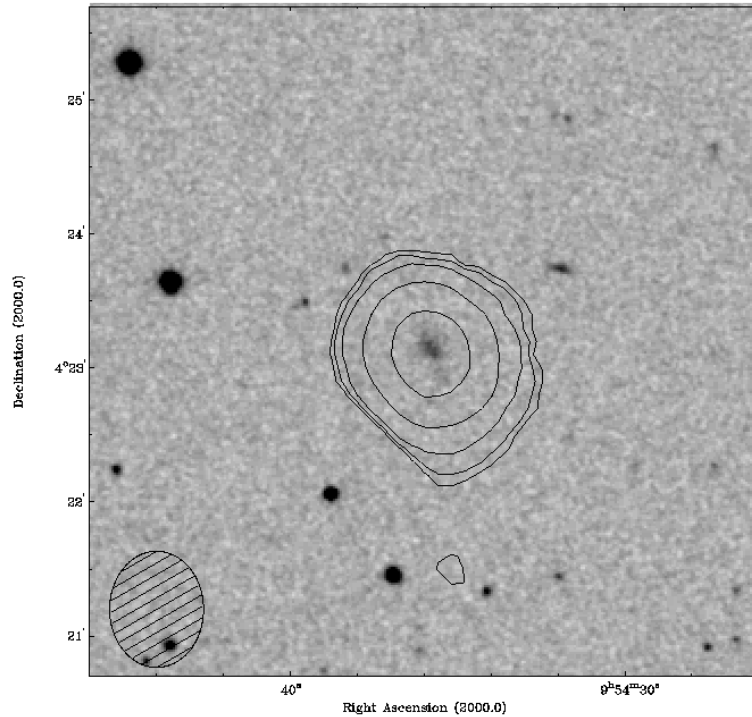


Figure 6-21. Contours of HI surface density overlaid on an optical DSS image of the "B" satellite. The contours are the same as in Figure 6-3.

In the case of NGC 3055, with the satellites' large separations (90 kpc), it is unlikely that they are having a particularly strong effect on the main galaxy itself. Other galaxies showing disturbances caused by small dwarf galaxies (NGC 1784, 3359, and 7749) either have the dwarf very close in, or have already cannibalized the dwarf. We calculate a tidal disruption radius for NGC 3055 of 13 kpc, well inside the presumed orbits of these satellites. Further, the evidence points to the situation that these satellites are not bound to NGC 3055. A quick comparison of the gravitational potential energy due to NGC 3055 at a radius of 90 kpc to the kinetic energy of the satellites relative to NGC 3055 ($v \sim 50 \text{ km s}^{-1}$), shows that the kinetic energy of the satellites is greater by a factor of 10^4 . These satellites may have passed close to NGC 3055 once in the past, but are unlikely to do so again.

Even if we accept that the satellites are bound to NGC 3055, we calculate, using Eq. 7-27 from Binney & Tremaine (1987) a time of at least 5×10^9 years for the orbits of these satellites to decay. The time scale is a lower limit, because the equation was derived for satellite galaxies that exist in the extended halo of a main galaxy. It is unlikely that NGC 3055 possess a significant halo at 90 kpc. The only circumstance in which these satellites would feel appreciable friction would be if they were on strongly plunging orbits. Certainly, this is possible, but in either case it is unlikely that these companions will be consumed by NGC 3055 within a Hubble Time.

The slight asymmetry in NGC 3055's HI distribution and velocity field could be due to a close pass of one of the satellites during the past few Gyrs. As previously mentioned, even a small satellite (5% of the mass of the main galaxy) can produce significant effects on a large galaxy if in a close prograde orbit. We do not observe any HI trails connecting the satellites to the main galaxy, so it is not obvious if this is the case. We also can not rule out either a small or somewhat old merger of a third satellite as the cause of GNC 3055's dysmorphic features. It is also possible that NGC 3055's asymmetry is due to internal processes to the disk of the galaxy.

Summary

NGC 3055 is a relatively small but regular disk galaxy. It possesses an asymmetry in its HI distribution, but no other highly unusual features. NGC 3055 most likely possesses a warp in its disk. We discovered two HI companions in the NGC 3055 companions. These companions have regular appearing HI distributions and show optical, stellar, emission. One of these satellites appears to be large enough to be rotationally supported. The other appears to be supported by turbulence. It is unclear whether these satellites are the cause of NGC 3055's asymmetric HI distribution. They

do possess masses similar to galaxies in other systems which have resulted in altered morphologies and kinematics. However, their current projected distance from NGC 3055 of over 90 kpc, seems to indicate that right now their effect is very weak. We can not rule out a previous close passage of one of these satellites to NGC 3055.

CHAPTER 7
NEUTRAL HYDROGEN OBSERVATIONS OF NGC 3930

NGC 3930 is a rather non-descript optical galaxy that has not been previously studied in great detail by other authors. NGC 3930 has an optical diameter of 3.2' (12 kpc), giving it a large angular size relative to the sample, but a small physical size (Haynes et al. 1998). It is the closest of the galaxies in the sample, having a recessional velocity of 919 km s^{-1} (13 Mpc, where $H_0=70 \text{ km s}^{-1} \text{ Mpc}^{-1}$). Elmegreen & Elmegreen (1982) give this galaxy an arm classification of 4, because of its one armed structure. The southern optical arm appears to be longer, brighter, and associated with more star formation than its northern counterpart. Haynes et al. (1998) in single dish observations found NGC 3930 to be not particularly bright in HI, have a fairly narrow spectrum, and to have a somewhat asymmetric HI profile (Table 1-8).

Observations

Radio observations of NGC 3930 were obtained at the Very Large Array in May of 2003 using the D configuration. The spectrometer was composed of 64 channels with a 10.5 km s^{-1} velocity resolution. The total band width was 3.125 MHz (640 km s^{-1}), and the central heliocentric velocity was 919 km s^{-1} . The observing parameters for the observations are summarized in Table 7-1.

Table 7-1. Parameters of VLA HI observations of NGC 3930

Configuration	D
Number of antennae	27
$V_{\text{sys}} \text{ (km s}^{-1}\text{)}$	919
Phase calibrator	1150+242
Flux calibrator	1331+305
Time on source	3.7

The D configuration data set was edited, calibrated and continuum subtracted using the typical procedures of the Astronomical Image Processing System (AIPS) package. The data set was then imaged twice using the AIPS task IMAGR to provide us with two image cubes (α , δ , ν) reflecting the maximum range of spatial resolution and sensitivity that our data would allow. We created a low resolution cube by using a natural weighting scheme and a high resolution data cube by imaging the data with a uniform weighting scheme. We CLEANed the data cubes in AIPS down to an rms level of 0.4 and 0.6 mJy beam⁻¹ for the low resolution and high resolution images, respectively. Further details of the statistics for each data cube are presented in Table 7-2. Analysis on the completed and CLEANed image cubes was conducted using the Gronigen Image Processing System (GIPSY) package.

Table 7-2. Characteristics of Naturally Weighted CLEANed Channel Maps

Parameter	Low Resolution	High Resolution
FWHP synthesized beam (")	59" x 58"	37" x 34"
FWHP synthesized beam (kpc)	3.7 x 3.6	2.3 x 2.1
Theoretical rms noise (mJy beam ⁻¹)	0.62	0.62
Observed rms noise (mJy beam ⁻¹)	0.65	0.67
Rms noise (K)	0.20	2.0
Peak temperature (K)	16.5	90.5
Peak S/N	83	45

Neutral Hydrogen Morphology

The channel maps shown in Figures 7-1 and 7-2 were used in moment analyses to obtain global density and temperature weighted radial velocity images of the neutral hydrogen in NGC 3930. Moment maps were constructed with the AIPS task MOMNT. A flux cut off of three times the rms noise level (σ) of the unsmoothed data was used. The low resolution, naturally weighted global distribution of the neutral hydrogen in NGC 3930 is shown in grayscale in Figure 7-3 and overlaid on an optical image of the

galaxy in Figure 7-4. The high resolution, uniformly weighted global distribution of the neutral hydrogen is shown in grayscale in Figure 7-5 and overlaid on an optical image of the galaxy in Figure 7-6. The lowest contours are drawn at the 2σ level.

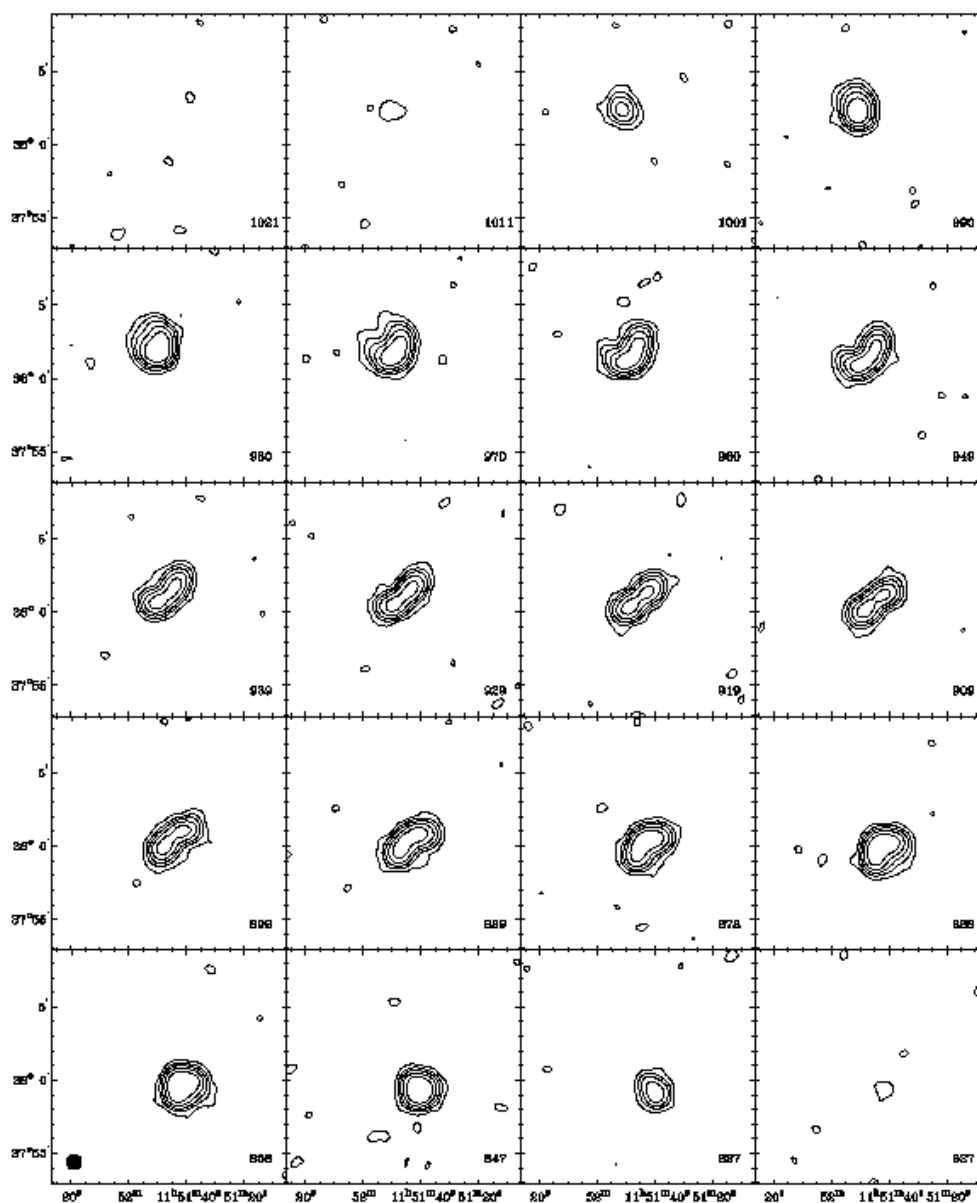


Figure 7-1. Individual, naturally weighted, CLEANed channel images of the low resolution data. Channel velocities are given in the lower left hand corner of each panel in km s^{-1} . The synthesized beam ($59'' \times 58''$) is shown above the velocity information in the upper right hand panel. Contours are at the 3 ($3.7 \times 10^{18} \text{ cm}^{-2}$), 10, 20, 40, and 80σ flux level.

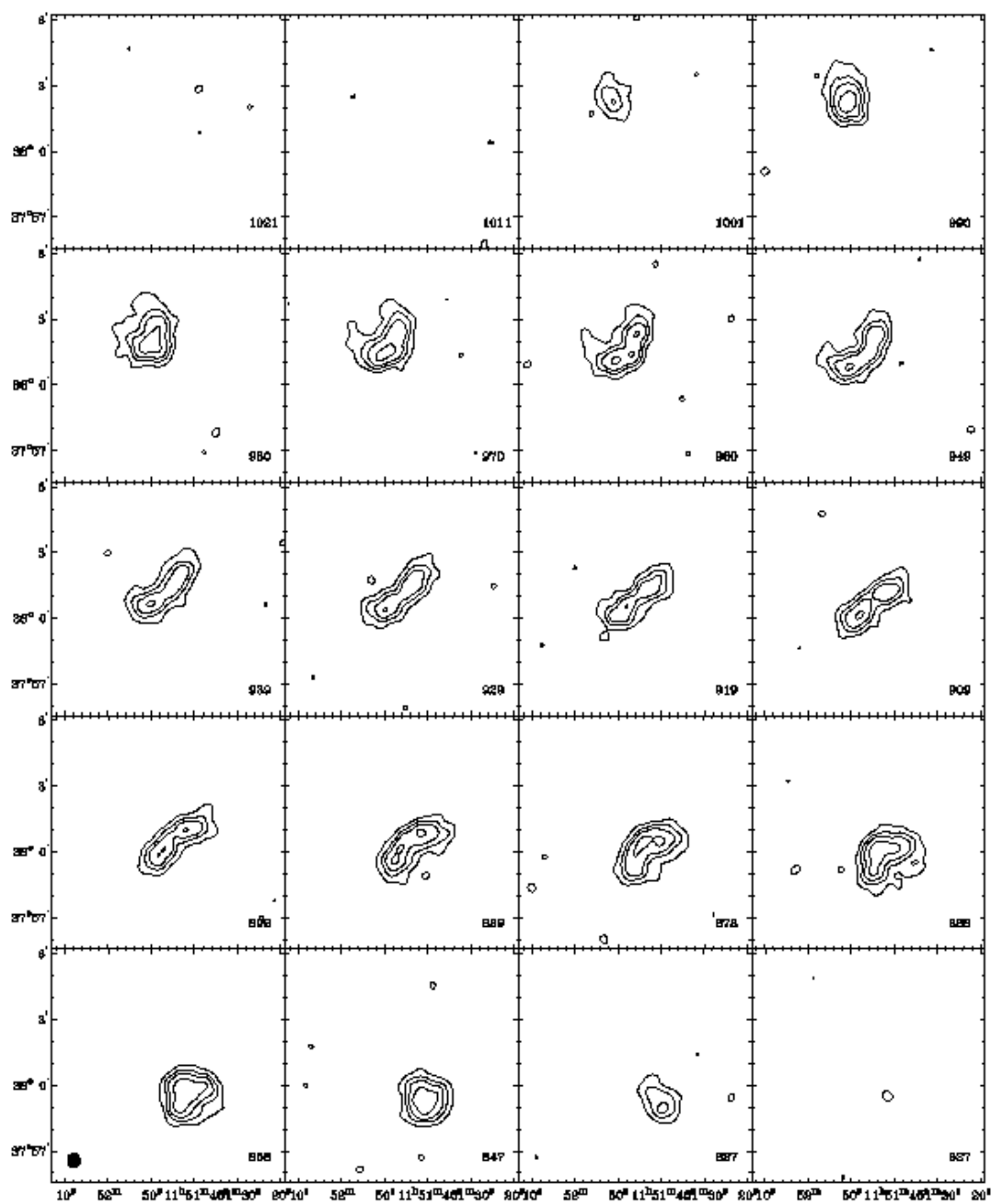


Figure 7-2. Individual, naturally weighted, CLEANed channel images of the high resolution data. Channel velocities are given in the lower left hand corner of each panel in km s^{-1} . The synthesized beam ($37'' \times 34''$) is shown at the bottom right of the lower left hand channel map. Contours are at the 3 ($1.7 \times 10^{19} \text{ cm}^{-2}$), 10, 20, and 40σ flux level, corresponding to $1.5 \times 10^{20} \text{ cm}^{-2}$.

Low Resolution Neutral Hydrogen Morphology

The low resolution channel maps in Figure 7-1 show a regular, well formed galaxy. There do not appear to be any rings, satellites, or gas at forbidden velocities. This regularity is reflected in the global HI distribution shown in Figures 7-2 and 7-3. The outer contours are symmetric and regular. Only in the inner regions do we find an asymmetry, with the peak of the HI emission ($N_{\text{HI}} = 1.08 \times 10^{21} \text{ cm}^{-2}$) lying south of the center of the galaxy. Figure 7-4 shows that the peak corresponds to the stronger, southern spiral arm. We find the HI diameter of the galaxy to be 7' (26 kpc) at the 2σ level, or 2.2 times the optical D_{25} for the galaxy.

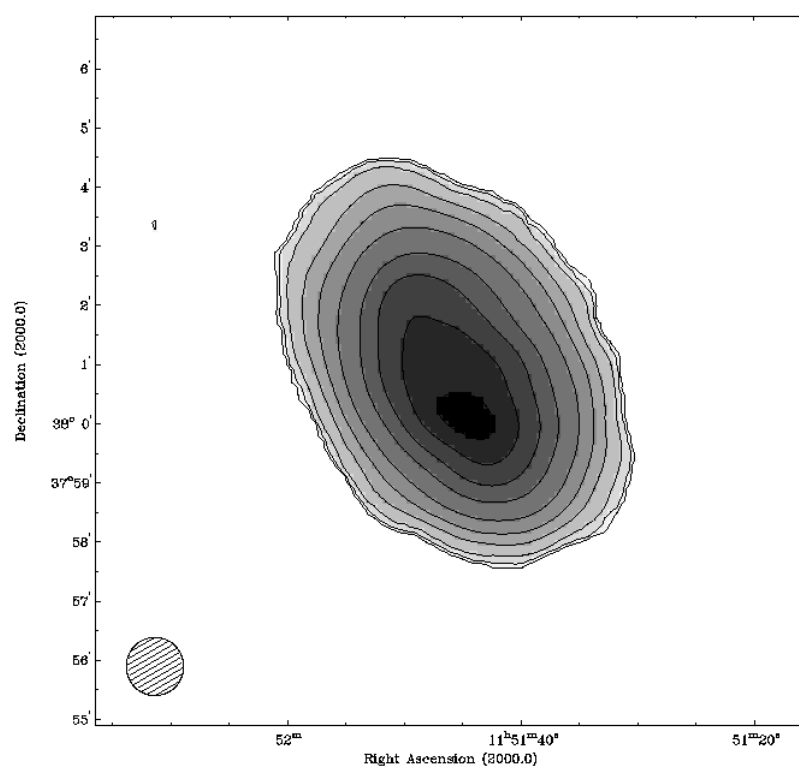


Figure 7-3. Grayscale with contours of the total HI surface density from the low resolution data set. The peak flux corresponds to a column density of $1.08 \times 10^{21} \text{ cm}^{-2}$. Contours are at .5 (the 2σ flux level), 1, 2, 3, 5, 10, 20, 40, 60, 80, and 95% of the peak flux. The synthesized beam (59" x 58") is shown at the bottom left.

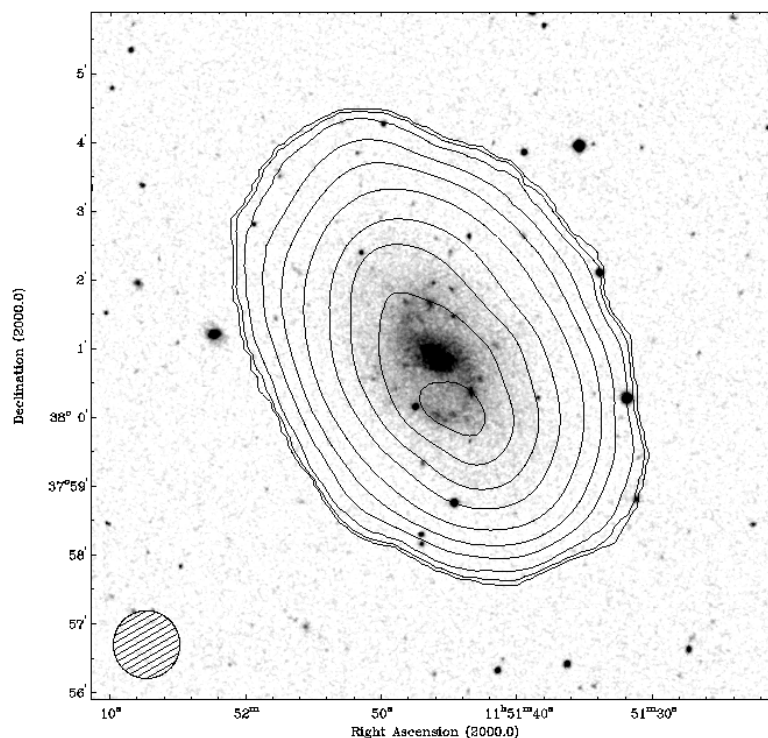


Figure 7-4. Grayscale with contours of the total HI surface density from the low resolution data set. Contours and resolution are the same as in Figure 7-3.

High Resolution Neutral Hydrogen Morphology

The channel maps in Figure 7-2 also show a well ordered galaxy even at higher resolution. The global asymmetry shows up again in Figures 7-5 and 7-6 and the peak of HI emission is more clearly associated with the spiral arm and star forming regions in the south of the galaxy. The peak HI column density region ($N_{\text{HI}} = 5.8 \times 10^{21} \text{ cm}^{-2}$) appears to be located on top of and adjacent to several star forming regions, and has an apparent surface density much higher than we have found in any other galaxy. This could be caused by HI surrounding a dense star forming region that is at the limits of our resolving power. Two other HI peaks circle around the bar region from the west to the north and also seem to be associated with regions of star formation. The HI distribution seems to track loosely the optical spiral arms, but lags behind the rotational sense of the galaxy

(assuming that the arms are trailing). Higher resolution observations are necessary to determine the true spatial correlation of HI peaks and star forming regions.

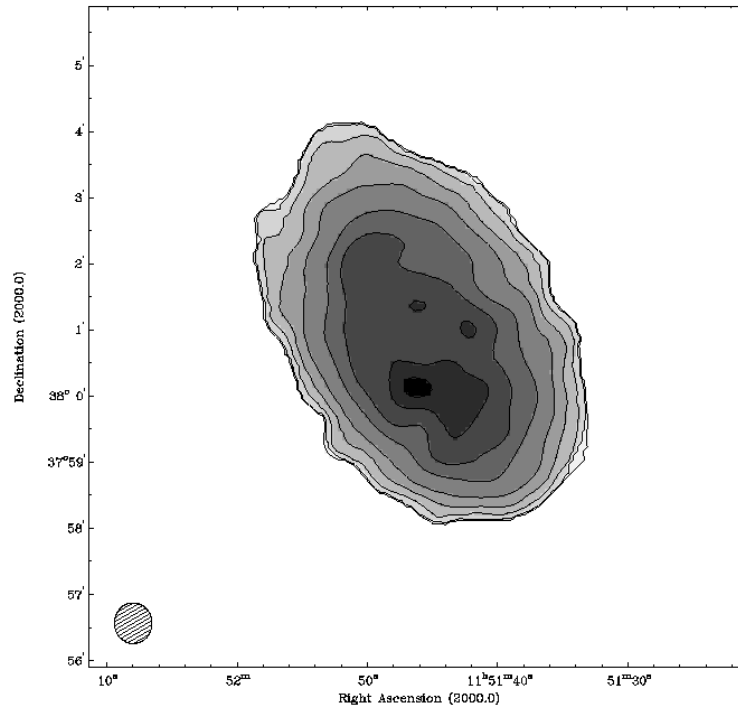


Figure 7-5. Grayscale and contours of the total HI surface density from the high resolution data set. The peak flux corresponds to $5.8 \times 10^{21} \text{ cm}^{-2}$. Contours are at 1 (the 2σ flux level), 2, 5, 10, 15, 20, 40, 60, 80, and 95% of the peak flux. The synthesized beam ($37'' \times 34''$) is shown at the bottom left.

HI does appear to be present in the bar region of NGC 3930 at this resolution.

However, this may be a beam smearing effect similar to what was seen in the low resolution images of NGC 1784. Higher resolution images of NGC 1784 revealed that the center of the galaxy had an HI depression, which closely followed the outline of the optical bar. Here we see that the HI is peaked on and near the weak spiral arms. Overall, the 3 peaks at 80% of the maximum emission form a partial circle around the bar region. The optical images of NGC 3930 revealed that the inner regions of the galaxy were blue relative to the rest of the galaxy, indicating that star formation is occurring. A deficiency in HI may either be due to ionization or molecule formation processes. Higher resolution

observations in HI are required to determine the presence and depth of an HI hole as well as its shape. H α observations are also warranted to assess the fraction of ionized hydrogen present in the bar region of NGC 3930.

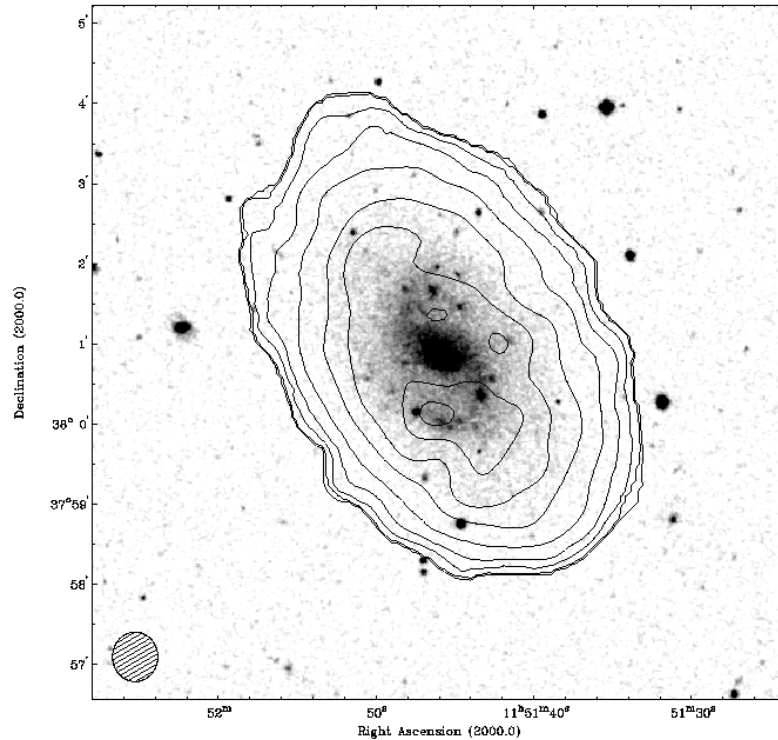


Figure 7-6. Contours of the high resolution HI surface density over a grayscale image of NGC 3930. Contours and resolution are the same as in Figure 7-5.

Global Neutral Hydrogen Properties

Figure 7-7 shows the HI spectrum of NGC 3930 created from our low resolution data. It shows the typical galactic two-horned pattern with the blue peak much brighter than the red. This is consistent with the asymmetry noted in Figure 7-3. We calculate the total HI flux of NGC 3930 to be $29.3 \pm 0.8 \text{ Jy km s}^{-1}$, corresponding to an HI mass of $1.16 \pm .13 \times 10^9 M_{\odot}$. This value is consistent with other single dish measurements such as Haynes et al. (1998) and de Vaucouleurs et al. (1991). From our spectrum of NGC 3930, we calculate a 3σ HI flux level of 0.006 Jy. This corresponds to a conservative minimum

mass detection level of $6.1 \times 10^7 M_{\odot}$ for an isolated HI cloud, assuming that it appears in 3 continuous channels.

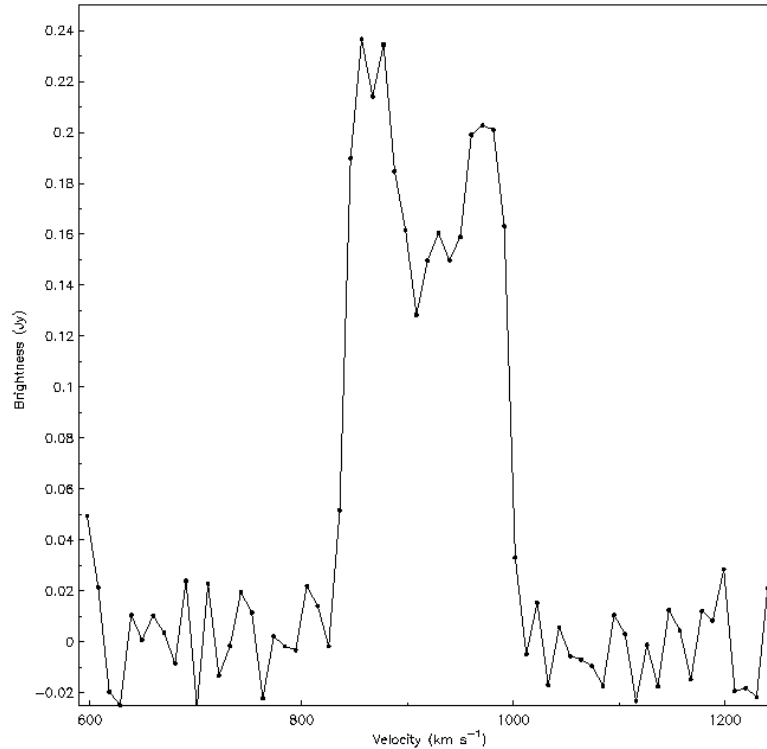


Figure 7-7. The HI flux density versus velocity for the low resolution data set. The velocity resolution here is 10 km s^{-1} .

Figure 7-8 is the radial HI profile from both the high and low resolution data set. This galaxy shows a similar profile to other late type galaxies (Moore & Gottesman 1998). We find that the HI emission cuts off at below the $1 \times 10^{20} \text{ cm}^{-2}$ level in accordance with the predictions of Maloney (1993).

Neutral Hydrogen Kinematics

Figure 7-9 shows the HI velocity field for NGC 3930 created with our low resolution data set. Figure 7-10 shows the HI velocity field for NGC 3930 created with our high resolution data set. Figure 7-11 shows this same field overlaid on an optical DSS image of the galaxy. The contours in all three images are separated by 10.5 km s^{-1} ,

and the central contour is at a systemic velocity of 919 km s^{-1} . Both the low and high resolution velocity fields show a largely symmetric velocity field as would be expected given the channel maps of Figures 7-1 and 7-2. Our high resolution image does not possess enough detail to observe effects of the spiral arms on the HI velocity field.

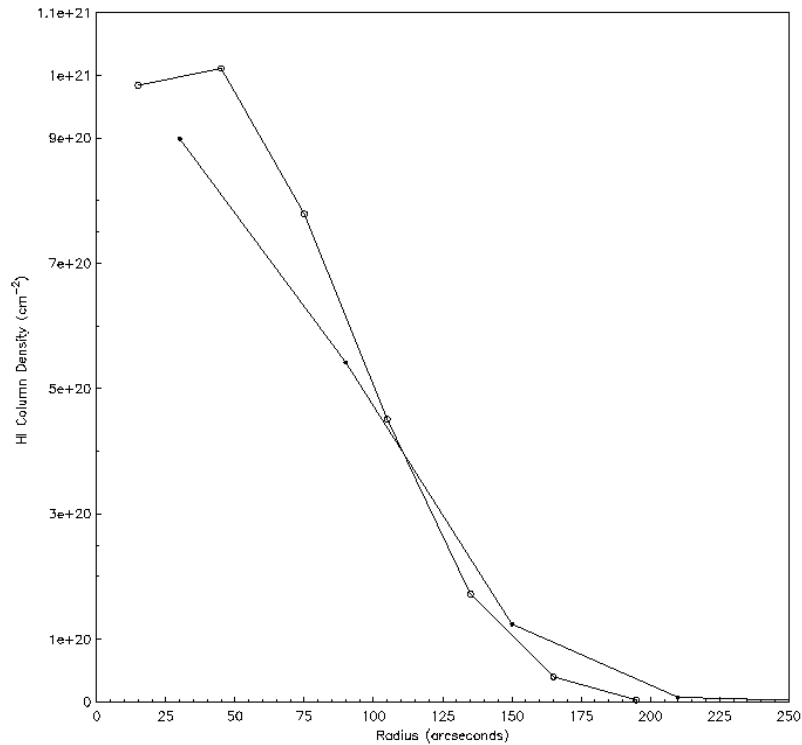


Figure 7-8. The HI radial density profiles from the low resolution data set (closed circles) and the high resolution data set (open circles)

In the high resolution velocity field, we see a kink at the outer edge of the galaxy. There is a slight hint of this in the lower resolution image, implying that the feature is real and not just an affect of low signal to noise in the high resolution image. However, the resolution is significantly worse, so the details are lost. The kink appears to exist at larger radii than the optical spiral arms (Figure 7-11), so it is unlikely that it is due to streaming motions. A small warp may be present at large radii in the HI disk in this galaxy, even though no formation mechanism is obvious for this warp.

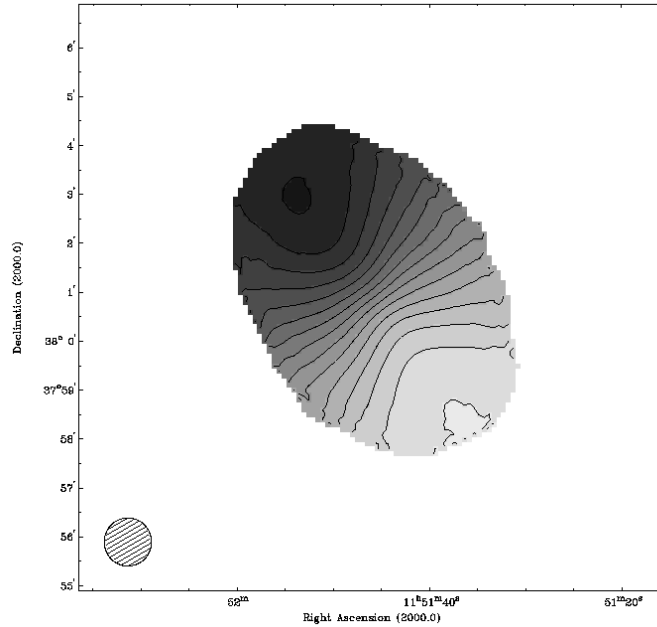


Figure 7-9. Intensity-weighted radial velocity contours of the low resolution data. Contours are separated by 10 km s^{-1} . Motion toward the observer is displayed with black contours and lighter grayscales. The systemic velocity of the galaxy is 919 km s^{-1} . The synthesized beam ($59'' \times 58''$) is displayed in the lower left.

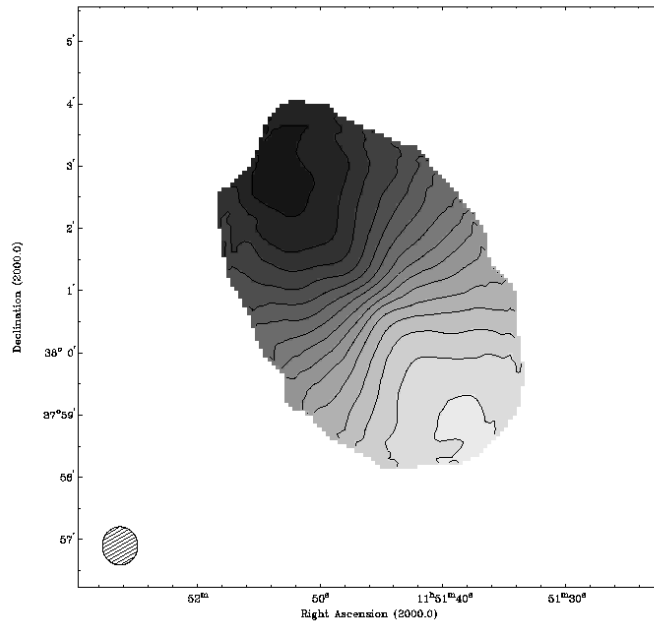


Figure 7-10. Intensity-weighted radial velocity contours of the high resolution data set. Contours are separated by 10 km s^{-1} . Darker grayscales correspond to motion away from the observer. The synthesized beam ($37'' \times 34''$) is displayed in the lower left hand corner.

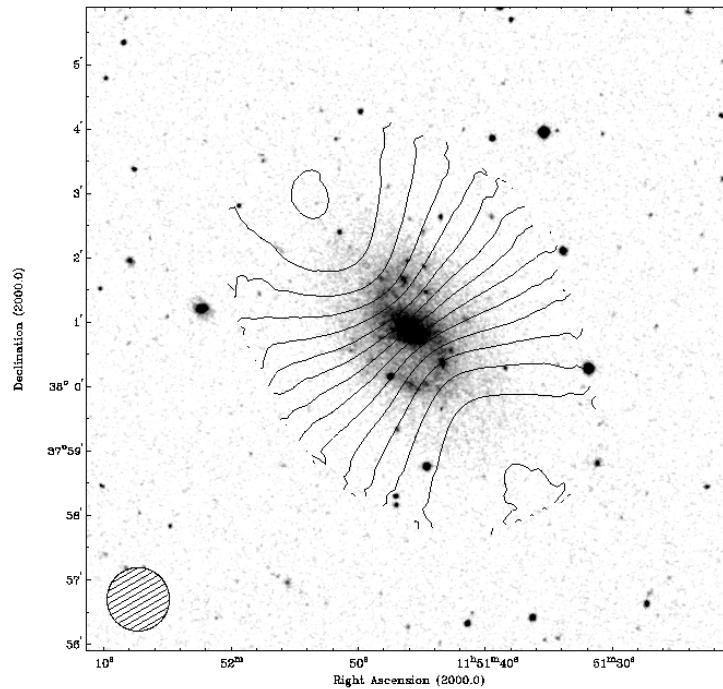


Figure 7-11. Intensity-weighted radial velocity contours of the high resolution data set overlaid on an optical DSS image of NGC 3930. Contours are the same as in Figure 7-10.

Position Velocity Plots

Figure 7-12 shows Position-Velocity (P-V) plots parallel to the major axis for NGC 3930 made with the high resolution data set. The lowest contour is drawn at the 3σ (2 mJy beam^{-1}) level. As with the channel maps and velocity fields, these plots show a fairly regular galaxy. There is confirmation of the global HI asymmetry as the upper right hand of all the slices tends to show a higher column density than the lower left, but the difference is not as pronounced as in other sample galaxies. Two of the slices show small protrusions, meaning there may be some gas at non-circular velocities. However, these protrusions are only at the 3σ level, are smaller than $1'$, and have a small velocity width (one or two channels). We would expect the masses of these regions to be on the order of $10^7 M_{\odot}$, and not significant to the dynamics of the system. Further very deep observations at $20''$ resolution may be able to resolve these regions into separate high

velocity clouds similar to those seen around other galaxies in this sample, such as NGC 1784.

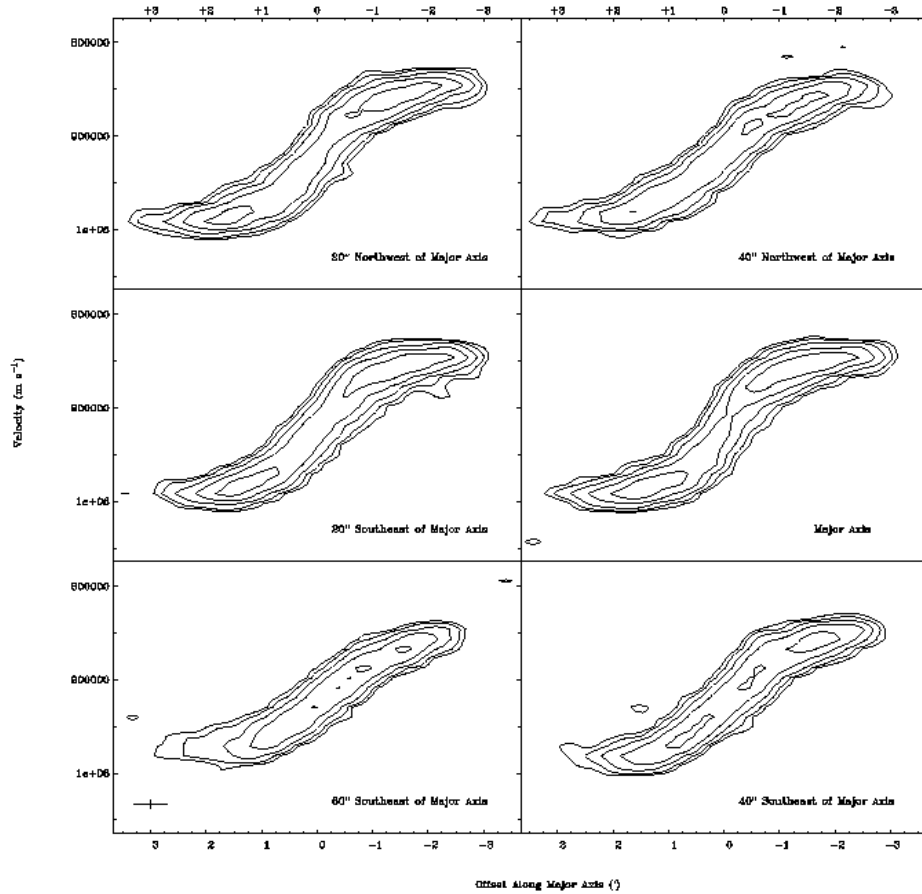


Figure 7-12. A set of P-V slices parallel to and along the major axis of NGC 3930. The contours are at 3, 5, 10, 20, 45, and 50 σ . The resolution is denoted by a cross in the lower left corner of the bottom left panel.

At the extreme ends of several of the slices (particularly 40'' Northwest and 40'' Southeast), we find further evidence of the warp in the disk of NGC 3930. At both +3' and -3', we see the velocity of the gas trending back towards the systemic velocity instead of remaining flat. This effect is short in distance and occurs at low column densities. Very little mass is associated with this warp. We believe that this feature is a warp, and not simply a falling rotation curve, because it is more prominent on the slices away from the major axis. A falling rotation curve would affect all slices.

Often, warps are associated with the close passage of a companion, such as in NGC 1784 or NGC 7479 (Laine & Gottesman 1998). Here we do not observe any HI or optical companions to NGC 3930. Casuso & Beckman (2001) have proposed a mechanism where large companions are not necessary for the creation of warps. Without obvious evidence for a companion, we conclude that warp in NGC 3930 is caused by processes within the disk and halo.

Figure 7-13 shows P-V plots parallel to the minor axis of NGC 3930. These images do not show any outstanding features. The overall gas distribution is skewed to the west. This is again consistent with the overall asymmetry seen in Figure 7-3. No satellites or gas at forbidden velocities are apparent.

Rotation Curves and Model Disks

In order to make rotation curves and model disks of NGC 3930, we used the GIPSY task 'reswri' to fit tilted rings to the velocity field. We used our high resolution data set to create our parameter curves. We fit rotational velocities at radii ranging from 20" to 200" in 30" wide annuli. We held the position of the kinematic center and the systemic velocity of the galaxy as fixed parameters, while allowing the rotational velocity, expansion velocity, position angle, and inclination to be set by the fit. We plot the results from the receding, approaching, and average of both sides of the galaxy. We plot the rotation velocity versus radius in Figure 7-14, expansion velocity versus radius in Figure 7-15, position angle versus radius in Figure 7-16, and inclination versus radius in Figure 7-17.

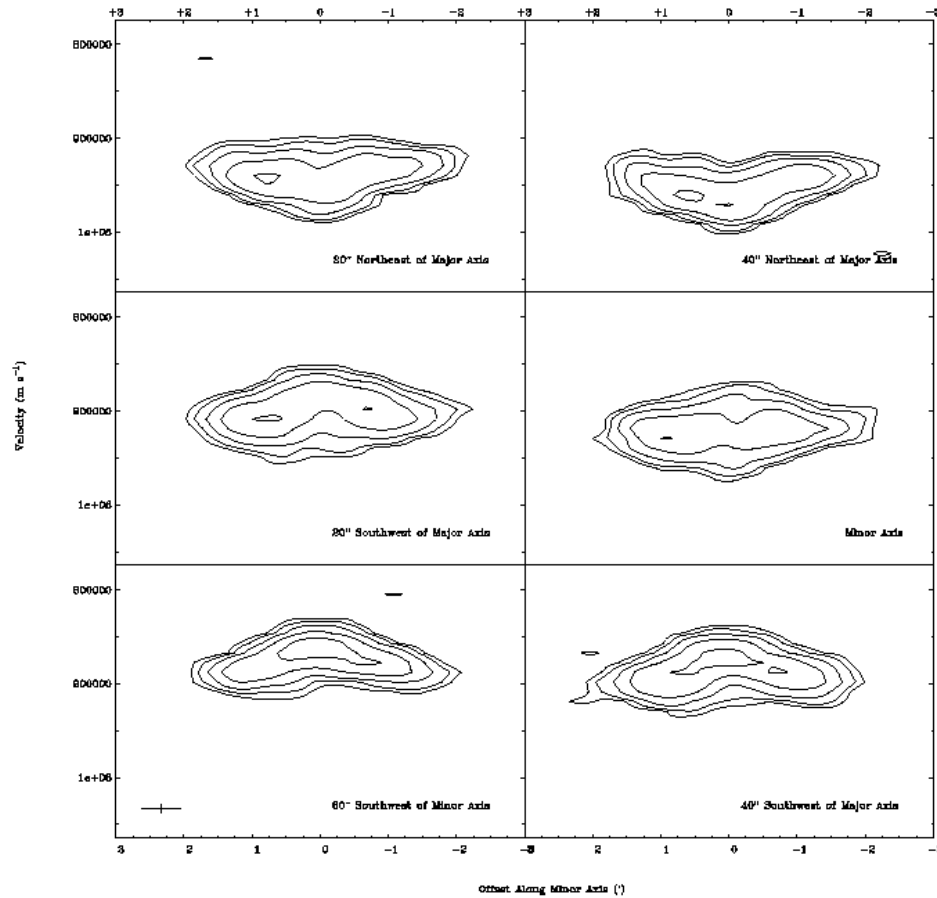


Figure 7-13. A set of P-V slices parallel to and along the minor axis of NGC 3930. The contours are at 3, 5, 10, 20, 45, 50 σ . The resolution function is shown as a cross in the lower left corner of the bottom left panel.

Figure 7-14 shows that NGC 3930 has a flat to rising rotation curve through 150". This is consistent with the findings of Elmegreen & Elmegreen (1990) for flocculent galaxies. The outermost point is coincident with the warp mentioned in regards to the velocity fields and P-V plots. This point is further evidence that some process is occurring at the outer edges of the galaxy. The actual value for this point is subject to concern, though, because of the limited flux at the edge of the galaxy. Other than this last point, we find a rather small value for the maximum rotational velocity of 95 km s⁻¹, especially considering the average to large physical size of the galaxy.

We calculated a value for the total mass of NGC 3930 interior to 170" (using the last point of the flat part of the rotation curve, given our concerns about the warp exterior to this). Using a Keplerian, $M = V^2 R G^{-1}$, to model the disk and halo, where $R = 170''$ (10.5 kpc) and $V(10 \text{ kpc}) = 95 \text{ km s}^{-1}$, we find $M(R) 2.42 \pm 0.05 \times 10^{10} M_{\odot}$. Comparing this with the HI mass calculated above, we find a value for the ratio $M_{\text{HI}} / M(R)$ of 5% for NGC 3930.

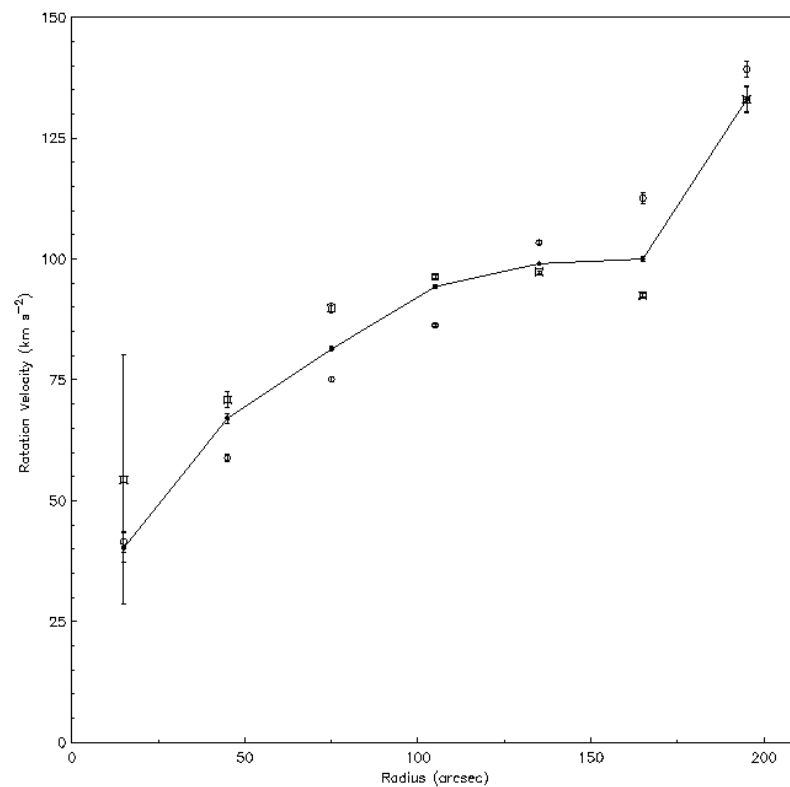


Figure 7-14. Rotation curve of NGC 3930 from the high resolution data set. Open squares represent the approaching half of the galaxy. Open circles represent the receding half of the galaxy. Filled circles represent the average of both.

The expansion velocity curve (Figure 7-15) is fairly flat, but offset to the positive values. This may be indicative of a slight error in the systemic velocity of the system, however, the error bars of many of the points on this plot do include 0 km s^{-1} , and their

overall value is within our velocity resolution of 10 km s^{-1} . The outermost point at $200''$ shows a value of 0 km s^{-1} , indicating that the warp does not seem to affect this parameter.

The position angle curve (Figure 7-16) shows a fairly flat, decreasing (about 10°) trend out to $170''$. The last point, corresponding to the radius of the warp in our major axis P-V plots (Figure 7-12) is significantly different, jumping by about 20° . The inclination curve (Figure 7-17) shows a similar trend, where most of the galaxy possesses a similar inclination, except for the very edge.

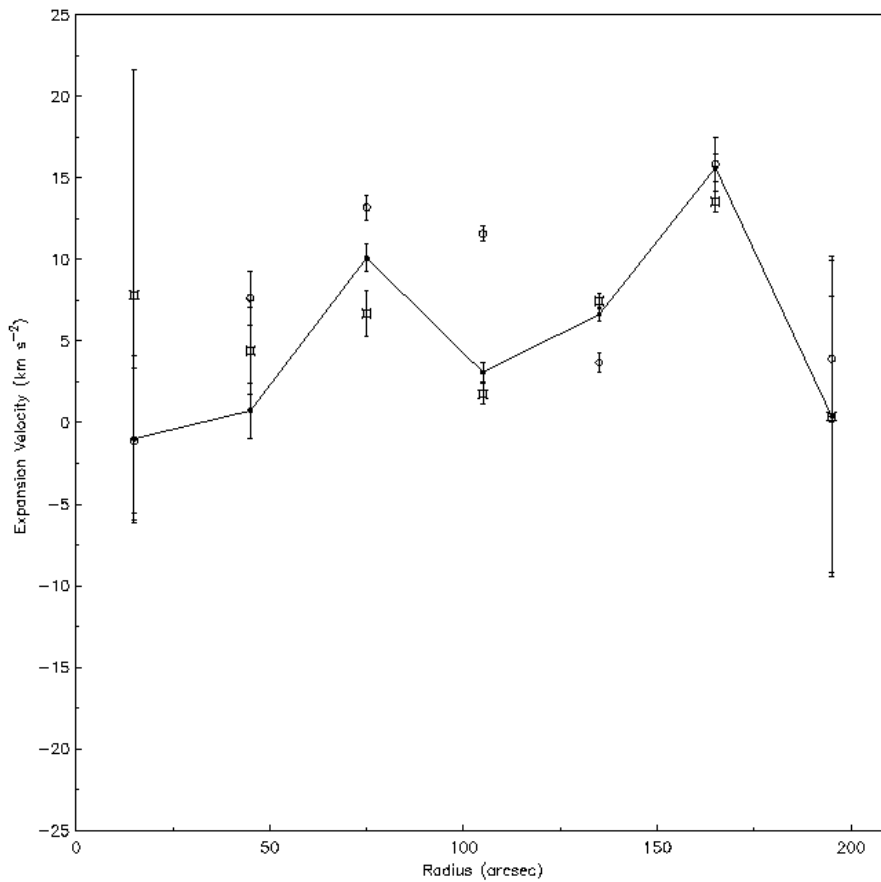


Figure 7-15. Expansion velocity as a function of radius for NGC 3930. Symbols are the same as in Figure 7-14.

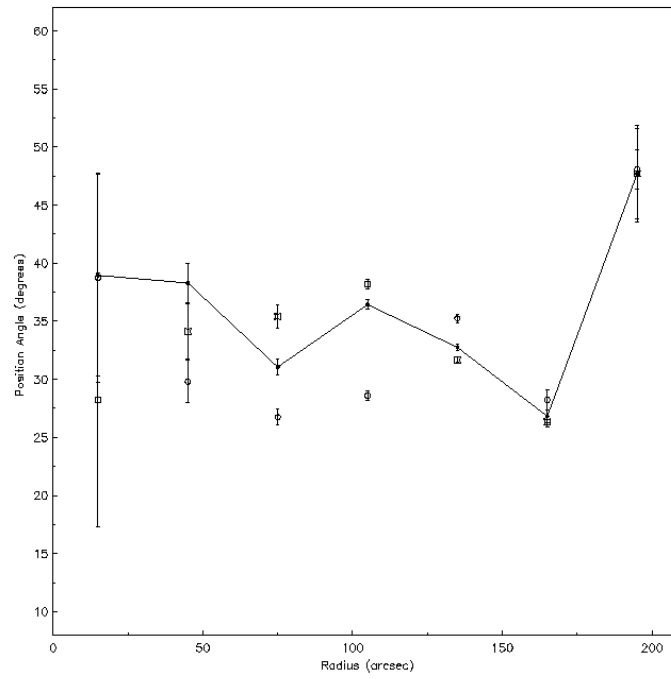


Figure 7-16. Kinematic position angle of NGC 3930 as a function of radius. Symbols are the same as in Figure 7-14.

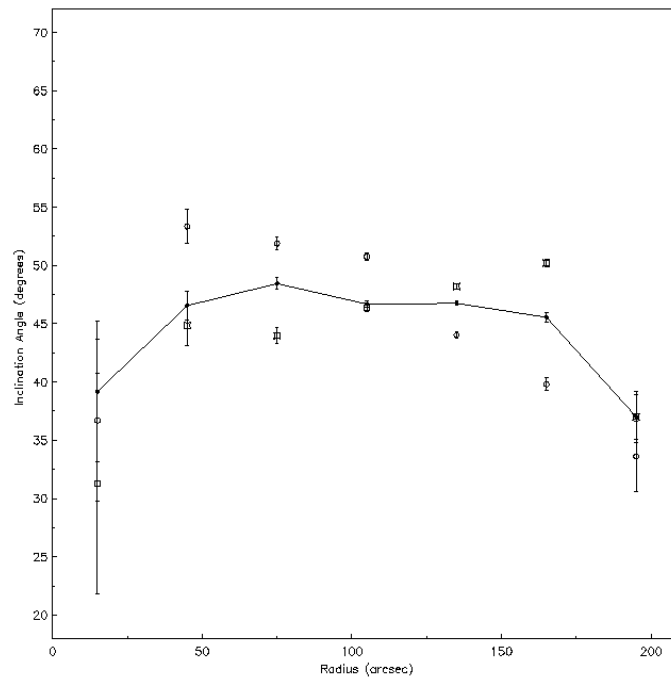


Figure 7-17. Inclination angle of NGC 6012 as a function of radius. Symbols are the same as in Figure 7-14.

The warp appears to be small (containing at most 1% of the HI mass of the galaxy), three dimensional (both twisted in the plane and out), not particularly violent (position angle and inclination differences are only 20°), and not associated with the star forming regions of the optical part of the galaxy. There is no obvious mechanism for the creation of this warp. Without obvious evidence of a companion nearby (<100 kpc) to NGC 3930, we must conclude that this warp is due to processes internal to the galaxy. Casuso & Beckman (2001) propose that the warp observed in the Milky Way is caused by the accretion of numerous $10^7 M_\odot$ clouds in a non-axisymmetric manner. Significantly deeper HI observations would be necessary to determine the presence of these objects.

We used the values of rotational velocity, position angle, and inclination to construct a model disk for NGC 3930 with the GIPSY task 'velfi'. The model disk is shown in Figure 7-18. This model disk shows a rather significant warp. We then subtracted this model field from our high resolution velocity field (Figure 7-8), to create a map of residual velocities. The residual velocity field is shown in Figure 7-19. The residual velocity field is largely bi-modal, with the western half of the galaxy having positive velocities and the eastern half having negative. This effect may be due to the slight positive offset in the expansion velocity. We constructed a second model velocity field, shown in Figure 7-20 where we have included the expansion velocities. We also smoothed the last data point at $200''$ to a value more fitting with the overall trend of the inner data. This velocity field looks much more like the observed velocity field in Figure 7-8. The subtraction of the two shows a good fit, but with very little structure. There is no indication of corotation as in Canzian (1993), NGC 1784, or NGC 3055. However this is not unexpected given our comparatively low resolution.

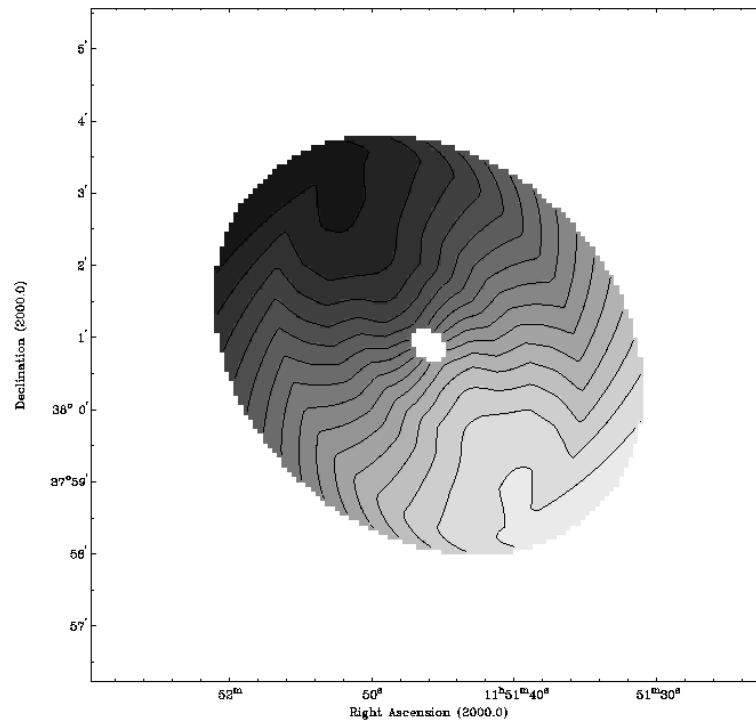


Figure 7-18. Model velocity field constructed from kinematical data in Figures 7-14, 7-16, and 7-17. Light grayscales represent approaching velocities.

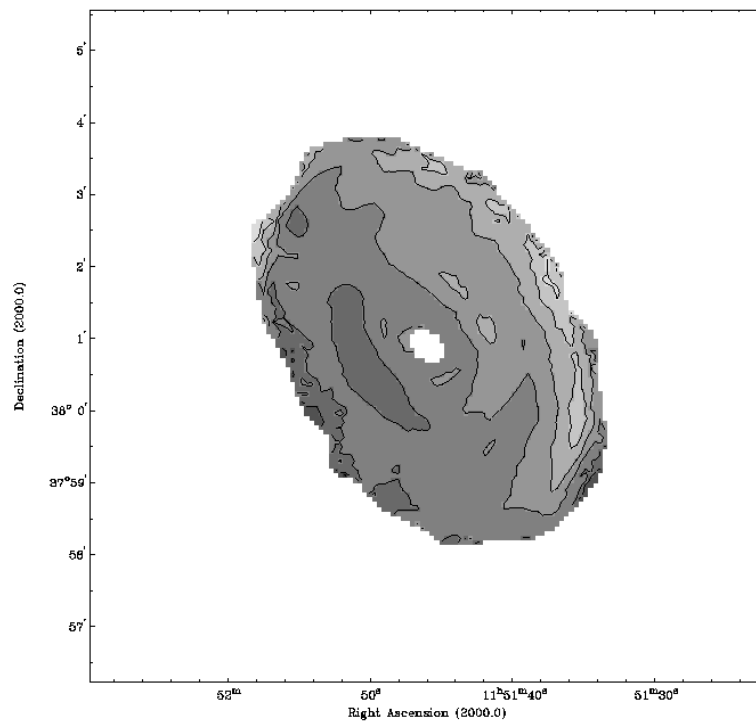


Figure 7-19. Residual velocity field made from model in Figure 7-18. Light grayscales represent approaching residuals. Contours are separated by 5 km s^{-1} .

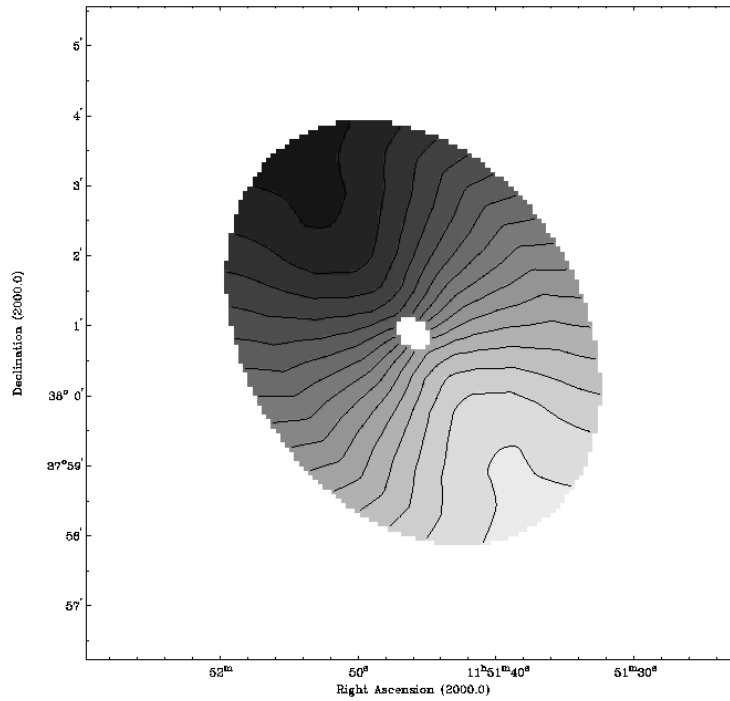


Figure 7-20. Model velocity field including values for expansion velocity and with all values smoothed at large radii

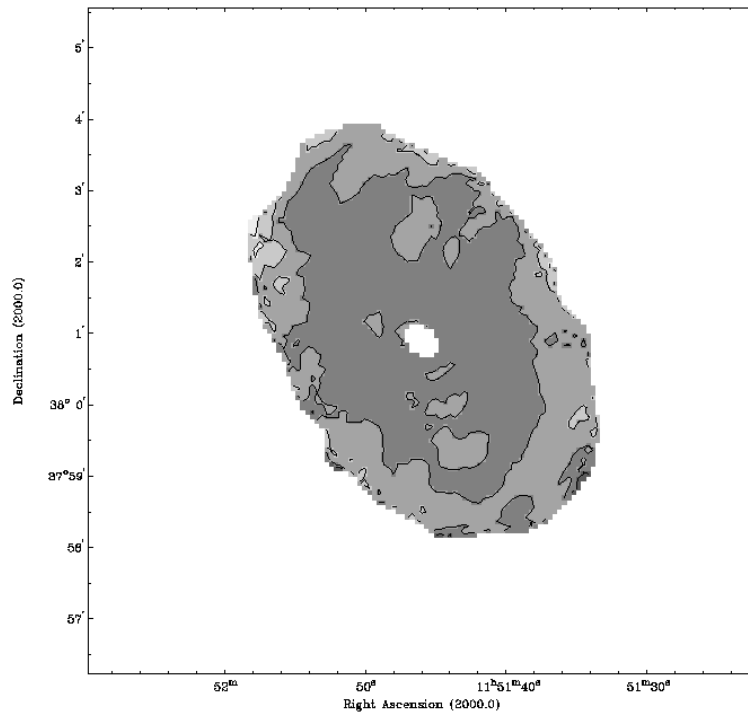


Figure 7-21. Residual velocity field made with the model from 7-20. Light grayscales indicate motion towards the observer. Contours are separated by 5 km s^{-1} .

Summary

NGC 3930 is a fairly regular, well formed disk galaxy. Its HI morphology is asymmetric, with the peak of its HI distribution aligned with the brighter of its two spiral arms. Also, NGC 3930 possesses a small warp in its outer disk. No large HI companions were found in our observations, nor is there direct evidence for a recent interaction / merger in this system. We conclude that the most likely explanation for the warp in the HI disk is internal disk/halo dynamical processes. Higher resolution observations are necessary to determine the effects of the interesting one-armed structure in this galaxy on the HI kinematics.

CHAPTER 8 NEUTRAL HYDROGEN OBSERVATIONS OF NGC 4900

NGC 4900 is a rather interesting optical galaxy. It is classified as having an arm class of "3" by Elmegreen & Elmegreen (1982), but in red images, there is really no coherent structure in the disk other than a large bar. The bar appears to be twisted in both the optical and near-infrared. Color maps show that the bar is blue, surrounded by a red ring. There also appear to be several blue regions of star formation scattered throughout the disk.

NGC 4900 is the second closest galaxy in our sample, having a recessional velocity of 969 km s^{-1} (14 Mpc, where $H_0 = 70 \text{ km s}^{-1} \text{ Mpc}^{-1}$). The galaxy has the smallest physical size in the sample, with an optical diameter of $2.2'$, corresponding to 9 kpc. Despite the galaxy's small size, it is fairly luminous and was not found to be deficient in HI in previous single dish observations (Giraud 1986). The galaxy is projected to be in the Virgo Southern Complex, however it is physically in front of this structure and is an isolated galaxy.

Observations

Radio observations of NGC 4900 were obtained at the Very Large Array in May of 2003 using the D configuration. The spectrometer was composed of 64 channels with a 10.5 km s^{-1} velocity resolution. The total band width was 3.125 MHz (640 km s^{-1}), and the central heliocentric velocity was 969 km s^{-1} . The observing parameters for the observations are summarized in Table 8-1.

Table 8-1. Parameters of VLA HI observations of NGC 4900

Configuration	D
Number of antennae	27
V_{sys} (km s ⁻¹)	969
Phase calibrator	1311-222
Flux calibrator	1331+305
Time on source	3.8

The D configuration data set was edited, calibrated and continuum subtracted using the typical procedures of the Astronomical Image Processing System (AIPS) package. The data set was then imaged twice using the AIPS task IMAGR to provide us with two image cubes (α , δ , ν) reflecting the maximum range of spatial resolution and sensitivity that our data would allow. We created a low resolution cube by using a natural weighting scheme and a high resolution data cube by imaging the data with a uniform weighting scheme. We CLEANed the data cubes in AIPS down to an rms level of 0.5 and 0.7 mJy beam⁻¹ for the low resolution and high resolution images, respectively. Further details of the statistics for each data cube are presented in Table 8-2. Analysis on the completed and CLEANed image cubes was conducted using the Gronigen Image Processing System (GIPSY) package.

Table 8-2. Characteristics of Naturally Weighted CLEANed Channel Maps

Parameter	Low Resolution	High Resolution
Fwhp synthesized beam (")	68" x 56"	43" x 39"
Fwhp synthesized beam (kpc)	4.6 x 3.8	2.9 x 2.6
Theoretical rms noise (mJy beam ⁻¹)	0.44	0.44
Observed rms noise (mJy beam ⁻¹)	0.5	0.66
Rms noise (K)	0.15	1.98
Peak temperature (K)	10.5	99
Peak S/N	70	50

Neutral Hydrogen Morphology

The channel maps shown in Figures 8-1, 8-2, 8-3, and 8-4 were used in moment analyses to obtain global density and temperature weighted radial velocity images of the neutral hydrogen in NGC 4900. Moment maps were constructed with the AIPS task MOMNT. A flux cut off of three times the rms noise level (σ) of the unsmoothed data was used. The low resolution, naturally weighted global distribution of the neutral hydrogen in NGC 4900 is shown in grayscale in Figure 8-5 and overlaid on an optical image of the galaxy in Figure 8-6. The high resolution, uniformly weighted global distribution of the neutral hydrogen is shown in grayscale in Figure 8-7 and overlaid on an optical image of the galaxy in Figure 8-8. The lowest contours are drawn at the 2σ level.

Low Resolution Neutral Hydrogen Morphology

The low resolution channel maps in Figure 8-1 and 8-2 show a significantly disturbed galaxy. We find two trends in the gas, as the observations move from high to low recessional velocity. One is the main body of the galaxy which starts in the channel with a velocity of 1062 km s^{-1} . This gas moves from west to east with an apparent position angle of 90° as the observational velocity decreases. The second body of HI appears much earlier in the observations, at a velocity of 1093 km s^{-1} . This body trends from the northwest to the southeast as the observational velocity decreases. This second body of gas may represent an inclined ring around disk of NGC 4900. It appears that there is a significant amount of gas in this ring. We will discuss this ring in a later section.

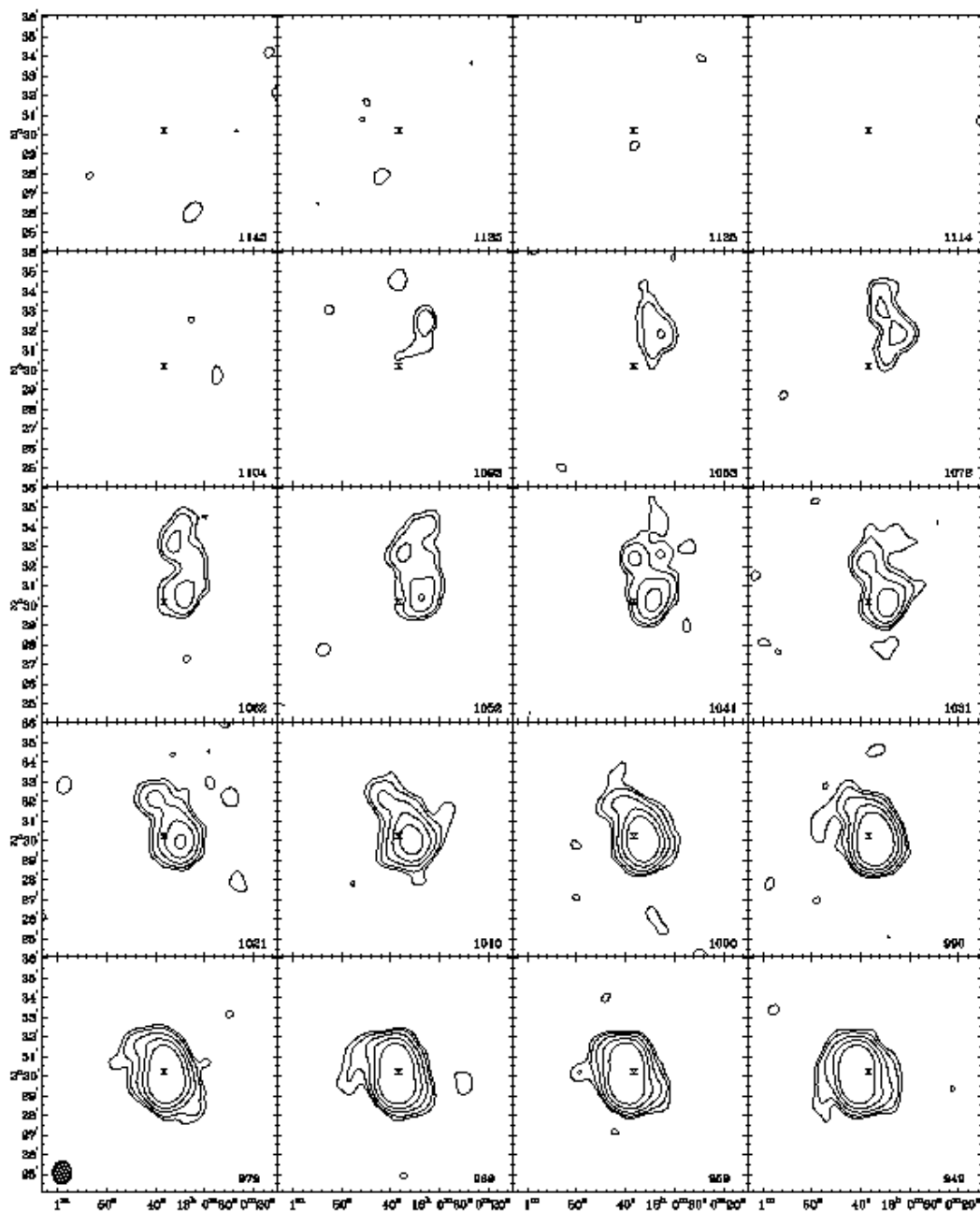


Figure 8-1. Individual, naturally weighted, CLEANed channel images of the low resolution data. Channel velocities are given in the lower left hand corner of each panel in km s^{-1} . The synthesized beam ($68'' \times 56''$) is shown in the lower left hand panel. Contours are at the 3 ($4.3 \times 10^{18} \text{ cm}^{-2}$), 5, 10, 20, and 40σ flux level.

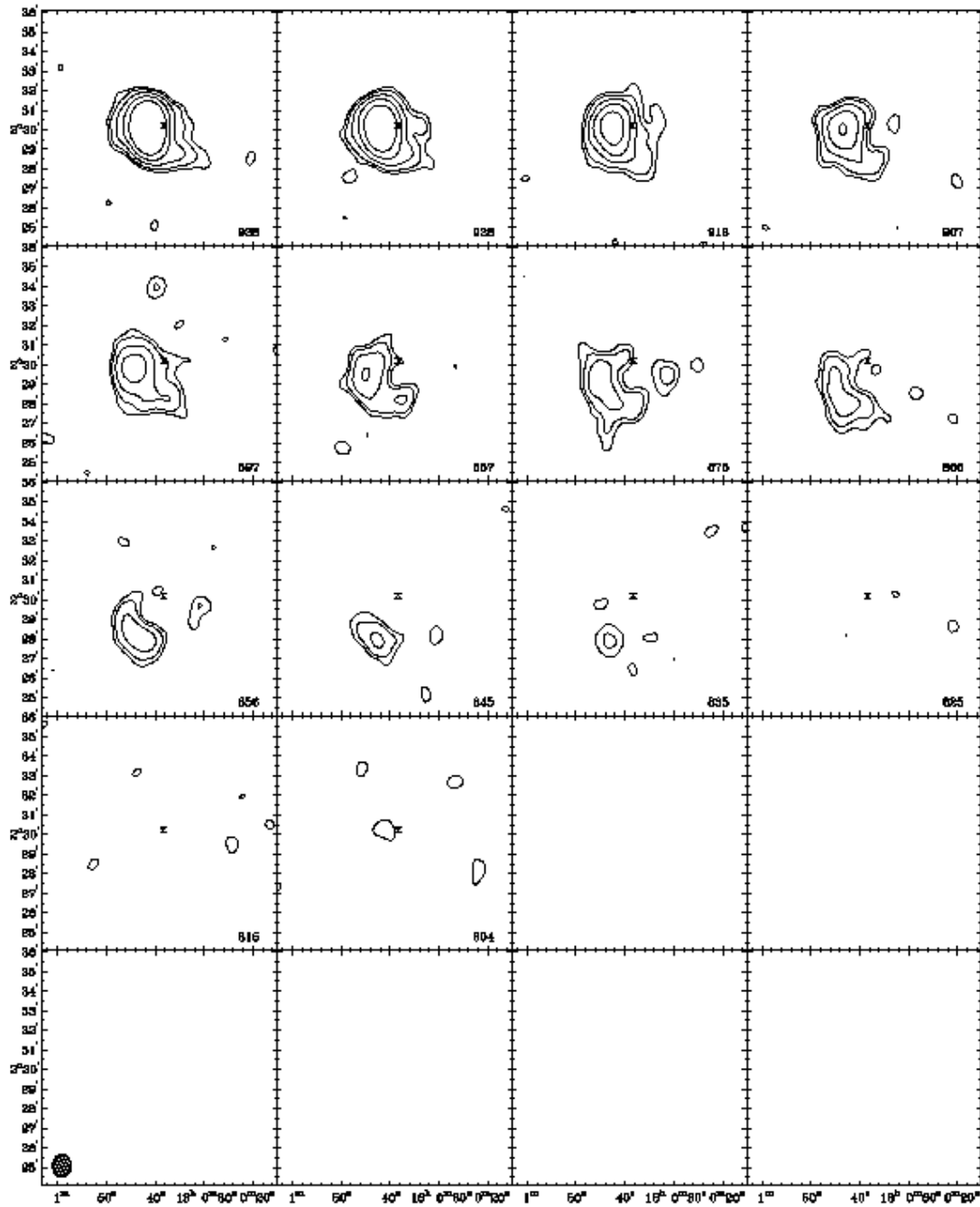


Figure 8-2. Individual, naturally weighted, CLEANed channel images of the low resolution data. The resolution and contour levels are the same as in Figure 8-1.

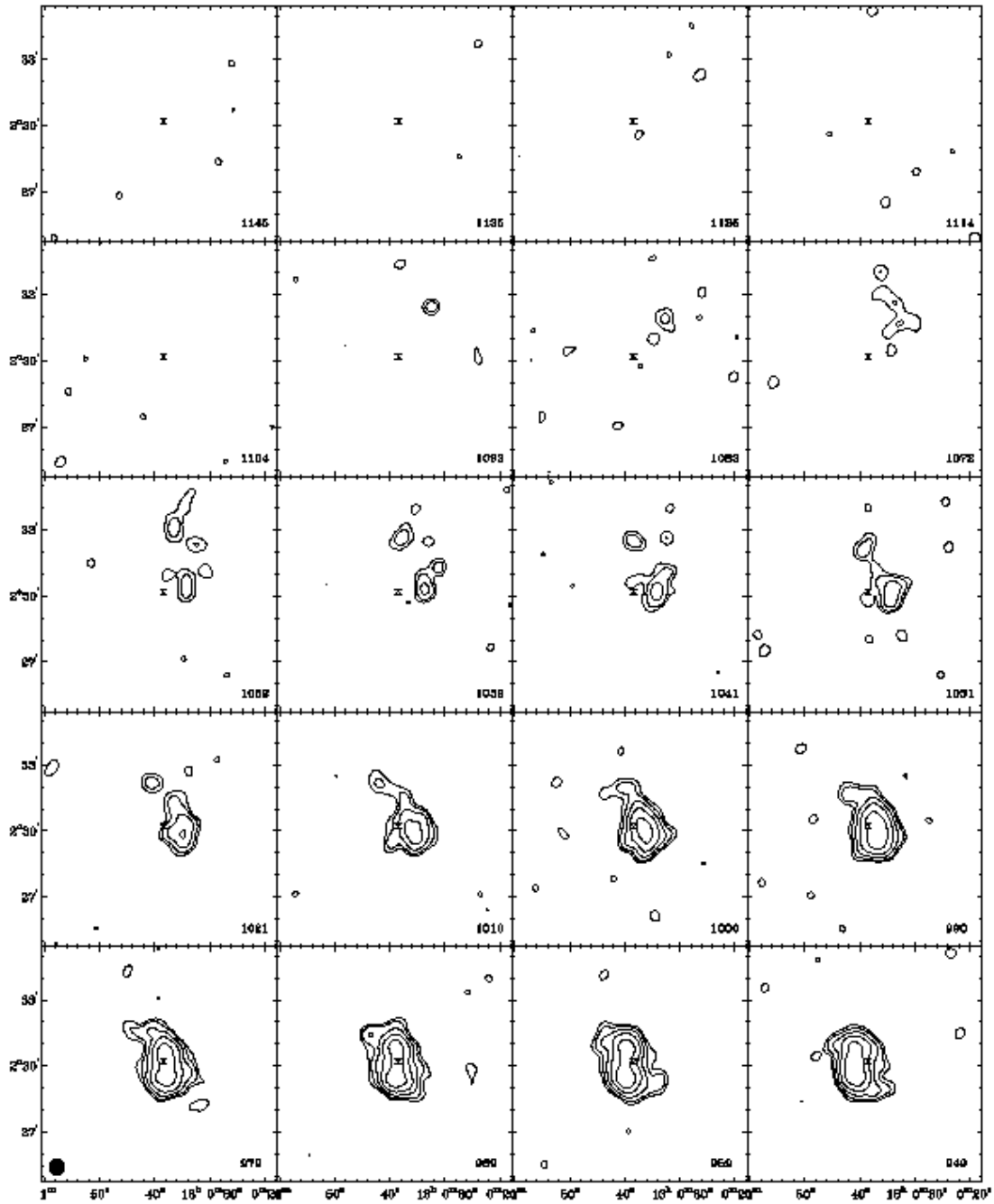


Figure 8-3. Individual, naturally weighted, CLEANed channel images of the high resolution data. Channel velocities are given in the lower right hand corner of each panel in km s^{-1} . The synthesized beam ($43'' \times 39''$) is shown at the bottom left of the lower left hand channel map. Contours are at the 3 ($1.3 \times 10^{19} \text{ cm}^{-2}$), 5, 10, 20, and 40σ flux levels.

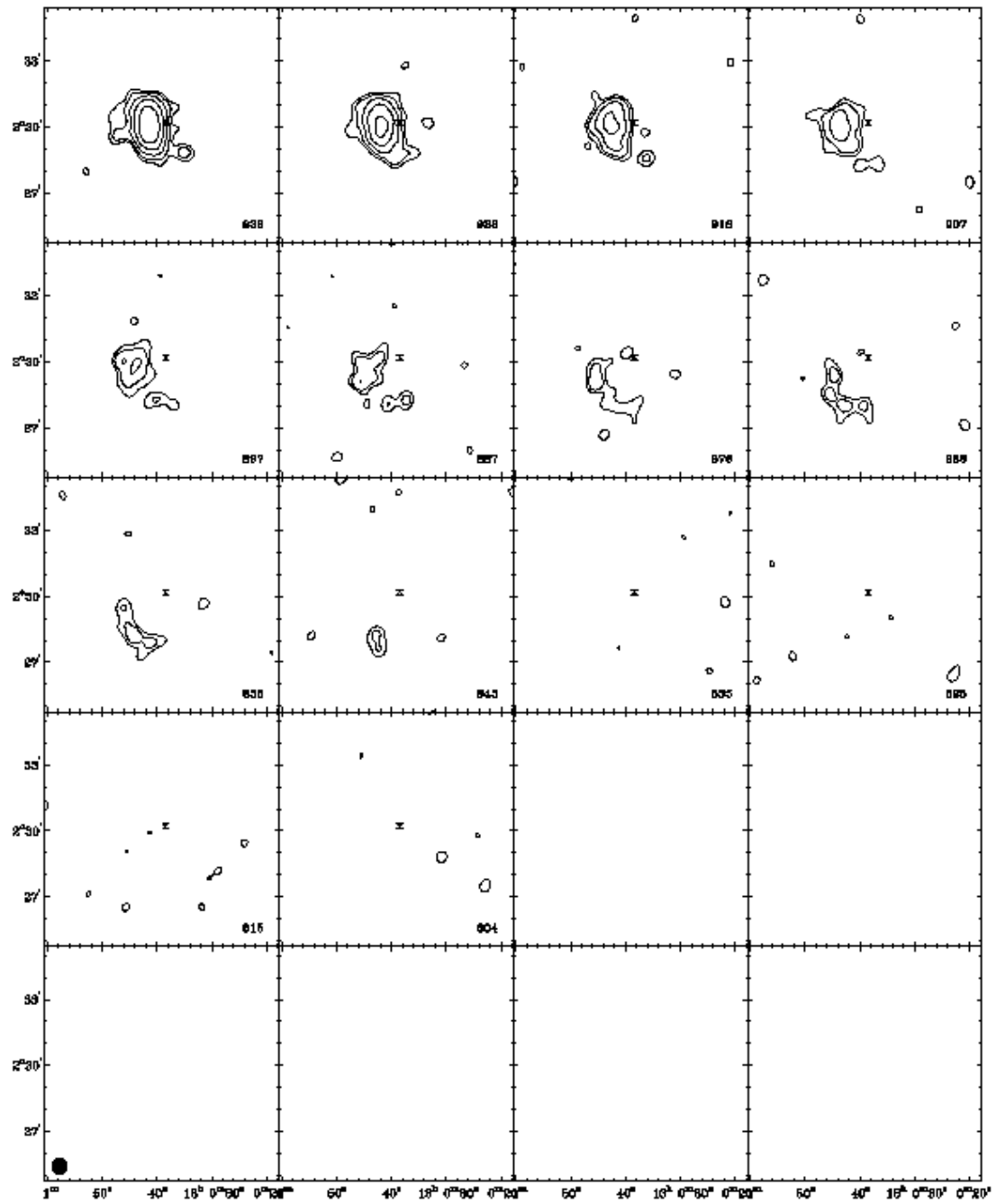


Figure 8-4. Individual, naturally weighted, CLEANed channel images of the high resolution data. The resolution and contour levels are the same as in Figure 8-3.

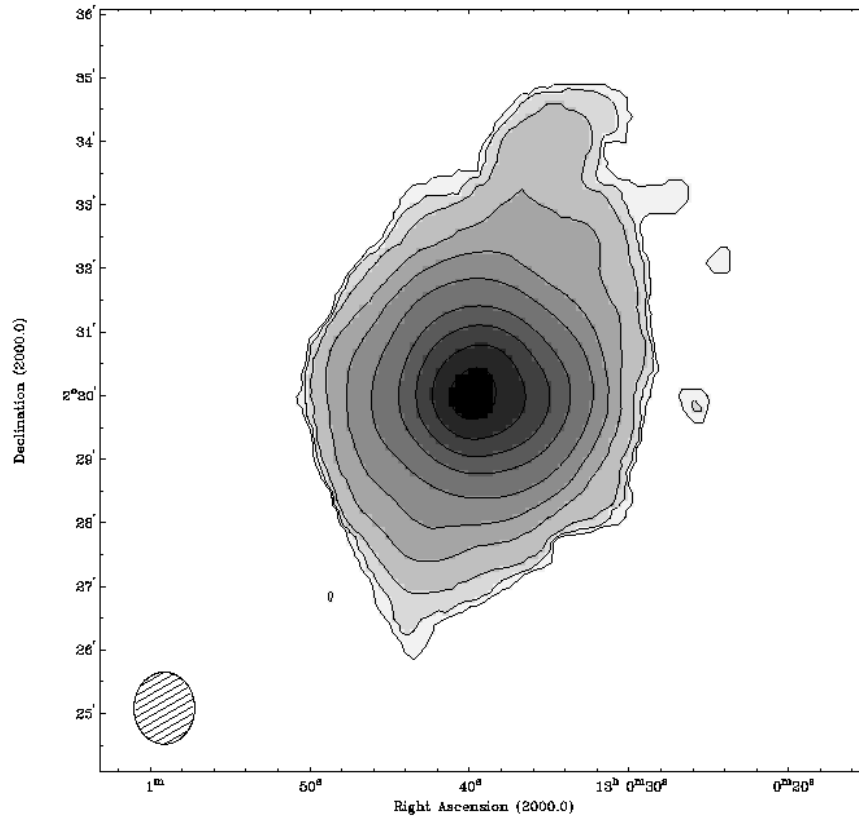


Figure 8-5. Grayscale with contours of the total HI surface density from the low resolution data set. The peak flux corresponds to a column density of $1.4 \times 10^{21} \text{ cm}^{-2}$. Contours are at 0.5 (the 2σ flux level), 1, 2, 3, 5, 10, 20, 40, 60, 80, and 95% of the peak flux. The synthesized beam ($68'' \times 57''$) is shown at the bottom left.

The morphology of the total HI intensity map (Figure 8-5) for NGC 4900 reflects the complex HI distribution in the channel maps discussed above. The overall shape of the HI distribution in NGC 4900 resembles an arrowhead pointed to the southeast. The contours at the center of the galaxy are close to being circular, even though the peak of the HI distribution ($N_{\text{HI}} = 1.4 \times 10^{21} \text{ cm}^{-2}$) seems to be somewhat off center. These contours are primarily associated with the main body of gas in NGC 4900. The arrowhead shape comes from second body of HI moving from northwest to southeast.

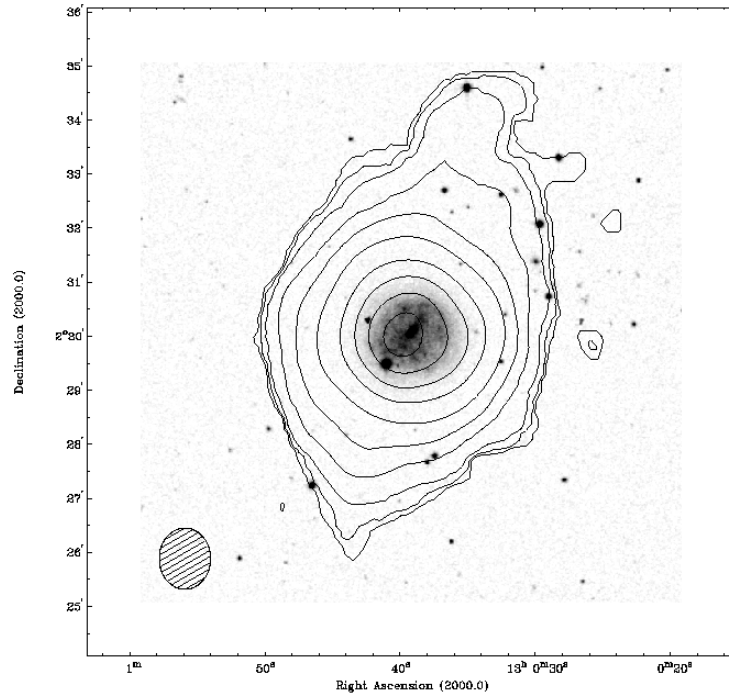


Figure 8-6. Contours of the total HI surface density from the low resolution data set overlaid on an optical DSS image of NGC 4900. Contour levels are the same as in Figure 8-5.

Figure 8-6 showing the low resolution total HI intensity overlaid on an optical DSS image of NGC 4900 shows that the center, circular contours do lie slightly off center and to the west of the optical distribution of the galaxy. Considering just the circular contours (down to 10% of the peak emission), the HI diameter of the galaxy would be on the order of 4' (16 kpc), or nearly twice the optical diameter. This value is typical for the other galaxies in our sample which do not show a significant HI disturbance. The HI diameter of the entire HI arrowhead structure surrounding NGC 4900 is nearly 9' (37 kpc), or over four times the optical diameter. This scale is on the order of the inner ring system surrounding NGC 1784, and also lies at approximately the tidal radius of NGC 4900, leading us to believe that the extended HI emission in NGC 4900 is resultant from an external source.

High Resolution Neutral Hydrogen Morphology

In the high resolution HI images of NGC 4900 we see properties similar to the low resolution images. The channel maps in Figure 8-3 show the two systems involved in NGC 4900 implied by Figure 8-1. Here, though, we see the ring system separated from the main body of NGC 4900 because of the higher resolution. In the channel maps from 1083 through 1021 km s^{-1} we see the ring arcing around the north of the galaxy, as well as evidence of the ring system superimposed on the main galaxy in the images of 1052 and 1041 km s^{-1} . In the channel corresponding to 959 km s^{-1} we see potentially both sides of the ring emanating from the northeast and southwest sides of the linear north-south main body of the galaxy. Again, as the emission from the main body of NGC 4900 ends in the images around 897 km s^{-1} , we see the ring wrapping around the south of the galaxy.

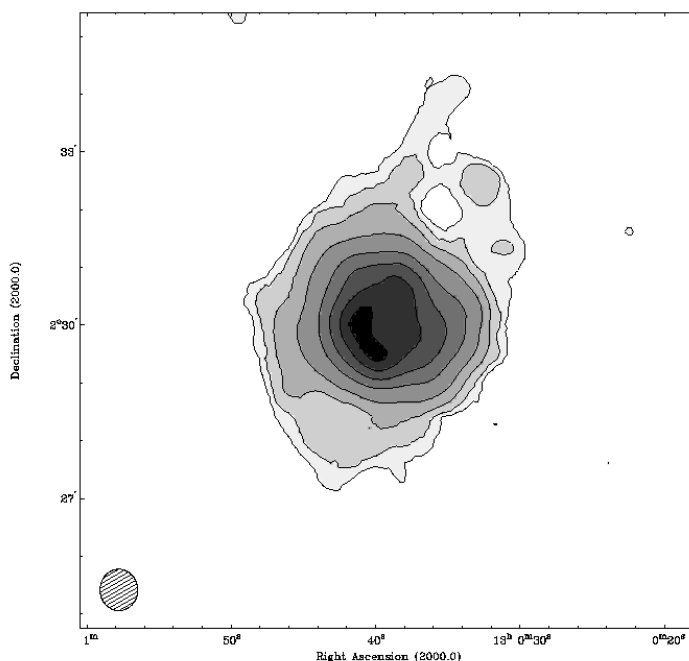


Figure 8-7. Grayscale and contours of the total HI surface density from the high resolution data set. The peak flux corresponds to $1.5 \times 10^{21} \text{ cm}^{-2}$. Contours are at 2 (the 2σ flux level), 5, 10, 15, 20, 40, 60, 80, and 95% of the peak flux. The synthesized beam ($43'' \times 39''$) is shown at the bottom left.

The high resolution HI total intensity map (Figure 8-7) shows the northern end of the ring to be somewhat separated from the body of NGC 4900, evidenced by the hole northwest of the galaxy. Again, in Figure 8-8, we find the peak of the HI distribution ($N_{\text{HI}} = 1.5 \times 10^{21} \text{ cm}^{-2}$) to be offset to the east of the center of the optical emission. We do not directly observe an HI hole associated with the bar in this galaxy, however, NGC 4900 shows a similar morphology to NGC 3930, where the HI peak curves around the bar. Higher resolution observations may reveal that the bar is deficient in HI.

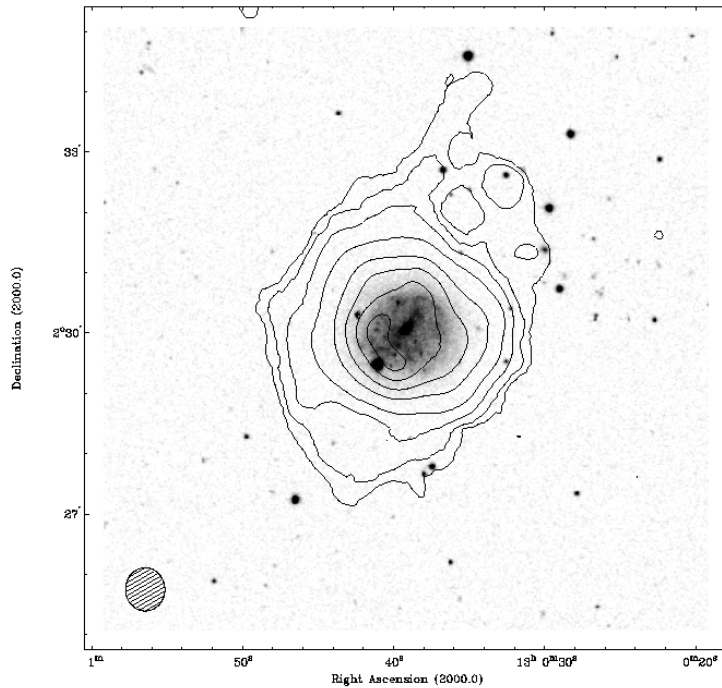


Figure 8-8. Contours of the total HI surface density from the high resolution data set overlaid on an optical DSS image of NGC 4900. Contours are at the same levels as in Figure 8-7.

Global Neutral Hydrogen Properties

Figure 8-9 shows the HI spectrum of NGC 4900 created with the low resolution data cube. This spectrum shows few of the typical features associated with a disk galaxy. There is no double horned pattern indicating differential rotation. The spectrum peaked around the central velocity and remains flat for two or three channels on either side.

Outside of this flat central area, the spectrum has broad shoulders on both sides. Several small peaks on the lower velocity side are a result emission from the HI ring, as can be determined from the channel maps (Figure 8-1). We calculate a total HI flux of $23.1 \pm .9$ Jy km s⁻¹. This corresponds to an HI mass of $1.07 \pm 0.15 \times 10^9 M_{\odot}$. This value is consistent with other single dish measurements as given by de Vaucouleurs et al. (1991). It is difficult to determine a proper velocity width to the spectrum of NGC 4900 due to its broad shoulders. If we use the small peak at 910 km s⁻¹ as one end of the main body of the galaxy, and the top of the shoulder at 1050 km s⁻¹ as the other, we estimate a velocity width of 140 km s⁻¹, which is similar to other galaxies in this sample. From our spectrum of NGC 4900, we calculate a 3σ HI flux level of 0.033 Jy. This corresponds to a conservative minimum mass detection level of $4.4 \times 10^7 M_{\odot}$ for an isolated HI cloud, assuming that it appears in 3 continuous channels.

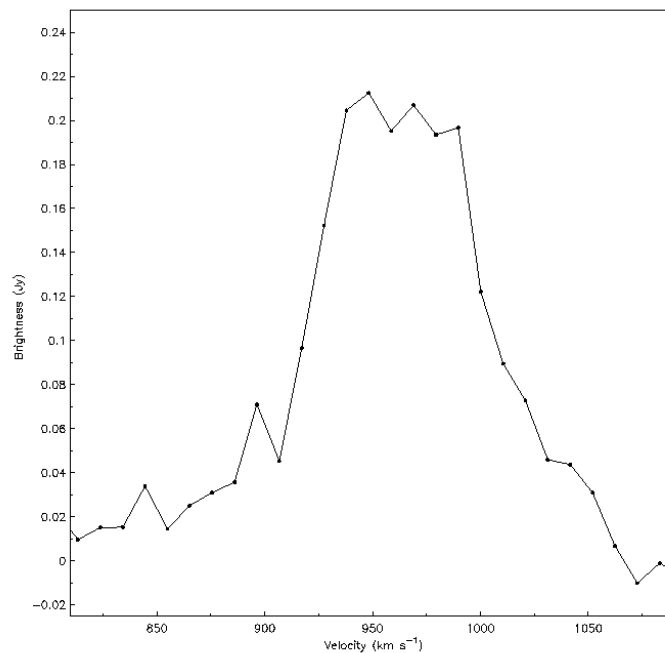


Figure 8-9. The HI flux density versus velocity for the low resolution data set. The velocity resolution here is 10 km s⁻¹. The spectrum does not show the typical galactic double horned pattern.

Figure 8-10 is the radial HI profile from both the high and low resolution data set. This galaxy shows a similar profile to other galaxies in the sample, despite the strange morphology and spectrum present in NGC 4900. This is likely because the HI ring does not possess a large amount of mass relative to the main galaxy. We find that the HI emission cuts off quickly below the $1 \times 10^{20} \text{ cm}^{-2}$ level in accordance with the predictions of Maloney (1993).

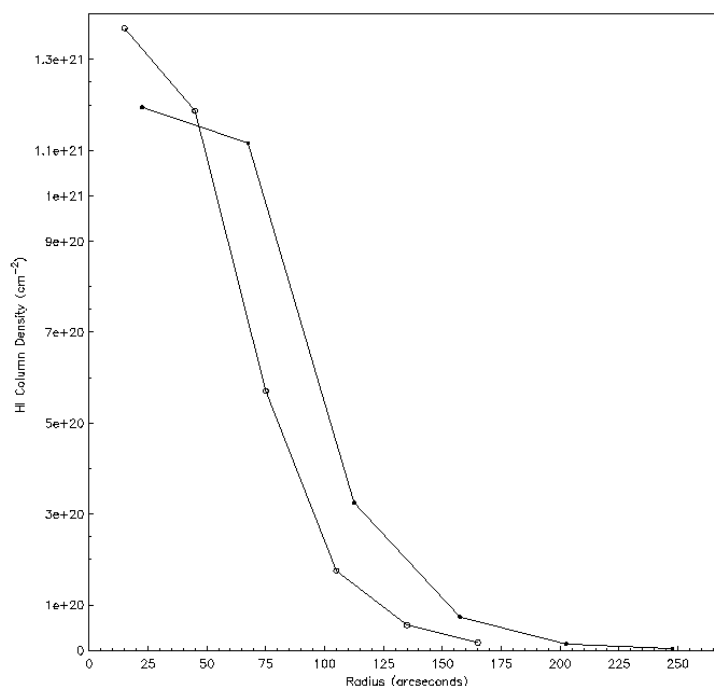


Figure 8-10. The HI radial density profiles from the low resolution data set (closed circles) and the high resolution data set (open circles)

Neutral Hydrogen Kinematics

Figure 8-11 shows the HI velocity field for NGC 4900 created with our low resolution data set. Figure 8-12 shows the HI velocity field for NGC 4900 created with our high resolution data set. Figure 8-13 shows this same field overlaid on an optical DSS image of the galaxy. The contours in all three images are separated by 10.5 km s^{-1} , and the central contour is at a systemic velocity of 969 km s^{-1} . The low resolution

velocity field is similar in structure what was observed in the channel maps. There seem to be two different position angles for the iso-velocity contours in this galaxy. The contours at the center of the galaxy run north-south, while the contours in the southeast and northwest are closer to east-west. Through the middle of the galaxy, the contours possess an "S" like shape. This is likely due to a transition region between the central galaxy and the ring which has not been resolved.

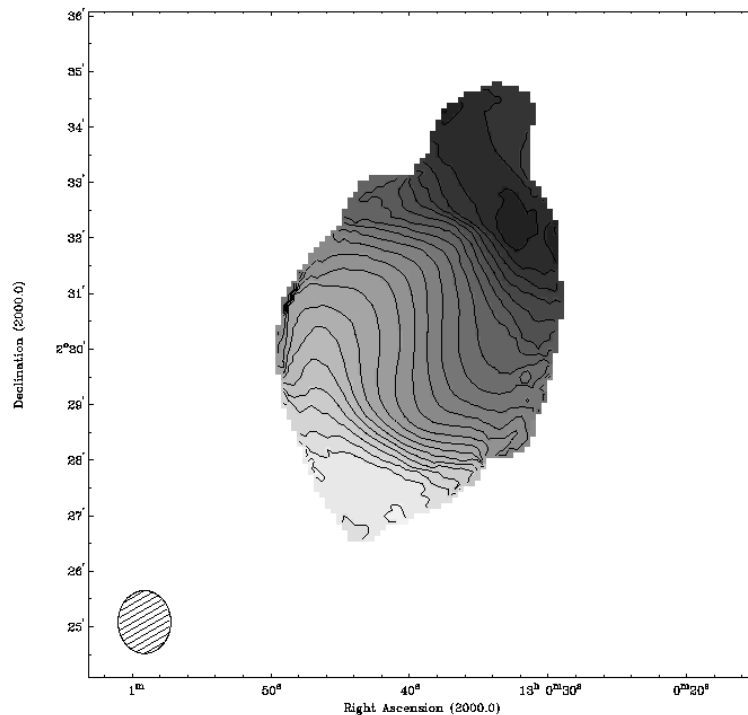


Figure 8-11. Intensity-weighted radial velocity contours of the low resolution data. Contours are separated by 10 km s^{-1} . Motion toward the observer is displayed with lighter grayscales. The central velocity contour is at 969 km s^{-1} . The synthesized beam ($68'' \times 57''$) is displayed in the lower left.

The high resolution velocity field does seem to separate the ring out from the main galaxy. In Figure 8-12 there are two regions (one in the north and one in the south) where the iso-velocity curves stack up. This indicates a very steep gradient in velocity, and is similar to the region in the velocity field of NGC 1784 between the ring and galaxy. The steep gradient region in NGC 4900 surrounds a circular region where the

iso-contours run north-south. In the high resolution optical overlay (Figure 8-13), we do not find any optical emission associated with the regions with velocities corresponding to the ring. Our resolution is not high enough to determine the impact of any spiral arms, star forming regions, or the bar on the HI velocity field.

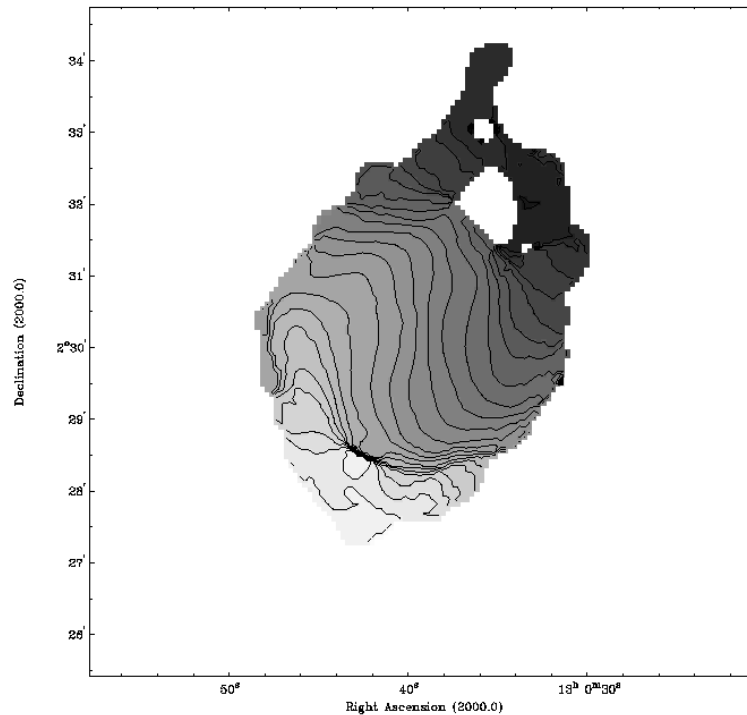


Figure 8-12. Intensity-weighted radial velocity contours of the high resolution data set. Contours are separated by 10 km s^{-1} . Darker grayscales correspond to motion away from the observer.

Position-Velocity Plots

In Figure 8-14, we show Position-Velocity (P-V) plots taken along the supposed major axis of the main body of NGC 4900 ($\text{PA} = 90^\circ$) using the high resolution data cube. This major axis was defined by the model disk calculation, described in a later section. These plots show in all slices, a linear trend in velocity from one side of the galaxy to the other. This is not typical for disk galaxies, which usually show a turn-over to a flat region of rotation. The rotation observed here is more akin to solid body

rotation. The individual slices are very broad, and show significant bearding at their ends, even at this relatively low spatial resolution. These regions have a typical size of about $0.5'$ (2 kpc) and a velocity width of about 20 km s^{-1} . The protrusions are in regions of low surface density (at 3σ contours), but given their size may have dynamical masses of up to $10^7 M_{\odot}$ depending on their HI content. The slices made at and north of the major axis seem to show a curve to higher velocities at high negative radii. This is the opposite of what would be expected from a normal rotation curve. The slice made at $60''$ south of the major axis shows a second intensity peak at high positive radii. This second peak is associated with the ring area south of the galaxy.

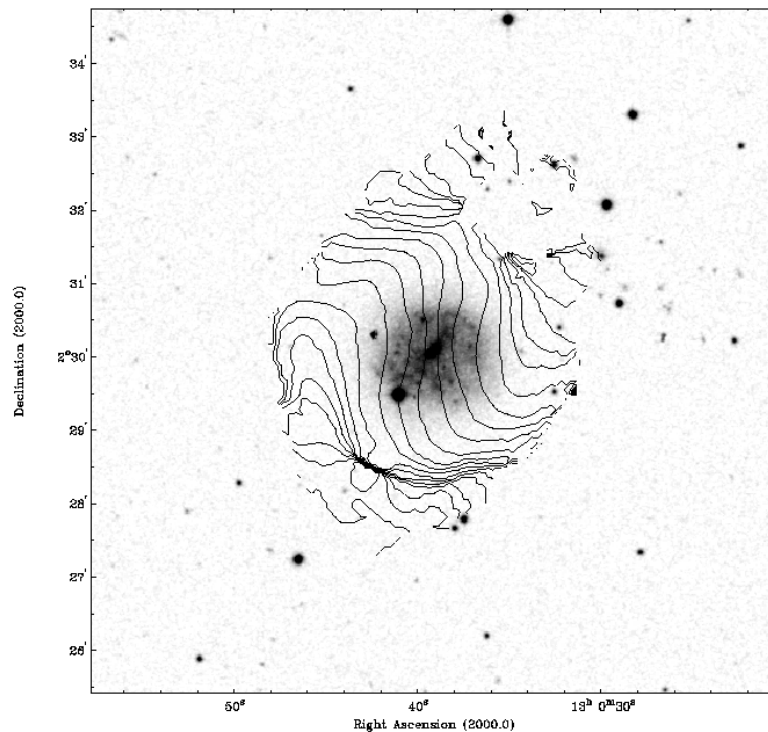


Figure 8-13. Intensity-weighted radial velocity contours of the high resolution data set overlaid on an optical DSS image. Contours are the same as in Figure 8-12.

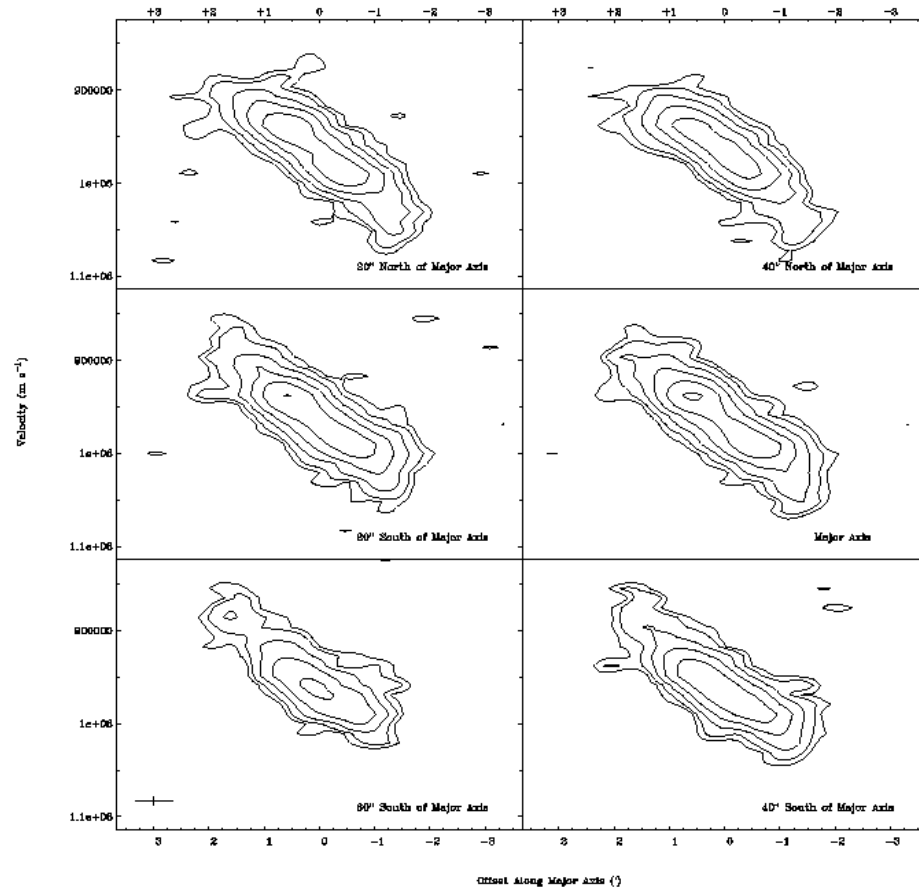


Figure 8-14. A set of P-V slices parallel to and along the major axis of the inner portion of NGC 4900. The contours are at $3, 5, 10, 20,$ and 40σ .

Figure 8-15 shows P-V plots made parallel to the major axis of the arrowhead feature ($PA = 135^\circ$). With these plots we attempted to determine the rotational properties of the ring feature. Similar to Figure 8-14, we found a very broad area of HI emission, again with many beards and protrusions. In the slices made northeast of the major axis, we find a separated island of HI at high negative radii (northwest of the galaxy). As the slices move to the southwest of the galaxy, we find a new island at high positive radii (southeast of the galaxy). The major axis appears to show both islands. If we examine the bubble found in the slices made southwest of the galaxy, we find that the bubble is about $1'$ (4 kpc) in diameter, extends over at least $1'$ of slices, and has a velocity spread of

approximately 40 km s^{-1} . This island has higher column densities than the protrusions mentioned above in Figure 8-14. The center of the island reaches the 10σ flux density level. This value is similar to the satellite found in NGC 1784. We calculate a dynamical mass for the island on the southwest side of the galaxy to be several $10^8 M_{\odot}$, which is in line with it being a satellite galaxy.

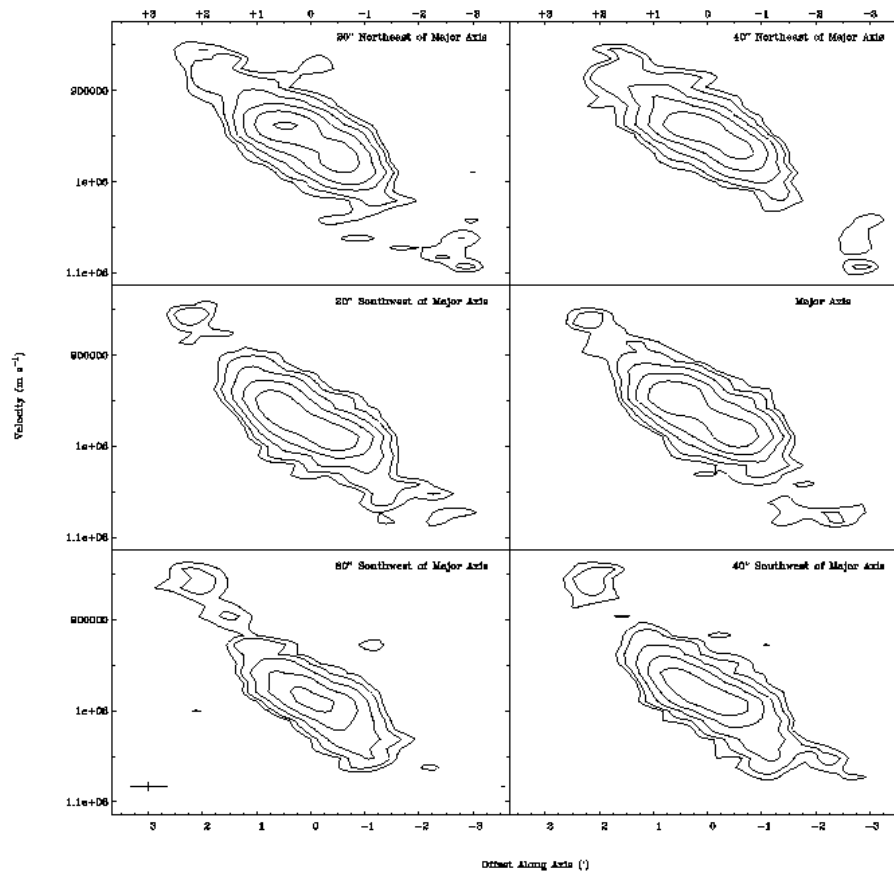


Figure 8-15. A set of P-V slices parallel to and along the supposed major axis of the outer regions of NGC 4900. The contours are at $3, 5, 10, 20,$ and 40σ .

Figure 8-16 shows P-V plots taken along the minor axis of the main galaxy (PA = 0°) made with the high resolution data cube. The HI distribution in the central regions of the galaxy is broad, but typical for a minor axis plot. Outside of $1.5'$, however, we see islands of HI at non-circular velocities. These islands are for the most part separated

from the main body of the galaxy, implying that the ring system is separate from the galaxy and not simply extended emission. The size of the islands in this image is similar to those in Figure 8-15, indicating our mass estimate, although naïve, is not inappropriate.

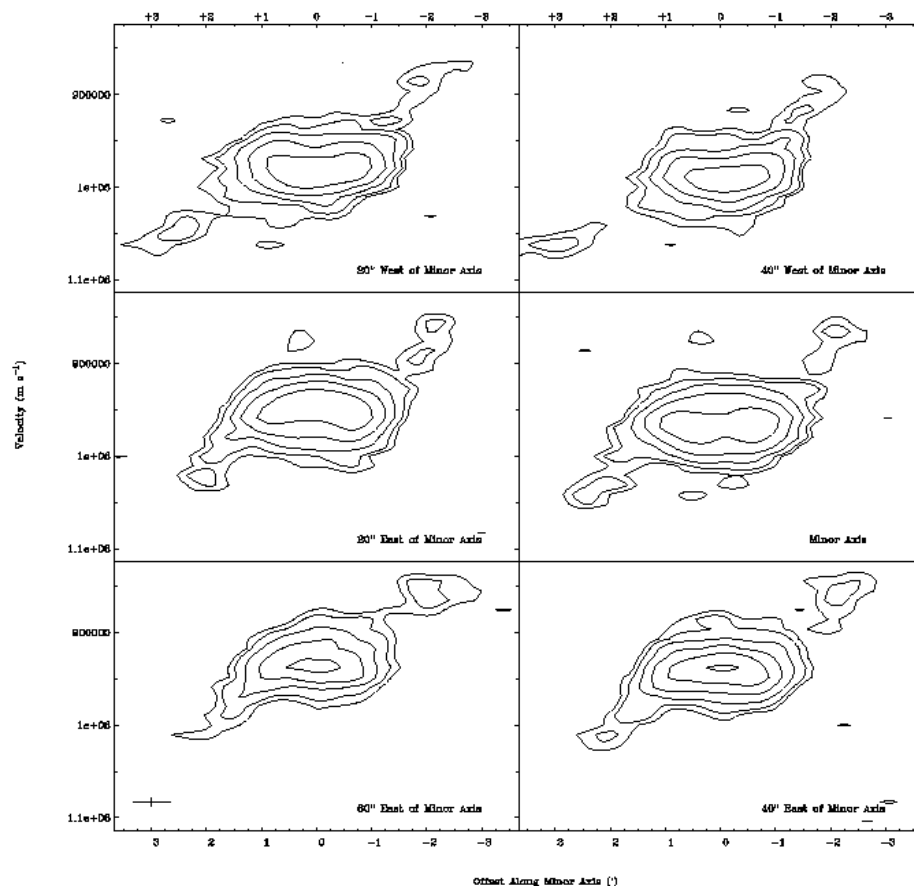


Figure 8-16. A set of P-V slices parallel to and along the minor axis of the inner regions of NGC 4900. The contours are at $3, 5, 10, 20,$ and 40σ .

Rotation Curves and Model Disks

In order to make rotation curves and model disks of NGC 4900, we used the GIPSY task 'reswri' to fit tilted rings to the velocity field. We used our high resolution data set to create our parameter curves. We fit rotational velocities at radii ranging from $20''$ to $140''$ in $30''$ wide annuli. We held the position of the kinematic center and the systemic velocity of the galaxy as fixed parameters, while allowing the rotational

velocity, expansion velocity, position angle, and inclination to be set by the fit. Because of limited flux, we used an average of both the receding and approaching sides of the galaxy. We plot the rotation velocity versus radius in Figure 8-17, expansion velocity versus radius in Figure 8-18, position angle versus radius in Figure 8-19, and inclination versus radius in Figure 8-20.

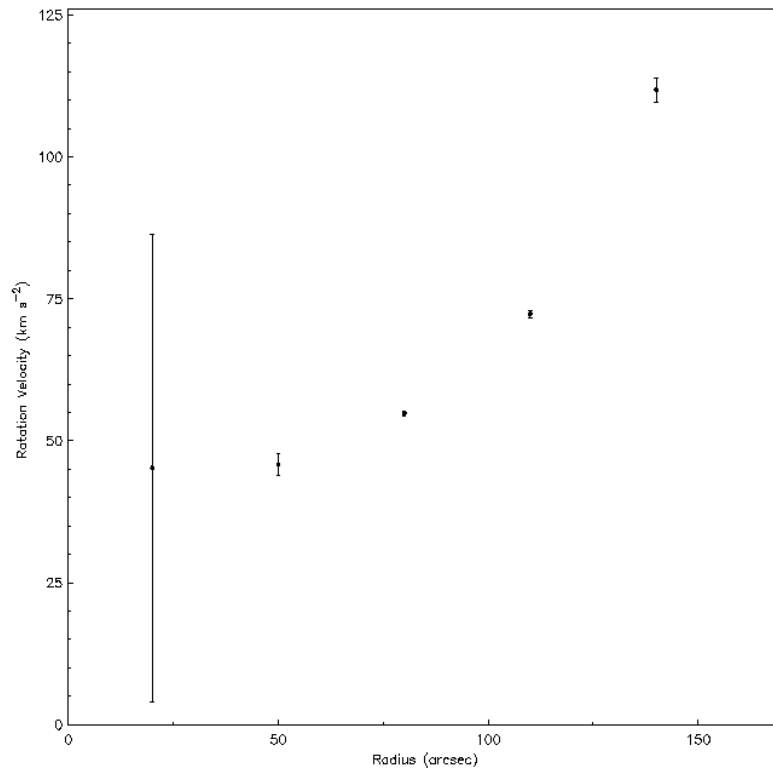


Figure 8-17. Rotation curve of NGC 1784 from the high resolution data set. Data points represent the average of both the receding and approaching sides of the galaxy.

Owing to the atypical characteristics of NGC 4900's morphology and kinematics, our plot of rotational velocity versus radius in Figure 8-17 is very unusual for a disk galaxy. We find that the rotational velocity increases with radius in a manner reminiscent of an exponential curve. Even though it has been suggested by Elmegreen & Elmegreen (1990) that flocculent galaxies are more likely to have a rising rotation curve, the rotation curves examined by Elmegreen & Elmegreen (1990) did have a turn over radius and

remained somewhat flat at large radii. NGC 4900 does not reflect this. The most likely explanation for the appearance of the rotation curve in this galaxy is that the fitting program was confused by the close separation of the ring to the disk. With deeper and higher resolution observations, the two components may be able to be separated, and a more accurate estimation of the rotation curve can be determined.

Using this odd shaped rotation curve, we calculate a value for dynamical mass inside of 140" (9.5 kpc), using a Keplerian, $M = V^2 R G^{-1}$, to model the disk and halo. We measure a radius, R , of 9.5 kpc and V at 9.5 kpc to be 110 km s^{-1} , yielding $M(R) = 2.94 \pm 0.05 \times 10^{10} M_{\odot}$. Comparing this with the HI mass calculated above, we find a value for the ratio $M_{\text{HI}} / M(R)$ of 4% for NGC 4900.

In Figure 8-18 we see that the value for the expansion velocity stays very near to 0 km s^{-1} for the vast majority of the disk. The large value for the innermost point has a large error, and is likely due to poor sampling at the center of the galaxy. The position angle curve (Figure 8-19) shows that the position angle changes by more than 50° over the length of the galaxy. The position angle is nearly horizontal east-west in the center of NGC 4900, and shifts to a northwest-southeast orientation at the outer edges. Similarly, the inclination angle (Figure 8-20) changes by more than 70° over the radius of the galaxy, from close to edge on to nearly face on in the outer regions. The implication in these plots that the position angle and inclination slowly change over the radius of the galaxy is unlikely. Our best resolution is 35". What we are observing in these plots is the effect of instrumental smoothing of emission from the galaxy and ring. With higher resolution observations, we should be able to pick out both features and obtain the proper kinematical parameters for each.

Due to the unusual morphology and kinematics of NGC 4900 we were unable to convert properly our rotational velocities, expansion velocities, position angle, and inclination from the previous figures into a model disk using the GIPSY task 'velfi'. We were able to, however, construct a model reflecting the possible two component configuration in NGC 4900. This model is shown in Figure 8-21. Here we have the inner disk with a position angle of 90° and an inclination of 30° . This region has a flat rotation curve extending out to a radius of $2'$. External to this point, the position angle jumps to 135° and the inclination becomes 70° . This outer region has a flat rotation curve as well. Expansion velocities are held to 0 km s^{-1} throughout the whole model. This model in Figure 8-21 does an adequate job of imitating the real high resolution velocity field shown in Figures 8-12 and 8-13. We see the changing orientations of the two components, as well as the large velocity gradients at the north and south ends of the main galaxy. We are unable to create the twisting "S" shaped contours in the main galaxy seen in the real velocity field, but we interpret these to be resolution effects due to the superposition of ring material on the outer edges of the main galaxy. We are unable to determine the rotational velocity structure of the ring, due to the limited flux in this region.

Neutral Hydrogen Ring

As mentioned in the previous sections, the most probable explanation for NGC 4900's disturbed morphology and kinematics is the presence of an inclined HI ring about the main body of the galaxy. This ring is similar to the one seen in NGC 1784, however, the overall system is less massive (galaxy + ring is $1 \times 10^{10} M_\odot$ for NGC 4900 and a few $10^{11} M_\odot$ for NGC 1784), the ring is relatively more massive in NGC 4900 (10%

compared to less than 5%), the sense of the ring's rotation is prograde, and the observations are not of as high quality as with NGC 1784.

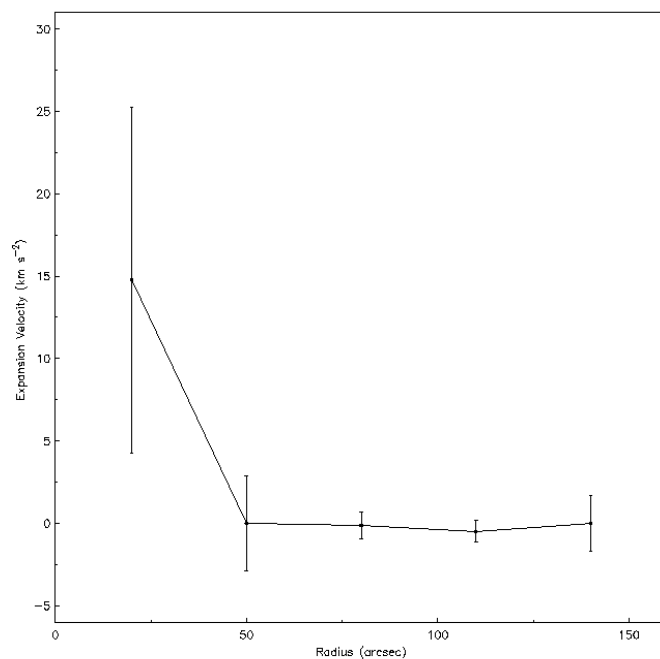


Figure 8-18. Expansion velocity as a function of radius in NGC 4900

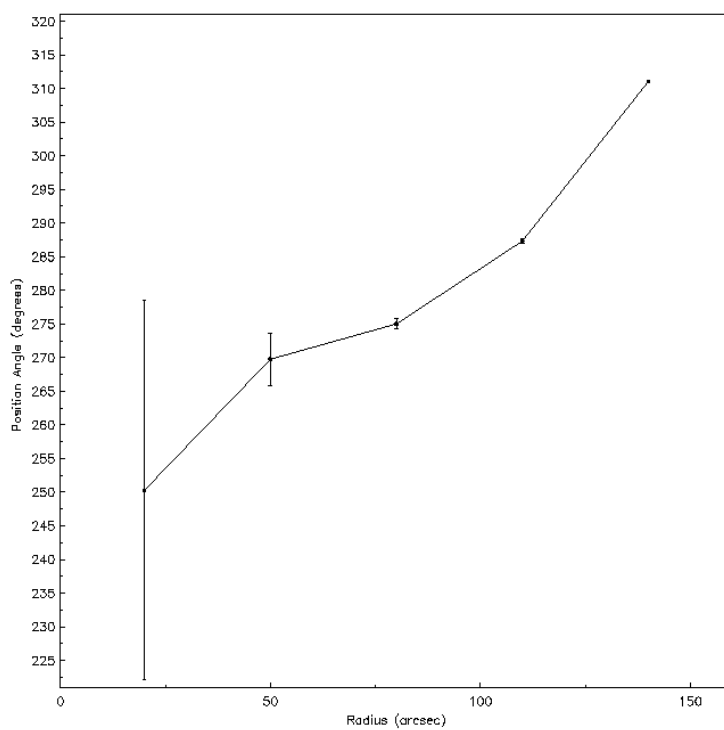


Figure 8-19. Kinematic position angle of NGC 4900 as a function of radius

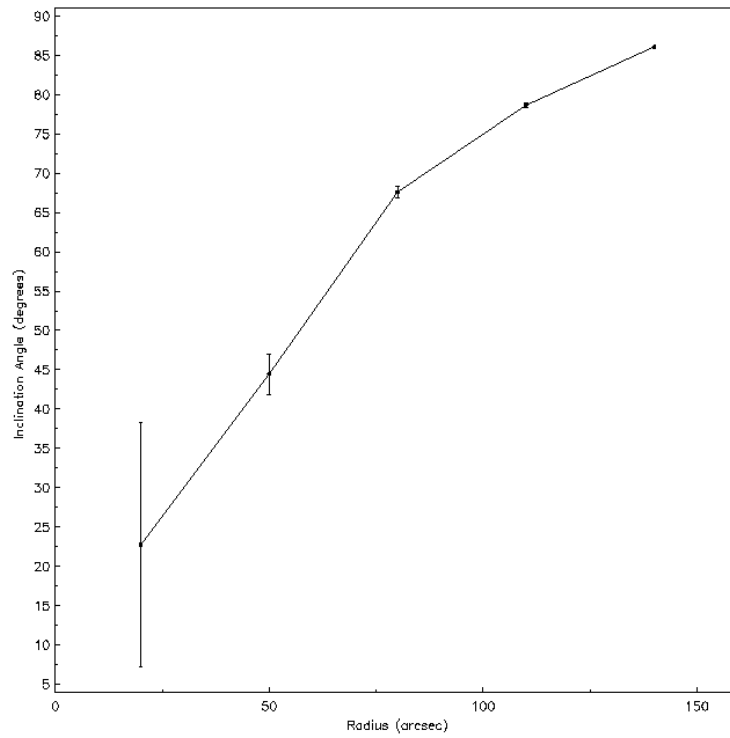


Figure 8-20. Inclination angle of NGC 4900 as a function of radius

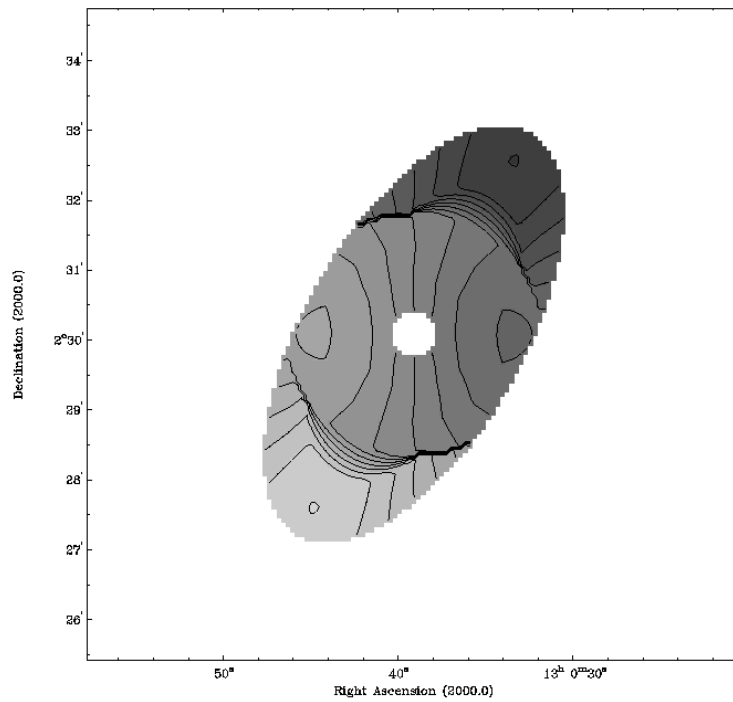


Figure 8-21. Model velocity field constructed from kinematical data of both the inner regions of NGC 4900 and the supposed ring

As with NGC 1784, the most likely production mechanism for this ring is an interaction with a small ($10^9 M_{\odot}$) satellite galaxy. The disturbed optical morphology of NGC 4900 gives us the first clue that an interaction has occurred. Besides the bright bar, there does not appear to be any coherent structure in the disk of NGC 4900. Large knots of star formation are present, but no spiral pattern is obvious. Disturbed optical disks are common in minor mergers / interactions, especially when the interaction is in the prograde sense. In the case of NGC 1784, there is evidence to believe that the interaction was retrograde, and this may explain why the optical disk is not greatly disturbed. NGC 4900's less massive disk (by an order of magnitude) and a prograde interaction could have contributed to its disturbed optical appearance.

From calculations shown in the P-V plot section of this chapter, we believe that the ring contains up to $10^9 M_{\odot}$ of material. It is uncertain if NGC 4900 has already cannibalized material from the past satellite. Assuming that the ring is mostly complete, the former satellite must have made at least one full orbit around NGC 4900. Given the small size of NGC 4900 and its ring, this could have been accomplished in several 10^8 years. We conclude based on the brightness of the bar, lack of optical structure in the disk, and presence of gas within the bar region of NGC 4900, that this interaction began very recently (~ 1 Gyr or less).

The ring, with a maximum projected radius of 18 kpc, lies within the tidal radius of NGC 4900. Depending on the clumpiness of the ring (higher resolution observations will be necessary to determine this), we can expect material from the ring to slowly fall on to the disk of NGC 4900 over the next several 10^9 years. We do not observe any optical material associated with the ring.

Summary

NGC 4900 is a rather disturbed disk galaxy system. NGC 4900 is potentially the richest in HI of our sample. We find an HI morphology that is most likely composed of two components, a galaxy disk and an inclined ring. Observations of the kinematics of NGC 4900 reinforce this picture, showing that the position angle of rotation for the disk is misaligned from the ring feature. We propose that the ring is the result of an interaction with a small ($10^9 M_{\odot}$) satellite galaxy in the not too distant past (< 1 Gyr). The satellite was most likely on an inclined, prograde orbit about NGC 4900 and passed very close to the disk, evidenced by the optical disturbance in the disk, and small radius of the ring. P-V slices through the disk of NGC 4900 show evidence of numerous small clouds ($10^7 M_{\odot}$) moving with non-circular velocities. These slices also show that the rotation of the disk may be solid body as opposed to differential. Further deep, high-resolution ($< 20''$) HI observations are necessary to determine the properties of the interaction, and to study the manner of disturbance in the disk.

CHAPTER 9 NEUTRAL HYDROGEN OBSERVATIONS OF NGC 4904

NGC 4904 is another galaxy in our sample that shows a disturbed optical morphology. It is classified by Elmegreen & Elmegreen (1982) as having an arm class of "2". This puts it on the very flocculent end of the arm strength spectrum. A close examination of the optical images shows that NGC 4904 has a very bright, but twisted bar, and a faint hint of three armed structure. Typically, three armed galaxies are found to be involved in interactions. Color maps of the galaxy show a strong dust lane along one side of the bar, with the galaxy disk being primarily red.

NGC 4904 is at a middle distance in our sample, with a recessional velocity of 1169 km s^{-1} (17 Mpc, where $H_0 = 70 \text{ km s}^{-1} \text{ Mpc}^{-1}$). This is one of the smaller galaxies in our sample, with an angular diameter of $2.2'$, corresponding to a physical diameter of 10.4 kpc. Single dish observations of the galaxy have been performed by Lewis et al. 1985, who found an HI flux of $10.76 \text{ Jy km s}^{-1}$, an HI line width of 200 km s^{-1} , and an HI mass of $1.28 \times 10^9 M_\odot$. Also, they found the HI spectra of NGC 4904 to be somewhat asymmetric. This galaxy, like NGC 4900, is projected into the Virgo Southern Complex, but was classified as isolated by Elmegreen & Elmegreen (1982).

Observations

Radio observations of NGC 4904 were obtained at the Very Large Array in September of 2002 and May of 2003 using the C and D configuration, respectively. The spectrometer was composed of 64 channels with a 10.5 km s^{-1} velocity resolution. The total band width was 3.125 MHz (640 km s^{-1}), and the central heliocentric velocity was

1169 km s⁻¹. The observing parameters for the observations are summarized in Table 9-

1.

Table 9-1. Parameters of VLA HI observations of NGC 4904

Configuration	C	D
Number of antennae	27	27
V _{sys} (km s ⁻¹)	1169	1169
Phase calibrator	1311-222	1311-222
Flux calibrator	1331+305	1331+305
Time on source	7.5	3.8

Table 9-2. Characteristics of Naturally Weighted CLEANed Channel Maps

Parameter	Low Resolution	High Resolution
FWHP synthesized beam (")	67" x 54"	21" x 19"
FWHP synthesized beam (kpc)	5.5 x 4.5	1.7 x 1.6
Theoretical rms noise (mJy beam ⁻¹)	0.25	0.25
Observed rms noise (mJy beam ⁻¹)	0.3	0.36
Rms noise (K)	0.09	1.08
Peak temperature (K)	6.9	34.6
Peak S/N	77	32

The C and D configuration data sets were edited, calibrated and continuum subtracted using the typical procedures of the Astronomical Image Processing System (AIPS) package. The data sets were combined using the AIPS task DBCON. The combined data set was then imaged twice using the AIPS task IMAGR to provide us with two image cubes (α , δ , ν) reflecting the maximum range of spatial resolution and sensitivity that our data would allow. We created a low resolution cube by using a natural weighting scheme and a high resolution data cube by imaging the data with a uniform weighting scheme. We CLEANed the data cubes in AIPS down to an rms level of 0.3 and 0.4 mJy beam⁻¹ for the low resolution and high resolution images, respectively. Further details of the statistics for each data cube are presented in Table 9-2. Analysis on

the completed and CLEANed image cubes was conducted using the Gronigen Image Processing System (GIPSY) package.

Neutral Hydrogen Morphology

The channel maps shown in Figures 9-1 and 9-2 were used in moment analyses to obtain global density and temperature weighted radial velocity images of the neutral hydrogen in NGC 4904. Moment maps were constructed with the AIPS task MOMNT. A flux cut off of three times the rms noise level (σ) of the unsmoothed data was used. The low resolution, naturally weighted global distribution of the neutral hydrogen in NGC 4904 is shown in grayscale in Figure 9-3 and overlaid on an optical image of the galaxy in Figure 9-4. The high resolution, uniformly weighted global distribution of the neutral hydrogen is shown in grayscale in Figure 9-5 and overlaid on an optical image of the galaxy in Figure 9-6. The lowest contours are drawn at the 2σ level.

Low Resolution Neutral Hydrogen Morphology

The low resolution channel maps of NGC 4904 (Figure 9-1) show a similar structure to those for NGC 4900. If we focus only on the highest contours in the system, we find a fairly symmetric well formed galaxy, where the gas moves bottom right to upper left as velocity decreases. In the lower contours, however, we see that the gas is stretched out along an east-west axis. In the channel maps corresponding to the highest recessional velocity ($v = 1272$ through 1231 km s^{-1}), we see gas extending west and north of the main body of the galaxy. In the central few channels ($v \sim 1169 \text{ km s}^{-1}$) the hydrogen takes on an "S" like morphology. This morphology is typically due to a warp or gas outside of the plane of the galaxy, as in NGC 1784 and NGC 4900. Finally, at the lowest velocities ($v = 1118 - 1067 \text{ km s}^{-1}$), the galaxy's gas is extended to the east.

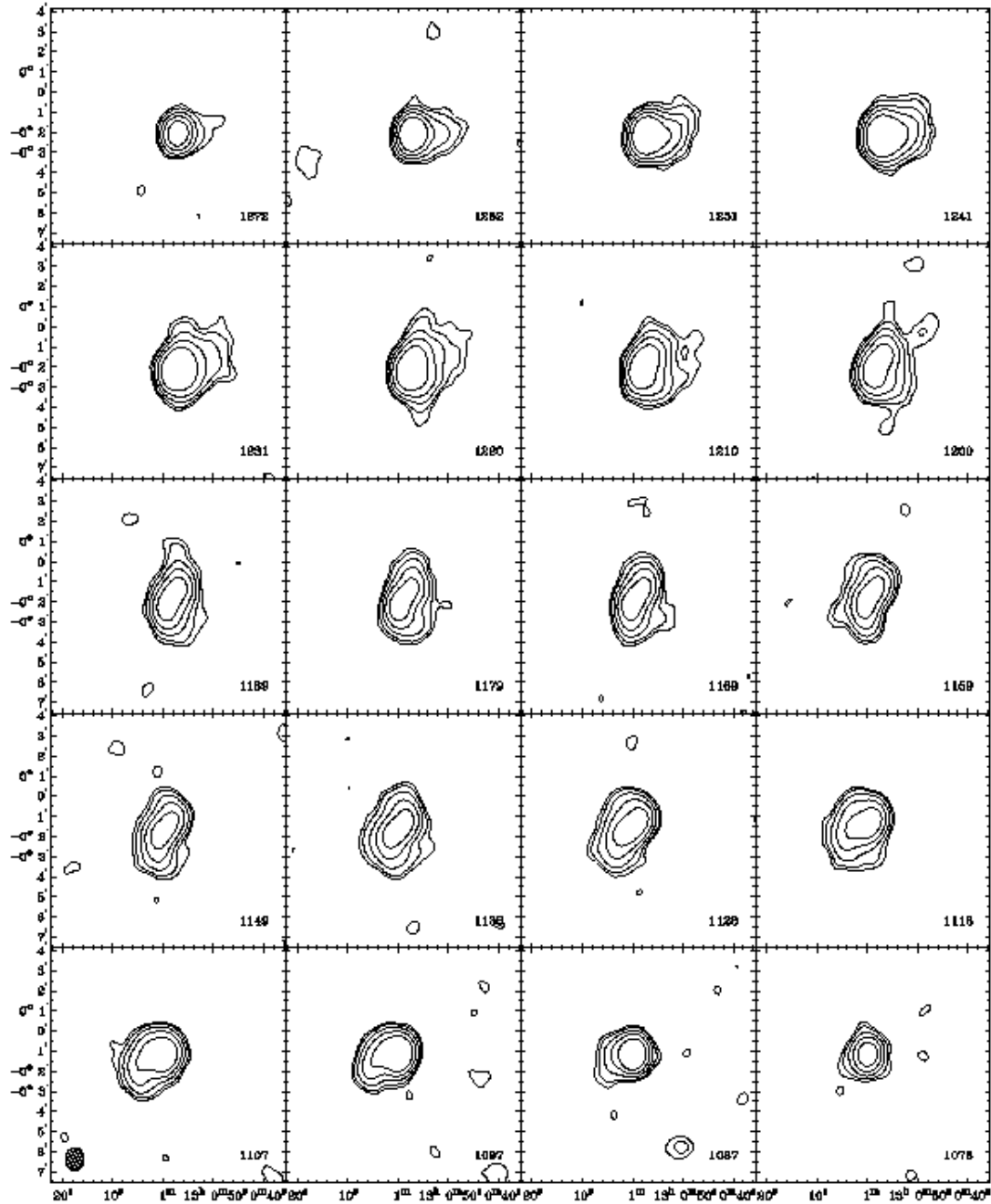


Figure 9-1. Individual, naturally weighted, CLEANed channel images of the low resolution data. Channel velocities are given in the lower right corner of each panel in km s^{-1} . The synthesized beam ($67'' \times 54''$) is shown in the lower left hand corner of the bottom left panel. Contours are at the 3 ($2.7 \times 10^{18} \text{ cm}^{-2}$), 5 , 10 , 20 , and 40σ flux levels.

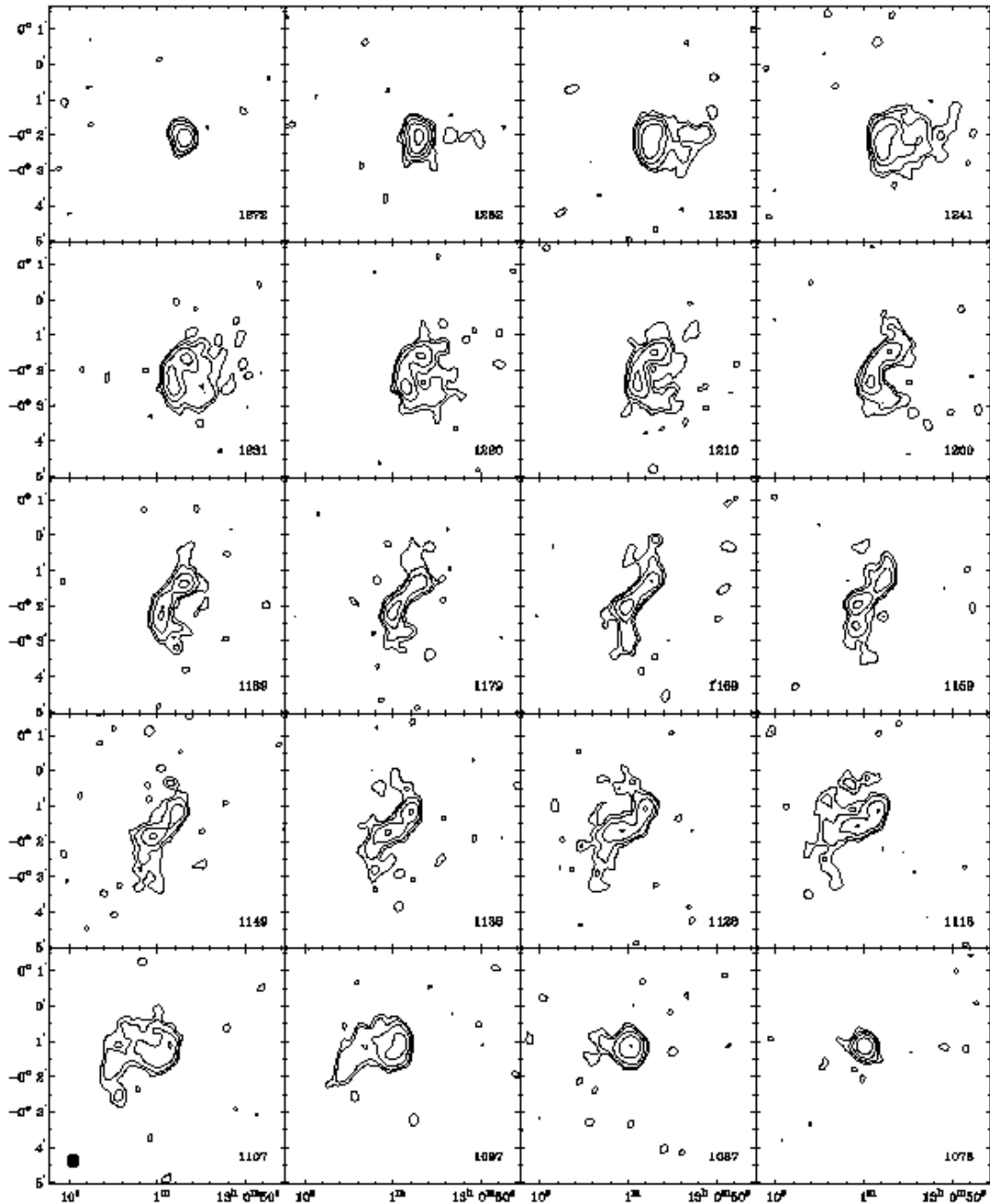


Figure 9-2. Individual, naturally weighted, CLEANed channel images of the high resolution data. Channel velocities are given in the lower right corner of each panel in km s^{-1} . The synthesized beam ($21'' \times 19''$) is shown at the bottom left of the lower left hand channel map. Contours are at the 3 ($3.0 \times 10^{19} \text{ cm}^{-2}$), 5, 10, 20, and 40σ flux levels.

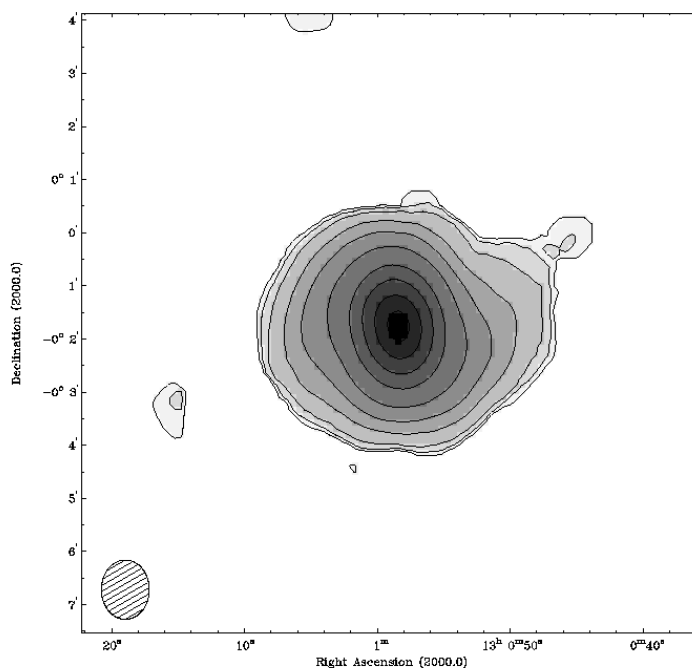


Figure 9-3. Grayscale with contours of the total HI surface density from the low resolution data set. The peak flux corresponds to a column density of $1.2 \times 10^{21} \text{ cm}^{-2}$. Contours are at 0.5 (the 2σ flux level), 1, 2, 3, 5, 10, 20, 40, 60, 80, and 95% of the peak flux. The synthesized beam ($67'' \times 54''$) is shown at the bottom left.

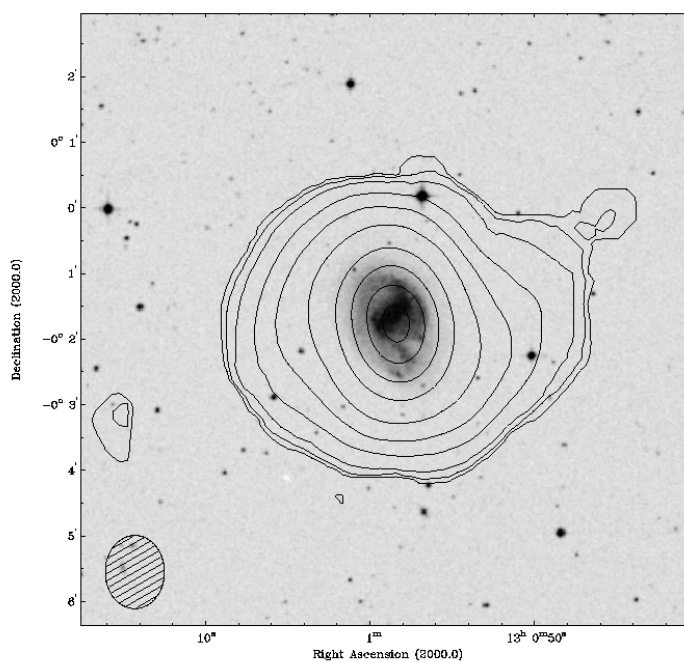


Figure 9-4. Contours of the total HI surface density from the low resolution data set over an optical DSS image of NGC 4904. Resolution and contour levels are the same as Figure 9-3.

The low resolution HI total intensity map (Figure 9-3) shows the same east-west stretching as the channel maps. The highest contour levels are regular and concentric, while the lowest levels are pulled horizontally, particularly towards the west. In fact, Figure 9-3 looks very similar to Figure 8-3 rotated clockwise one quarter turn. The object located at the eastern edge of the field is noise. Even though there is a 5σ contour associated with it, a spectrum of the region shows that there is no emission outside of one channel. Without a detection in multiple channels, we must conclude that the object is not real. Figure 9-4 shows that the central peak of the HI distribution is not significantly offset from the center of the optical galaxy. We find the peak low resolution column density of gas in NGC 4904 to be $1.23 \times 10^{21} \text{ cm}^{-2}$. The HI diameter of NGC 4904 is $5'$, corresponding to 24 kpc. This extended diameter is not quite as large as the potential ring system in NGC 4900. The HI diameter is slightly more than 2x the optical diameter. Considering just the more circular central HI contours, then the HI diameter would shrink to about $4'$, or 19 kpc.

High Resolution Neutral Hydrogen Morphology

Figure 9-2 shows the high resolution channel maps for NGC 4904. Here we again see gas stretched along an east-west axis in the early and late channel maps ($v \sim 1251 \text{ km s}^{-1}$ and $v \sim 1097 \text{ km s}^{-1}$). The central channels show a distinctive "S" shape as in NGC 1784 and NGC 4900. In all cases, the gas stretched out from the main body of the galaxy only reaches the 5 - 10σ level, so it is unlikely that there is a significant amount of mass involved in any second system.

Figure 9-6 shows that the overall high resolution morphology of NGC 4904 is twisted into an "S" like shape. The highest, central contours are aligned north-south,

while the outer contours follow more of an east-west pattern. Figure 9-6 shows that the peak HI column densities are aligned with the bar and star forming regions of the western side of the galaxy. No significant area of star formation is associated with the highest column densities of HI. We also find that the bar of NGC 4904 is rich in HI. As in NGC 4900, this may be an indication of the young age of the bar. We find the peak column density to be $1.69 \times 10^{21} \text{ cm}^{-2}$.

Global Neutral Hydrogen Properties

Figure 9-7 shows the HI spectrum of NGC 4904 created with the low resolution data set. We find a typical double horned spectrum that is skewed to higher velocities. This is consistent with Figure 9-3, showing that the galaxy extends further to the west. We calculate a total HI flux of $11.5 \pm .8 \text{ Jy km s}^{-1}$. Our flux measurement is similar to Lewis et al. (1985). This flux corresponds to an HI mass of $8.0 \times 10^8 M_{\odot}$. We measure a velocity width of 200 km s^{-1} , similar to Lewis et al. (1985). A V^2R calculation gives us a total mass for the galaxy of $2.8 \times 10^{10} M_{\odot}$. We calculate a $M_{\text{HI}} / M_{\text{tot}}$ ratio to be 3%. This value may be, in fact, a lower limit due to the extended nature of the HI morphology. If the outer edges of the low resolution HI map are associated with a separate structure rather than the main galaxy, then it is possible that we have overestimated the radius of the galaxy for this calculation. An downward adjustment of 1' in the angular radius of the galaxy would yield a reduction of 4 kpc in the physical radius of the galaxy. This change would push our mass ratio up nearer to 5%, which would be higher than most galaxies in this sample. From our spectrum of NGC 4904, we calculate a 3σ HI flux level of 0.023 Jy. This corresponds to a conservative minimum

mass detection level of $4.5 \times 10^7 M_{\odot}$ for an isolated HI cloud, assuming that it appears in 3 continuous channels.

Figure 9-8 is the radial HI profile from both the high and low resolution data set. This galaxy shows a similar profile to other galaxies in the sample. We find that the HI emission cuts off quickly below the $1 \times 10^{20} \text{ cm}^{-2}$ level in accordance with the predictions of Maloney (1993).

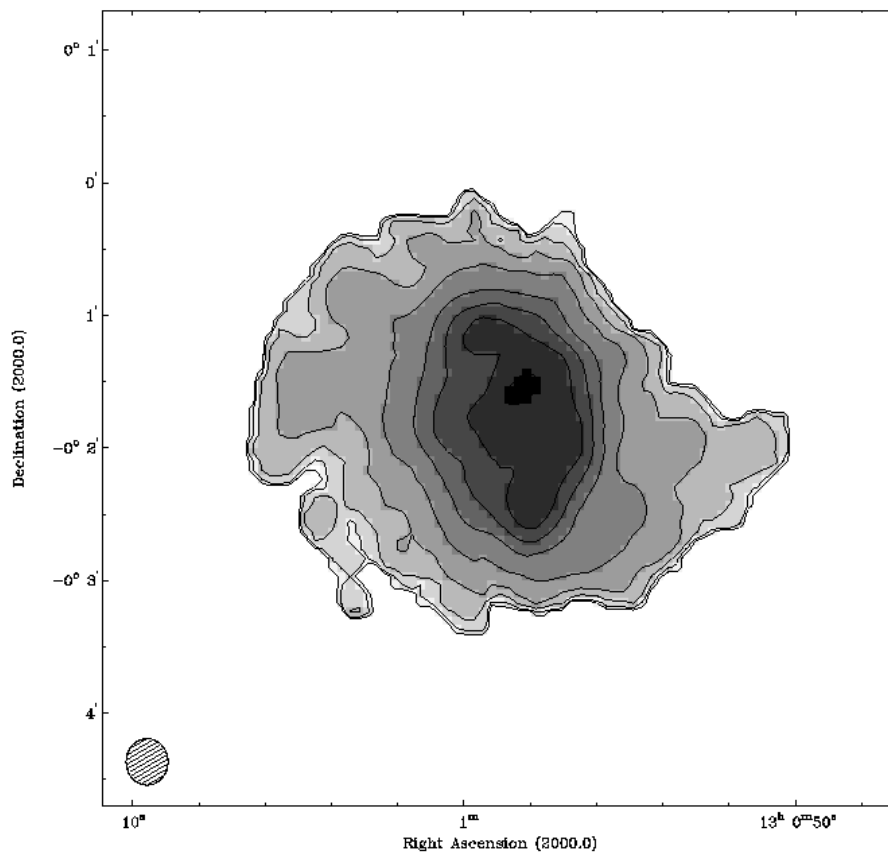


Figure 9-5. Grayscale and contours of the total HI surface density from the high resolution data set. The peak flux corresponds to $1.7 \times 10^{21} \text{ cm}^{-2}$. Contours are at 1 (the 2σ flux level), 2, 5, 10, 15, 20, 40, 60, 80, and 95% of the peak flux. The synthesized beam (21" x 19") is shown at the bottom left.

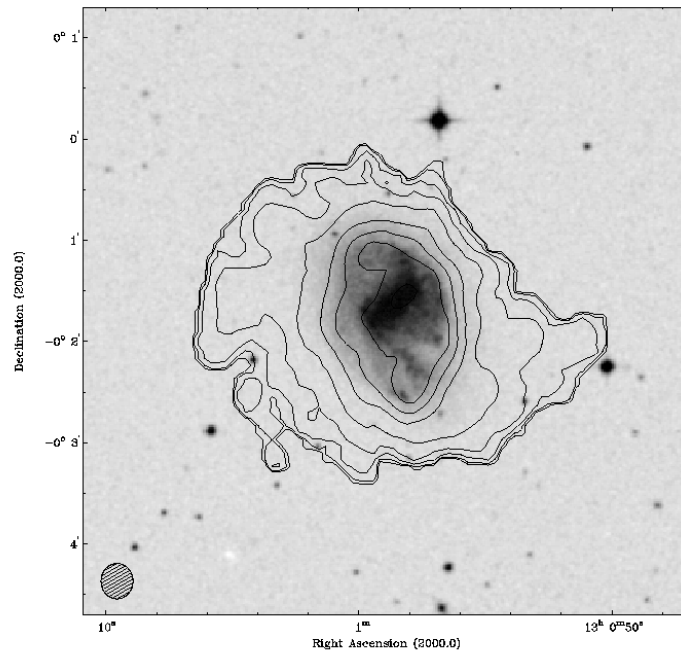


Figure 9-6. Contours of the total HI surface density from the high resolution data set overlaid on an optical DSS image of NGC 4904. Resolution and contour levels are the same as Figure 9-5.

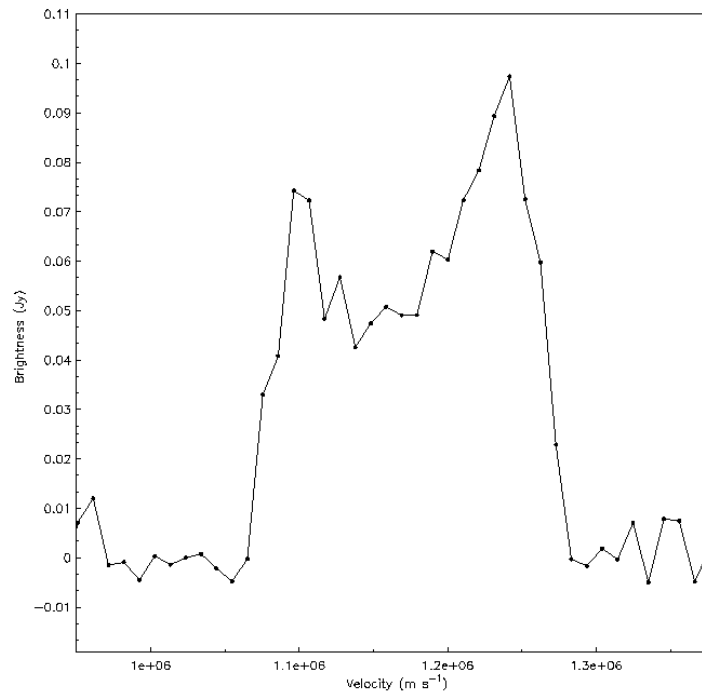


Figure 9-7. The HI flux density versus velocity for the low resolution data set. The velocity resolution here is 10 km s^{-1} .

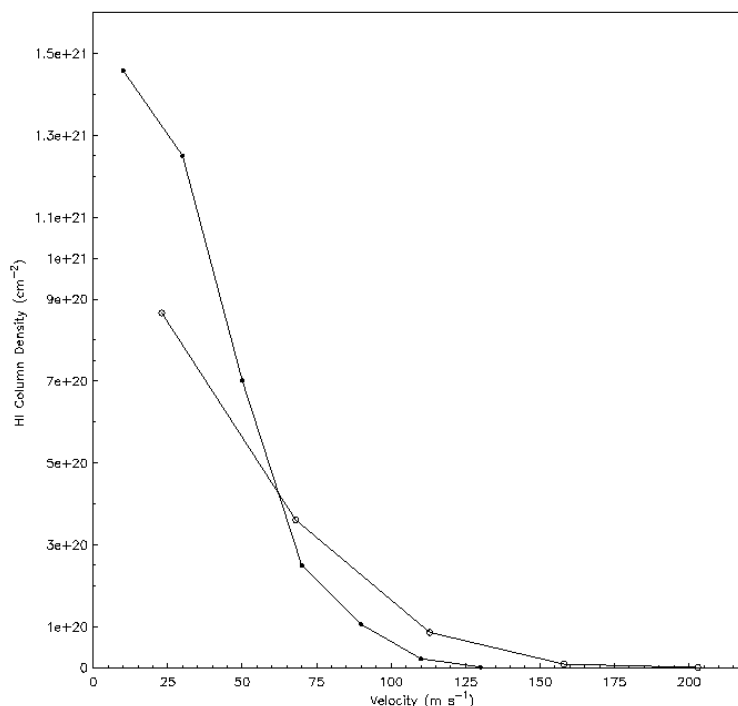


Figure 9-8. The HI radial density profiles from the high resolution data set (closed circles) and the low resolution data set (open circles)

Neutral Hydrogen Kinematics

Figure 9-9 shows the HI velocity field for NGC 4904 created with our low resolution data set. Figure 9-10 shows the HI velocity field for NGC 4900 created with our high resolution data set. Figure 9-11 shows this same field overlaid on an optical DSS image of the galaxy. The contours in all three images are separated by 10.5 km s^{-1} , and the central contour is at a systemic velocity of 1169 km s^{-1} . The low resolution velocity field shows iso-velocity curves that are generally curved into an "S" pattern similar to the channel maps in Figures 9-1 and 9-2. The outer edges of the galaxy show a region of constant velocity that still seems to be twisted. The high resolution velocity field shows a much more interesting picture. The general sense of the inner part of the galaxy seems to be aligned from northeast to southwest. This is interesting, because the optical bar of the galaxy runs along the minor axis of the velocity field. This can easily

be seen in Figure 9-11. Further study at higher resolution (B configuration at the VLA) may allow us to determine radial motions of the gas in the bar. This has not been typically accomplished before. In Figure 9-11, we see the iso-velocity curves begin to twist outside of the optical galaxy. At the edge of the field, we see secondary peaks in the velocity, and the position angle of rotation is nearly east-west. We believe that the twist and secondary peak are due to a ring of gas similar to the one in NGC 1784 and NGC 4904.

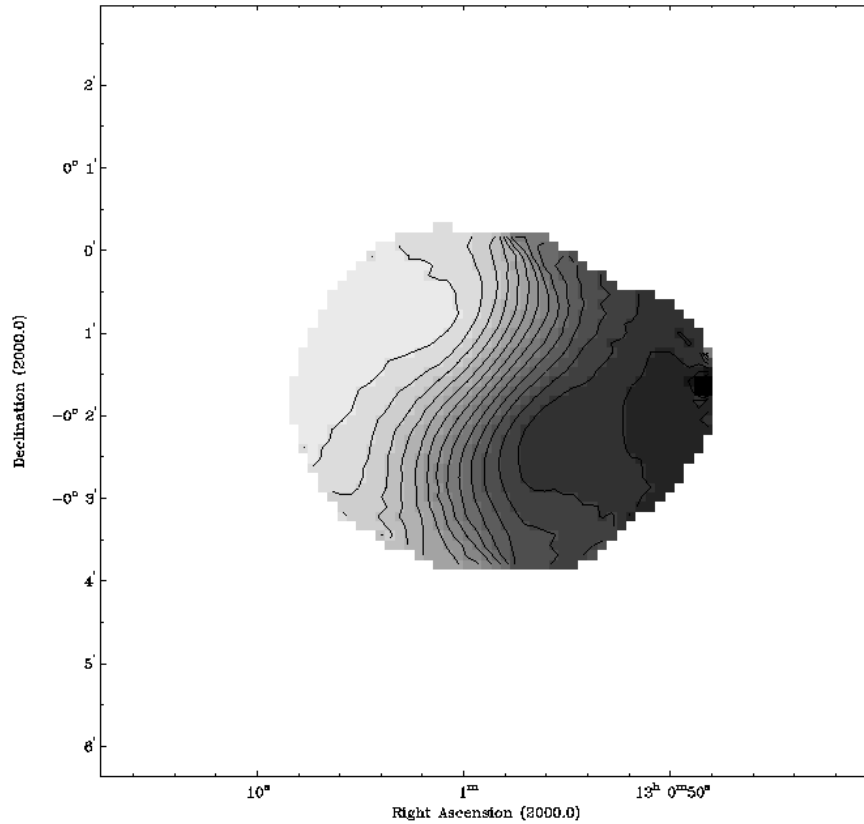


Figure 9-9. Intensity-weighted radial velocity contours of the low resolution data. Contours are separated by 10 km s^{-1} . Motion toward the observer is displayed with lighter grayscales. The central velocity contour is at 1169 km s^{-1} .

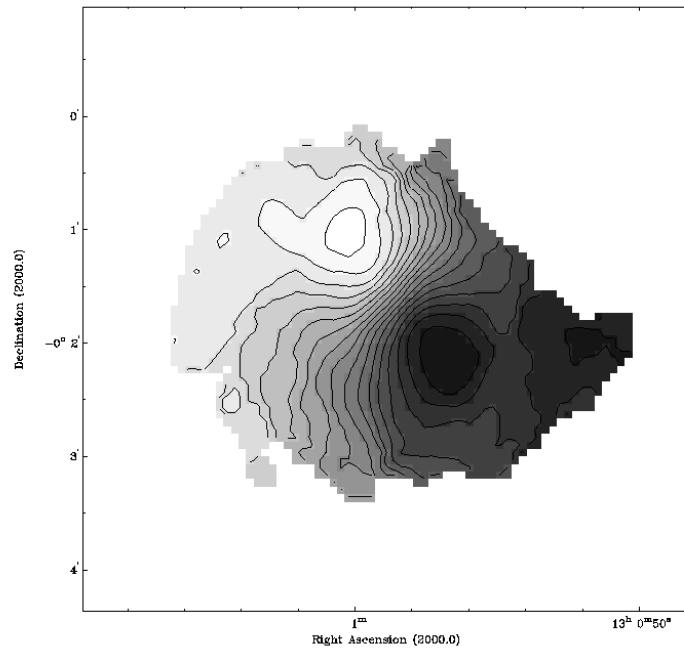


Figure 9-10. Intensity-weighted radial velocity contours of the high resolution data set. Contours are separated by 10 km s^{-1} . Darker grayscales correspond to motion away from the observer.

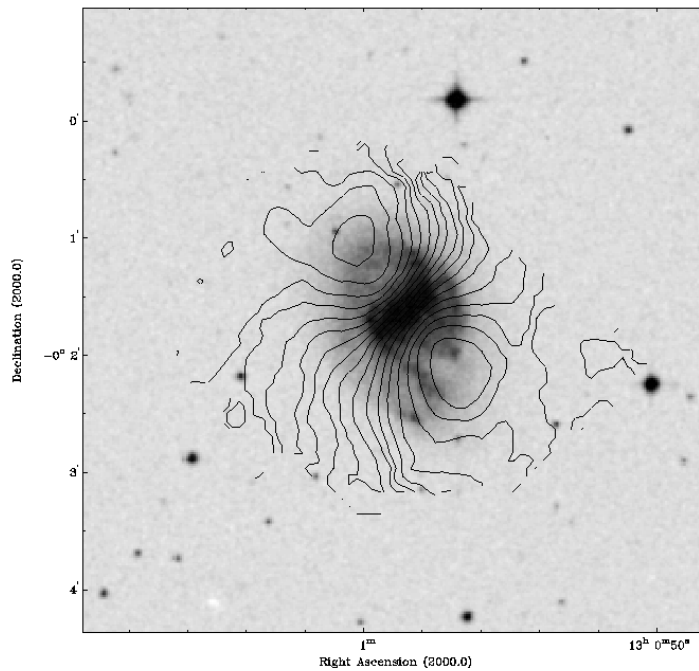


Figure 9-11. Intensity-weighted radial velocity contours of the high resolution data set overlaid on an optical DSS image of the galaxy. Contours are the same as in Figure 9-10.

Position-Velocity Plots

In Figure 9-12, we show Position-Velocity (P-V) slices taken parallel to the major axis of the inner part of NGC 4904 (PA = 45) made with the high resolution data cube. The major and minor axes of the inner parts of the galaxy were determined by examining the iso-velocity curves in the inner regions of the galaxy and initially determining by eye their position angle. These values were bootstrapped to the values used here in the determination of our model disks (later section). The position angle of the outer ring was determined by eye. The shape of the major axis P-V plot is fairly typical, however, we do note that the negative RA edge of the galaxy is very broad in velocity. Overall, most of the plots show a trend back towards the central velocity at the outer RA edges. This effect is not as pronounced as in NGC 1784, but could still be indicative of a warp in the galaxy. In the cuts northwest of the major axis, we find a disturbed and broad positive RA edge of the galaxy. In both cuts we see a hole in the HI distribution. The 40" northwest cut shows a large tongue of gas extending below the hole. The cause of this hole is unclear. Perhaps this is evidence of the second component (ring) about the galaxy. It is difficult to estimate the mass of the gas in this tongue because it only appears in one cut. All of the cuts, except for the major axis, seem to show significant bearding, most likely due to the presence of numerous, small $10^7 M_{\odot}$ clouds.

Figure 9-13 shows a set of P-V plots parallel to the position angle of the outer edges of the HI field (PA = 90). Here we see similar features to the major-axis P-V slices, but overall the cuts are more dysmorphic. In the cuts made 40" northwest and 40" southeast of the central slice, we see secondary peaks of HI emission. For the northwest cut, the secondary peak is at -2' RA. For the southeast cut, the secondary peak is at just less than +2' RA. These peaks are our best evidence for a secondary system (ring) of HI

associated with NGC 4904. The regions around the peaks seem to exist for most of the slices, but at a very low emission level. It is unlikely that very much mass is associated with any possible ring system in this galaxy. The secondary peaks only occur at the 5- 10σ level. At the largest, the ring system would have a total mass on the order of about $10^7 M_{\odot}$. However, with a prograde orbit, and a close approach (10 - 15 kpc), an interacting satellite could cause significant upheaval in the main galaxy.

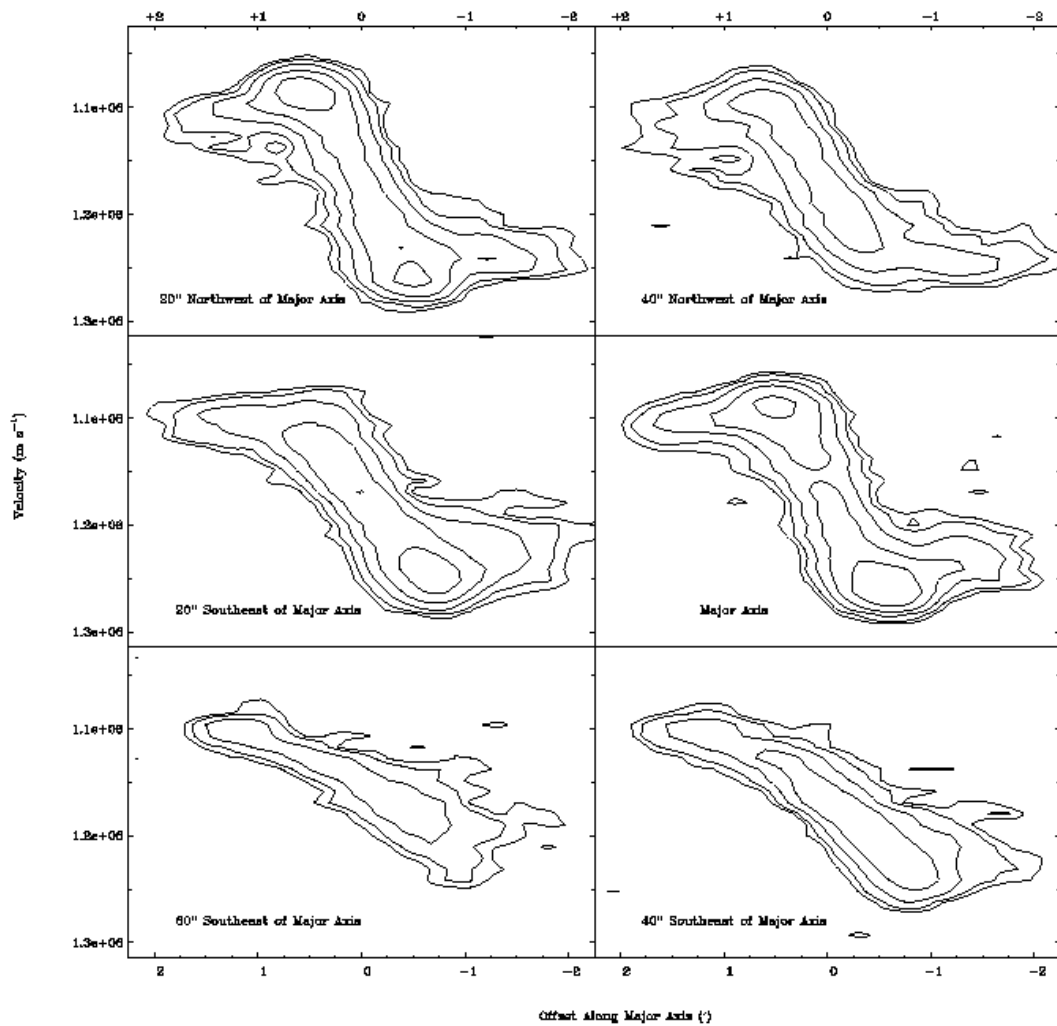


Figure 9-12. A set of P-V slices parallel to and along the major axis of NGC 4904. The contours are at 3, 5, 10, 20, and 30σ .

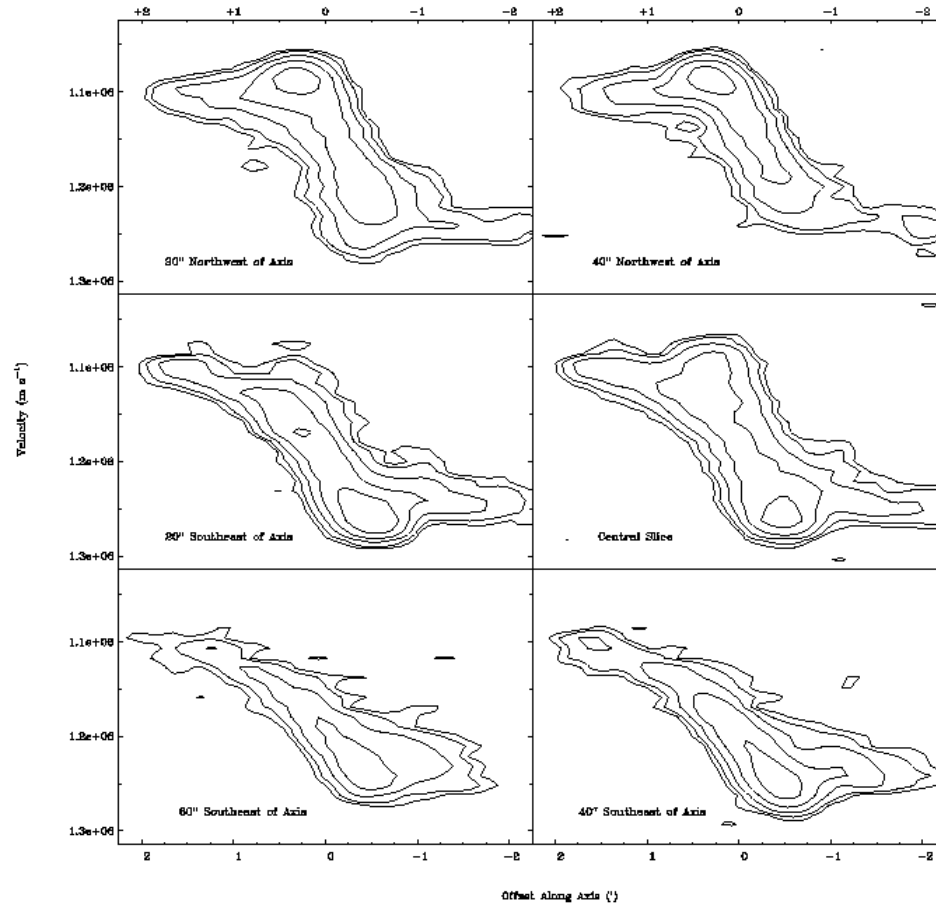


Figure 9-13. P-V plots along and parallel to the position angle of the outer ring. Contours are at 3, 5, 10, 20, and 30σ .

In Figure 9-14, we show plots made parallel to the minor axis of the inner part of the galaxy, or along and parallel to the optical galaxy. The cut along the minor axis shows a very broad velocity profile. This is in some sense probably due beam smearing combined with the small angular size of the galaxy. However, it likely also represents a significant amount of gas either out of the plane of the galaxy or at non-circular velocities. We can not determine the motion of gas in the bar in this image due to the small angular size of the bar. Our resolution, even at its best, does not get down to this level. Cuts made north of the galaxy down to $20''$ southwest of the minor axis show the a finger of gas reaching to positive RA's. Cuts made south of the minor axis show a finger

of gas reaching to negative RA's. In a similar sense to Figure 9-13, this is gas associated with the ring. We even observe a secondary peak in the cut made 60" southwest of the minor galaxy. Unfortunately, we do not possess the resolution or sensitivity to separate this gas from the main body of the galaxy. Given that the column densities of HI in the ring region do not appear to rise much above $5 \times 10^{19} \text{ cm}^{-2}$, and that the cross sectional area of the ring is about $0.5'$, we conclude that the HI mass of the ring shouldn't be more than a few $10^7 M_{\odot}$ and that the total mass should not be much more than 10 - 20 times that value, given typical values of $M_{\text{HI}} / M_{\text{dyn}}$ seen in other systems.

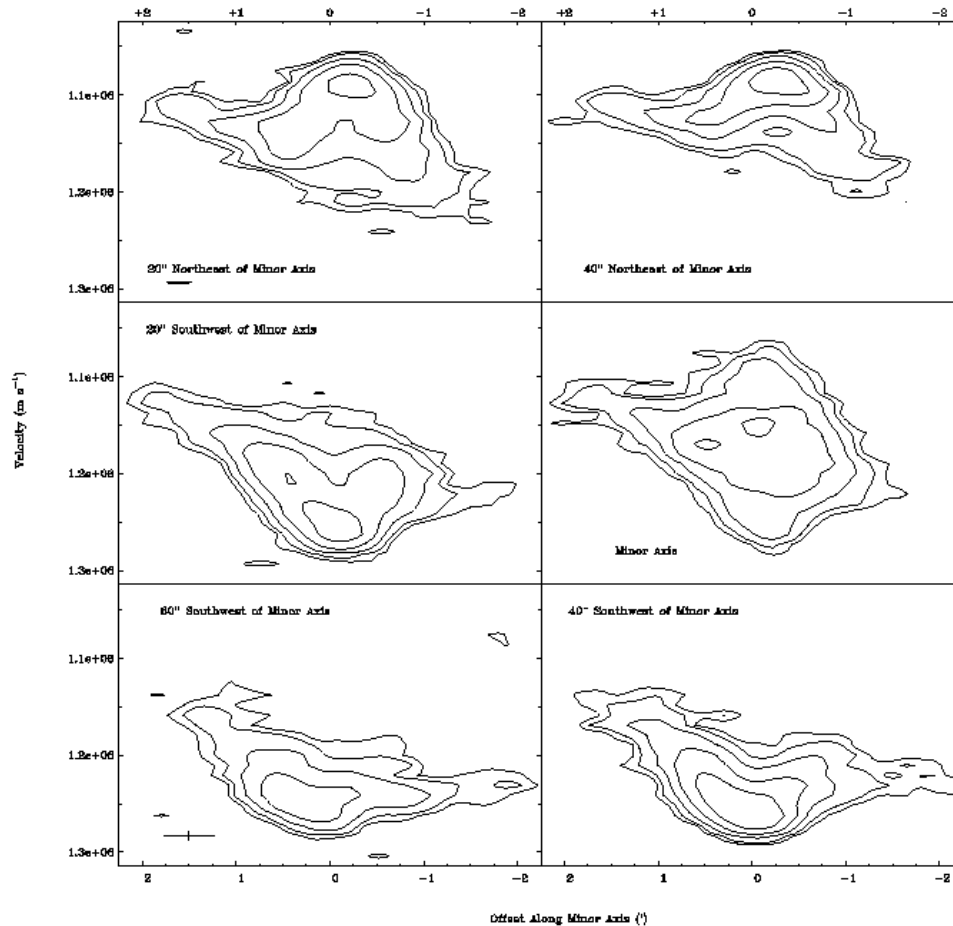


Figure 9-14. A set of P-V slices parallel to and along the minor axis of NGC 4904. The contours are at $3, 5, 10, 20,$ and 30σ .

Rotation Curves and Model Disks

In order to make rotation curves and model disks of NGC 4904, we used the GIPSY task 'reswri' to fit tilted rings to the velocity field. We used our high resolution data set to create our parameter curves. We fit rotational velocities at radii ranging from 20" to 140" in 30" wide annuli. Because of limited flux, we used an average of both the receding and approaching sides of the galaxy. Unfortunately, due to the unusual nature of the velocity field in NGC 4904, 'reswri' could not converge to a meaningful result. In order to examine the dynamic properties of the disk, we 'bootstrapped' a rotation curve. We assumed a flat rotation curve and held that fixed while the program calculated values for position angle and inclination. We then entered all of these values into the program and let the rotation velocity run free until the values for all parameters converged. We present the results for the 'bootstrapped' rotation curve in Figure 9-15, the position angle in Figure 9-16, and the inclination angle in Figure 9-17. Since we assumed a flat rotation curve, the final curve in Figure 9-15 is not significantly different. The position angle and inclination angle plots show that these values change abruptly from the inner parts of the galaxy to the outer. In these plots we do not really reach the edges of the where the ring system may lie, since we used the high resolution data cube. The position angle changes by about 40 degrees over the radius of the galaxy and the inclination angle changes by about 15 degrees. This implies that the ring system may lie very near to the plane of the galaxy. Our values of inclination are consistent with those found by Chapelon et al. (1999) who used optical measurements.

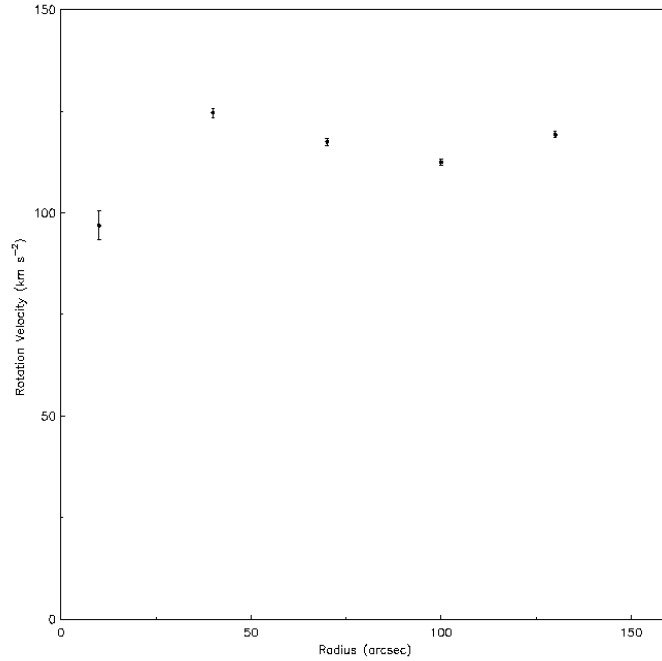


Figure 9-15. Rotation curve of NGC 1784 from the high resolution data set. Data points represent the average of both the approaching and receding sides of the galaxy.

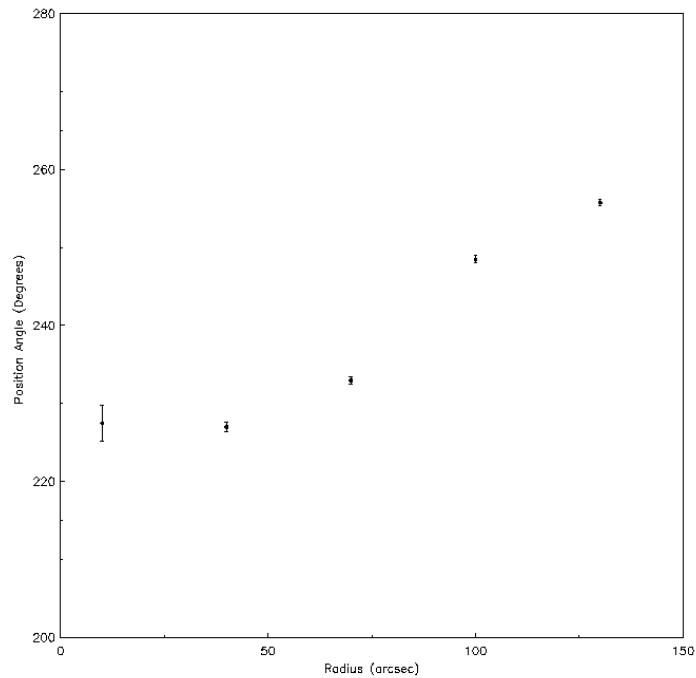


Figure 9-16. Kinematic position angle of NGC 1784 as a function of radius

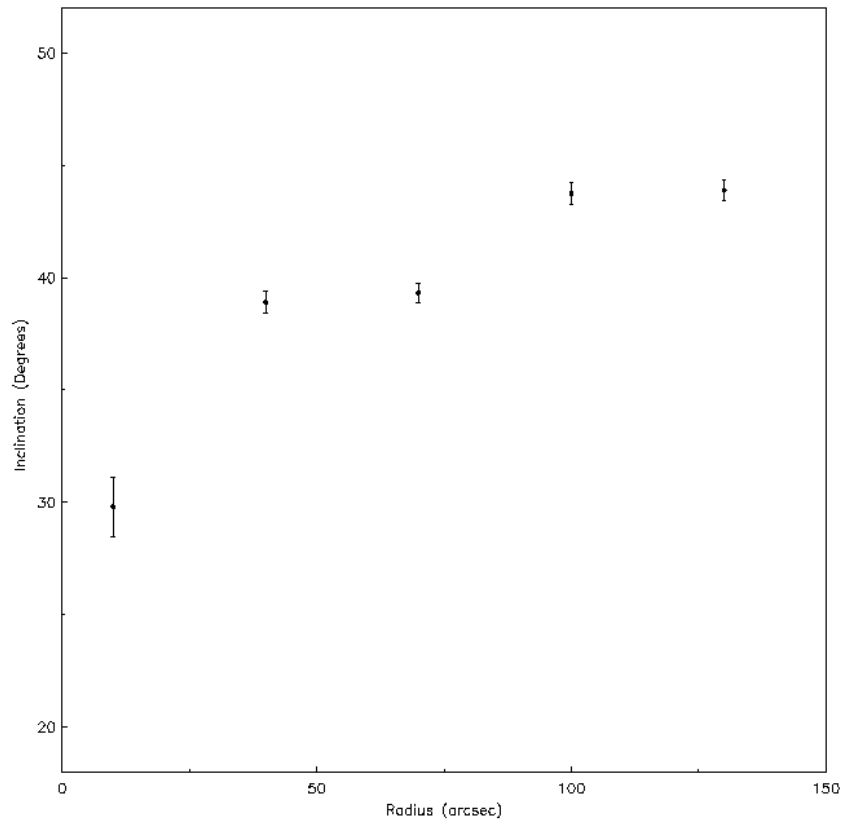


Figure 9-17. Inclination angle of NGC 1784 as a function of radius

We formed a model disk, shown in Figure 9-18, using the 'bootstrapped' data and the GIPSY task 'velfi'. This model disk does resemble the high resolution velocity field for NGC 4904 except for the disturbed morphology. We created another model disk, shown in Figure 9-19, where we held the position and inclination angles constant in the inner regions of the disk and then abruptly changed them at 2' radius. This model disk best represents what the velocity field of a slightly tilted misaligned ring would look like. Again, this velocity field is similar to the real high resolution velocity field for NGC 4904, and in many ways, particularly the inner velocity peaks, better is a better representation than the first model.

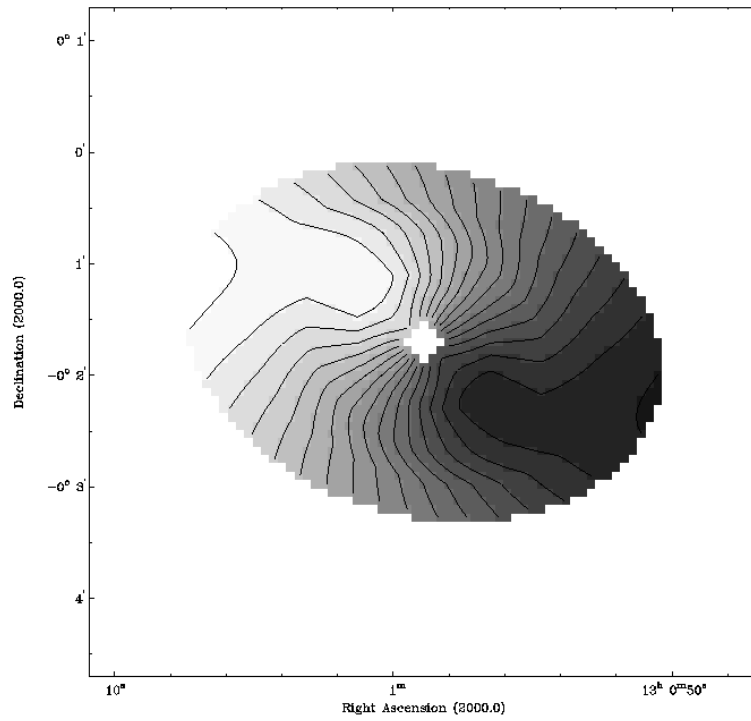


Figure 9-18. Model velocity field constructed from kinematical data in Figures 9-15, 9-16, and 9-17. Light grayscales represent approaching velocities.

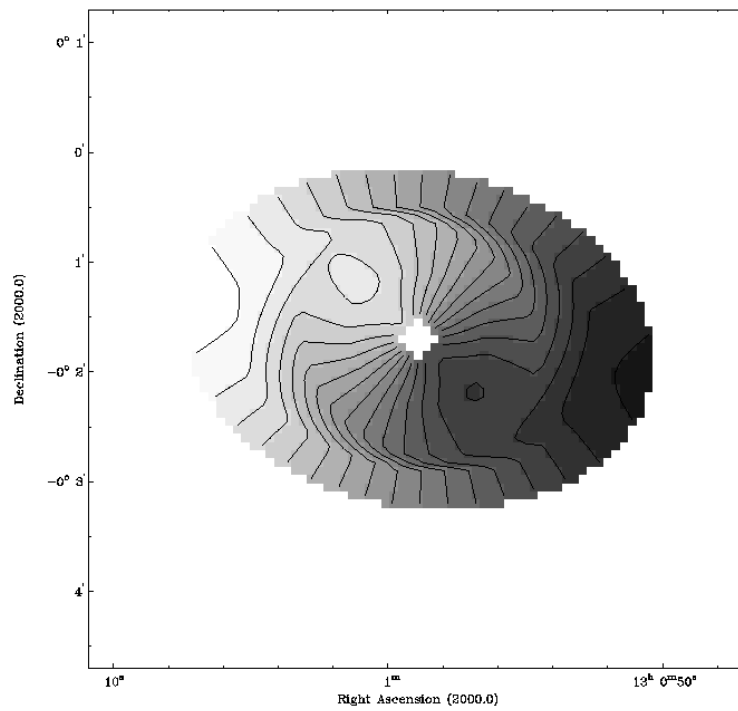


Figure 9-19. Model disk velocity field for NGC 4904 with tilted outer ring. Light grayscales represent approaching velocities.

Summary

NGC 4904 presents many of the same features as NGC 4900. Unfortunately, its small size prevents us from determining without doubt many of its features. We believe that the HI possesses two components. One component is the main disk of the galaxy having an HI mass of several $10^8 - 10^9 M_{\odot}$. The second component is a partial or complete ring, the position angle of this is misaligned to the disk. The ring is not highly inclined, and has an HI mass of one to a few $10^7 M_{\odot}$. The radius of this ring is on the order of 10-15 kpc. The ring is in prograde motion and may have been formed by a close, prograde interaction with a small satellite. No optical or radio components external to the galaxy were found in these observations. Other interactions with small satellites in this sample, NGC 1784, have been shown to cause significant disturbance to the HI disk of a galaxy. In this case, the optical disk is somewhat disturbed as well, showing a twisted bar and possible three-armed structure. Due to the small total mass of the galaxy, it would be very possible for the satellite that created the ring to disturb the star forming regions of the galaxy as well. It is likely that the interaction occurred in the recent past, possibly as recent as 10^8 years ago, given the optically disturbed bar and presence of HI in the bar region.

Further high resolution HI observations of this galaxy are warranted. With higher resolution and higher signal observations, we may be able to separate the outer ring of the galaxy and determine its orbital properties. Also, because the bar lies along the minor axis of HI rotation, further study of the gas motion in the bar region of NGC 4904 would help us learn more about the dynamics of these objects.

CHAPTER 10 NEUTRAL HYDROGEN OBSERVATIONS OF NGC 5300

Compared to NGC 4900 and NGC 4904, NGC 5300 appears to be a much calmer and well formed system. It is classified as having an arm class of "2" by Elmegreen & Elmegreen (1982), meaning that it has very little coherent spiral structure. Optical images of the galaxy show very little asymmetry and few dysmorphic features. NGC 5300 has one of the shortest and roundest bars in the sample. Its bar could best be described as an oval distortion. One strong arm originates from the northwest end of the bar, bends sharply to the north, and then disappears within a radius of 30". Color maps of the galaxy indicate that the bar region is red.

NGC 5300 is at a very similar distance as NGC 4904. It has a recessional velocity of 1171 km s^{-1} , corresponding to a distance of 17 Mpc ($H_0 = 70$). The optical galaxy is rather large in this sample, having a D_{25} of 3.8' (Marquez & Moles 1996). This corresponds to a physical size of 18kpc. There have been few previous studies of the galaxy. Xu et al. (1994) calculated a dynamical mass of $1.7 \times 10^{10} M_{\odot}$ for NGC 5300 using near-infrared measurements.

Observations

Radio observations of NGC 5300 were obtained at the Very Large Array in May of 2003 using D configuration. The spectrometer was composed of 64 channels with a 10.5 km s^{-1} velocity resolution. The total band width was 3.125 MHz (640 km s^{-1}), and the central heliocentric velocity was 1171 km s^{-1} . The observing parameters for the observations are summarized in Table 10-1.

Table 10-1: Parameters of VLA HI observations of NGC 5300

Configuration	D
Number of antennae	27
V_{sys} (km s ⁻¹)	1171
Phase calibrator	1353-021
Flux calibrator	1331+305
Time on source	3.6

The data set was edited, calibrated and continuum subtracted using the typical procedures of the Astronomical Image Processing System (AIPS) package. The data set was then imaged twice using the AIPS task IMAGR to provide us with two image cubes (α , δ , ν) reflecting the maximum range of spatial resolution and sensitivity that our data would allow. We created a low resolution cube by using a natural weighting scheme and a high resolution data cube by imaging the data with a uniform weighting scheme. We CLEANed the data cubes in AIPS down to an rms level of 0.4 and 0.9 mJy beam⁻¹ for the low resolution and high resolution images, respectively. Further details of the statistics for each data cube are presented in Table 10-2. Analysis on the completed and CLEANed image cubes was conducted using the Gronigen Image Processing System (GIPSY) package.

Table 10-2. Characteristics of Naturally Weighted CLEANed Channel Maps

Parameter	Low Resolution	High Resolution
FWHP Synthesized Beam (")	68" x 57"	40" x 36"
FWHP Synthesized Beam (kpc)	5.6 x 4.7	3.2 x 3.0
Theoretical rms Noise (mJy beam ⁻¹)	0.45	0.45
Observed rms Noise (mJy beam ⁻¹)	0.47	0.9
Rms Noise (K)	0.14	0.27
Peak Temperature (K)	11.5	8.4
Peak S/N	83	31

Neutral Hydrogen Morphology

The channel maps shown in Figures 10-1 and 10-2 were used in moment analyses to obtain global density and temperature weighted radial velocity images of the neutral hydrogen in NGC 5300. Moment maps were constructed with the AIPS task MOMNT. A flux cut off of three times the rms noise level (σ) of the unsmoothed data was used. The low resolution, naturally weighted global distribution of the neutral hydrogen in NGC 5300 is shown in grayscale in Figure 10-3 and overlaid on an optical image of the galaxy in Figure 10-4. The high resolution, uniformly weighted global distribution of the neutral hydrogen is shown in grayscale in Figure 10-5 and overlaid on an optical image of the galaxy in Figure 10-6. The lowest contours are drawn at the 2σ level.

Low Resolution Neutral Hydrogen Morphology

The low resolution channel maps of NGC 5300 are reminiscent of those for NGC 3930. Here we see a regular, symmetric distribution of HI moving from northwest to southeast as observational velocity decreases. In several of the channels (1212, 1202, 1191, 1130, 1119, and 1109 km s⁻¹) we see small tongues of gas leading out from the main body of the galaxy. It is uncertain whether these regions are real or are noise. They appear only at the 3σ level, and only in the case of 1130 and 1119 km s⁻¹ do they appear in the same location in multiple channels. If real, these features are most likely small, $10^6 M_{\odot}$ (in HI) high velocity clouds that are unresolved.

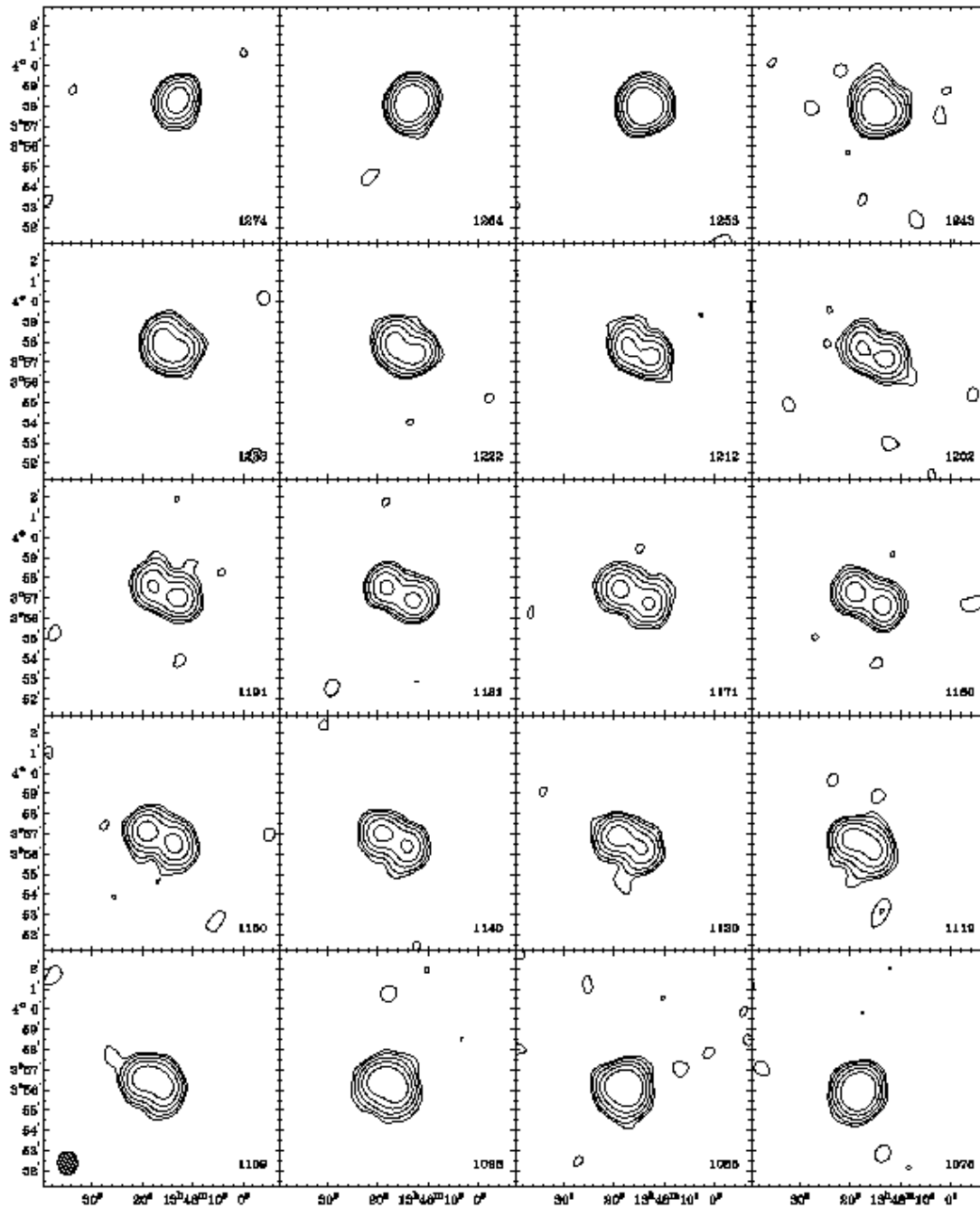


Figure 10-1. Individual, naturally weighted, CLEANed channel images of the low resolution data. Channel velocities are given in the lower right hand corner of each panel in km s^{-1} . The synthesized beam ($68'' \times 57''$) is shown in the lower left corner of the bottom left panel. Contours are at the 3 ($3.4 \times 10^{18} \text{ cm}^{-2}$), 5, 10, and 20σ flux levels.

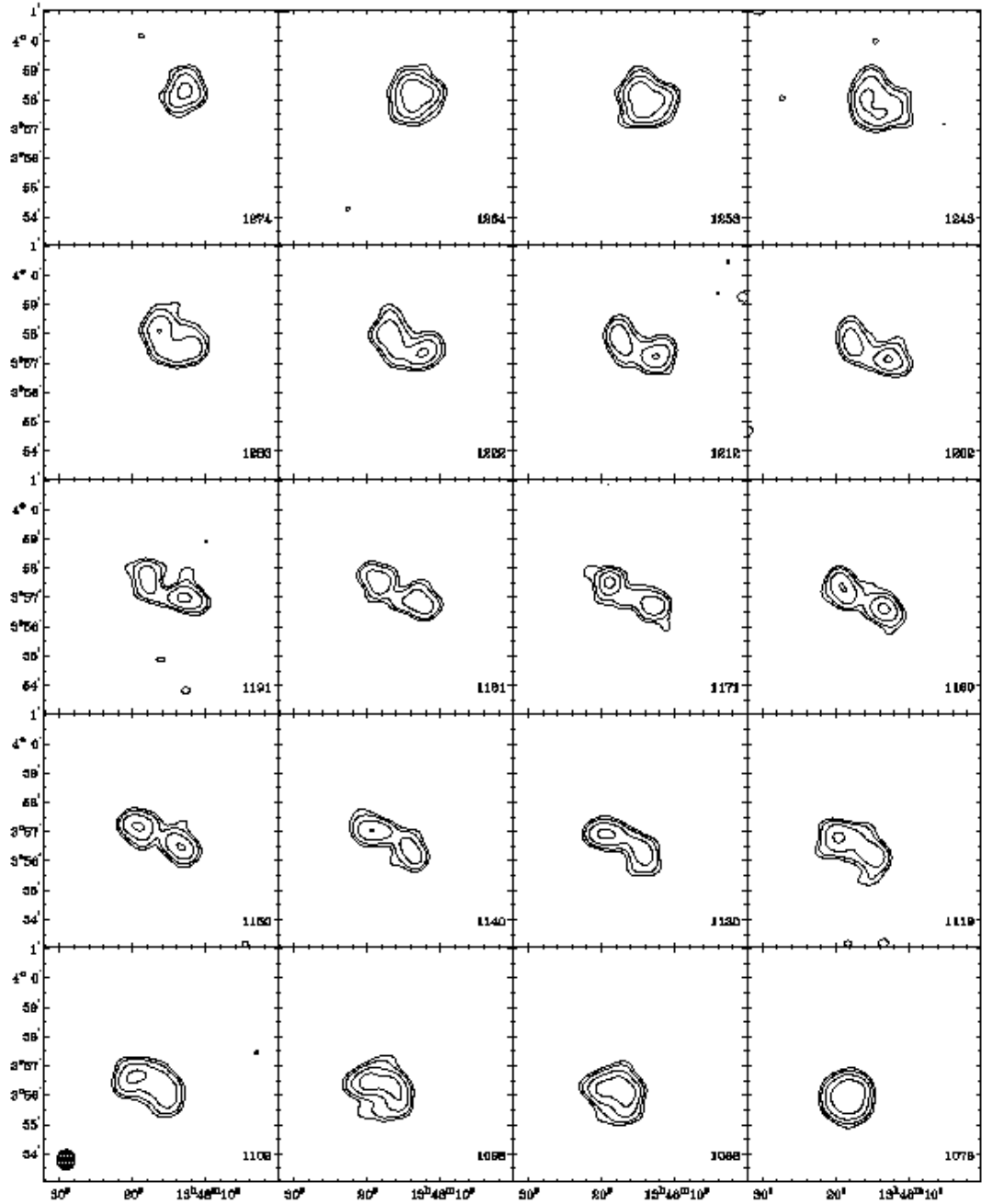


Figure 10-2. Individual, naturally weighted, CLEANed channel images of the high resolution data. Channel velocities are given in the lower right hand corner of each panel in km s^{-1} . The synthesized beam ($40'' \times 36''$) is shown at the bottom left of the lower left channel map. Contours are at the 3 ($2.0 \times 10^{19} \text{ cm}^{-2}$), 5 , 10 , and 20σ flux levels.

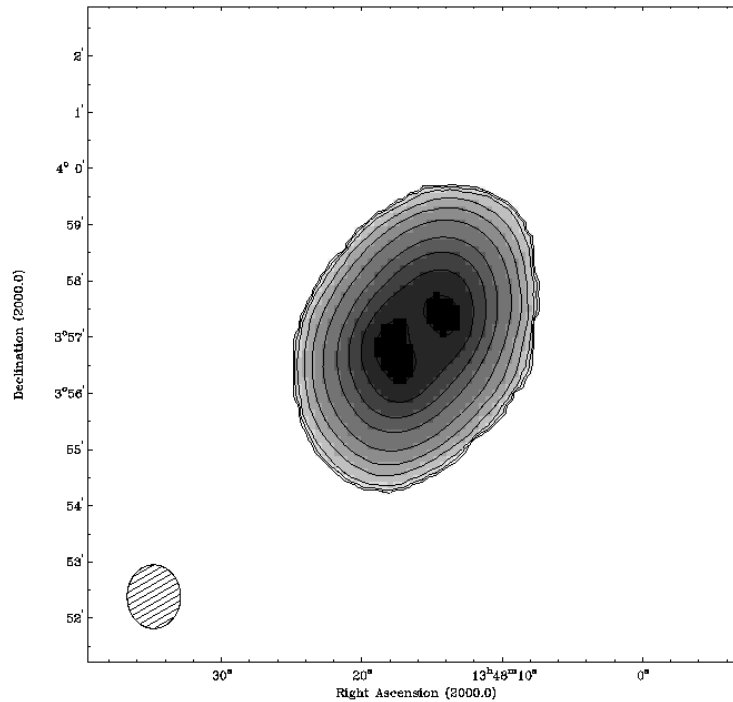


Figure 10-3. Grayscale with contours of the total HI surface density from the low resolution data set. The peak flux corresponds to a column density of $8.4 \times 10^{20} \text{ cm}^{-2}$. Contours are at 0.5 (the 2σ flux level), 1, 2, 3, 5, 10, 20, 40, 60, 80, and 95% of the peak flux. The synthesized beam ($68'' \times 57''$) is shown at the bottom left.

The low resolution HI total intensity map (Figure 10-3) shows a similarly symmetric galaxy. The peak of the HI emission in the south of the galaxy is a bit broader than the one in the north, but only slightly so. We calculate a peak column density of HI to be $8.4 \times 10^{20} \text{ cm}^{-2}$. We calculate an HI diameter for the galaxy of $5.5'$, corresponding to a physical diameter of 26 kpc. The ratio of HI diameter to optical diameter is about 1.5. The optical overlay in Figure 10-4 shows that the peak HI emission lies on either end of NGC 5300's bar. The peak HI emission regions correspond to the arm feature in the northwest of the galaxy and other star forming regions to the southeast. It appears from these images that NGC 5300's bar is deficient in HI. There do not seem to be any companion or ring systems associated with this galaxy.

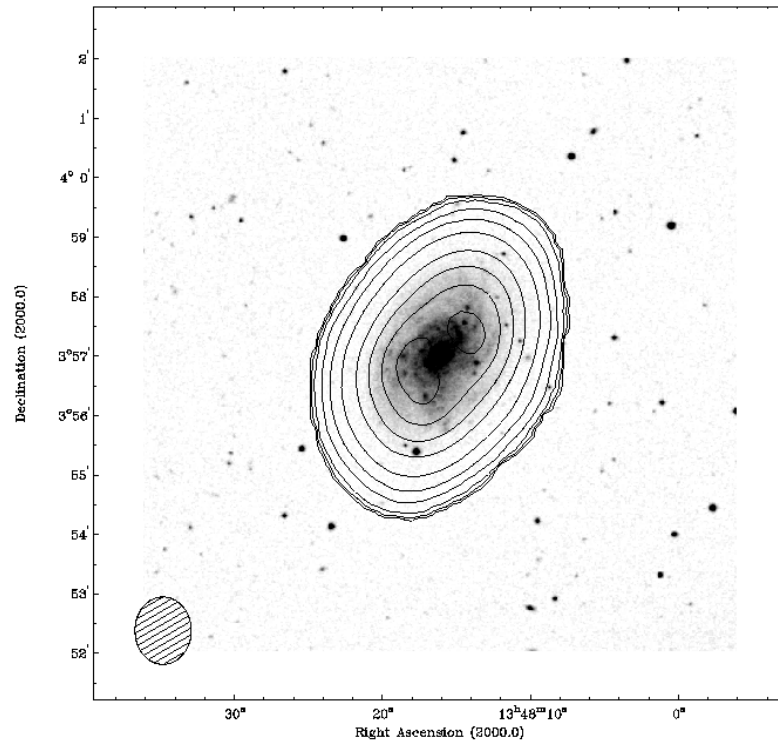


Figure 10-4. Contours of the total HI surface density from the low resolution data set overlaid on an optical DSS image of NGC 5300. Contours and resolution are the same as in Figure 10-3.

High Resolution Neutral Hydrogen Morphology

The high resolution channel maps shown in Figure 10-2 are similar in nature to the low resolution maps of Figure 10-1. Since we only had D configuration observations of this galaxy, our resolution did not improve markedly from the low to the high. In a couple of the channels, we see slight hints of asymmetries (e.g. 1233, 1191, and 1098 km s^{-1}), but overall the channel maps are what one would expect for a normal, undisturbed galaxy. Higher resolution observations with high signal to noise would be needed to explore the physical causes behind the few channel maps with asymmetries.

The high resolution total intensity map in Figures 10-5 and 10-6 shows that the central regions of NGC 5300 are deficient in HI compared to the areas at the immediate ends of the bar. The peaks of the HI distribution seem to curve around the central bar

region and follow the slight hints of spiral structure in the galaxy. We calculate a peak column density of HI to be $1.03 \times 10^{21} \text{ cm}^{-2}$ in this image. The peak HI column density corresponds to a region of star formation in the southeast of the galaxy. In this image, we see that the peak of the HI distribution at the northwestern end of the bar does not lie on top of the optical arm feature. A HI hole exists slightly south of the center of the bar region. The outer contours are fairly symmetric and follow the outline of the optical galaxy.

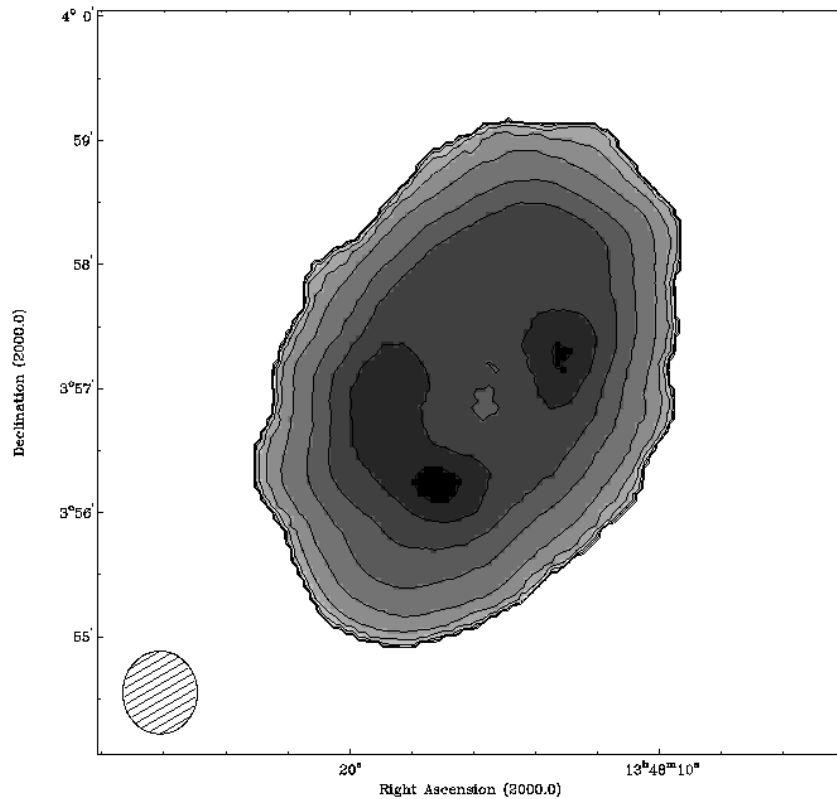


Figure 10-5. Grayscale and contours of the total HI surface density from the high resolution data set. The peak flux corresponds to a column density of $1.0 \times 10^{21} \text{ cm}^{-2}$. Contours are at 0.5 (the 2σ flux level), 1, 2, 5, 10, 20, 40, 60, 80, and 95% of the peak flux. The synthesized beam (40" x 36") is shown at the bottom left.

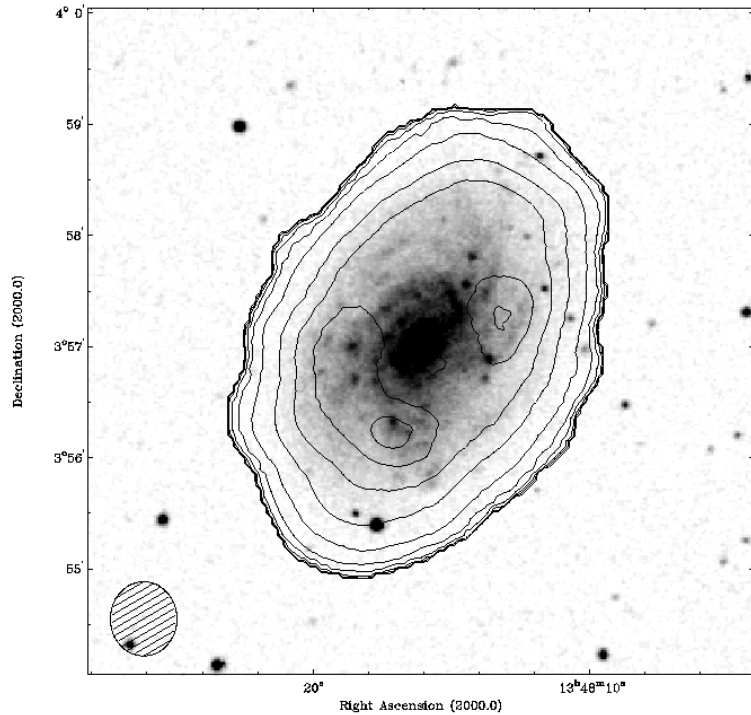


Figure 10-6. Contours of the high resolution data set overlaid on a DSS image of NGC 5300. Contours and resolution are the same as in Figure 10-5.

Global Neutral Hydrogen Properties

Figure 10-7 shows the HI spectrum of NGC 5300 made from the low resolution observations of the galaxy. The spectrum is not as bright as many of the others in our sample, but is symmetric. Beyond the typical two horned pattern of the spectrum, the central channel appears to be more deficient in HI others around it. This is likely due to the HI hole at the center of the galaxy. We calculate an HI flux for the galaxy of $15.5 \pm .9 \text{ Jy km s}^{-1}$. This corresponds to an HI mass of $1.06 \times 10^9 M_{\odot}$. We calculate a velocity width of 210 km s^{-1} . From our spectrum of NGC 5300, we calculate a 3σ HI flux level of 0.059 Jy . This corresponds to a conservative minimum mass detection level of $1.16 \times 10^8 M_{\odot}$ for an isolated HI cloud, assuming that it appears in 3 continuous channels.

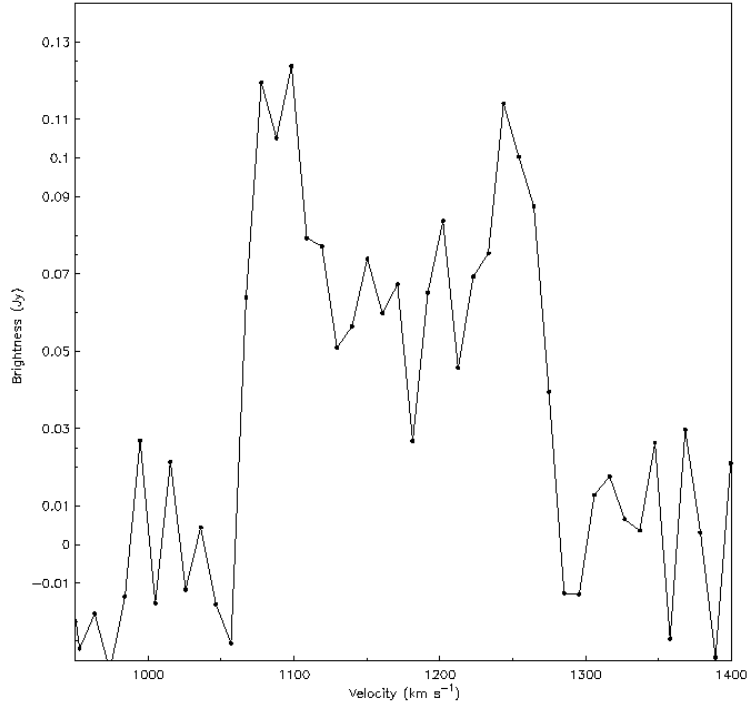


Figure 10-7. The HI flux density versus velocity for the low resolution data set. The velocity resolution here is 10 km s^{-1} .

Figure 10-8 is the radial HI profile from both the high and low resolution data sets. This galaxy shows a similar profile to other galaxies in the sample. We see evidence for the lack of HI in the center of the galaxy in the high resolution radial profile, where the ring at $40''$ shows a greater column density than the interior ring. We find that the HI emission does not extend significantly below the $1 \times 10^{20} \text{ cm}^{-2}$ level in accordance with the predictions of Maloney (1993).

Neutral Hydrogen Kinematics

Figure 10-9 shows the HI velocity field for NGC 5300 created with our low resolution data set. Figure 10-10 shows the HI velocity field for NGC 5300 created with our high resolution data set. Figure 10-11 shows this same field overlaid on an optical DSS image of the galaxy. The contours in all three images are separated by 10.5 km s^{-1} , and the central contour is at a systemic velocity of 1171 km s^{-1} . The low resolution

velocity field presents a very symmetric pattern. The central iso-velocity curves are straight, and have no indication of warps or "S" curves. The velocity field does not turn over at the ends of the major axis, as with other galaxies in this sample. The high resolution velocity field shows a very similar structure. There is a very slight twisting of the position angle at the ends of the major axis, but otherwise the field is symmetric. In this higher resolution image, we see the velocities reach a maximum on the northwest side of the galaxy. There is no corresponding maximum on the southeast side of the galaxy. Due to the low resolution of these observations compared to our optical observations, we do not see the effects of spiral structures or the bar on the HI velocity field.

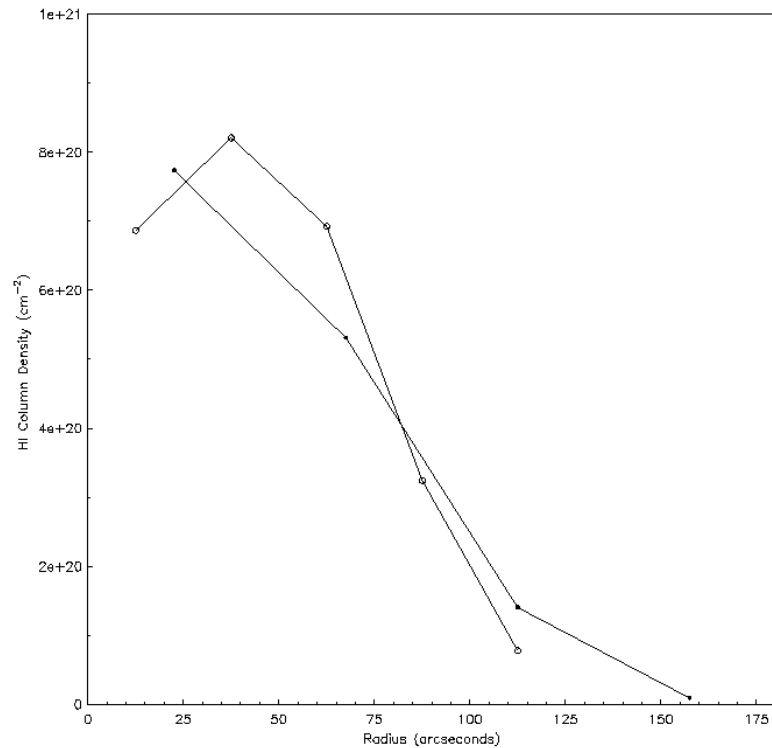


Figure 10-8. The HI radial density profiles from the low resolution data set (closed circles) and the high resolution data set (open circles)

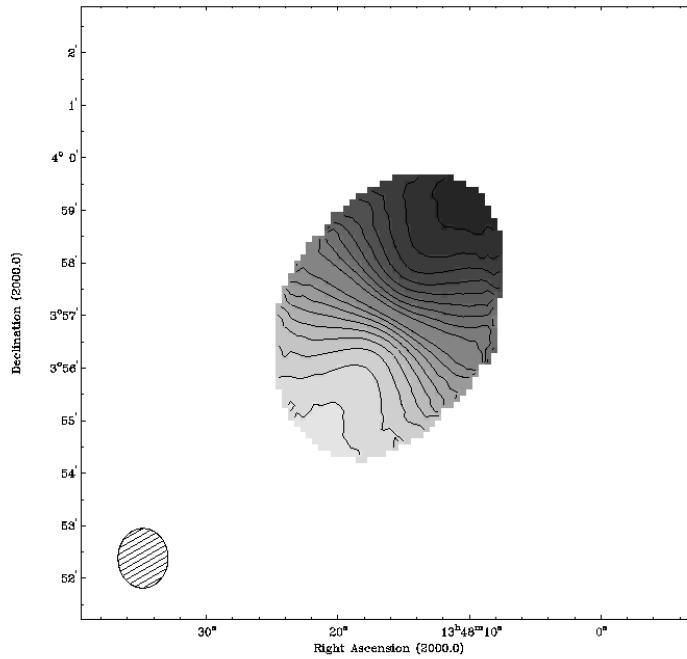


Figure 10-9. Intensity-weighted radial velocity contours of the low resolution data. Contours are separated by 10 km s^{-1} . Motion toward the observer is displayed with lighter grayscales. The central velocity contour is at 1171 km s^{-1} . The synthesized beam ($68'' \times 57''$) is displayed in the lower left.

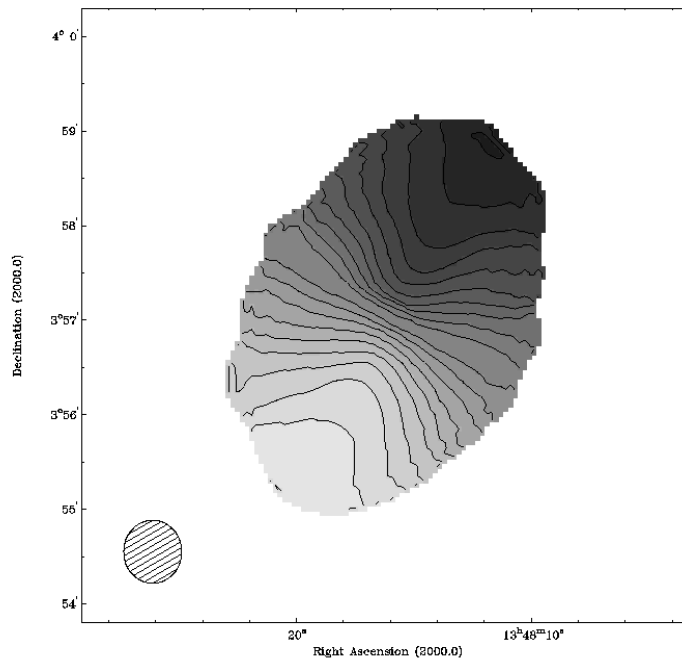


Figure 10-10. Intensity-weighted radial velocity contours of the high resolution data set. Contours are separated by 10 km s^{-1} . Darker grayscales correspond to motion away from the observer. The synthesized beam ($40'' \times 36''$) is displayed in the lower left hand corner.

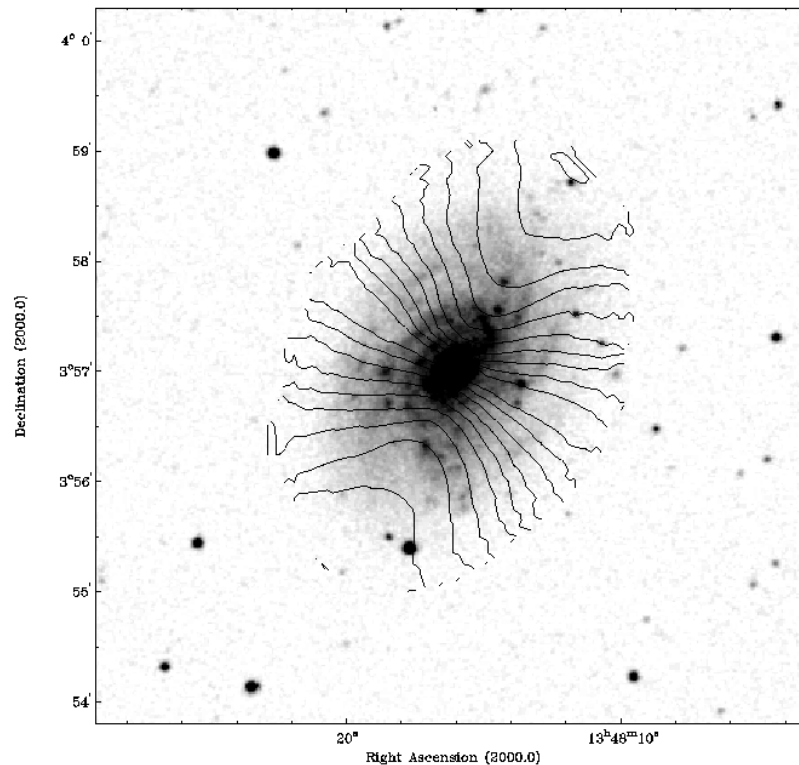


Figure 10-11. Intensity-weighted radial velocity contours of the high resolution data set overlaid on an optical DSS image of NGC 5300. Contours are the same as in Figure 10-10.

Position-Velocity Plots

Figure 10-12 shows Position-Velocity (P-V) plots made parallel to the major axis of NGC 5300, made with our high resolution data set. In a similar way to NGC 3930, these plots show very little disturbance in this galaxy. The cut made along the major axis shows a decrease in the column density of HI at the center of the galaxy. There does not appear to be any large quantities of gas at forbidden velocities in this galaxy. There are some small "beards" coming off the main body of gas. However, it is uncertain if these features are real or noise. They exist only in one slice, typically, and are very narrow in their velocity range. If real, they may represent $10^6 M_{\odot}$ high velocity clouds.

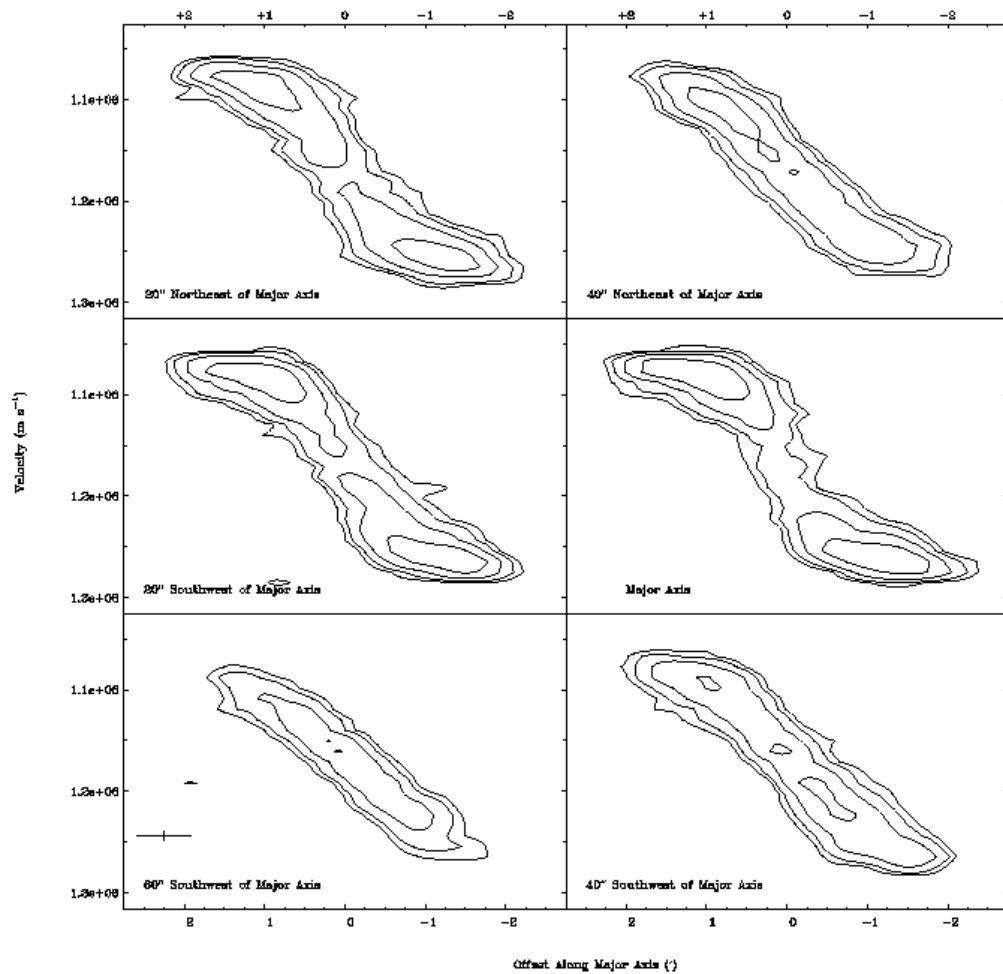


Figure 10-12. A set of P-V slices parallel to and along the major axis of NGC 5300. The contours are at 3, 5, 10, 20σ .

Figure 10-13 shows P-V plots made parallel to the minor axis of NGC 5300.

Again, in these plots we do not see any unexpected features. The cut along the minor axis shows a broad velocity spread, probably due to resolution effects, but no major asymmetries. The cut made 40'' southeast of the minor axis does appear to be somewhat more asymmetric than any of the other plots. This likely reflects the slightly higher HI column densities to the south of the galaxy, and is not of dynamical importance.

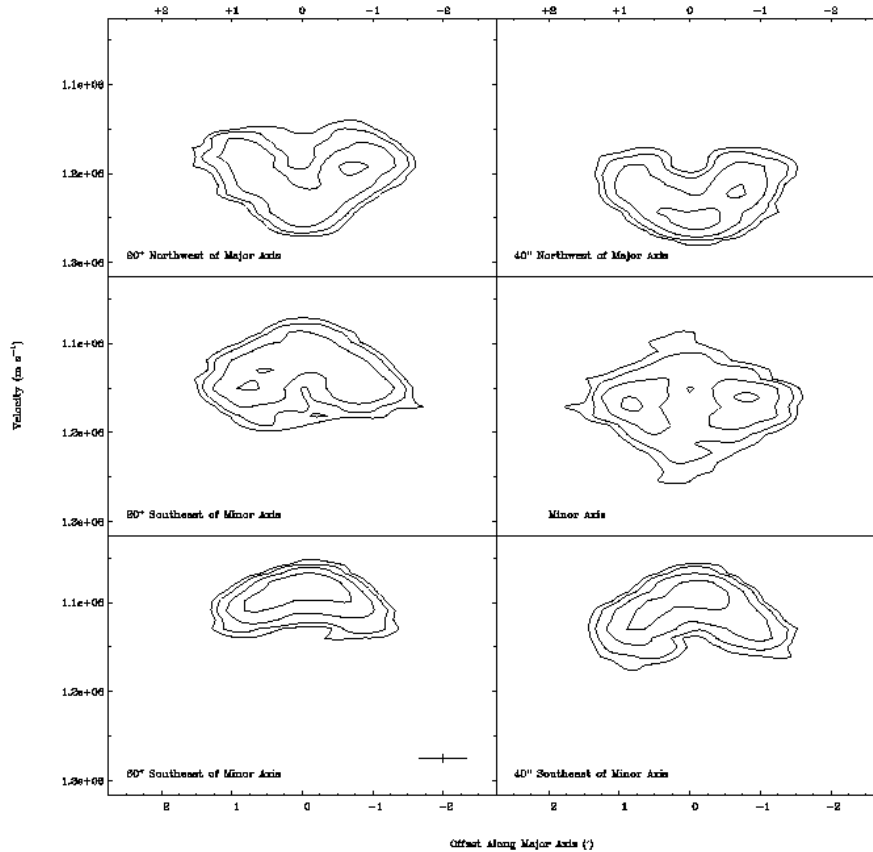


Figure 10-13. A set of P-V slices parallel to and along the minor axis of NGC 5300. The contours are at $3, 5, 10,$ and 20σ .

Rotation Curves and Model Disks

In order to make rotation curves and model disks of NGC 5300, we used the GIPSY task 'reswri' to fit tilted rings to the velocity field. We used our high resolution data set to create our parameter curves. We fit rotational velocities at radii ranging from $20''$ to $125''$ in $20''$ wide annuli. We held the position of the kinematic center and the systemic velocity of the galaxy as fixed parameters, while allowing the rotational velocity, expansion velocity, position angle, and inclination to be set by the fit. We plot the results from the receding, approaching, and average of both sides of the galaxy. We plot the rotation velocity versus radius in Figure 10-14, expansion velocity versus radius

in Figure 10-15, position angle versus radius in Figure 10-16, and inclination versus radius in Figure 10-17.

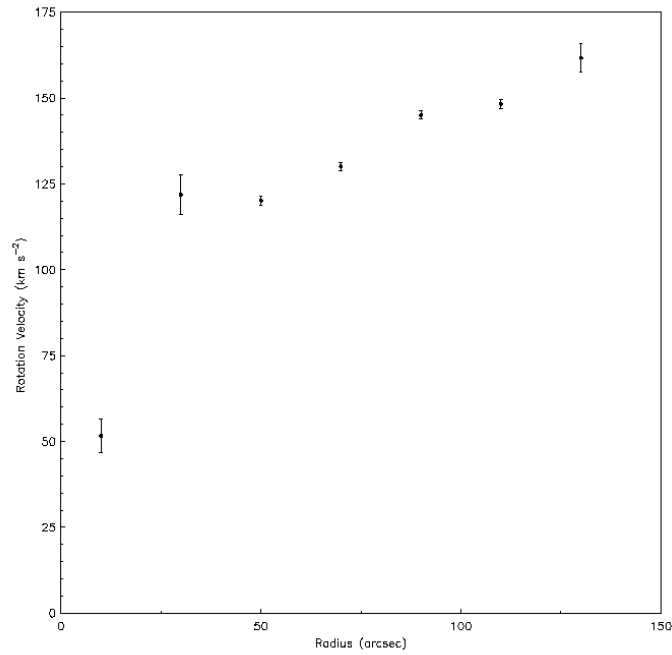


Figure 10-14. Rotation curve of NGC 5300 from the high resolution data set. Data points represent the average of both the receding and approaching sides of the galaxy.

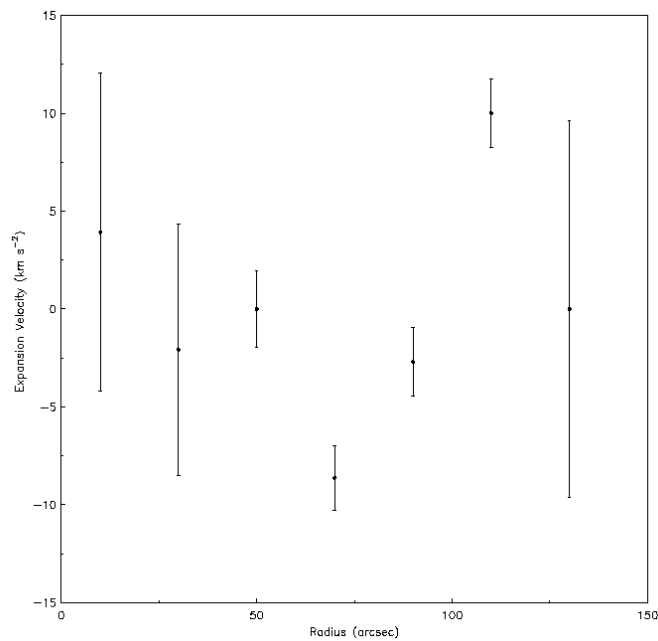


Figure 10-15. Expansion velocity versus as a function of radius for NGC 5300

We find that NGC 5300 has a flat rotation curve through its inner 50", and then shows a rising rotation curve through a radius of 120". This finding is consistent with the velocity fields shown in Figure 10-9 and 10-10, where there are no closed iso-velocity contours. Rising rotation curves are thought to be associated with flocculent galaxies, and it is postulated that this is due to a lower disk to halo mass ratio (Elmegreen & Elmegreen 1990).

Using the rotation curve, we can calculate a value for the total mass of NGC 5300 interior to 140". With a Keplerian, $M = V^2 R G^{-1}$, to model the disk and halo, where $R = 11.2$ kpc and $V(11.2 \text{ kpc}) = 160 \text{ km s}^{-1}$, we find $M(R)$ to be $7.34 \pm 0.05 \times 10^{10} M_{\odot}$. Comparing this with the HI mass calculated above, we find a value for the ratio $M_{\text{HI}} / M(R)$ of 1% for NGC 5300, the lowest in the sample.

The values of expansion velocity with respect to radius all lie fairly near to 0 km s^{-1} . The largest divergences from this value are on the order of 10 km s^{-1} which is the limit of our velocity resolution. Figures 10-16 and 10-17 show that the position angle and inclination angle are constant across the radius of the galaxy to within 10° . NGC 5300 possesses the most constant values for these measurements in our sample. As with the velocity fields and P-V plots, these measurements indicate that if NGC 5300 possesses a warp, it is exceedingly small.

We used the values of rotational velocity, expansion velocity, position angle, and inclination to construct a model disk for NGC 3930 with the GIPSY task 'velfi'. The model disk is shown in Figure 10-18. This model disk shows the same symmetry as the real velocity fields, along with the slight twisting at large radii. We then subtracted this model field from our high resolution velocity field (Figure 10-10), to create a map of

residual velocities. The residual velocity field is shown in Figure 10-19. The residual velocity field is somewhat bi-modal at small radii, but then becomes more confusing at larger radii. There is no indication of corotation as in Canzian (1993). However this is not unexpected given our comparatively low resolution.

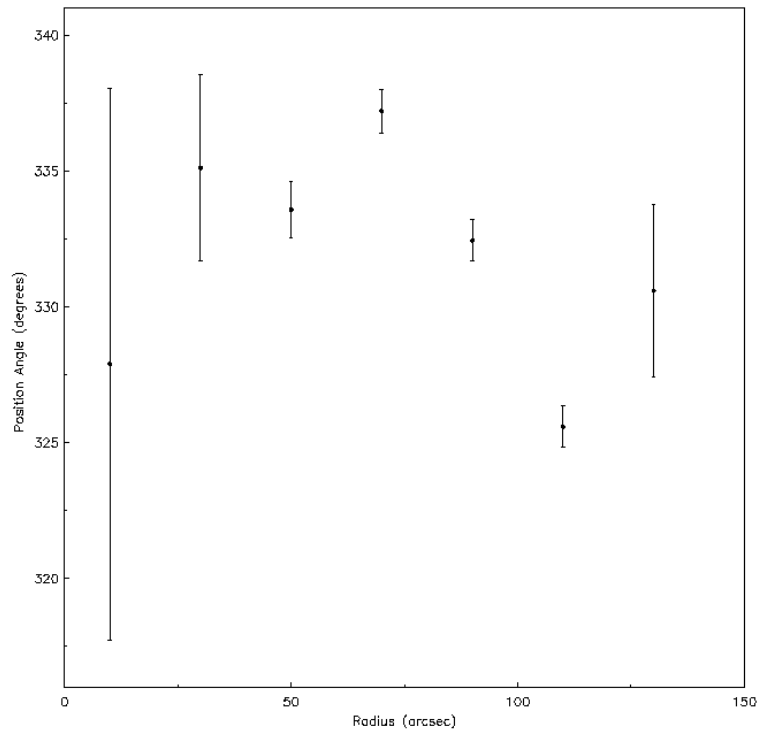


Figure 10-16. Kinematic position angle of NGC 5300 as a function of radius

Summary

NGC 5300 is the most normal example of a disk galaxy in this sample. Its HI morphology is largely symmetric, with only a slightly higher peak column density in the southern end of the galaxy. NGC 5300 does not seem to possess any large scale warp. No large HI companions were found in our observations, but we can not rule out the presence of small mass ($10^7 M_{\odot}$) and angular size ($<20''$) clouds. Because NGC 5300 possesses a red bar, is deficient in HI in its bar region, does not possess significant star forming regions, and does not possess a significant galactic warp, we conclude that NGC

5300 has not been involved in any minor (10% mass ratio) mergers in the past several 10^9 years. Higher resolution observations are necessary to determine the properties of the interesting one-armed structure in the northwest of the galaxy, and the effects of small armlets on the HI kinematics of the disk.

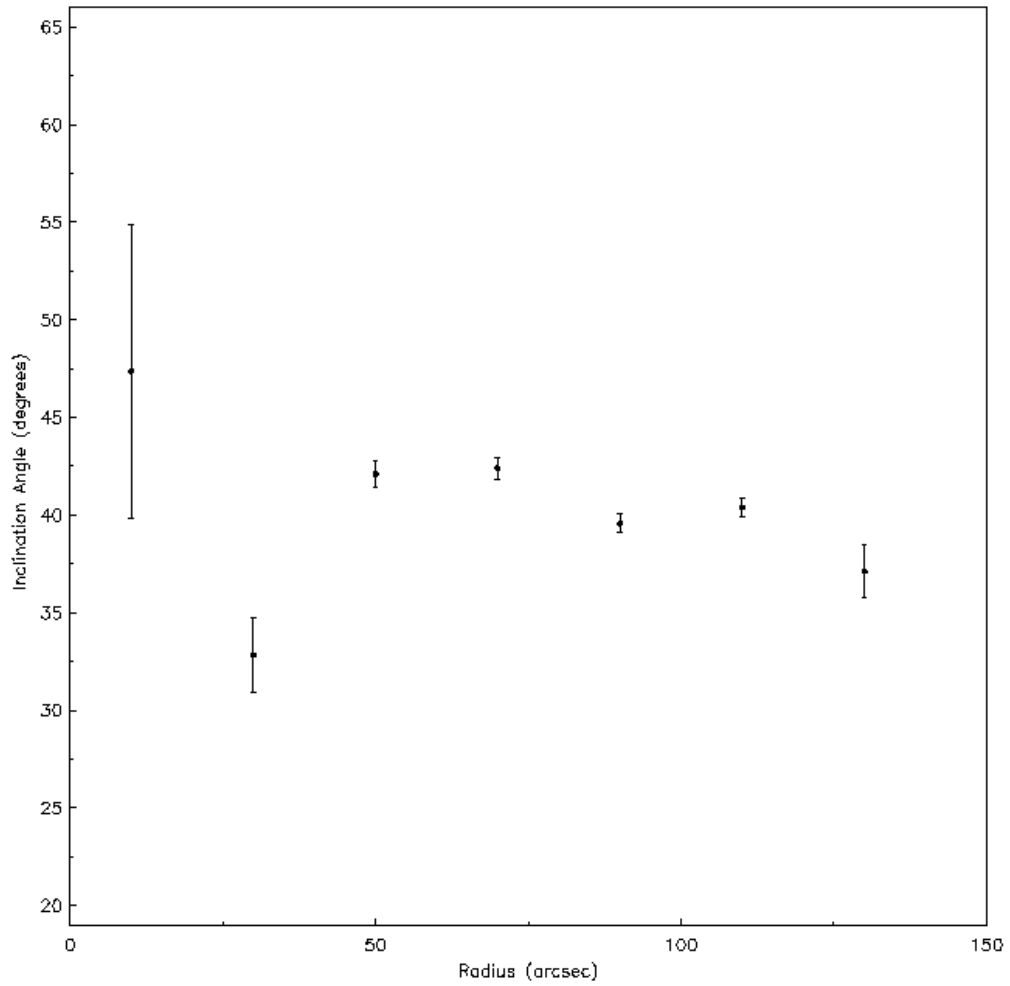


Figure 10-17. Inclination angle of NGC 5300 as a function of radius

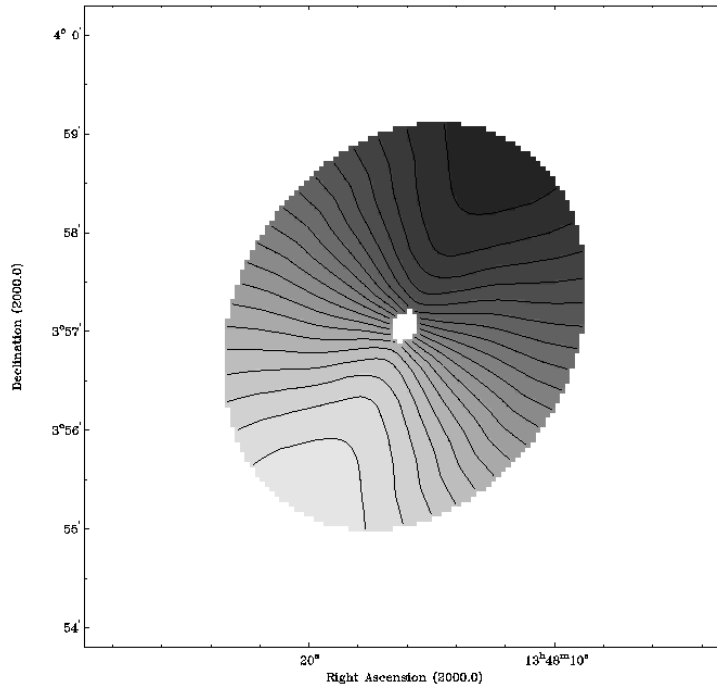


Figure 10-18. Model velocity field constructed from kinematical data in Figures 10-14, 10-15, and 10-16, and 10-17. Light grayscales represent approaching velocities.

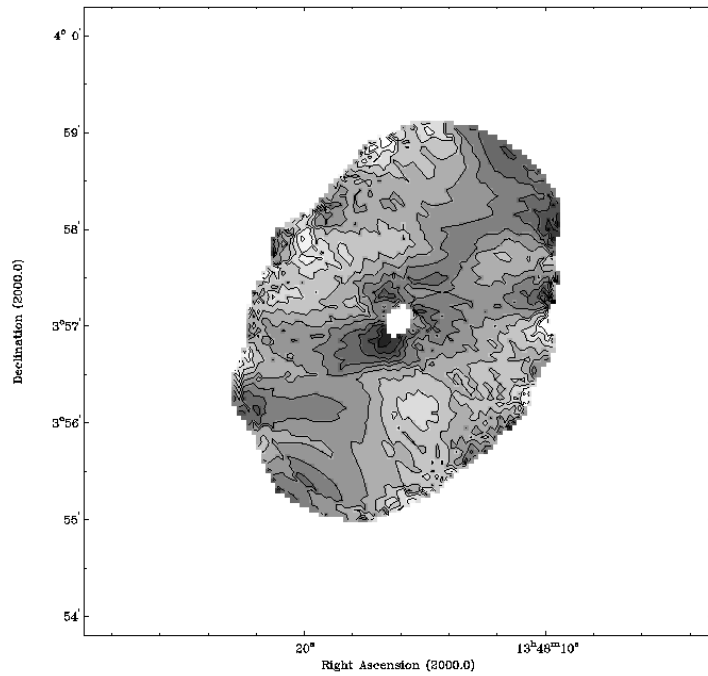


Figure 10-19. Residual velocity field made from model in Figure 10-18. Light grayscales represent gas approaching the observer. Contours are separated by 5km s⁻¹.

CHAPTER 11 NEUTRAL HYDROGEN OBSERVATIONS OF NGC 6012

NGC 6012 is the last and largest of our galaxies. Elmegreen & Elmegreen (1982) give this galaxy a "3" for its arm classification. However, this probably is an overstatement of the strength of the galaxy's arms. A look at the optical image shows that the galaxy is dominated by a bright, long bar. There is a subtle ring of optical emission at the end of the bar. Outside of this, there is a large expanse of very low level optical emission. In fact, due to the presence of two, bright foreground stars, it is difficult to tell exactly the size of the galaxy. De Voucelours et al. (1991) give the angular diameter of the galaxy as 2.1'. At a distance of 26Mpc ($V_r = 1854 \text{ km s}^{-1}$ and $H_0 = 70 \text{ km s}^{-1} \text{ Mpc}^{-1}$), this corresponds to a physical diameter of 15.2 kpc.

NGC 6012 appears to be forming stars in its bar region. The color map shows that one end of the bar has a large and blue HII region. There also appears to be dust lanes down the length of the bar. Outside of the bar, however, there does not appear to be much star formation. Previous single dish neutral hydrogen observations of the galaxy found that it does not possess an extremely large HI flux, $12.1 \text{ Jy km s}^{-1}$, but is quite massive in HI, $4.87 \times 10^9 M_\odot$ (van den Bergh 1985). Van den Bergh (1985) found the galaxy to have a velocity width of 177 km s^{-1} and to have a slightly asymmetric HI spectrum.

Observations

Radio observations of NGC 6012 were obtained at the Very Large Array in September of 2002 and May of 2003 using the C and D configurations, respectively. The

spectrometer was composed of 64 channels with a 10.5 km s^{-1} velocity resolution. The total band width was 3.125 MHz (640 km s^{-1}), and the central heliocentric velocity was 1171 km s^{-1} . The observing parameters for the observations are summarized in Table 11-1.

Table 11-1. Parameters of VLA HI observations of NGC 6012

Configuration	C	D
Number of antennae	27	27
V_{sys} (km s^{-1})	1854	1854
Phase calibrator	1602+334	1602+334
Flux calibrator	1331+305	1331+305
Time on source	7.5	3.7

Table 11-2. Characteristics of Naturally Weighted CLEANed Channel Maps

Parameter	Low Resolution	High Resolution
FWHP synthesized beam (")	62" x 52"	16" x 16"
FWHP synthesized beam (kpc)	7.8 x 6.6	2.0 x 2.0
Theoretical rms noise (mJy beam^{-1})	0.26	0.26
Observed rms noise (mJy beam^{-1})	0.37	1.5
Rms noise (K)	0.11	4.5
Peak temperature (K)	6.2	85.5
Peak S/N	57	19

The data set was edited, calibrated and continuum subtracted using the typical procedures of the Astronomical Image Processing System (AIPS) package. The data set was then imaged twice using the AIPS task IMAGR to provide us with two image cubes (α , δ , ν) reflecting the maximum range of spatial resolution and sensitivity that our data would allow. We created a low resolution cube by using a natural weighting scheme and a high resolution data cube by imaging the data with a uniform weighting scheme. We CLEANed the data cubes in AIPS down to an rms level of 0.3 and $0.5 \text{ mJy beam}^{-1}$ for the low resolution and high resolution images, respectively. Further details of the statistics for each data cube are presented in Table 11-2. Analysis on the completed and

CLEANed image cubes was conducted using the Gronigen Image Processing System (GIPSY) package.

Neutral Hydrogen Morphology

The channel maps shown in Figures 11-1 and 11-2 were used in moment analyses to obtain global density and temperature weighted radial velocity images of the neutral hydrogen in NGC 6012. Moment maps were constructed with the AIPS task MOMNT. A flux cut off of three times the rms noise level (σ) of the unsmoothed data was used. The low resolution, naturally weighted global distribution of the neutral hydrogen in NGC 6012 is shown in grayscale in Figure 11-3 and overlaid on an optical image of the galaxy in Figure 11-4. The high resolution, uniformly weighted global distribution of the neutral hydrogen is shown in grayscale in Figure 11-5 and overlaid on an optical image of the galaxy in Figure 11-6. The lowest contours are drawn at the 2σ level.

Low Resolution Neutral Hydrogen Morphology

The low resolution channel maps for NGC 6012 (Figure 11-1) are reminiscent of those for NGC 1784, but without the counter-rotating ring. The inside regions of the galaxy appear to be well formed, without major asymmetries. The outer regions of the galaxy appear to be stretched out and slightly warped. The central channel at 1854 km s^{-1} shows some "S" like twisting, indicating a warped disk. The emission on the eastern and southern side of the galaxy in the channel corresponding to 1813 km s^{-1} is reminiscent of the large southern expanse of gas in NGC 1784. A small 3σ object appears in two channels (1793 and 1783 km s^{-1}) to the west of the galaxy. Due to the low signal, it is unclear if this object is some type of large High Velocity Cloud. If so, it would have a

total mass on the order of $10^7 M_{\odot}$. It is also unclear with these observations, if this object is gas intrinsic to the galaxy, or the remnant of some ancient satellite.

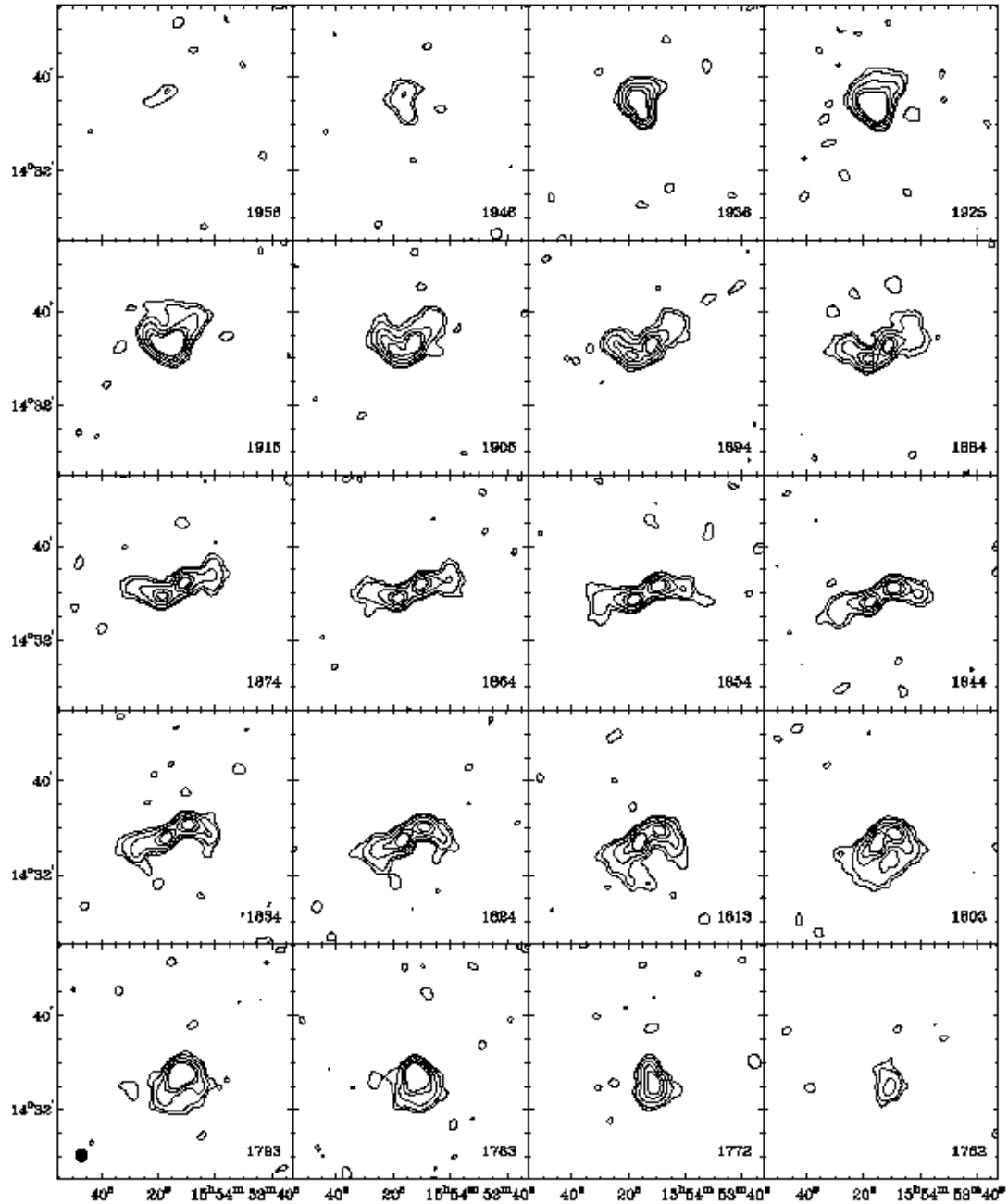


Figure 11-1. Individual, naturally weighted, CLEANed channel images of the low resolution data. Channel velocities are given in the lower right hand corner of each panel in km s^{-1} . The synthesized beam ($62'' \times 52''$) is shown in the lower left hand panel. Contours are at the 3 ($3.7 \times 10^{18} \text{ cm}^{-2}$), 6, 15, 30, and 45σ flux levels.

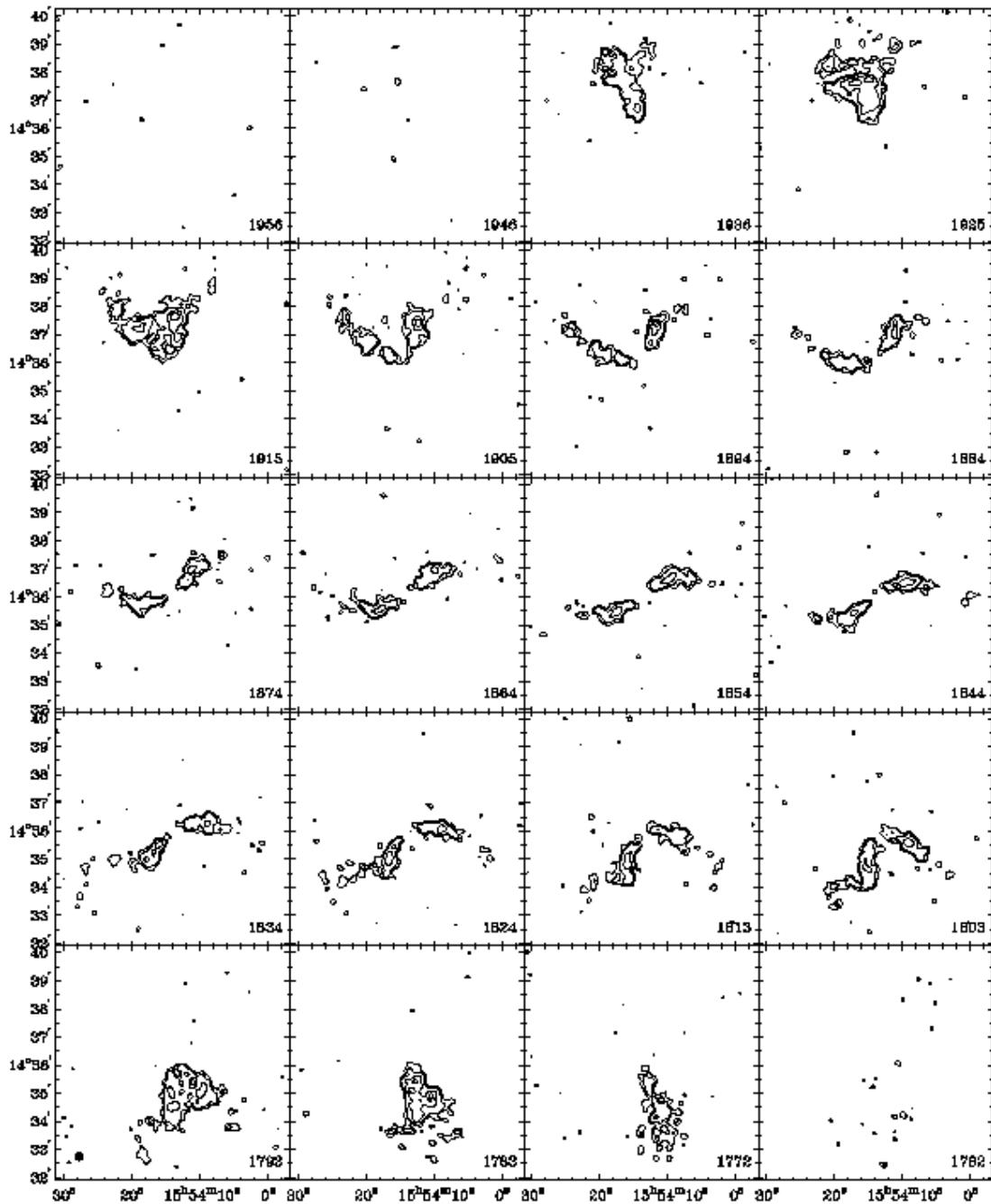


Figure 11-2. Individual, naturally weighted, CLEANed channel images of the high resolution data. Channel velocities are given in the lower right hand corner of each panel in km s^{-1} . The synthesized beam ($16'' \times 16''$) is shown the lower left hand channel map. Contours are at the 3 ($1.4 \times 10^{20} \text{ cm}^{-2}$), 5 , and 10σ flux level.

The low resolution total intensity map of NGC 6012 (Figure 11-3) shows the large scale of the galaxy. We measure an angular HI diameter of $9'$, which corresponds to

a physical diameter of 65kpc, larger than all other galaxies in the sample, except for NGC 1784. Even at low resolution, the HI morphology of this galaxy is asymmetric. The position angle of the contours rotates counter-clockwise with radius. Figure 11-4 shows that the inner contours are aligned with the bar, with the peak of the HI emission lying just past the north end of the bar. This side of the bar is the one with the large, blue HII region. Figure 11-4 also shows the extreme size of the HI emission compared to the optical. We measure a ratio of HI diameter to optical diameter of over 4. This is again the largest in our sample. The outer contours of the HI emission appear to have protrusions on the northwest and southeast sides. It is unclear what causes these shapes. Possibly they are related to some underlying spiral structure. There are a few possible small companions external to the main body of HI. These appear only at the level of noise in this image, may correspond to clouds with HI masses on the order of $10^6 - 10^7 M_{\odot}$.

High Resolution Neutral Hydrogen Morphology

In the high resolution channel maps (Figure 11-2), we focus on emission from the central regions of NGC 6012. Overall, there do not appear to be indications of large scale asymmetries or gas at forbidden velocities. However, there does appear to be evidence for a disk warp at this level. The central channel (1854 km s^{-1}) shows a twist beyond a radius of $2'$ ($\sim 15 \text{ kpc}$) on both sides of the galaxy. In the lower velocity channels ($< 1834 \text{ km s}^{-1}$), there is a significant twist on the eastern arm beyond $2 - 3'$ of radius. The channels at the velocity extremes in both directions show lumpy and fragmented emission. The channel corresponding to 1925 km s^{-1} even shows a hole in the HI emission. This hole does not appear to be due to a puncture, but rather some type of twisting.

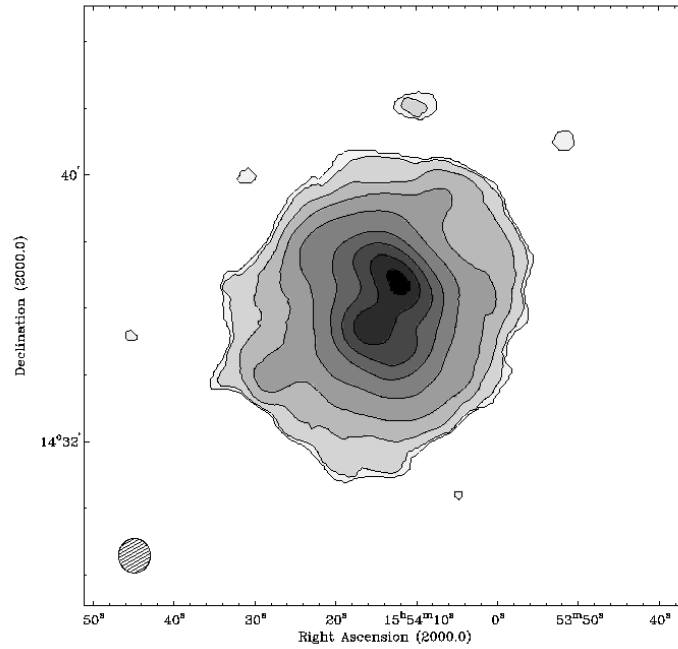


Figure 11-3. Grayscale with contours of the total HI surface density from the low resolution data set. The peak flux corresponds to a column density of $6.9 \times 10^{20} \text{ cm}^{-2}$. Contours are at 1 (the 2σ flux level), 2, 3, 5, 10, 20, 40, 60, 80, and 95% of the peak flux. The synthesized beam ($62'' \times 52''$) is shown at the bottom left.

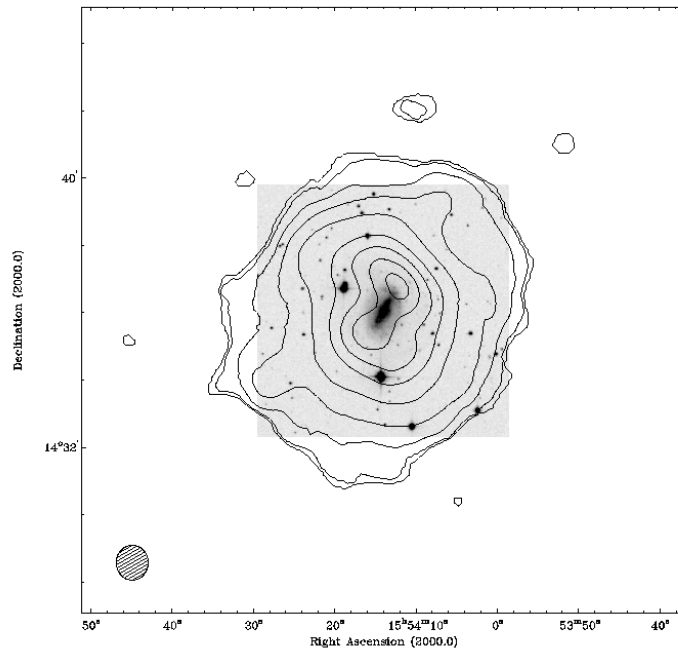


Figure 11-4. Contours of the total HI surface density from the low resolution data set overlaid on an optical DSS image of the galaxy. Resolution and contour levels are the same as in Figure 11-3.

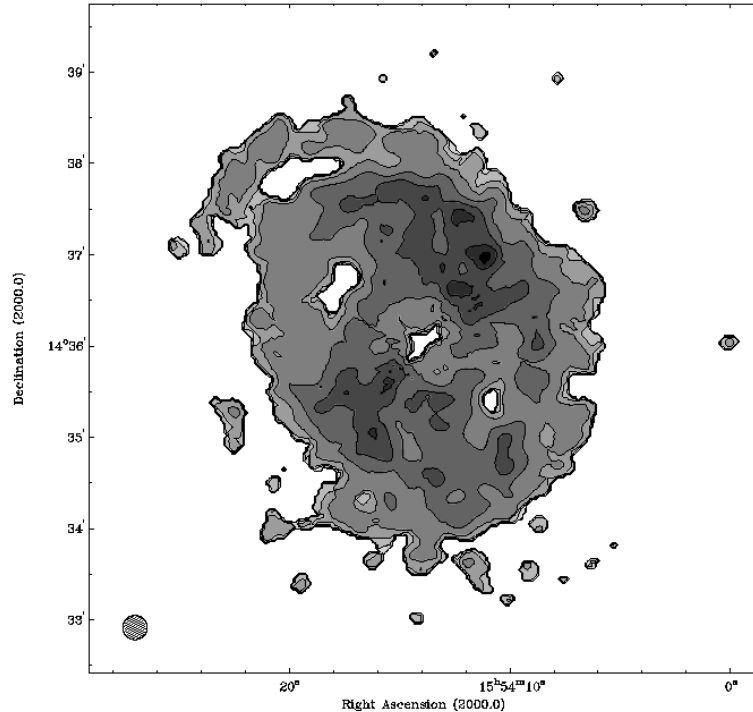


Figure 11-5. Grayscale and contours of the total HI surface density from the high resolution data set. The peak flux corresponds to $7.1 \times 10^{20} \text{ cm}^{-2}$. Contours are at 5 (the 2σ flux level), 10, 15, 20, 40, 60, 80, and 95% of the peak flux. The synthesized beam ($16'' \times 16''$) is shown at the bottom left. For later reference, hole "A" is 1' northeast (up and left) of the galactic center. Hole "B" is located at the galactic center. Hole "C" is 1' southwest (down and right) of the galactic center.

Figure 11-5 shows the high resolution total intensity map for NGC 6012. Here we see emission resembling spiral structure. Comparing to the optical (Figure 11-6), the peak emission again lies just beyond the northern end of the bar. A slightly lower emission maximum lies just beyond the southern end of the bar. The regions of peak emission appear to wrap counter-clockwise around the galaxy in a similar manner to the low resolution images. The center of the bar is deficient in HI, indicating that the bar is old. The HI hole follows the shape of the bar fairly well, as in NGC 1784. There are holes 1' northeast and southwest of the bar that are similar in structure to the one in the bar. Although these HI holes represent an area of low HI column density between the

weak spiral arms, we examine them for the presence of gas at forbidden velocities in a later section. None of the peak HI emission regions appear to be associated with star formation outside of the bar. We calculate a peak column density of $7.1 \times 10^{20} \text{ cm}^{-2}$, in a region just beyond the north edge of the bar.

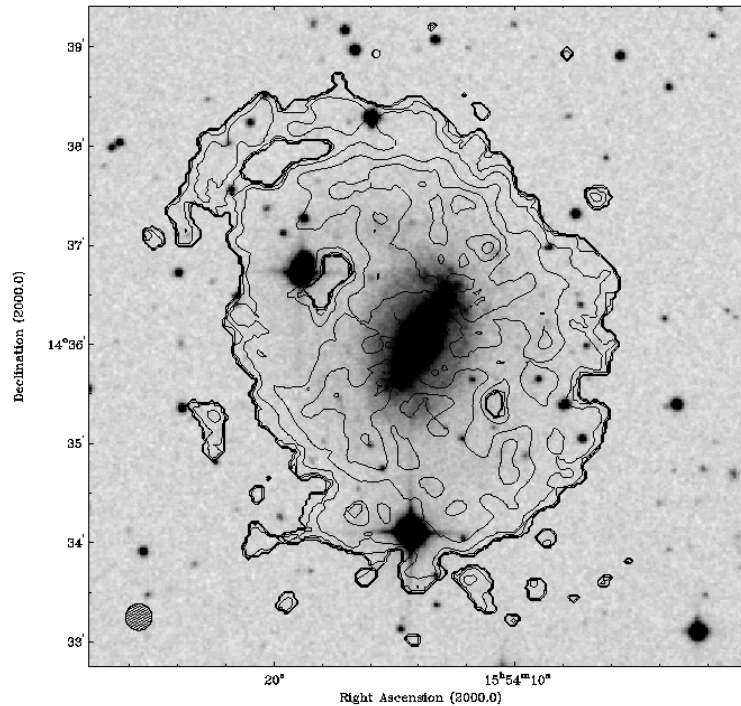


Figure 11-6. Contours of the high resolution data set overlaid on a DSS image of NGC 6012. The peak flux and contours are the same as in Figure 11-5. The synthesized beam is shown at the bottom left.

Global Neutral Hydrogen Properties

Figure 11-7 shows the HI spectrum of NGC 6012 made from the low resolution observations of the galaxy. The spectrum is symmetric at first estimation, and shows a classic double horned pattern. We calculate an HI flux for the galaxy of $22.9 \pm .9 \text{ Jy km s}^{-1}$. This corresponds to an HI mass of $3.7 \times 10^9 M_{\odot}$. We calculate a velocity width of 180 km s^{-1} . From our spectrum of NGC 6012, we calculate a 3σ HI flux level of 0.027

Jy. This corresponds to a conservative minimum mass detection level of $1.3 \times 10^8 M_{\odot}$ for an isolated HI cloud, assuming that it appears in 3 continuous channels.

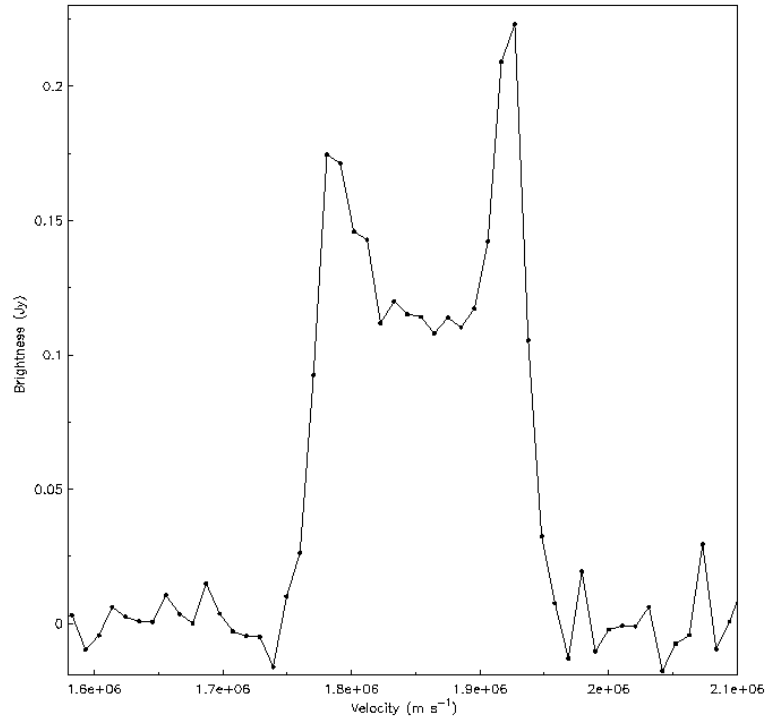


Figure 11-7. The HI flux density versus velocity for the low resolution data set. The velocity resolution here is 10 km s^{-1} .

Figure 11-8 is the radial HI profile from both the high and low resolution data sets. This galaxy shows a similar profile to other galaxies in the sample. The high resolution data shows significant evidence for the HI hole in the center of the galaxy, since the central ring has a column density less than half of the ring outside of it. We find that the HI emission cuts off quickly below the $1 \times 10^{20} \text{ cm}^{-2}$ level in accordance with the predictions of Maloney (1993).

Neutral Hydrogen Kinematics

Figure 11-9 shows the HI velocity field for NGC 4904 created with our low resolution data set. Figure 11-10 shows the HI velocity field for NGC 4900 created with our high resolution data set. Figure 11-11 shows this same field overlaid on an optical

DSS image of the galaxy. The contours in all three images are separated by 10.5 km s^{-1} , and the central contour is at a systemic velocity of 1854 km s^{-1} . The low resolution velocity field shows signs of twisting and warping. The central iso-velocity curve is bent into a slight "S" shape. It also appears that the kinematic position angle changes with radius in the galaxy, particularly in the southern half. The high resolution velocity field shows a similar picture. Here we see, on both sides of the galaxy, multiple velocity peaks along the kinematic major axis. This effect is more pronounced in the northern half of the galaxy, and is likely due to warping of the disk. The velocity field overlaid on the optical image shows that the bar lies very close to the kinematic minor axis, similar to that in NGC 4904. Higher resolution observations may yield more information about radial flows within the bar. In fact, the multiple velocity peaks may be related to the bar, as the inner peaks are coincident with its outer edge.

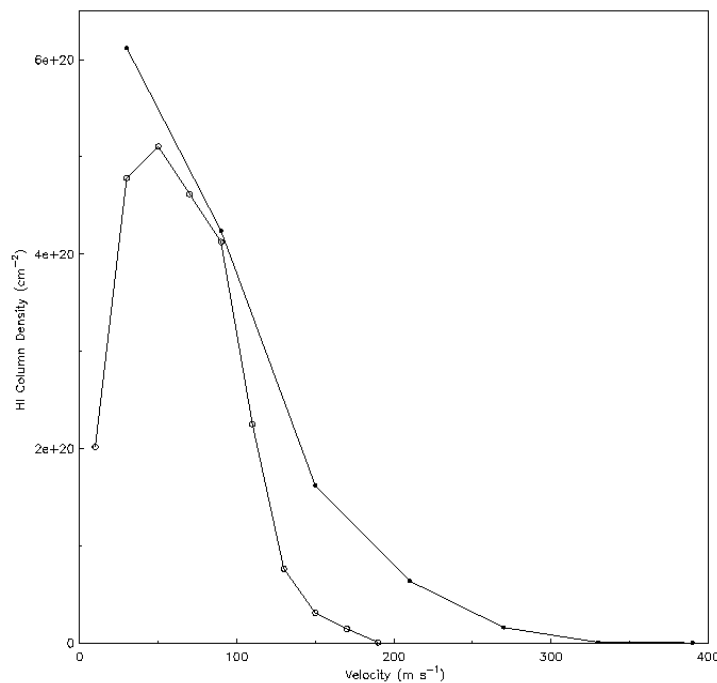


Figure 11-8. The HI radial density profiles from the low resolution data set (closed circles) and the high resolution data set (open circles)

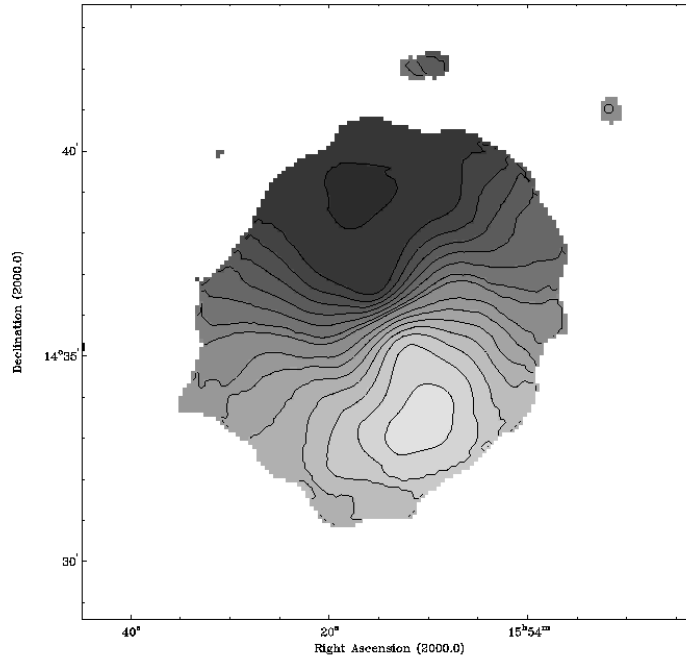


Figure 11-9. Intensity-weighted radial velocity contours of the low resolution data. Contours are separated by 10 km s^{-1} . Motion toward the observer is displayed with lighter grayscales. The central velocity contour is at 1854 km s^{-1} .

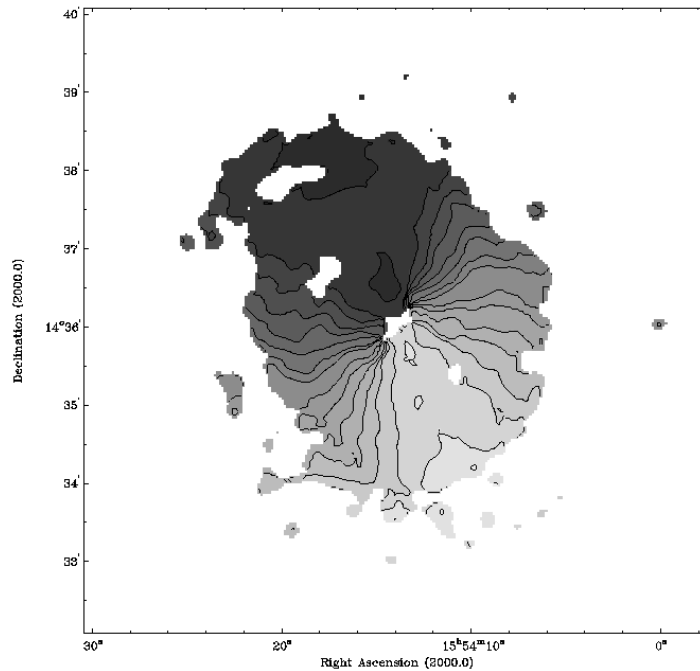


Figure 11-10. Intensity-weighted radial velocity contours of the high resolution data set. Contours are separated by 10 km s^{-1} . Darker grayscales correspond to motion away from the observer.

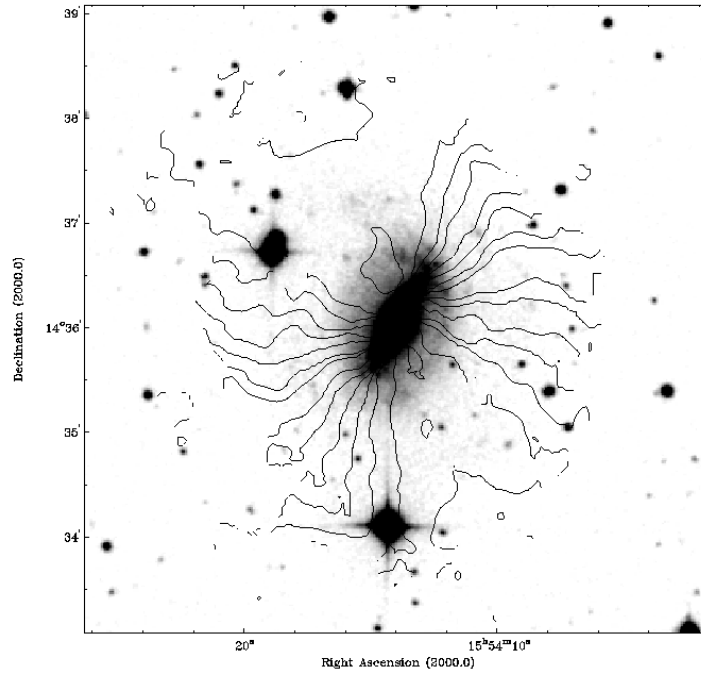


Figure 11-11. Intensity-weighted radial velocity contours of the high resolution data set overlaid on an optical DSS image of NGC 6012. Contours and resolution are the same as in Figure 11-10.

Position-Velocity Plots

Figure 11-12 shows Position-Velocity (P-V) plots made parallel to and along the major axis of NGC 6012 using the high resolution data set. At first glance, these plots are most similar to those of our sample's more regular galaxies, NGC 3900 and NGC 3930. We see the large scale of NGC 6012 present in these plots, as the gas emission stretches for nearly 8'. The plot made through the major axis is fairly symmetric at large scales. It does, however, have some interesting smaller features. On the eastern side of the center of the galaxy, we see a small loop of gas. Typically features like this are indicative of expanding gas (Moore & Gottesman 1998). Here, the diameter of this loop is 30', or on the order of 7 kpc. The column density of gas is low in this loop (only a 3σ detection), however, the size of the feature indicates that a great deal of energy would be needed to push this much mass this far. It is highly unlikely that a single supernova

would be the cause of this feature. More likely, it is the result of some small gas cloud passing through the disk of NGC 6012, similar to what was seen in NGC 1784 (Chapter 5). We measure the radius of the loop to be 3.5 kpc and the velocity width of the loop to be 30 km s^{-1} . This yields a timescale for an interaction to have occurred about 0.2 Gyr ago. Given the low column densities involved, it is unclear whether this potential impactor would have had enough mass to create the warps seen in the outer parts of the galaxy. Perhaps this impactor is one of a family of small objects, creating the situation envisioned by Casuso & Beckman (2001). We also observe in the major axis plot, a trail of gas leading upwards at the western edge of the galaxy to a small clump at a forbidden, counter-rotating velocity.

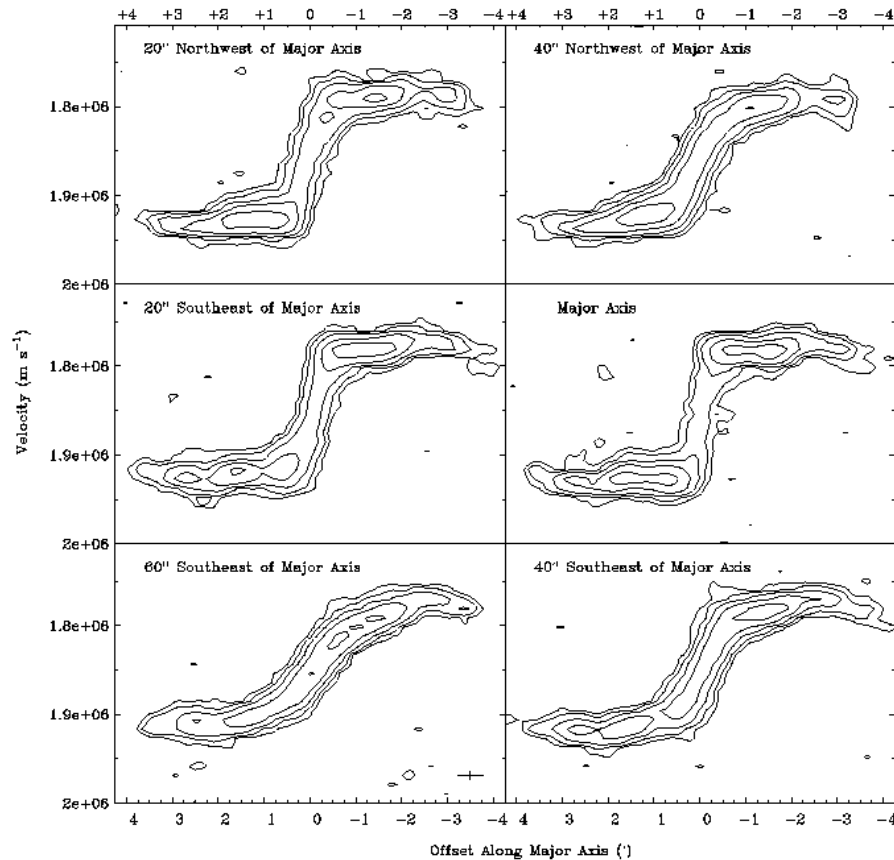


Figure 11-12. A set of P-V slices parallel to and along the major axis of NGC 6012. The contours are at $3, 5, 10, 20,$ and 40σ .

Figure 11-13 shows P-V plots made along and parallel to the minor axis of NGC 6012 using the high resolution data set. Here the warp in the disk of NGC 6012 is readily apparent. The minor axis plot shows a significant "S" shape outside of a radius of 2'. All of the other slices show a similar structure and are lopsided one way or the other. As the contours become very narrow in velocity width outside of the central region of the galaxy, it is possible that this gas was not initially extended this far. A small companion galaxy involved in an interaction with NGC 6012 at some time in the distant past could have pulled this gas out to these large radii. This would explain the seemingly regular central regions of the galaxy, and the more disturbed outer region. The interaction could have been similar to the one in NGC 1784, but was not as violent and occurred in the more distant past. The minor-axis P-V plots of NGC 1784 and NGC 6012 look very similar and lend credibility to this argument.

High Resolution Small Scale P-V Plots

We created P-V plots for the three major holes seen in the high resolution total HI intensity map (Figure 11-5). These plots are shown in Figure 11-14. Hole "A" is the HI depression located 1' northeast of the center of NGC 6012 in Figure 11-5. Hole "B" is the HI depression at the center of the galaxy. Hole "C" is the depression located 1' southwest of the center of the galaxy. The convention we use here is that the plots on the left are parallel to the major kinematic axis of NGC 6012, and the plots on the right are parallel to the minor axis of the galaxy. None of these plots seem to show any gas at forbidden velocities, or any zones of expansion. We conclude that these holes are simply the empty regions located between the weak spiral arms.

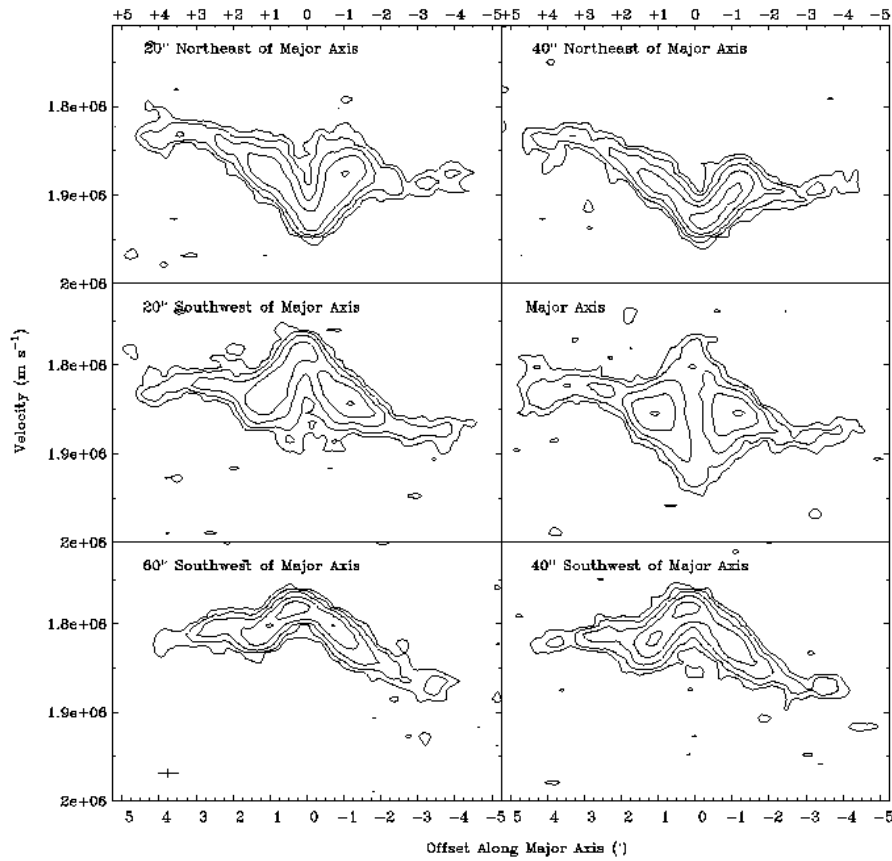


Figure 11-13. A set of P-V slices parallel to and along the minor axis of NGC 6012. The contours are at 3, 5, 10, 20, and 40σ .

Rotation Curves and Model Disks

In order to make rotation curves and model disks of NGC 6012, we used the GIPSY task 'reswri' to fit tilted rings to the velocity field. We used our high resolution data set to create our parameter curves. We fit rotational velocities at radii ranging from 20" to 250" in 30" wide annuli. We held the position of the kinematic center and the systemic velocity of the galaxy as fixed parameters, while allowing the rotational velocity, expansion velocity, position angle, and inclination to be set by the fit. We plot the results from the average of both sides of the galaxy. We plot the rotation velocity versus radius in Figure 11-15, expansion velocity versus radius in Figure 11-16, position angle versus radius in Figure 11-17, and inclination versus radius in Figure 11-18.

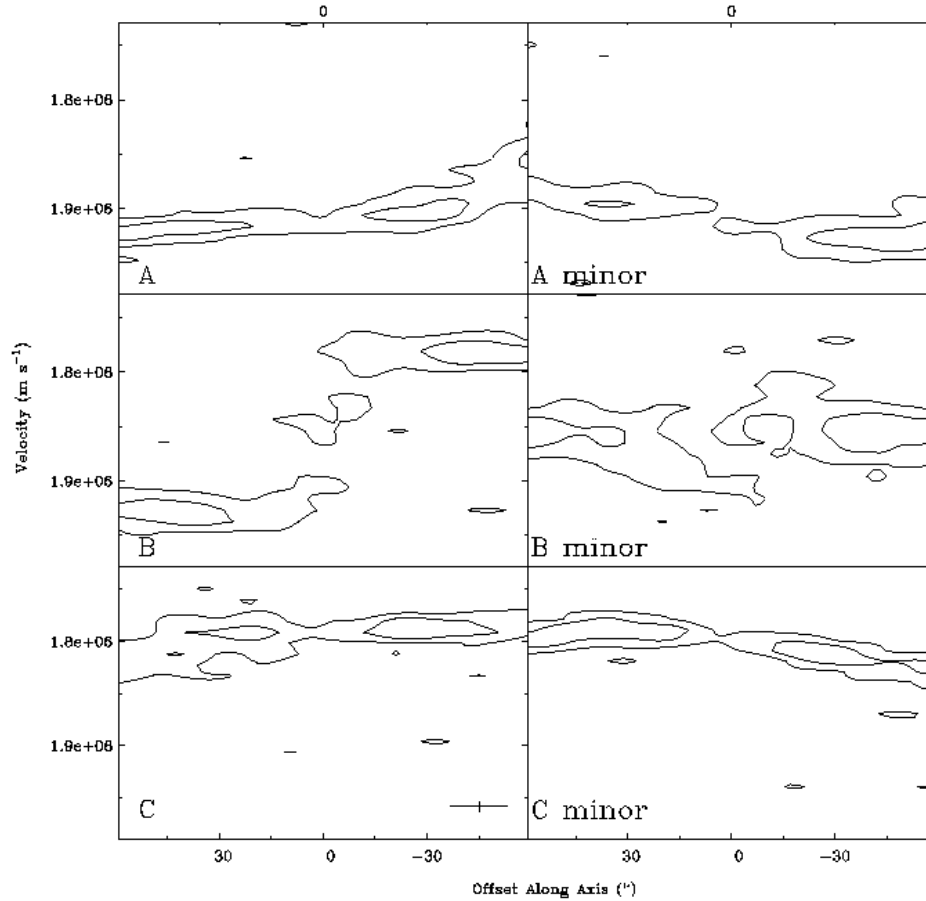


Figure 11-14. Small scale P-V plots made through HI holes found in Figure 11-5. The slices on the left are parallel to the major kinematic axis of NGC 6012. The slices on the right are made parallel to the minor axis of NGC 6012.

NGC 6012's rotation curve (Figure 11-16) appears to be generally flat to rising over its radius. This is consistent with other galaxies in this sample and flocculent galaxies in general (Elmegreen & Elmegreen 1990). If the value of rotational velocity at 250" is to be believed, the rotation curve rises steeply in the extreme outer galaxy. We calculated a value for the total mass of NGC 6012 interior to 220". We ignore the last data point in the rotation curve, because it is in the zone affected by the warp. Using a Keplerian, $M = V^2 R G^{-1}$, to model the disk and halo, where $R = 30$ kpc and $V(30 \text{ kpc}) = 145 \text{ km s}^{-1}$, we find $M(R)$ to be $2.42 \pm 0.05 \times 10^{10} M_{\odot}$. Comparing this with the HI mass calculated above, we find a value for the ratio $M_{\text{HI}} / M(R)$ of 2% for NGC 6012.

The plot of expansion velocity versus radius for NGC 6012 (Figure 11-17) is unusual. Large sections of the galaxy do not show any expansion velocities, but two rings show large velocities in opposite directions. It is not clear why this would occur.

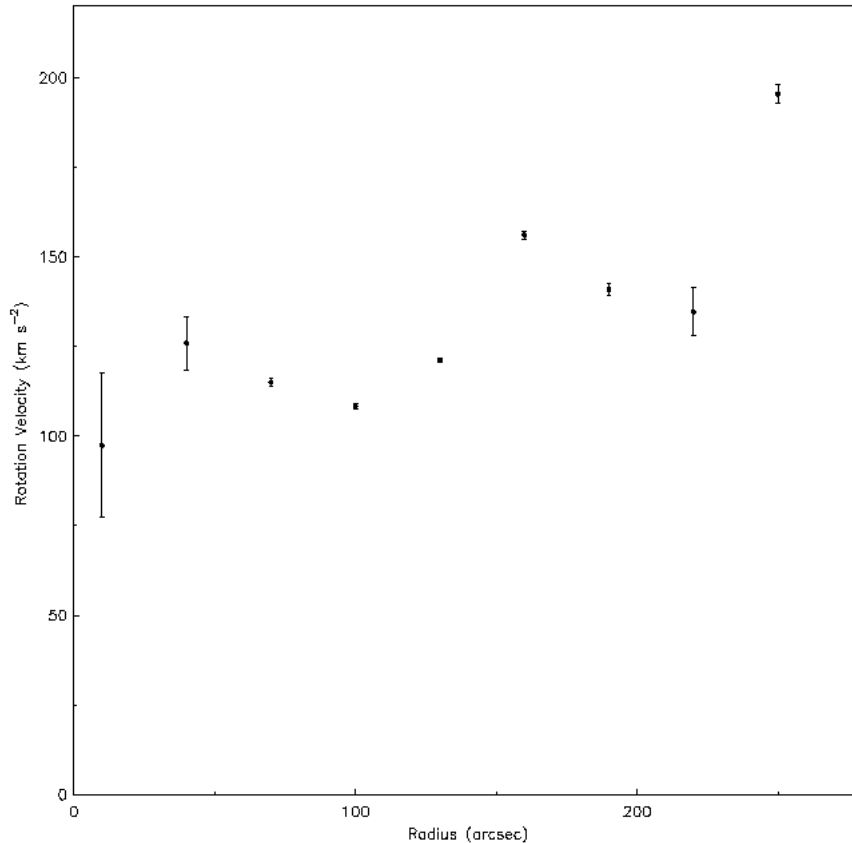


Figure 11-15. Rotation curve of NGC 6012 from the high resolution data set. Data points represent the average of values from both the approaching and receding sides of the galaxy.

The position angle of NGC 6012 is largely consistent across the galaxy (Figure 11-18), with only deviations at the center and outer edge of the galaxy. This plot shows that the warping seen in the channel maps and P-V plots is largely in the vertical direction and not a twisting of the disk. Figure 11-19, the inclination angle curve of the galaxy shows this trend, where the inclination changes 20° over the radius of the galaxy.

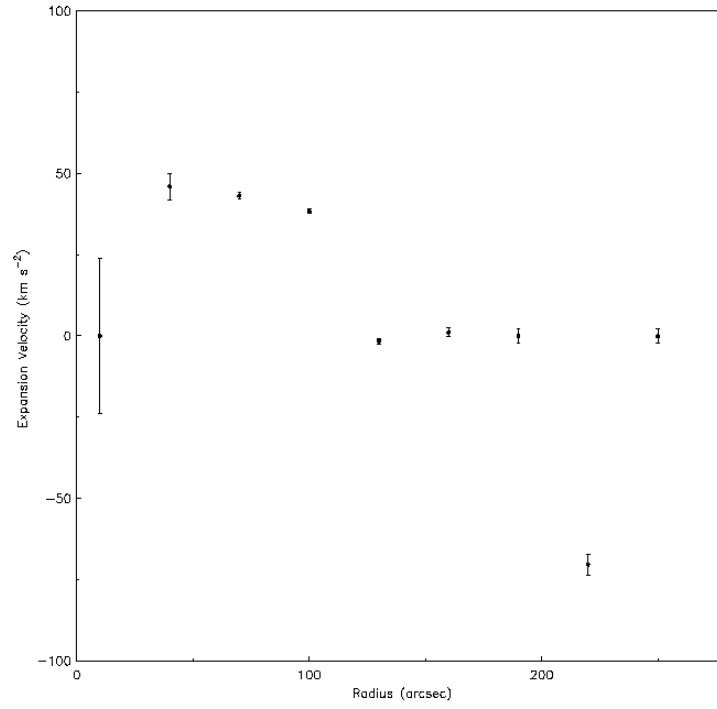


Figure 11-16. Expansion velocity as a function of radius for NGC 6012

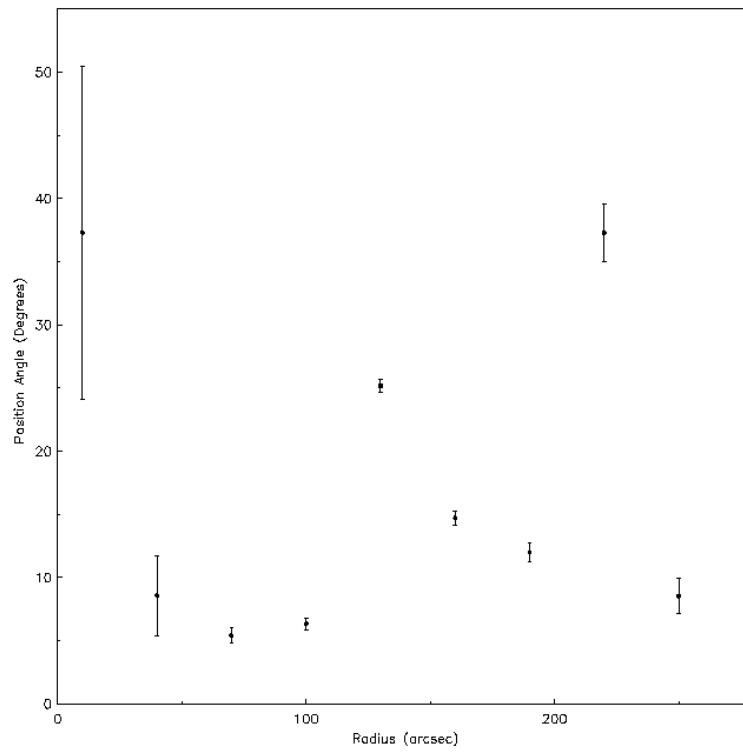


Figure 11-17: Kinematic position angle of NGC 6012 as a function of radius

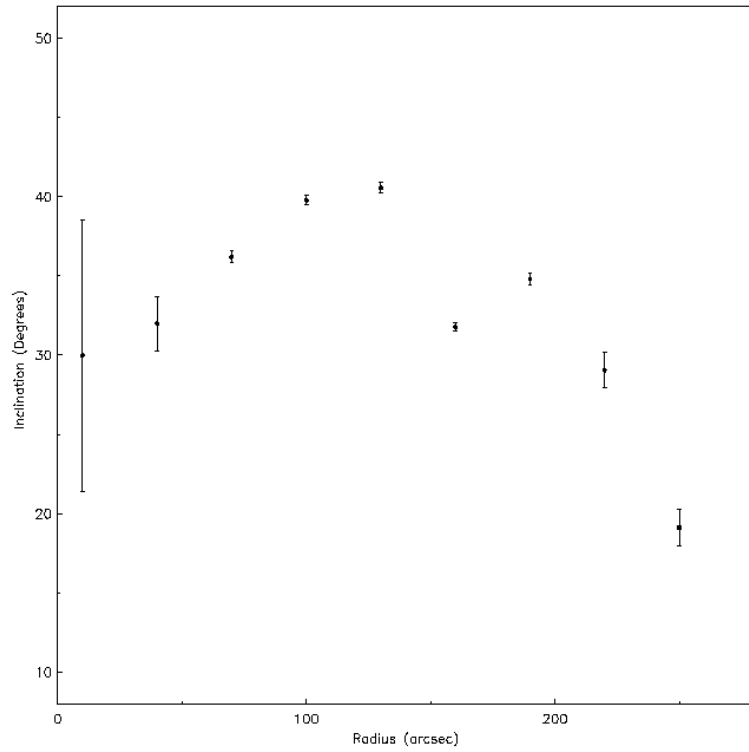


Figure 11-18. Inclination angle of NGC 6012 as a function of radius

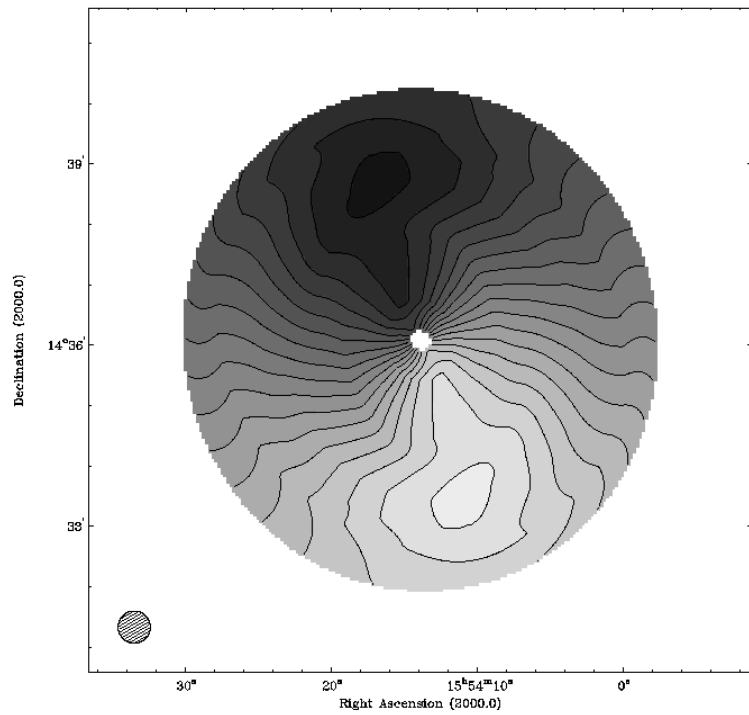


Figure 11-19. Model velocity field constructed from kinematical data in Figures 11-16, 11-17, 11-18, and 11-19. Light grayscales represent approaching velocities.

We used the values of rotational velocity, expansion velocity, position angle, and inclination to construct a model disk for NGC 3930 with the GIPSY task 'velfi'. The model disk is shown in Figure 11-19. This model disk shows the same symmetry as the real velocity fields, along with the slight twisting at large radii. We then subtracted this model field from our high resolution velocity field (Figure 11-10), to create a map of residual velocities. The residual velocity field is shown in Figure 11-20.

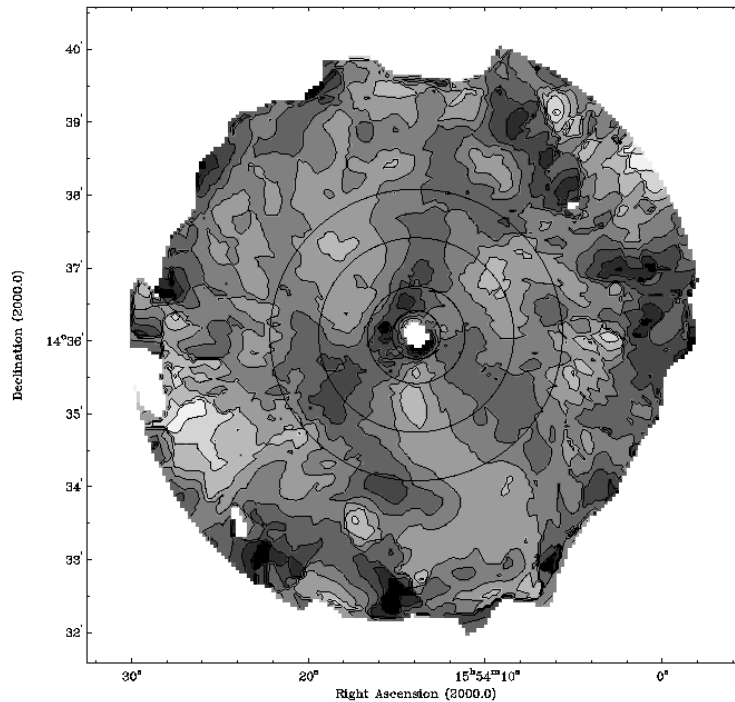


Figure 11-20. Residual velocity field made from model in Figure 11-20. Light grayscales represent approaching residuals. Contours are separated by 5 km s^{-1} . Concentric circles at the center of the galaxy denote where azimuthal profiles were made for later figures.

The model velocity field does resemble the real velocity field fairly well. However, the real velocity field shows twisting iso-velocity curves primarily in the southern half of the galaxy, where the model shows them in both halves. This is a result of the 'velfi' task, which does not take into account differences in the receding and approaching sides of the galaxy. The residual field is complex, but shows interesting

structure. Canzian (1993) postulated that corotation could be found in a galaxy's residual velocity field where the pattern of the residuals switched from an $m=1$ system to an $m=3$. At middle radii in NGC 6012 we see clearly a 3-spoked pattern. Closer to the center, although convoluted, there does appear to be a 2-sided pattern. To explore these features further, we made azimuthal plots of the residual velocity at 20, 40, 80, and 120" (the circles drawn on Figure 11-21 are the locations of these radii). The azimuthal plots are shown in Figures 11-22, 11-23, 11-24, and 11-25. The plot at 20" (Figure 11-21) shows a distinctive one-up and one-down pattern. The residuals never go below 0 km s^{-1} , but this is probably due to some systematic shift in the residual velocity and does not affect the shape of the plot. The plot at 40" (Figure 11-22) shows 3-ups and 3-downs, where one of the downs is significantly stronger than the other two. The plot at 80" (Figure 11-23) shows a pattern of 3 definite ups and downs. The plot at 120" (Figure 11-24) is very confusing, most likely because it is out in the warped region of the galaxy, and the kinematics are disturbed. We conclude then, that the transition from the $m=1$ pattern to $m=3$ pattern occurs slightly inside of a radius of 40". This is consistent with the typical view of corotation occurring just beyond the end of the optical bar. NGC 6012's bar has a radius of about 30" (7 kpc). It is likely that the ring seen in optical observations of the galaxy is associated with the corotation radius. Higher resolution observations are necessary to pin down the exact transition radius between the $m=1$ and $m=3$ regions, and the use of other methods for determining corotation, such as optical colors, would be necessary to confirm our findings. This is, however, an interesting result, since few other papers than Canzian's (1993) original work have shown real galaxies making this transition at their corotation radius.

Summary

NGC 6012 is an unusually large galaxy in HI distribution. It does not show large amounts of gas at forbidden velocities, but does show significant warping of its disk at large radii. We conclude that NGC 6012, like NGC 1784 was involved in an interaction with a small ($10^9 M_{\odot}$) companion in the somewhat distant past. The lack of HI gas in the bar region of the galaxy and lack of significant star formation in the disk point to an older interaction, possibly a few 10^9 years ago. The satellite that presumably pulled gas from the central regions out into the large extended, warped disk shows no remnants today. There are a few minor clouds visible in the channel maps, total intensity maps, and P-V plots, but these are of low mass and uncertain origin. As opposed to the interaction in NGC 1784, this case may have seen a prograde interaction where the companion was incorporated into the galaxy in a much shorter time scale. Potentially the companion could also have been ejected into intergalactic space. Large field total HI intensity maps did not find any companions, so we conclude that the satellite was cannibalized. Further study of this galaxy is certainly warranted, due to this interesting interaction scenario as well as the possible discovery of an HI measure of corotation.

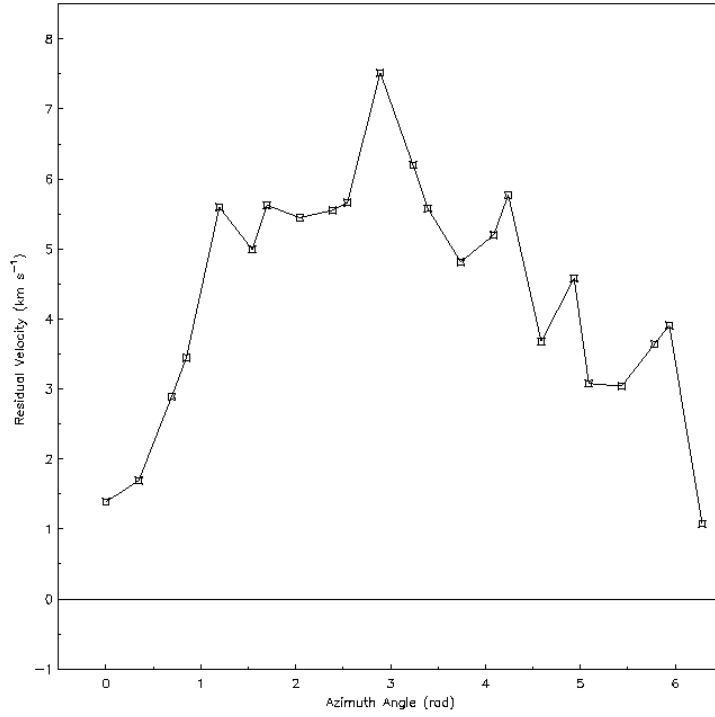


Figure 11-21. Azimuthal plot of NGC 6012's residual velocity field made at a radius of 20"

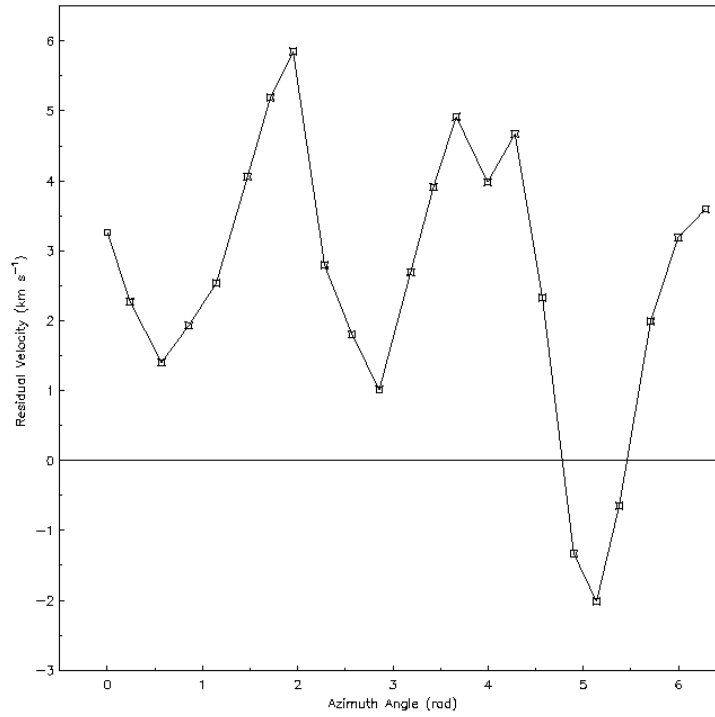


Figure 11-22. Azimuthal plot of NGC 6012's residual velocity field made at a radius of 40"

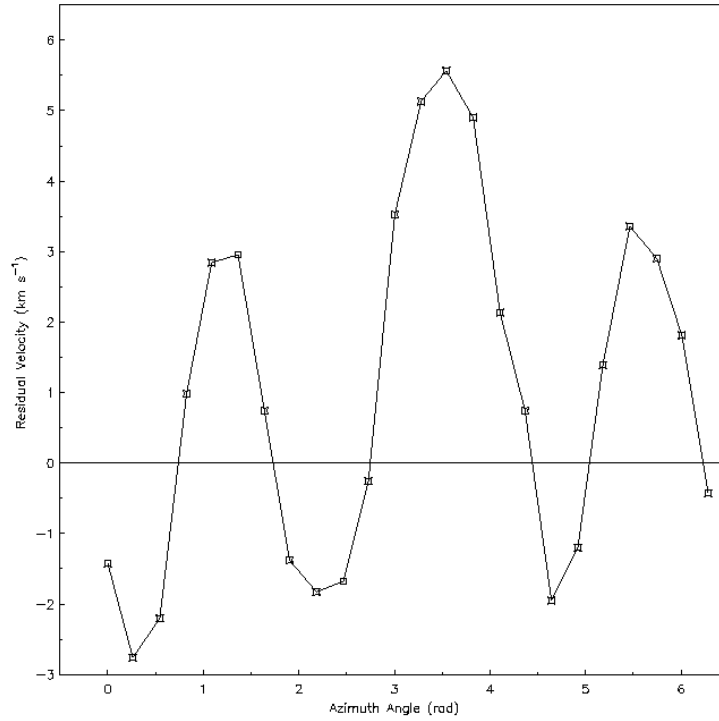


Figure 11-23. Azimuthal plot of NGC 6012's residual velocity field made at a radius of 80"

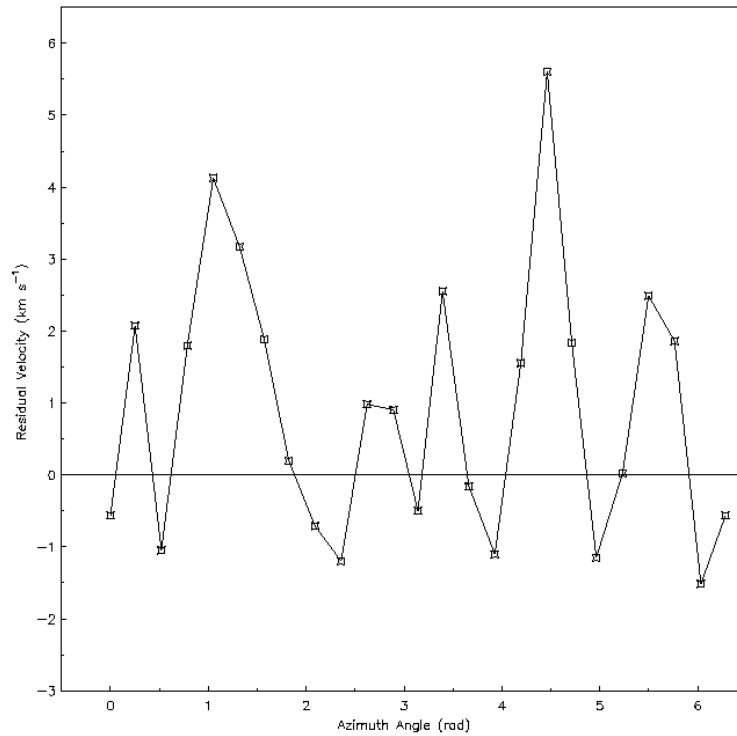


Figure 11-24. Azimuthal plot of NGC 6012's residual velocity field made at a radius of 120"

CHAPTER 12 ANALYSIS, SUMMARY, AND FUTURE WORK

This, final, chapter presents a analysis of the data collected in the optical, near infrared and radio studies of the sample galaxies. We perform this analysis by addressing the primary research questions laid out in Chapter 1.

Are Elmegreen & Elmegreen's (1982) Arm Structure Classifications Valid For Our Sample Galaxies?

We find that we agree with Elmegreen & Elmegreen's (1982) optical classification of our sample galaxies. None of the galaxies of which we possess optical observations show the typical features of grand design galaxies. Granted, we did not perform a proper Fourier analysis on the optical emission of the galaxies, but neither did Elmegreen & Elmegreen (1982). If we were to suggest any changes to the classifications, we would typically move the galaxies to a more flocculent classification, such as with NGC 4900. We find that the bar classification of the galaxies may be somewhat overstated, however. Although the galaxies do not fit in the grand design classification, we find it interesting that Elmegreen & Elmegreen (1982) included one arm systems into the flocculent side of the arm spectrum (arm class "4"), since they do not fit the "even disk of stars" criteria of a typical flocculent. This group included NGC 3055 and NGC 3930. This group may be more rightly given its own arm classification group. Further dynamical study of these objects should be performed to determine if their disk processes are different from other flocculents, or if their arm structure is the result of either minor or major interactions.

NGC 3930, NGC 4793, and NGC 5300 are classified as SAB galaxies. This classification is tenuous at best. The bar region of NGC 3930 seems to be an oval area of stars where the arms join at the center of the galaxy. It is unlikely that this feature is the result of the same dynamical processes that created the bar in NGC 6012, for instance. The bar region in NGC 5300 is not very well defined, and it is likely that another group classifying this object could list it as an S galaxy. A detailed examination of this galaxy's bar isophotes is warranted.

Do the Galaxies in the Sample Possess Near Infrared Spiral Structure?

We find tenuous results within our sample for this research area. We find that the near infrared spiral structure NGC's 2500, 3055, 3887, 4900, 4904, and 6012 to be similar those galaxy's optical spiral structure. Images from the 2MASS survey did not possess enough sensitivity to determine the disk properties of the other galaxies in our sample. It is possible that our sample galaxies do possess stronger spiral structure in the near infrared, but our images were not particularly deep (other than with NGC 3055 and NGC 6012) and were not of particularly high resolution. We find that a great deal of observing time must be invested in order to see the disk structure of these galaxies in near infrared wavelengths. The galaxies are not particularly bright, and do not possess a great deal of star formation in their disks. Large surveys, such as 2MASS, are inadequate for this work, since the observation time on any one particular galaxy is short.

Assuming that we take our results at face value, (i.e. that none of our sample galaxies possessed stronger spiral structure in the near infrared than in optical) we conclude that barred, flocculent galaxies have this morphology in all populations of stars present in the galaxy. Flocculence is the natural state of these galaxies and not just a transient feature of the young stars and gas. A theory of galaxy kinematics for these

systems must be formulated to ensure that the motions of both the old and young stars are not largely driven by large scale spiral density waves.

Does the Sample of Optically Barred Galaxies Possess Near Infrared Bars?

In all cases, it appears that our sample galaxies with optical bars possess bars in the near infrared as well. Due to the resolution limits of our near infrared observations, we can not largely determine if the near infrared bars are of a different size or shape than the optical bars. In NGC 4904, it does appear that the near infrared bar is thicker and more symmetric than the B-band bar, but again, this classification is at the limits of our resolution.

As with the spiral structure, since the stellar bars exist in both the young stars as well as the old stars, the bar is a property of the galaxy itself and not a transient feature of one population. This indicates that the bars in these galaxies are either very long lived, or must have been formed not only of new stars, but also of stars transferred into bar orbits. This may be an indication that the presence of a bar and lack of spiral structure in these galaxies is due to external forces, such as previous encounters with small companions, as opposed to internal disk dynamics.

What are the Nature of the Optical and Near-Infrared Bars?

We repeat here some of the discussion and figures from the last section of Chapter 3. For convenience, we repeat Figures 3-46 through 3-48 as Figures 12-1 through 12-3. These figures show the distribution of bar axis ratio in the sample as a function of Elmegreen arm class, the distribution of bar length to galaxy radius ratio in the sample as a function of Elmegreen arm class, and the distribution of bar length to galaxy radius ratio in the sample as a function of bar axis ratio.

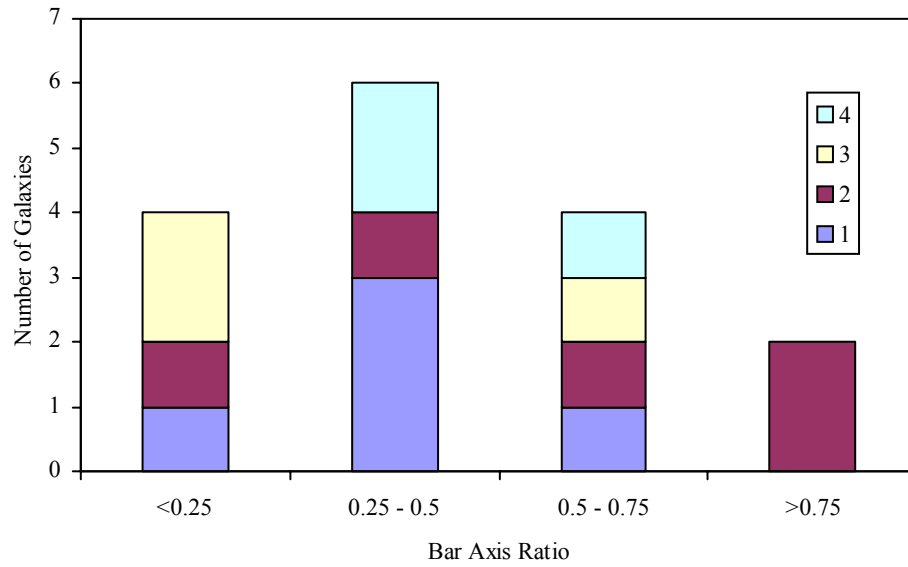


Figure 12-1. Distribution of the bar axis ratio for the sample set. The strips across the columns represent the Elmegreen arm class of the galaxies (labeled at right) with in the particular bar axis ratio bin.

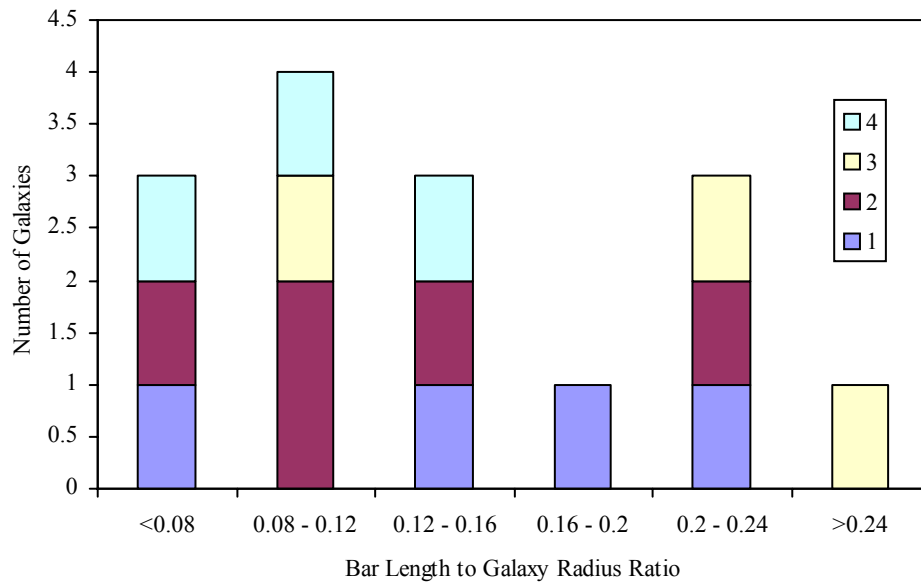


Figure 12-2. Distribution of the bar length to galaxy radius ratio for the sample set. The strips across the columns represent the amount of galaxies from particular Elmegreen arm class (labeled at right) within that bar length ratio bin.

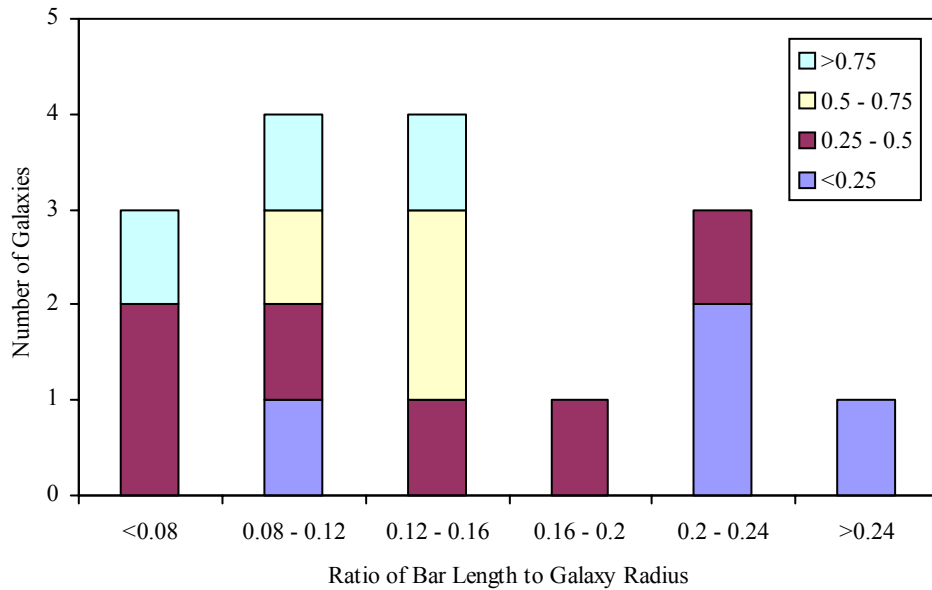


Figure 12-3. Comparison of bar axis ratio to bar/galaxy length ratio. Strips across the columns represent the number of galaxies within a range of bar axis ratio with respect to the bar length bin.

These figures show that there does not appear to be a dependence of either bar axis ratio or bar length to galaxy radius ratio on the Elmegreen arm class. As an overall quality, the degree of flocculence is independent of the bar processes in our sample. Figure 12-3 shows that skinny bars are also long relative to the size of the galaxy. This has been seen in other studies, and these bars are typically referred to as strong. We find that several of the galaxies on the right side of this plot were also found or presumed to be in HI interactions (NGC's 1784, 4900, and 6012), where the majority of galaxies on the left side of the plot have not been found to be involved in interactions. We conclude that interactions have a strong effect on the relative size and shape of galactic bars in this sample.

Figure 12-4 shows the distribution of bar symmetries in the sample set as a function of Elmegreen arm classes. Bar symmetries are determined by eye using the bar

isophotes. The asymmetric category represents bars that are not twisted, but show some global difference from one side of the bar to the other. For example, the two ends of the bar in NGC 1784 are different shapes. The obviously twisted category refers to the cases in NGC's 4904 and 5147 where there appears to be a strong kink in the center of the bar.

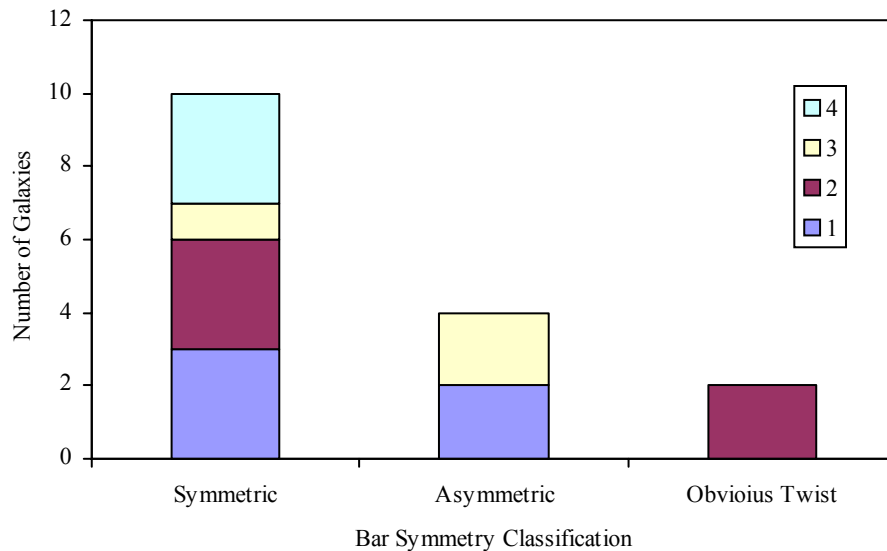


Figure 12-4. Distribution of bar symmetries for the sample set. Strips across the columns represent the different Elmegreen arm classes.

We do not find an obvious trend in the Elmegreen classification of the bar symmetries. Although the two galaxies seen in the "Obvious Twist" category are in class "2", these are small numbers to draw a conclusion from, particularly when several class "2" objects appear in the "symmetric" category as well. We continue this analysis in Figure 12-5, where we plot the galaxies in the same bar symmetry classifications versus the bar length to galaxy radius ratio. Here we see that there does not appear to be a correlation between the relative bar length and the symmetry of the bar. Naively, one might think that there might be a correlation here as both asymmetric bars and long

skinny bars (as shown above) are associated with galactic interactions. However, the processes appear to be more complex.

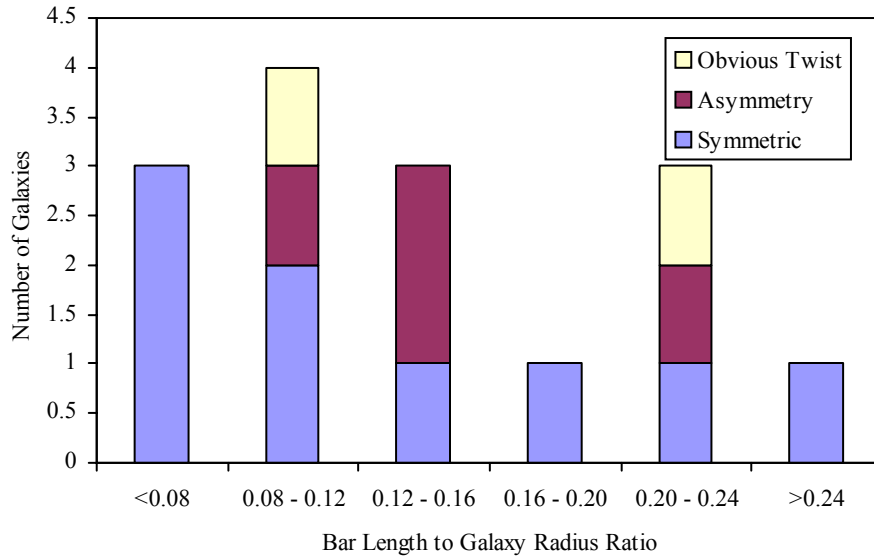


Figure 12-5. Distribution of bar length to galaxy radius ratio in the sample set. Strips across the columns represent the symmetry status of the bar.

We conclude that the galactic bars in our sample are a heterogeneous group. There do not appear to be similar characteristics among the bars across the class of barred, flocculent galaxies. We are able to see some similarities in a few galaxies. We believe that the processes which created the bars in NGC 1784, NGC 4904, and NGC 6012 are similar. Since we observe HI companions, or highly asymmetric HI morphologies in all of these galaxies, we further conclude that the bars in these three galaxies are created through the process of interaction and merger. On the other hand, the smaller bars present in NGC's 3055, 3687, 3930, 5300, and 5783 are more likely to be due to internal processes of the disk. NGC 4900 likely is a middle ground. It was observed to have a highly asymmetric HI distribution most likely due to an interaction, but its bar does not have the same size relative to the optical galaxy as with NGC 1784, NGC 4904, and NGC

6012. This may be due to the small overall size of NGC 4900, but the processes are uncertain.

Are The Mass Distributions Of Galaxies Similar?

We find that of the seven sample galaxies observed in HI, four galaxies show rising rotation curves, one shows a flat rotation curve, and one shows a flat/falling rotation curve. NGC 4904 was fit *a priori* to have a flat rotation curve, so we do not consider it here. Elmegreen & Elmegreen (1990) state that flocculent galaxies typically have flat to rising rotation curves, because their disk mass relative to the halo mass is lower than for grand design galaxies. The relative importance of the halo mass in these galaxies prohibits the formation of spiral density waves and the galaxies remain flocculent. We find a similar result, but a higher number of our sample needs to be observed in HI in order to draw more conclusions. Figure 12-6 shows the distribution of Elmegreen arm classes within the sample set as a function of rotation curve shape. Figure 12-7 shows the distribution of bar length to galaxy ratio as a function of rotation curve shape.

We find that the shape of the rotation curve is not related to the Elmegreen arm classification in Figure 12-6. Although our sample size of seven (six if NGC 4904 is discounted) is small, Figure 12-6 seems to indicate that a galaxy's degree of flocculence is not simply related to the ratio of halo to disk mass, as Elmegreen & Elmegreen (1990) suggest. It may be globally true that flocculent galaxies are more likely to have rising rotation curves, but there must be other factors at work controlling the disk structure. The bar status of this sample may make them different than flocculent galaxies in general. Figure 12-7 shows that there is no correlation between the relative bar length and the rotation curve shape. It is interesting to note that we selected no galaxies with

middle relative bar lengths to observe in HI. In order to confirm our findings from these two figures, more of the sample must be observed in HI.

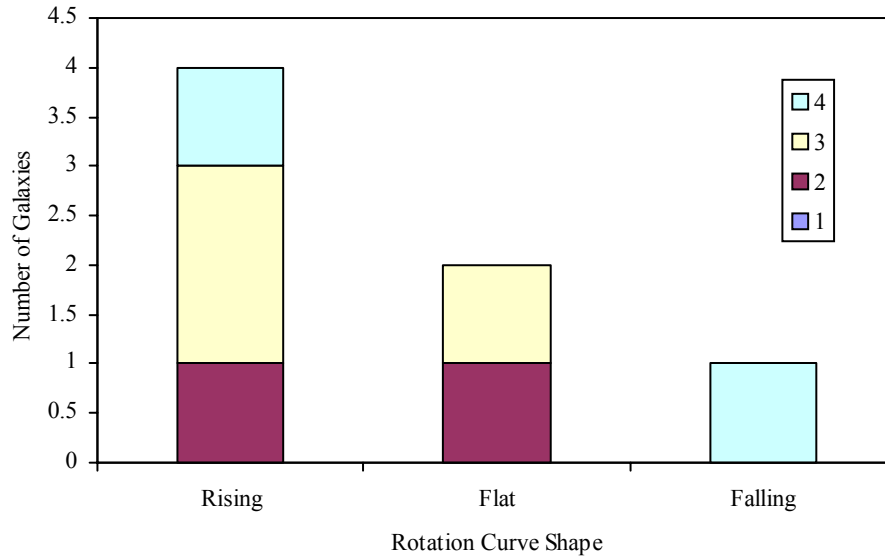


Figure 12-6. Distribution of HI Rotation curve shapes within the sample set. Strips across the columns represent the different Elmegreen arm classifications. We did not observe in HI any galaxies that were in Elmegreen arm class "1".

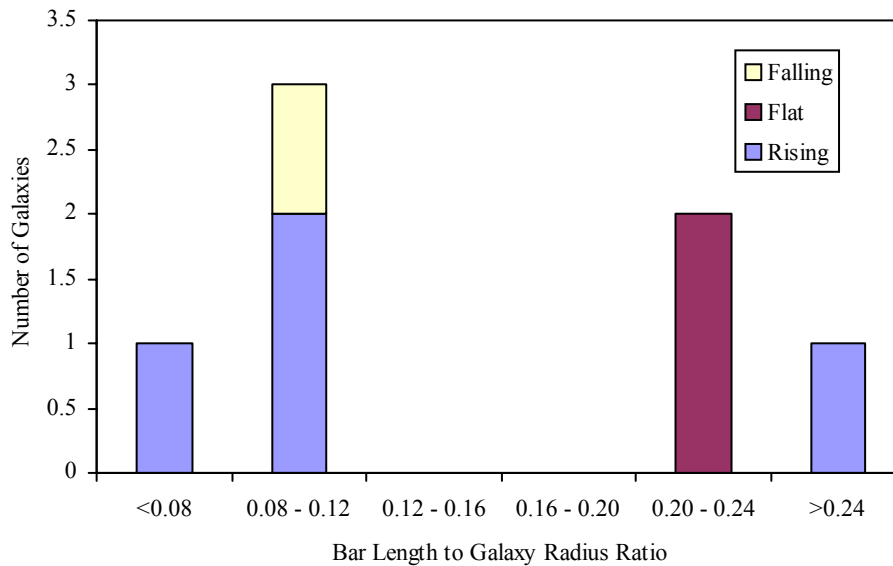


Figure 12-7. Distribution of Bar length to galaxy radius ratio in galaxies observed in HI. Strips across the columns represent the shape of the rotation curve.

Does the Sample of Optically Barred, Flocculent Galaxies Possess Similar Neutral Hydrogen Mass Ratios and Morphologies?

Of the seven galaxies in our sample that we observed in HI, we found that 6 of the galaxies possessed what could be classified as an HI asymmetry. NGC 5300 possessed no sizeable asymmetry. The asymmetries found in NGC 3055 and NGC 3930, however, were small, and only involved the distribution of the peak HI regions within the galaxy. NGC's 1784, 4900, 4904, and 6012 possessed sizeable asymmetries and warps. Pisano & Wilcots (1999) reported that another galaxy in our sample, NGC 3246, possessed an HI asymmetry. Mazzei (1995) categorizes NGC 2793 as a ring galaxy consistent with a head on encounter, so we also include it in our list of galaxies with HI asymmetries. In all asymmetric cases, 1 - 3% of the galaxy mass, if not more, was contained in warps, bubbles, or separate dynamical systems. We contend that the kinematics of the warps and asymmetries in these 4 galaxies are a result of interactions with small companions.

We found in all cases that the HI diameter of the galaxy was significantly bigger than the optical size of the galaxy. Figure 12-8 shows the distribution of HI diameters in the sample set. Figure 12-9 shows the distribution of optical to HI diameter ratio. We use the HI diameter of NGC 3246 found by Pisano & Wilcots (1999) in this plot. The smallest HI to optical diameter ratio was in NGC 5300, which had a value of 1.4 (24 kpc / 14 kpc). The largest HI to optical diameter ratio was in NGC 6012, which had a value of 4.3 (65 kpc / 15 kpc). The average HI to optical diameter ratio was 2.5 for the sample. We find a trend that galaxies with significantly more disturbed HI morphologies have large HI to optical diameter ratio values. NGC 6012 with the highest ratio has a large, extended warp region about the main body of the galaxy. Similarly, NGC 4900, with a diameter ratio of 4.1 probably possesses an HI ring due to an ongoing encounter. NGC

5300, on the other hand, has the lowest diameter ratio, and does not show any significant asymmetries.

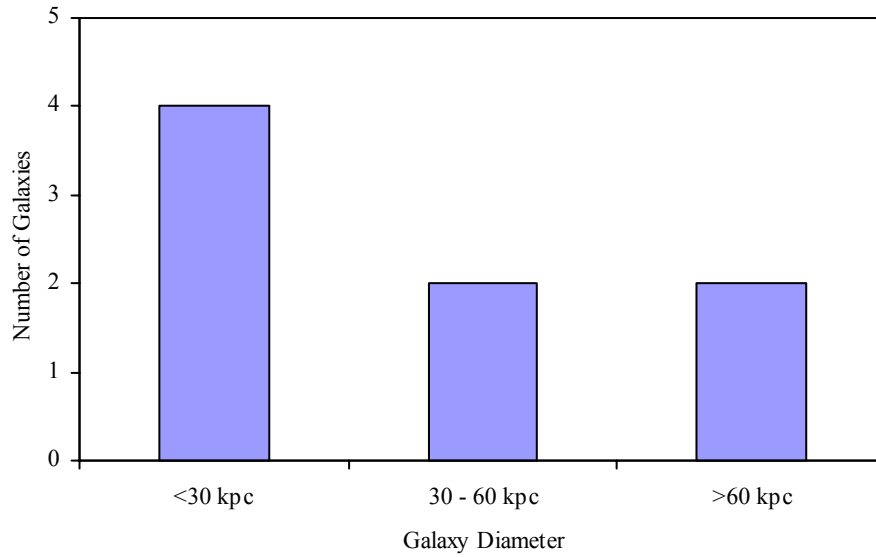


Figure 12-8. Distribution of HI diameters in the sample set

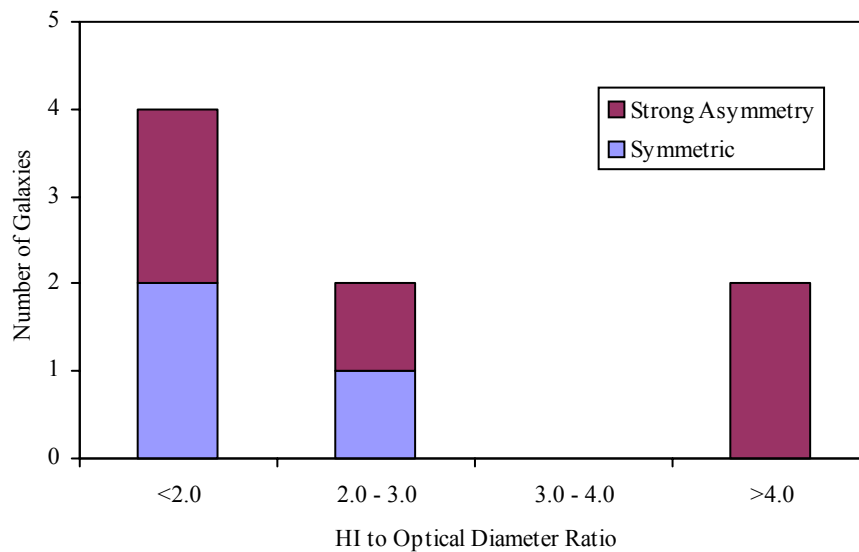


Figure 12-9. Distribution of HI to Optical Diameter Ratios within the sample set. Strips across the columns correspond to the symmetry of the HI distribution.

In Figure 12-10, we examine the length of the bar relative to the optical size of the galaxy versus the HI to optical diameter ratio. Here, unlike previous graphs of the

relative bar length, we only break the bar length distribution into two bins. The plot seems to indicate that galaxies with smaller HI to optical diameter ratios also have smaller bar to galaxy length ratios. NGC 1784 has one of the longer relative bars in the sample, but has a small HI to optical diameter ratio. However, with slightly lower HI resolution, we would measure the HI diameter of NGC 1784 as almost two times higher. This is perhaps the case in NGC 4900 and NGC 4904. We conclude that the HI to optical diameter ratio is a good indicator of the interaction state of a galaxy, as is a long, skinny bar.

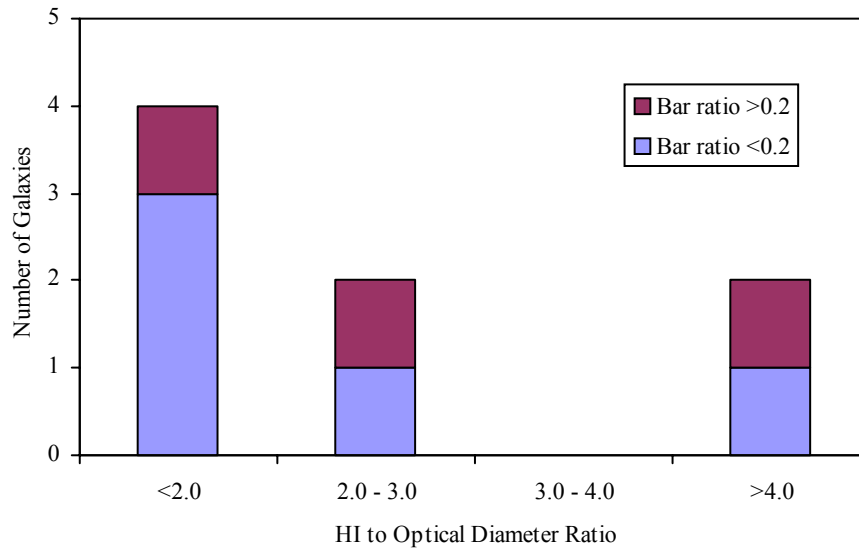


Figure 12-10. Distribution of HI to optical diameter ratios. Strips across the bar represent the bar to galaxy length ratio.

Figure 12-11 shows the distribution of HI masses in the sample set. We calculate HI mass values for NGC's 3687, 3887, 5645, and 5783 from HI fluxes listed in the literature (Haynes et al. 1998). Figure 12-12 shows the distribution of M_{HI} to M_{dyn} ratios for the sample, including NGC 3246 from Pisano & Wilcots (1999). Figure 12-13 shows this same distribution, but compared to the sample's Elmegreen arm classifications.

Galaxies in the literature which only had values of the HI line width were not included for this plot, since our dynamical masses were derived from a rotation curve analysis. Our analysis eliminated the inclination term present in these other velocity width measurements.

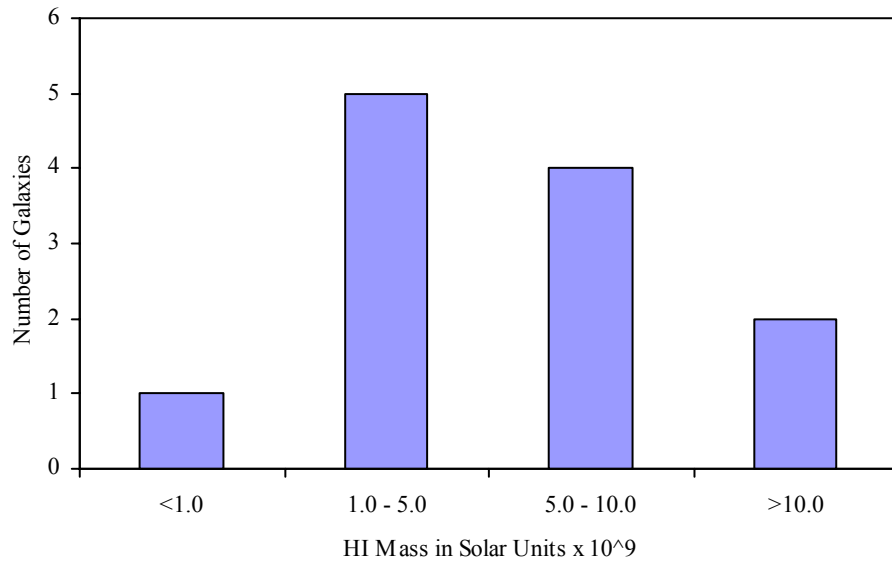


Figure 12-11. Distribution of HI masses in the sample set

We found the most massive galaxy in terms of HI to be NGC 3246, while the least massive was NGC 4904. NGC 3246 is some 20 times more massive in HI than NGC 4904. This result is not unexpected, given the physical size difference between the two galaxies. NGC 3930 possessed an unusually high peak column density of HI, on the order of $6 \times 10^{21} \text{ cm}^{-2}$, while none of the other galaxies reached above $2.5 \times 10^{21} \text{ cm}^{-2}$. It is unclear why the peak column density was higher in this galaxy.

In terms of the ratio of HI mass to the dynamical mass of the galaxy, we find that most of the galaxies cluster around the 3-5 % region, however, none are higher than 6% in the sample. We calculate an average mass ratio of 3.8%. This is in line with what is found with other typical spiral galaxies. We also do not see a correlation with higher HI

mass fraction and the HI diameter of the galaxy relative to the optical galaxy. Either the excess HI in the richer galaxies is center of the galaxy, or the optical distribution extends out further to compensate in these galaxies.

Figure 12-13 shows that there does not appear to be a correlation between the HI mass fraction and Elmegreen arm classification.

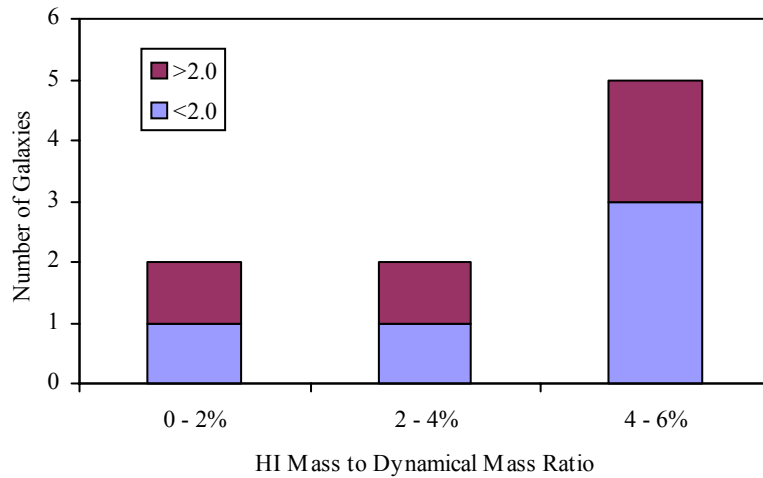


Figure 12-12. Distribution of HI Mass fraction for the sample set. The strips across the columns represent the distribution of HI to optical diameter ratios.

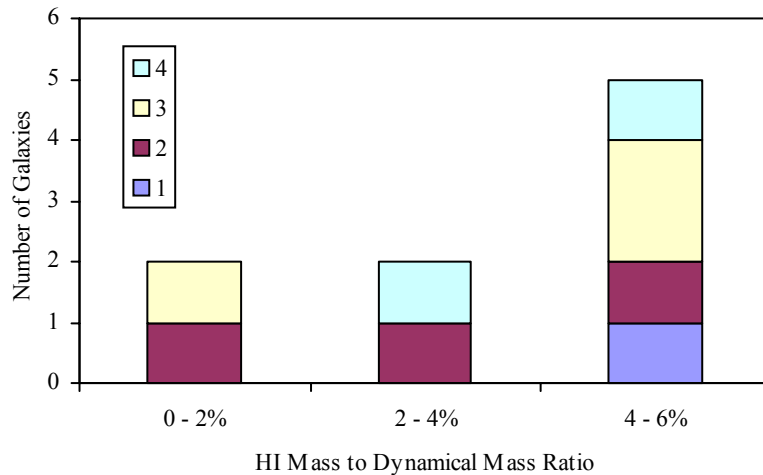


Figure 12-13. Distribution of HI Mass fraction for the sample set. The strips across the columns represent the Elmegreen arm classification of the set.

Do the Optically Barred, Flocculent Galaxies Possess HI Companions?

Of the seven galaxies with HI observations in this project, we found that two, NGC 1784 and NGC 3055 possess direct evidence of HI companions. NGC 1784 possesses counter-rotating ring of HI around the galaxy that must be from an external source, and NGC 3055 possesses two small satellites at rather large radius (~ 90 kpc). NGC 1784's satellite system does not show any optical emission, while both of NGC 3055's satellites do. We found two additional galaxies, NGC 4900 and NGC 4904, which show strong evidence that they are currently involved in interactions. Both galaxies show velocity fields which have more than one kinematic position angles, and have channel maps that are indicative of an HI ring encircling these galaxies. Unfortunately, the angular resolution of our observations in both of these cases is insufficient to resolve out any possible companion system. Finally, NGC 6012 shows an asymmetry in its HI disk morphology that is likely a result of a previous interaction. NGC 6012 shows a warp and extended HI emission very similar to NGC 1784, and it is for this reason, that we feel it was involved in a similar interaction in the distant past. In galaxies that we did not observe in HI ourselves, Pisano & Wilcots (1999) report that NGC 3246 is involved in an interaction, and Mazzei (1995) reports that NGC 2793 is also, due to its optical distribution.

Overall, the number of companions positively identified, 3, and even the number of presumed companions, 6 or 7, compared to the number of galaxies in the HI sample, 15, is in line with the observational work of Pisano & Wilcots (2003). They found that over a large sample of isolated galaxies, there were not as many small, non-stellar, HI companions as would be predicted by typical λ CDM models. They concluded that the

epoch of galaxy formation is for the most part over, at least for isolated galaxies. We do not observe numerous small, intergalactic HI clouds around our sample galaxies, even though our observations are fairly deep for several galaxies. Where we do find small HI clouds, as in NGC 1784, it is more likely that these are the remnants of one large interaction, as opposed to many independent interactions.

What are the Physical and Orbital Properties of the HI Companions?

We do not find an overall pattern among the HI companions in this sample. The different galaxies show very different companions, or evidence of previous companions. The companion being cannibalized by NGC 1784 has a dynamical mass on the order of $10^{10} M_{\odot}$ and a $M_{\text{HI}} / M_{\text{tot}}$ value of 3 - 5%. It is an apparently retrograde orbit, although, there is a small chance that the orbit could be prograde if it is nearly polar. The interaction is probably a few 10^9 years old. We have not found an optical counterpart to NGC 1784's companion. The two companions to NGC 3055 are a bit smaller, with a dynamical mass of a few $10^9 M_{\odot}$, and a similar $M_{\text{HI}} / M_{\text{tot}}$ value. It appears that they are on prograde orbits, since the companion's internal velocity fields reflect the side of NGC 3055 on which they lie. We did not discover any rings or arcs of HI gas linking the satellites to NGC 3055 or tracing their previous paths. It is hard to comment on the effect of these satellites on NGC 3055, since currently they reside at such a large distance. In addition, our discussion in Chapter 7 showed that it is unlikely that the satellites are gravitationally bound to NGC 3055. A past closer encounter would be a good explanation for NGC 3055's one-armed optical pattern and small HI asymmetry.

Of the presumed companions, NGC 4900 and NGC 4904 seem to be in similar states. The best interpretation of our data is that both galaxies are currently surrounded

by an HI ring of total mass, $10^9 M_{\odot}$. These rings are the result of a satellite orbiting the galaxies and breaking up. The orbit of the satellite has a small radius and is prograde.

In the case of NGC 6012, we assume that it has undergone an interaction much like the one NGC 1784 is involved currently. The large extension of HI and its warp are both similar to NGC 1784's HI morphology and kinematics. We might expect a similar sized satellite ($\sim 10^9 M_{\odot}$) as in NGC 1784 would be all that was needed to cause these effects. If the interaction was somewhat older, by 10^9 years, and somewhat less energetic than in NGC 1784, the satellite may have already been consumed and large scale star formation may have already ended in NGC 6012.

Are Barred, Flocculent Galaxies Different Than the Average Galaxy?

To assess the validity of our selection of a sample set, we must compare our results from above with surveys of similar properties of general galaxy populations. To complete our study, we also must define a control set of barred, grand design galaxies. This set is discussed below in the Future Work section of this paper.

Elmegreen & Elmegreen (1982) find that grand design galaxies are slightly brighter than flocculent galaxies. They find that galaxies of arm class '1' have a mean absolute blue magnitude of -20, where class '12' galaxies have a mean absolute blue magnitude of -21. We find that our set has a mean absolute blue magnitude of -19.1. This fits the trend, and may imply that barred, flocculent galaxies are dimmer still, although a larger sample set from both Elmegreen & Elmegreen (1982) and in our own sample set would be required to reduce scatter. Elmegreen & Elmegreen (1982) also find that flocculent galaxies are preferentially late type galaxies. We find the same situation in our set, with the median galaxy being a Sc.

Martin (1995) studies the optical bar properties of a large sample of nearby, normal galaxies. This study found that the relative bar length in early-type galaxies is about a factor of three larger than the bar length of late-type galaxies. In Martin (1995) the relative bar length of late-type galaxies is less than 0.2 of the galaxy diameter. We find similar results in our sample, where NGC 6012 is the only galaxy with a relative bar length significantly longer than 0.2. It is significant that NGC 6012 is also the earliest galaxy in our sample. Martin (1995) finds no trend for bar axis ratio across Hubble Type. This is similar to our results. Martin (1995) finds that the bar axis ratio of active galaxies is particularly low, but shows no trend for quiescent galaxies. We find a similar result in that none of our sample is reported to be active, and the bar axis ratio of our sample shows no trend.

Broeils & van Woerden (1994) studied the HI properties of regular, nearby spiral galaxies, and looked for galaxies with extended HI emission. They found that the typical HI radius for these galaxies was 1.8 times the optical D_{25} for the galaxy. The HI radii for the galaxies in our sample are similar, but may be a bit larger due to the interactions in our sample. Half of our galaxies show HI radii less than or equal to the value in Broeils & van Woerden (1994), the other half are significantly larger, and correspond to galaxies involved in interactions. Unfortunately, we possess measurements of HI radii for eight of our galaxies. Broeils & van Woerden (1994) also provide an average value for the HI masses in nearby spirals. Their mean value of $5.9 \times 10^9 M_{\odot}$ falls within our range of 1 to $10 \times 10^9 M_{\odot}$. Similarly, Roberts & Haynes (1994) provide HI mass ranges for a variety of Hubble Types. Our values fall very much in line with the late type galaxies in that study. The work of Pisano & Wilcots (2003) shows that our galaxies are typical in their

number of interactions and companions. Our sample does not appear to be undergoing an unusual number of interactions. It may still be that these galaxies are more likely to be involved in an interaction than grand design galaxies due to their large average HI radius, but we will have to wait until observations of our control group are complete.

Through comparison with other large scale survey projects, we find that our sample is representative of normal galaxies. There does not seem to be some unique property that is special to barred, flocculent galaxies. They may be slightly dimmer and larger in HI (possibly more likely to be involved in an interaction), than typical galaxies, but they are not globally different. We must conclude that the flocculent and barred states of these galaxies are due to processes which occur within the galaxy. Theories involving bar structure and the interaction between the galactic disk and halo may have important implications on the spiral structure of the disk as well. The fact that we have found rising rotation curves in our sample seems to indicate this. Other theories, such as Casuso & Beckman's (2001) regarding the presence of numerous small ($10^6 M_{\odot}$) HI clouds influencing galactic disk warps may be important as well. These types of clouds are below our sensitivity limits. If it is true that these types of clouds can produce disk warps, then perhaps they can influence spiral structure as well. Additional, very deep observations of HI in isolated spiral galaxies are warranted. We conclude that further dynamical study of galaxies with smaller and weaker bars is also necessary.

Summary

The overall picture we get of the sample galaxies in our study is that they are a varied bunch. There are some trends among the galaxies that seem to be apparent. We believe that NGC 1784, NGC 6012, NGC 4904, and NGC 4900 are similar galaxies, but follow a trend of decreasing physical size and mass. All four of these galaxies show

strong bars, evidence for star formation, disk warps, and either confirmed or possible companions. The interaction with a small companion seems to be the trigger for the optical and radio morphologies of these galaxies. The timescale of presumed interaction is in line with the age of the bar. The seemingly older bars in NGC 6012 and NGC 1784 (assumed because of the large HI holes in the center of these galaxies) are associated with older or finished interactions. In NGC 4900 and NGC 4900 we see interactions that appear to be beginning coupled with bars that are still filled with HI and appear to be actively star forming. Similarly, the lack of a strong interaction with a companion galaxy seems to be the reason for the regular HI morphology in NGC 3930 and NGC 5300.

We draw the large conclusion that interactions, or the lack there of, are very important to the morphology of barred, flocculent galaxies. Left to themselves, all of the galaxies in this sample would most likely look like NGC 5300, flocculent and not strongly barred. In fact, Elmegreen & Elmegreen (1982) find that of isolated, unbarred galaxies the majority are flocculent. Although slightly barred, perhaps due to some internal disk processes, NGC 5300 fits this bill well. When the galaxy is approached by a small companion galaxy, the morphology changes. Typically, galaxies with companions become grand design and grow bars (Elmegreen & Elmegreen 1982; Byrd & Howard 1992). However, the nature of the interactions in NGC's 1784, 4900, 4904, and 6012 somehow prevented spiral arms from being formed, but allowed the bar to grow. Perhaps in NGC 1784 this process is related to the retrograde nature of the interaction. Although this work must be done in the future with better near infrared images, a determination of the Q_B parameter will likely turn up that although the bar is strong in these four galaxies,

it does not control the processes in the outer disk, and that flocculence in these cases is a result of external factors.

Future Work

The future study of this group of galaxies involves two thrusts. First of all, more and better observations of the barred, flocculent galaxies need to be obtained. All 15 galaxies in the sample should be observed for a total of 10 to 15 hours at 21 cm using the D and C arrays of the VLA. This will allow us to image HI clouds down to $10^7 M_{\odot}$ at resolutions ranging from 1 to 10 kpc for the entire sample. For the galaxies that are particularly bright, or where high resolution observations are warranted (NGC 4900, NGC 4904, and NGC 6012), B configuration observations should be made. The realization of the Enhanced VLA in the near future should enable these observations to be made. With an increase of a factor of 10 in sensitivity, observing times could be reduced by a factor of 3 with the same sensitivity.

Further optical and near infrared observations of the current galaxy sample should be performed as well. Better near infrared observations than the ones presented in this document are needed in order to perform the Q_B analysis devised by Block & Puerari (1999). The determination of this value would give us confirmation that the bars in even the most strongly barred systems in the sample are not strong enough to have a great effect on the spiral structure of the galactic disks. Further optical observations at higher resolution than 2" will be necessary in determining the star formation properties of these galaxies as well as tracing dynamical resonances. We believe that we have tentative evidence for the location of corotation in NGC 6012, but confirmation will require a second method of determination, such as the B-R method put forth by Beckman (1991).

Optical observations with a resolution of at least 1" would be necessary for this determination.

The second track of future work would be the determination of a control sample. A set of barred grand design galaxies of similar sizes and masses has been selected from Elmegreen & Elmegreen (1982). This control set contains NGC's 2776, 3344, 3891, 4051, 4500, 4999, 5127, 5248, 5652, 5735, 5921, and 6004. Figure 12-14 shows the distribution of Elmegreen arm classes for this set. Figure 12-15 shows the distribution of Hubble class for these objects. Figure 12-16 shows the bar classification for this set. These control galaxies should be observed in the same three wavelength regimes as the barred, flocculent galaxies to determine their properties. Close attention should be paid to the number and types of HI companions possessed by these objects.

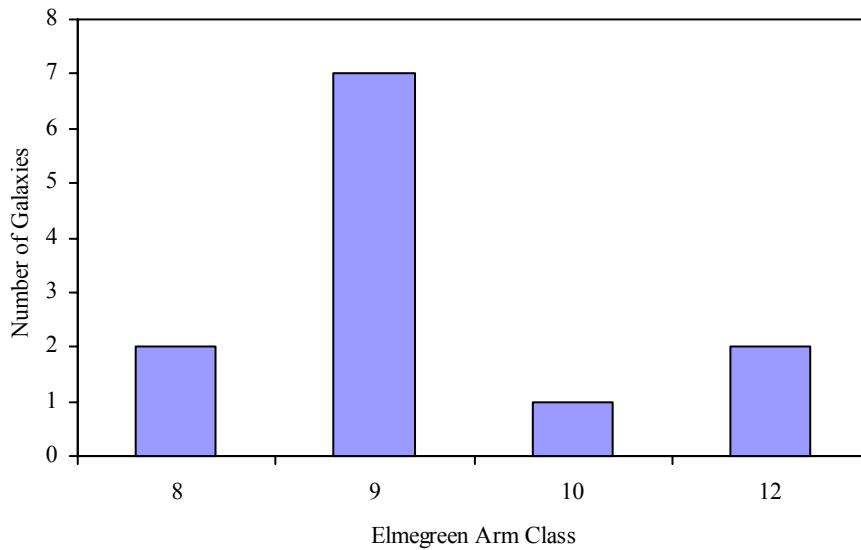


Figure 12-14. Distribution of Elmegreen arm classes in the control sample set

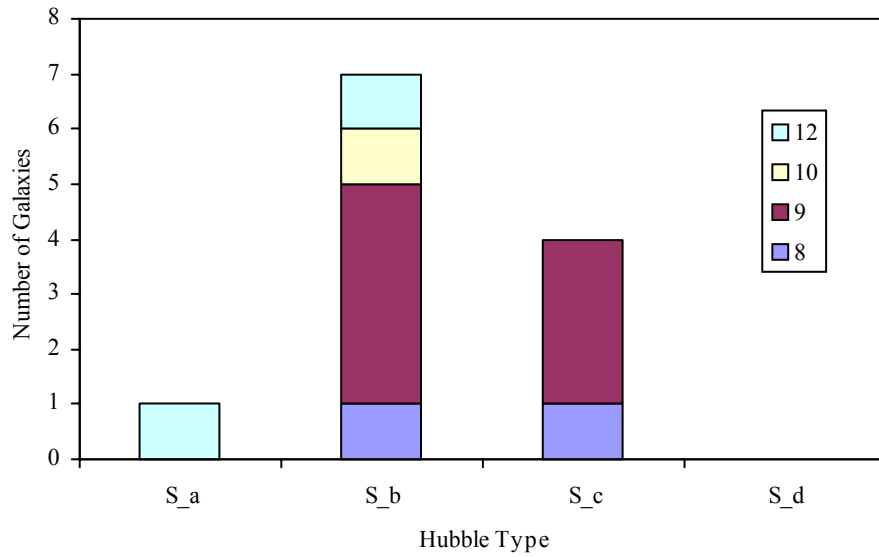


Figure 12-15. Distribution of Hubble Types in the control sample set. Strips across the columns represent the Elmgreen arm classes within the group.

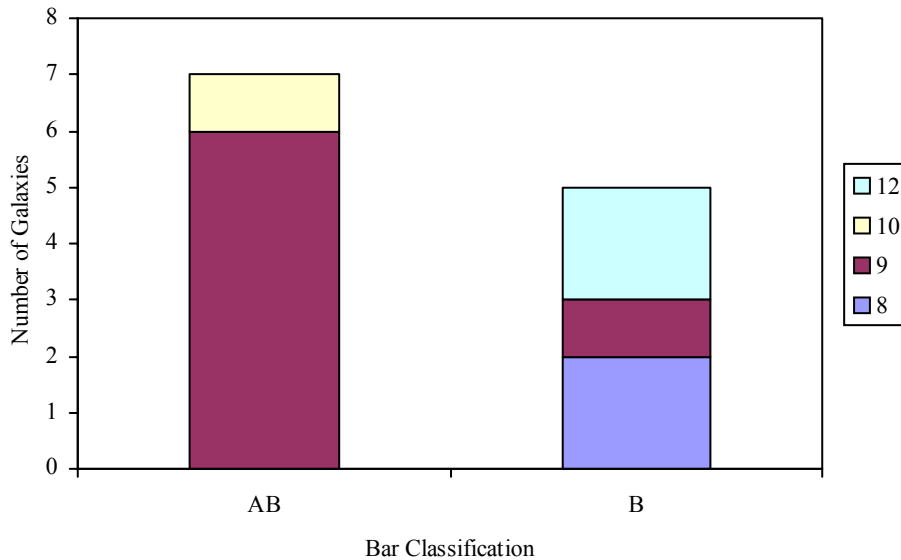


Figure 12-16. Bar classification distribution of the control sample. Strips across the column indicate the Elmgreen arm class of the control set.

The study of galaxy morphology and dynamics, although almost as old as modern astronomy itself, is still in many ways in its infancy. The study of galactic dynamics has tended to focus on large bright galaxies or active galaxies. It is reasonable to see why

this is so, but in order for a true global theory of galactic formation and dynamics to exist the smaller, less exciting galaxies, such as the ones in this project, must be examined as well. As we have discovered, many of these galaxies are very interesting in their own right, even if they are a bit off of the beaten path. An understanding of the processes that cause galaxies to look and move the way that they do today, will constrain theories about the formation of the universe as well as the formation of stars. This paper supports the study of all spiral galaxies regardless of morphology, and includes that study in our future work.

LIST OF REFERENCES

- Aguerri, J. A. 1999. *Astr. Ap.*, **351**, 43.
- Aguerri, J. A., Munoz-Tonon, C., Varela, A. M., and Prieto, M. 2001, *Astr. Ap.*, **361**, 841.
- Andersen, V. 1996, *A. J.*, **111**, 1805.
- Ashby, M. L., Hovek, J. R., and Matthews, K. 1995, *Ap. J.*, **447**, 545.
- Athanassoula, E. 1992, *M.N.R.A.S.*, **259**, 328.
- Beckman, J. E. 1991, In *Primordial nucleosynthesis and evolution of early universe*, (Proceedings of the International Conference Vol. 93), p. 23.
- Belfort, P., Mocharitch, R., and Deneffeld, M. 1987, *Astr. Ap.*, **176**, 1.
- Binney, J. and Tremaine, S. 1987, *Galactic Dynamics*, (Princeton: Princeton University Press).
- Block, D. L., Elmegreen, B. G., and Wainscoat, R. K., 1996, *Nature*, **381**, 674.
- Block, D. L. and Puerari, I., 1999, *Astr. Ap.*, **342**, 627.
- Brinks, E. and Bajaja, E. 1986, *Astr. Ap.*, **169**, 14.
- Broeils, A. H. and van Woerden, H. 1994, *Astr. Ap. Sup.*, **107**, 129.
- Byrd, G. and Howard, S. 1992, *A. J.*, **103**, 1089.
- Canzian, B. 1993, *Ap. J.*, **414**, 487.
- Castro-Rodriguez, N., Lopez-Corredoira, M., Sanchez-Saavedra, M. L. and Battaner, E. 2002, *Astr. Ap.*, **391**, 519.
- Casuso, E. and Beckman, J. 2001, *Ap. J.*, **557**, 681.
- Cepa, J. and Beckman, J. 1990, *Astr. Ap.*, **239**, 85.
- Cepa, J., Prieto, M., Beckman, J., and Munoz-Tunon, C. 1988, *Astr. Ap.*, **193**, 15.
- Chapelon, S., Contini, T., and Davoust, E. 1999, *Astr. Ap.*, **345**, 81.
- Christiansen, W. N. and Hogbom, J. A. 1985, *Radiotelescopes*, (New York: Cambridge University Press).
- Condon, J. J., Frayer, D. T., and Broderick, J. J. 1991, *A. J.*, **101**, 362.
- Corbelli, E. and Schneider, S. E., 1990, *Ap. J.*, **356**, 14.

- David, C. P., Jones, C., and Forman, W. 1992, *A. J.*, **388**, 82.
- Debattista, V. and Sellwood, J. 2000, *A. J.*, **543**, 704.
- Devereux, N. 1989, *Ap. J.*, **346**, 126.
- Elmegreen, B. G. and Elmegreen, D. M. 1985, *Ap. J.*, **288**, 438.
- Elmegreen, B. G. and Elmegreen, D. M. 1989, *Ap. J.*, **342**, 677.
- Elmegreen, B. G. and Salzer, J. D. 1999, *A. J.*, **117**, 764.
- Elmegreen, B. G. and Thomasson, M., 1993, *Astr. Ap.*, **272**, 37.
- Elmegreen, D. M. 1981, *Ap. J. Sup.*, **47**, 229.
- Elmegreen, D. M. and Elmegreen, B. G. 1982, *M.N.R.A.S.*, **201**, 1021.
- Elmegreen, D. M. and Elmegreen, B. G. 1983, *Ap. J. Sup.*, **54**, 127.
- Elmegreen, D. M. and Elmegreen, B. G. 1987, *Ap. J.*, **314**, 3.
- Elmegreen, D. M. and Elmegreen, B. G. 1990, *Ap. J.*, **364**, 412.
- Elmegreen, D. M., Elmegreen, B. G., Chromey, F. R., Hasselbacher, D. A., and Bissel, B. A. 1996, *A. J.*, **111**, 1980.
- England, M. N. 1986, *Kinematics and Dynamics of Barred Spiral Galaxies*, (Gainesville: University of Florida).
- Eskridge, P. B., Frogel, J. A., Pogge, R. W., Quillen, A. C., Berlind, A. A., Davies, R. L., DePoy, D. L., Gilbert, K. M., Houdashelt, M. L., and Kuchinski, L. E. 2002, *Ap. J. Sup.*, **143**, 73.
- Florkowski, D. R. 1980, Ph.D. Thesis, University of Florida.
- Fomalont, E. B. and Perley, R. A. 1989, In *Synthesis Imaging in Radio Astronomy*, eds. R. A. Perley, F. R. Schwab, and A. H. Bridle (ASP Conference Series Vol. 6), p. 83.
- Fraternali, F., van Moorsel, G., Sancisi, R., and Oosterloo, T. 2002, *A. J.*, **123**, 3124.
- Frogel, J. A., Quillen, a. C., and Pogge, R. W., 1996, in *New Extragalactic Perspectives in New South Africa*, ed. Block, D.(Kluer: Dordecht), p. 65.
- García-Ruiz, I., Kuijken, K., and Dubinski, J. 2002a, *M.N.R.A.S.*, **337**, 459.
- García-Ruiz, I., Sancisi, R., and Kuijken, K. 2002b, *Astr. Ap.*, **394**, 726.

- Gerritsen, J. P. and Icke, V. 1997, *Astr. Ap.*, **325**, 972.
- Giraud, E. 1986, *Astr. Ap.*, **167**, 25.
- Grosbol, P. J. 1985, *Astr. Ap. Sup.*, **60**, 261.
- Grosbol, P. J. and Patsis, P. A. 1998, *Astr. Ap.*, **336**, 840.
- Haynes, M., van Zee, L., Hogg, D. E., Roberts, M. S., and Maddelena, R. J. 1998, *A. J.*, **115**, 62.
- Hjellming, R. M. and Bignell, R. C. 1982, *Science*, **216**, 1279.
- Huchtmeier, W. K. and Richter, O. 1989, *Astr. Ap.*, **210**, 1.
- Hunter, J. H. and Gottesman, S. T. 1996, in *Barred Galaxies*, eds. R. Buta, D. A. Crocker and B. G. Elmegreen (Astronomical Society of the Pacific Conference Series, Vol. 91) p. 398.
- Jorsater, S., and van Moorsel, G. A. 1995, *A. J.*, **110**, 2037.
- Jungwiert, V., Combes, F., and Axon, D. J., 1997, *Astr. Ap. Sup.*, **125**, 479.
- Kandalyan, R. A., Al-Naimiy, H. M., and Khassawneh, A. M., 2000, *Astr. and Space Science*, **273**, 105.
- Knapen, J. H. 1997, *M.N.R.A.S.*, **286**, 403.
- Kormendy, J. and Norman, C. A. 1979, *Ap. J.*, **155**, 721.
- Laine, S. and Heller, C. H. 1999, *M.N.R.A.S.*, **308**, 557.
- Laine, S. and Gottesman, S. T. 1998, *M.N.R.A.S.*, **297**, 1041.
- Lewis, B. M. 1987, *Ap. J. Sup.*, **63**, 515.
- Lewis, B. M., Helou, G., and Salpeter, E. E. 1985, *Ap. J. Sup.*, **59**, 161.
- Lopez-Corredoira, M., Cabrera-Lavers, A., Garzon, F. and Hammersley, P. L. 2002, *Astr. Ap.*, **394**, 883.
- Maloney, P. 1993, *Ap. J.*, **414**, 41.
- Marquez, I. and Moles, M. 1996, *Astr. Ap. Sup.*, **120**, 1.
- Martin, P. 1995, *A. J.*, **109**, 2428.
- Martin, P. and Friedli, D. 1999, *Astr. Ap.*, **346**, 769.

- Martinet, L. and Friedli, D. 1997, *Astr. Ap.*, **323**, 363.
- Mazzarella, J. M., Bothem, G. D., and Boroson, T. A. 1991, *Ap. J. Sup.*, **62**, 751.
- Mazzei, P., Curir, A., and Bonoli, C. 1995, *A. J.*, **110**, 559.
- Mihalas, D. and Binney, J. 1981, *Galactic Astronomy: Structure and Kinematics*, (San Francisco: W. H. Freeman and Co.).
- Mihos, C. and Hernquist, L. 1994, *Ap. J.*, **425**, L13.
- Moore, E. M. and Gottesman, S. T. 1998, *M.N.R.A.S.*, **294**, 353.
- Patsis, P. A. and Athanassoula, E. 2001, *Astr. Ap.*, **358**, 45.
- Pisano, D. J. and Wilcots, E. M. 1999, *A. J.*, **117**, 2168.
- Pisano, D. J. and Wilcots, E. M. 2003, *Ap. J.*, **584**, 228.
- Pisano, D. J., Wilcots, E. M., and Elmegreen, B. G. 1998, *Ap. J.*, **115**, 975.
- Puxley, P. J., Hawarden, T. G., and Mountain, C. M. 1988, *M.N.R.A.S.*, **231**, 465.
- Rautiainen, P. and Salo, H. 2001, *Astr. Ap.*, **362**, 465.
- Rhee, M. H. and van Albada, T. S. 1996, *Astr. Ap. Sup.*, **115**, 407.
- Roberts, M. S. and Haynes, M. P. 1994, *Ann. Rev. Astr. Ap.*, **32**, 115
- Romanishin, W. 1985, *Ap. J.*, **289**, 570.
- Romanishin, W. 1990, *A. J.*, **100**, 373.
- Roussel, H., Sauvage, M., Vigroux, L., Bosma, A., Bonoli, C., Gallais, P., Hawarden, T., Madden, S., and Mazzei, P. 2001, *Astr. Ap.*, **372**, 406.
- Rush, B., Malkan, M. A., and Spinoglio, L. 1993, *Ap. J. Sup.*, **89**, 1.
- Sakamoto, K. 1996, *Ap. J.*, **471**, 173.
- Sanders, D. B., Scoville, N. Z., and Soiter, B. T. 1991, *Ap. J.*, **370**, 158.
- Seigar, M. S. and James, P. A. 1998a, *M.N.R.A.S.*, **299**, 672.
- Seigar, M. S. and James, P. A. 1998b, *M.N.R.A.S.*, **299**, 685.
- Sellwood, J. 1993, *P.A.S.P.*, **105**, 648.
- Sellwood, J. and Sparke, L. 1988, *M.N.R.A.S.*, **231**, 25.

- Sperandio, M., Chincarini, G., Rampazzo, R., and de Souza, R. 1995, *Astr. Ap.*, **110**, 279.
- Stark, A. A., Elmegreen, B. G., and Chance, D. 1987, *Ap. J.*, **322**, 64.
- Tenorio-Tagle, G. and Bodenheimer, P. 1988, *Ann. Rev. Astr. Ap.*, **26**, 145
- Thompson, L. 1977, *Ap. J.*, **211**, 684.
- Thornley, M. D. 1996, *Ap. J.*, **465**, 45.
- Thornley, M. D. and Mundy, L. G. 1997, *Ap. J.*, **484**, 202.
- Tully, R. B. 1988, *Nearby Galaxies Catalog*, (New York: Cambridge University Press).
- van den Bergh, S. 1995, *A. J.*, **110**, 613.
- van der Hulst, T. and Sancisi, R. 1988, *A. J.*, **95**, 1354.
- Warmels, R. H. 1988, *Astr. Ap. Sup.*, **73**, 453.
- Warner, P. J., Wright, M. C. H., and Baldwin, J. E. 1973, *M.N.R.A.S.*, **163**, 163.
- Xu, C., Lisenfeld, U., and Wunderlich, E. 1994, *Astr. Ap.*, **282**, 19.
- Zaritsky, D., Kennicutt, R. C., and Huchra, J. P. 1994, *Ap. J.*, **420**, 87.

BIOGRAPHICAL SKETCH

Douglas L. Ratay was born on August 16, 1976, in Pittsburgh, Pennsylvania. He attended Washington Elementary, Pine Middle, Richland High, and Pine-Richland High during his childhood in the northern suburbs of Pittsburgh. In 1994, he began studies at Connecticut College in New London, Connecticut. During college, Doug spent a semester studying physics at University College London in London, England. He graduated with honors and distinction in May of 1998 from Connecticut College, with a Bachelor of Arts degree in Physics. He began graduate school at the University of Florida in Gainesville, Florida in September of 1998, obtaining a Master of Science degree in Astronomy in May of 2000. In the spring and summer of 2001, Doug studied astronomy at the Instituto de Astrofisica de Canarias in Tenerife, Spain. Outside of the astronomical research world, Doug has been the Science Education Director at O2BKids in Gainesville, Florida, an intern with the Education Trust in Washington, D.C., and an active participant in astronomy outreach programs in local schools. He also has served as the president of the Graduate Student Council and as a member of the Student Senate at the University of Florida. He received his Ph.D. in August of 2004 from the University of Florida. He plans to move to Washington, D.C. to work in the field of science education policy and government.